8-2009

Structure and Properties of Nanoclay Reinforced Polymer Films, Fibers and Nonwovens

Raghavendra Ratnakar Hegde
University of Tennessee - Knoxville, indrahegde@gmail.com

To the Graduate Council:

I am submitting herewith a dissertation written by Raghavendra Ratnakar Hegde entitled "Structure and Properties of Nanoclay Reinforced Polymer Films, Fibers and Nonwovens." I have examined the final electronic copy of this dissertation for form and content and recommend that it be accepted in partial fulfillment of the requirements for the degree of Doctor of Philosophy, with a major in Polymer Engineering.

Gajanan Bhat,, Major Professor

We have read this dissertation and recommend its acceptance:

Roberto Benson, Joseph Spruiell, David Joy

Accepted for the Council:

Carolyn R. Hodges

Vice Provost and Dean of the Graduate School

(Original signatures are on file with official student records.)

To the Graduate Council:

I am submitting herewith a dissertation written by Raghavendra Ratnakar Hegde entitled "Structure and Properties of Nanoclay Reinforced Polymer Films, Fibers and Nonwovens." I have examined the final electronic copy of this dissertation for form and content and recommend that it be accepted in partial fulfillment of the requirements for the degree of Doctor of Philosophy, with a major in Polymer Engineering.

Gajanan Bhat, Major Professor

We have read this dissertation
and recommend its acceptance:

Roberto Benson

Joseph Spruiell

David Joy

Accepted for the Council:

Carolyn R. Hodges, Vice Provost and
Dean of the Graduate School

(Original signatures are on file with official student records.)

STRUCTURE AND PROPERTIES OF NANOCLAY REINFORCED POLYMER FILMS, FIBERS AND NONWOVENS

A Dissertation
Presented for the
Doctor of Philosophy
Degree
The University of Tennessee, Knoxville

Raghavendra Ratnakar Hegde
August 2009

With

Eternal Love and Respect to

My

Mother – Geeta Ganapati Bhat

ACKNOWLEDGEMENTS

I would like to express sincere thanks to following people who made this work possible: First my academic adviser, Dr. Gajanan Bhat, for his advice, guidance and encouragement throughout the PhD studying. I am also grateful to all of my committee members-Dr. Joseph Spruiell, Dr David Joy and Dr. Roberto S. Benson for all the invaluable source of advice and support to my research. Dr Svetlana Zivanovic for allowing to access characterization facilities in Food science and Technology laboratory. I would like to thank the staff and professors of TANDEC for their help through this research. Special thanks to Van Brantley for training me to become acquainted with all nonwoven testing instruments. Thanks to Dr. Bhushan Deshpande who is one of the industrial advisors for my PhD degree, for his active participation, providing raw materials and important input for this research. Also don't want to miss an opportunity to express thanks to Dr. Joseph Spruiell for training me to use x-ray characterization facilities.

I am truly thankful to Dr.Dayakar Penumadu for providing the financial support for the last semester of my PhD degree. The financial support for this research from Techmer PM through the Center for Materials Processing (CMP) is truly appreciated. Also special thanks to Techmer PM for providing the polymer concentrates and the nanoclay reinforced samples.

Finally and most importantly, I express my special gratitude to my mother Geeta G Bhat, wife Dhanu Hegde, sister Ramya Hegde for their constant support, love and encouragement.

Thanks to Vanitakka, Bava, Sneha and Sunay in Knoxville for all their love and encouragement during my stay in Knoxville and making me feel at home every time I visited them. Thanks to all my colleagues and friends in Knoxville who helped me in various ways and made my stay enjoyable at The University of Tennessee.

ABSTRACT

In this research, influence of different levels of Closite Na^+ additives on the microstructure, morphology and mechanical properties of polymer products was studied. Importance was given to understand the additive level, extent of dispersion in matrix, change in microstructure and respective property observed in the end product. Polypropylene spunbond and meltblown web samples with various levels of Closite Na^+ additives were produced and characterized. Injection molded polypropylene nanocomposite with 1 to 15 wt% nanoclay additives were also prepared and characterized for microstructure and mechanical properties.

Crystallization kinetics studies showed significant increase in crystallization rates on nylon 6 even at 0.25 wt % additives. Near surface and bulk stiffness of the film significantly increased in the presence of nanoclay additives. Intercalated and flocculated morphology was observed for all the polypropylene concentrate and the same morphology was retained in spunbond fibers also. About 25 to 30 % increase in cross direction tear strengths were observed for 1 to 2 wt % clay loading. Fibers with even as low as 1 % clay retains their morphology and integrity in bond point after thermal bonding. At higher weight percentage, stiffness of webs significantly increased and tear strength of webs decreased due to exclusion of excess clay platelets in the interspherulite regions.

Property benefits were not observed in the case of melt blown samples with nanoclay additives, but the additives were well dispersed in the fiber web. Compared to control meltblown webs, stiff and open web structure with high irregularity was obtained for samples with clay additive.
In case of injection-molded polypropylene composite, significant increase in breaking energy was observed for sample with just with 1 wt % clay additive. At higher weight percentage, segregation was observed in the inter-spherulitic region and failure mode shifted from ductile to brittle.

TABLE OF CONTENTS

Chapter Page No

LIST OF TABLES

LIST OF FIGURES

Abbreviations

PPCN-Polypropylene/montmorillonite nano-composites
PLSN- Polymer-layer silicate nanocomposites
MMT-Montmorillonite
OMMT-Organo-montmorillonite
PP/MMT-Polypropylene/montmorillonite
PET- Poly (ethylene terephthalate)
PP- Polypropylene
i-PP- isotactic Polypropylene
N6-Nylon 6
ΔG –Free energy
ΔH–Entropy
AFM-Atomic force microscopy
DSC-Differential scanning calorimetry
TGA-Thermo gravimetric analysis
TMA-Thermo mechanical analysis
EDS- Energy dispersive spectrometers
MB-Melt blowing
SB- Spunbonding
Control PP - Commercial spunbond grade 35MFR polypropylene-PP 3155
Closite Na+- Natural nanoclay
Closite 15A- Organo modified nanoclay
m-PP- Maleated polypropylene
PP-Polypropylene
GSM-Grams per square meter
MFR- Melt flow rate
TEM -Transmission Electron Microscope
WXRD -Wide angle X-ray Diffraction
FWHM-full width half maximum
PD1/PD2- proprietary dispersion agent used by Techmer PM to produce samples

CHAPTER I

1. INTRODUCTION

With increasing demand for high performance materials, the focus of recent research has been to produce products with enhanced properties at minimal changes in the equipment, process and cost of inputs. In an attempt to achieve these objectives, researchers are investigating various polymer nanocomposites with different additives. In the last 20 years, there has been tremendous research and development interest in polymer nanocomposites (PNC). Polymer nanocomposites are polymers (thermoplastics, thermosets or elastomers) that have been reinforced with small quantities (less than 5% by weight) of very high aspect ratio (l/t > 300) fillers in the matrix. Since past two decades, incorporation of inorganic particles such as mica, talc, $CaCO_3$ and glass beads to enhance toughness, and stiffness has increased. Superior mechanical properties have been achieved with poly (vinyl chloride) (PVC)/$CaCO_3$,[1] high-density polyethylene (HDPE)/$CaCO_3$, nylon-6/$CaCO_3$[2-4], HDPE/glass bead and poly (propylene) (PP)/ $CaCO_3$[5, 6]. Advances in microscopy: scanning tunneling microscopy, scanning electron microscopy and transmission electron microscopy have led to a deeper understanding of polymer nanocomposites. With these powerful characterization tools, scientists are able to better comprehend and account surface topology, structure and morphology up to atomic scale [7].

Among different types of fillers, those based on clay and natural silicates are very widely used because of their abundance and easy availability[8]. Polymer silicate nanocomposites are new class of multifunctional materials filled with the nanoclay with few nanometer thickness and hundreds to thousands of nanometer in length. These composites are formed by intercalation of polymers within the platelets of fillers. Uniformly dispersed nanoclay of very high aspect ratio has proved to provide a wide variety of added advantages by the combination of mechanical, thermal, electrical, optical and several other physical properties to the material [9,10]. Continual studies have shown enhanced properties in final products derived by loading nanoclay just as low as 0.5 wt % compared to conventional composites with large amount of micron size additives fillers such as metal, glass and wood particles[11, 12].

Nanoclay is derived from montmorillonite, a mineral deposit that has layered structure of dimension around 1 nm thick and a specific surface area of 700-800 m^2/g[13]. Nanoclay is currently being used to improve modulus and tensile strength, barrier properties, flame resistance, and thermal properties of many plastics.

There is continuing effort to take advantage of recent advances in nanotechnology, in the textile industry. P. Persico et. al. studied the possible use of melt compounded nylon 6 nanocomposite with different percentage of clay/jajoba oil for cosmetotextile application. They studied the desorption of oil from nanoclay composite fiber with different morphology[14]. Study of the structure and properties of polypropylene/montmorillonite hybrid composite and melt spun fibers showed that good intercalation of clay in PP matrix improves the spinnability[15]. It has been claimed that the addition of clay slightly reduced the viscoelasticity due to disruption of chain entanglement by high aspect ratio of clay platelets, and also eliminates the surface melt fracture, and postpones the critical shear rate for onset of melt fracture[16]. At same draw ratio, fiber with clay had higher crystallinity, lower orientation, improved moisture absorption and dye affinity[17].

Even though significant literature is available to demonstrate the improvements in properties from nanoclay additives, polymer products manufactured using different processing condition using concentrates produced in industrial environment are still not addressed. Influence of clay additives on the processibility, microstructure, and properties of blown films has not been studied. Effect of different processing conditions, dispersion agents on the extent of additive dispersion and respective property benefits is not reported.

The main objective of the investigation was to understand the influence of nanoclay additive on the processing behavior, structure and properties of nylon and polypropylene products. It is believed that by using suitable additives, or by process modification, one can achieve good dispersion of nanoclay in polymeric products, and achieving good dispersion or intercalation will result in improved properties of the products. This research was conducted to examine if clay dispersion/intercalation is successfully accomplished and if so, weather they result in property improvement. Specifically these investigations were done with nylon 6 and polypropylene with various levels of nanoclay and processing aids.

CHAPTER II

LITERATURE REVIEW

2.1. Nanoclay

Clay is a weathering product produced by disintegration and chemical decomposition of igneous rocks with fine texture of particle size less than 0.002 mm (2 micron). Finest part of clay is similar to colloid, with fine grain size, stickiness, and plasticity characteristics when wet[18].

There are two main types of clay structures 1:1 kaolinite type and 2:1 layer silicates. Both contain stacks of layers held together by hydrogen bond (as in 1:1) or by interlayer cations (as in 2:1). Kaolinite 1:1 consists of metal-hydroxide and silicon-oxygen network of sheets fused together by hydrogen bonding as shown in Figure 2.1 (a). The 2:1 layer silicates include mica, smectite, vermiculite, and chlorite. Smectite group is further divided into montmorillonite (MMT), nontronite, saponite and hectorite species [19,20].

Among these layered silicates, MMT is widely used as reinforcement for the polymer–clay nanocomposite synthesis because it is environmentally friendly, readily available in large quantities at a relatively low cost, and its intercalation chemistry is well understood [21].

Montmorillonite is extremely fine-grained, do not form macroscopic crystals and swell on addition of water or organic liquids [22, 23]. Montmorillonite is a 2:1 type consisting of two silicon-oxygen sheets held together by intervening cations with water molecules in the interlayer spaces. Schematic of MMT is shown in Figure 2.1 (b)[24].

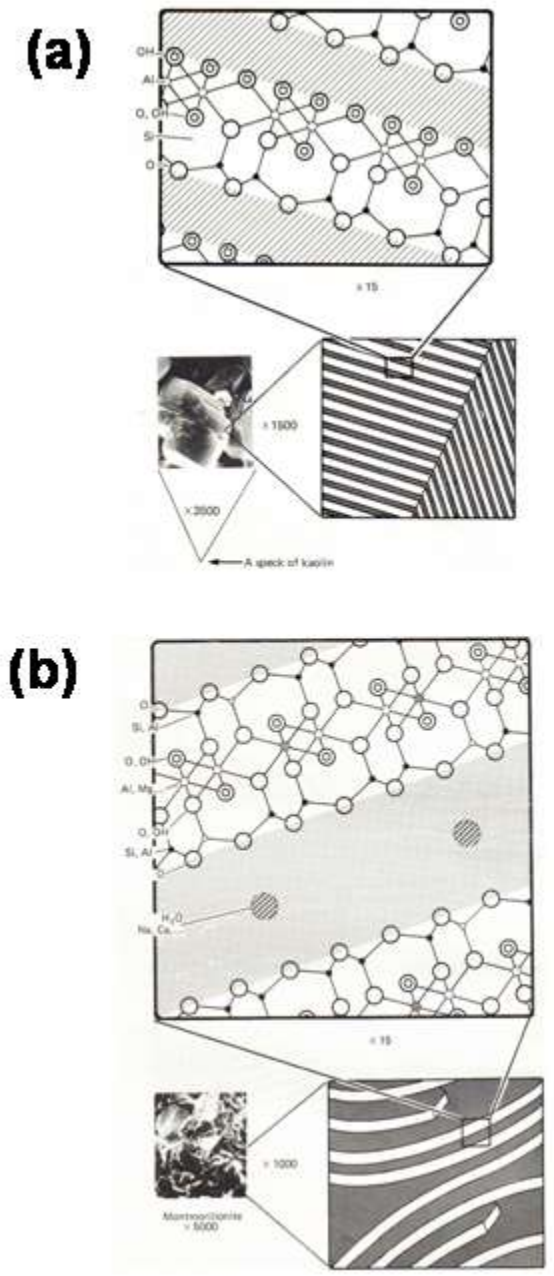

Figure 2. 1. Schematic of (a) Kaolinite (1:1 silicate layer) structure, individual layers made up of two kinds of network or sheet, metal hydroxide and silicon-oxygen, fused together, (b) montmorillonite structure, 2:1 layer silicate with two silicon-oxygen sheets in each layer)[24].

2.1.1 Crystal structure of sodium montmorillonite

Figure 2.2 illustrates the schematic crystal structure of sodium montmorillonite. Two outer tetrahedral layers, containing Si and O atoms, are fused to an inner octahedral layer, containing Al and Mg atoms that are bonded to oxygen or hydroxyl groups. Individual clay particle has "platey" structure with lateral dimention of 200 to 600 nanometers and thickness of only 0.96 nm[13].

These layers organize themselves to form stalks by van der waals force of attraction between them. Force of attraction occurs due to sharing of different forms of charge between them. Isomorphic substitution of charges between the layers for e.g., Al^{3+} replaced by Mg^{2+} or Fe^{2+} replaced by Mg^{2+} replaced by Li^{2+} generates negative charges that are counter balanced by the earth cations, Na_{+} or Ca_{2+} in between the layers. Small amount of cations on surface is balanced by majority of these cations located on inside galleries. So in pristine form, clay is hydrophilic (platelets contain Na^{+} or K^{+} ions)[25]. The attraction force between layers is relatively weak so polymer molecules can be intercalated between them[8,21, 26]. Charge on the surface is expressed as cation exchange capacity (CEC) meq/100 g[27].

In natural form, clay can disperse only in hydrophilic polymers like Poly (ethylene oxide) and Poly (vinyl alcohol) [28, 29]. In order to render the surface more organophilic, hydrated cations of clay surface are replaced by cationic surfactants (alkylammonium or alkylphosphonium/ onium) to lower the surface energy. Sodium ions in natural clay are exchanged with an amino acid such as 12-aminododecanoic. Schematic of reaction is shown in Equation 1 [30].

Equation 1. Modification of natural clay

$$Na^{+}\text{- Clay} + HO_2C\text{-R-}NH_3{}^{+}Cl^{-} \longrightarrow HO_2C\text{-R-}NH_3 + \text{-CLAY} + NaCl$$

The cations receding between the layers cause the organic molecules to radiate away and increase the interlayer spacing between platelets.

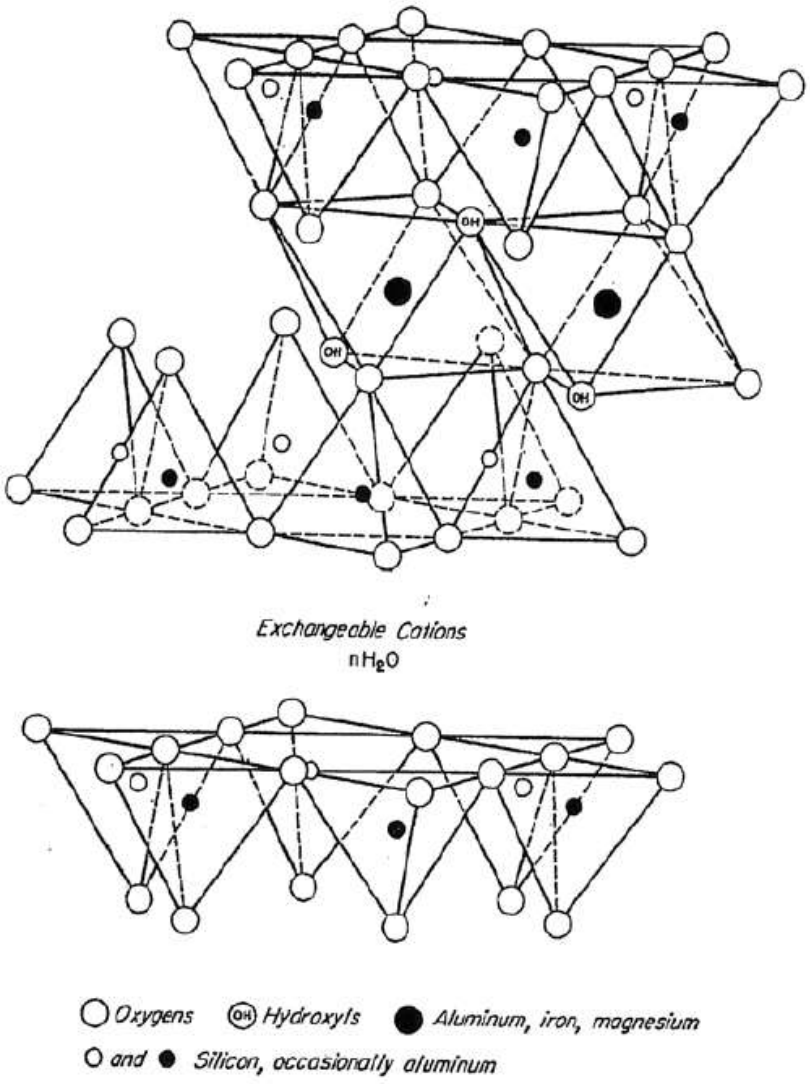

Figure 2. 2. Crystal structure of 2:1 sodium montmorillonite[13].

So modified clay is more compatible and facilitates the intercalation of polymer chain between the clay galleries. At a given temperature, layer spacing depends on the organic chain length and CEC of layered silicate. X-ray diffraction data have shown that based on the length of chain, packing density, polymer chains arrange to form mono or bimolecular tilted 'paraffinic' arrangement [31].

2.1.2 Different morphologies of melt blended nanocomposite

Advantage of clay compared to other mineral fillers for plastics, such as talc and mica, comes from its ability to be delaminated and dispersed into individual layers of the order of about 10Å thickness. Based on the extent of dispersion of platelets in matrix, polymer nanoclay based composites are classified in to three widely known morphologies: intercalated, exfoliated and delaminated, as shown in Figure 2.3. The term intercalation describes the case where a small amount of polymer chain seep in between clay galleries and cause about 20 – 30Å separation between the platelets. Un-separated clay layers and agglomerates in polymer matrix are often referred to as tactoids. Exfoliation or delamination occurs when polymer further separates the clay platelets, e.g., by 80 – 100Å or more. Delaminated structure refers to dispersion and homogeneous spreading of platelets in the polymer matrix beyond 100Å[32,33].

Nam et al.[11] have ascertained the hierarchical morphology of intercalated polypropylene/clay nanocomposites using wide angle x-ray scattering, small angle x-ray scattering, transmission electron microscopy, polarized optical microscopy and light scattering. Schematic of structure and representative values of these parameters are shown in Figure 2.4 (a) and (b.) [11]. In an intercalated structure, where the inter-layer spacing d(001) is usually 1–4 nm and in an exfoliated or partially exfoliated systems, the particle separation (ξp) is about 20–50 nm[34, 35].

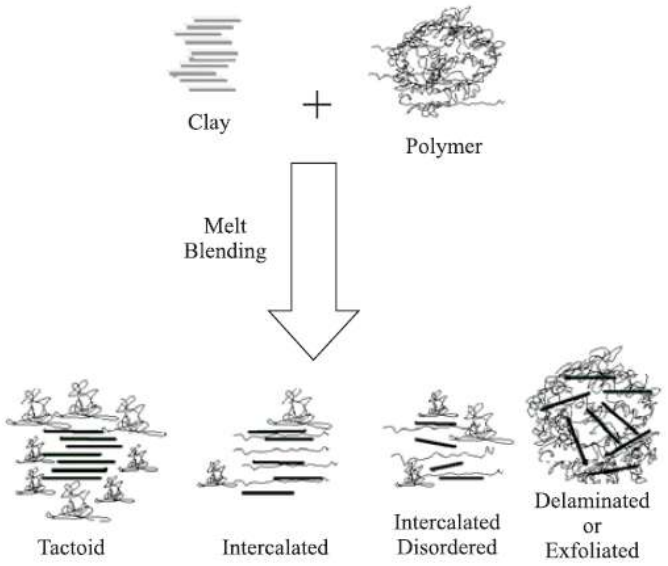

Figure 2. 3. Morphology of different melt blended polymer nanocomposite [33].

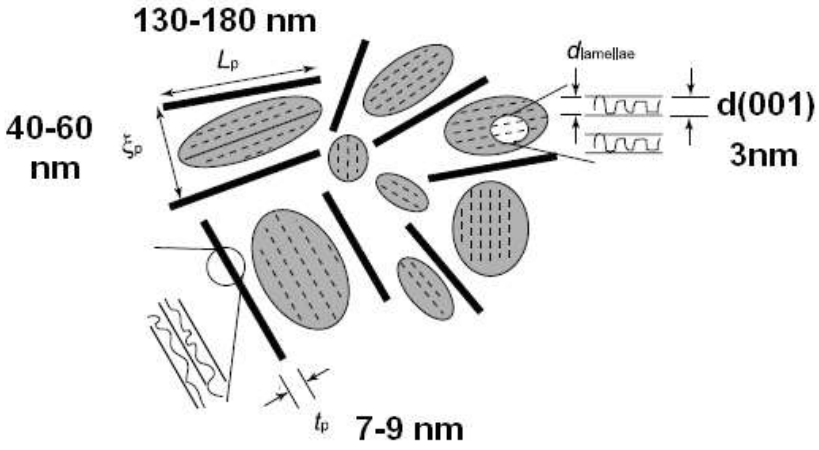

(b)

Symbol	Characteristic parameter	Typical value (nm)
L_p	Length of the dispersed clay particles	130–180
ξ_p	Correlation between particles (inter-particle spacing)	40–60
t_p	Thickness of the clay particles	7–9
$d_{(001)}$	Inter-layer spacing of the (001) plane in intercalated clay	3
$d_{lamellae}$	Average lamellae thickness of polymer matrix crystallite	7
$L_{lamellae}$	Long-period lamellae thickness of polymer crystallite	15

Figure 2. 4. (a) Schematic of hierarchical morphology and, (b) characteristic parameters for PPCN with 4 wt% clay[34, 35].

2.1.3 Influence of processing condition on nanoclay dispersion

Processing conditions have significant influence on the delamination and dispersion of clay additive in the matrix. Okamoto et. al investigated the elongational flow-induced structure formation of nanocomposites. Specimens elongated under high strain rate, showed alignment of silicate layers (edges) along stretching direction. Whereas specimen elongated at low strain rates, silicate layers (edges) align perpendicular to stretching direction[36].

S. G. Hatzikiriakos et. al., studied the effect of nanoclay additives on the processability of polyolefins[37]. According to their claim, addition of nanoclay eliminates the surface melt fracture and elevates the critical shear rate for onset of melt fracture. Higher melt viscosity is known to impose higher shear stresses to platelets during melt mixing in extruder. According to Newtonian law;

$$\text{Shear stress } \sigma = \eta \dot{\gamma} \quad \text{Equation 2}$$

Where, η- melt viscosity, γ-Shear rate,

The higher shear stress in the extruder breaks the organoclay particles into stacks of platelets or tactoids, which can be subsequently sheared apart into smaller platelets as shown in Figure 2.5 [33].

2.1.4 Thermodynamics of mixing

Dispersion of nanoclay in thermoset matrix can be predicted by thermodynamic principles. The free energy, ΔG for complete exfoliation of clay within polymer matrix is the sum of the free energy contributed by the polymer matrix (ΔG_{po}) and nanoclay (ΔGnc). For polymer matrix,

$\Delta G_{po} = \Delta H_{po} - T\Delta S_{po}$ Equation 3

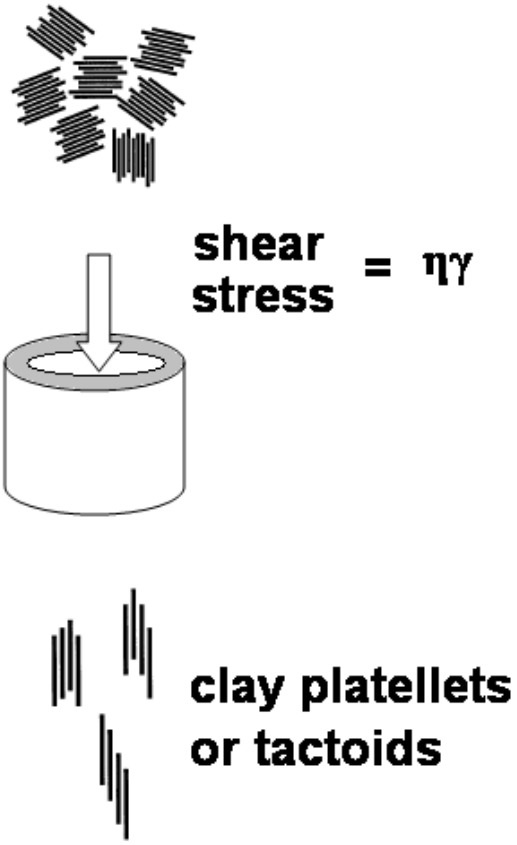

Figure 2. 5. Schematic of delamination and dispersion of clay platelets with shear rate[33].

For nanoclay additive,

$\Delta Gnc = \Delta H_{nc} - T\Delta S_{nc}$ Equation 4

The total free energy change is

$\Delta G_{total} = (\Delta H_{po} + \Delta H_{nc}) - T(\Delta S_{po} + \Delta S_{nc}) = \Delta H_{total} - T\Delta S_{total}$ Equation 5

$\Delta H_{po}\ (t \leq t_g) \geq \Delta H_{nc}$ Equation 6 [38].

The entropy change is negative when monomer or polymer chains penetrate into the crevices of nanoclay platelets, while expansion of the clay gallery shows positive entropy change. The extent of exfoliation depends on the total enthalpy. The condition for complete exfoliation is that the heat released due to polymerization within the intergallary before the gel point has to be larger than the van-der waals attractive energy between the interlayer.

2.2 Nylon 6 nanoclay composites

Nylon 6 is known for its strong hydrogen bond formation. Chains tend to maximize the number of hydrogen bonds within and between polymer chains. Physical properties of nylon-6 are largely governed by the hydrogen bond and nature of these hydrogen bonds. Maximization of hydrogen-bonds in the crystalline state requires the polyamide chains to adopt fully extended or twisted configuration [39]. Considerable portion of hydrogen bonds exist in the molten state. In the crystalline forms, all possible hydrogen satisfied and majority of hydrogen bonds are consummated in the amorphous regions [40].

Nylon 6 exhibits three different crystalline forms (α, β and γ) that are generally coexisting within the products at different percentage depending on the manufacturing and processing conditions [41]. Schematic of α-form and γ-crystalline forms of nylon 6 are shown in Figure 2.6 (b). Closed circles represents chain axes projecting out of page and open circles represents chain axes projecting into the page. The hydrogen bond between chains is represented by dashed line. To attain α-form, the chain has to be fully extended in anti-parallel fashion to form sheets of hydrogen-bonded chains.

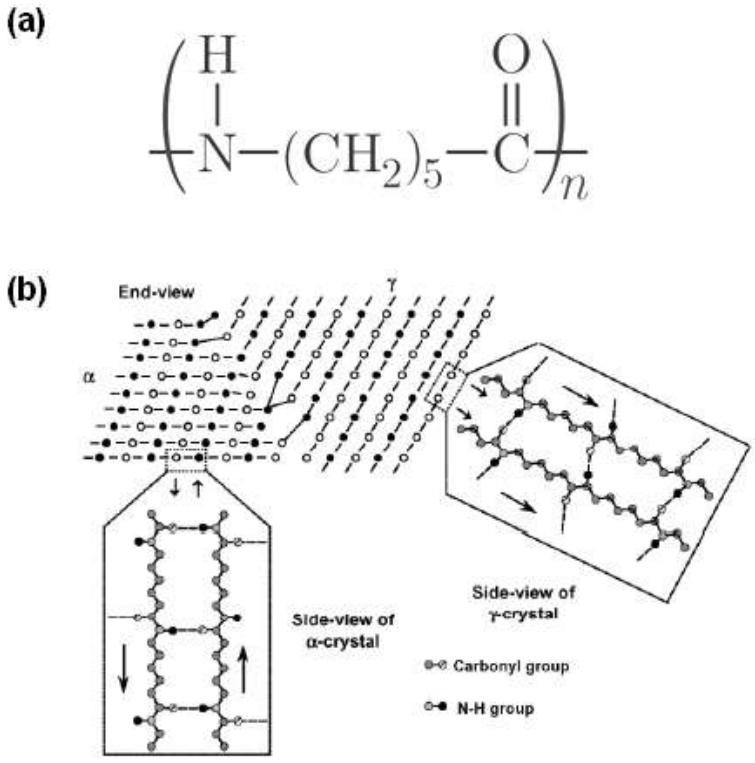

Figure 2. 6. Schematic of (a) nylon-6 chain (b) hydrogen bonding within α and γ -crystalline forms of nylon-6 [40, 42].

This structure repeats itself thereby creating stacks of H-bonded sheets in a monoclinic crystal. In case of γ-crystalline form of nylon 6, hydrogen bonds are formed between parallel polyamide chains, which require the amide (N-H) linkages to twist approximately 60° out the plane of these molecular sheets. Chain packing for the γ-form of nylon 6 closely resembles that of a hexagonal structure and is also referred to as pseudo-hexagonal[33, 43]. Processing conditions used during manufacturing greatly influences the crystalline forms. The γ-form crystals are observed in the case of quenching from the melt, while the α-form results from slow cooling of the melt [44].

Length of polymer chain also has influence on the crystal form[45]. The longer repeating units have higher tendency to assume the γ-crystalline configuration which might be due to the reduction of stress or steric hindrance caused by the rotation of the amide group around the C-CO and C-NH

single bonds to form a hydrogen bond between the adjacent parallel chains. Kamal et. al. have observed from infrared spectroscopy and crystallization kinetics experiments that the crystallization begins with the sterically favorable γ-form and assumes the thermodynamically stable α-form. Every chain has a statistically equal chance to meet a parallel adjacent chain and an antiparallel one, if the processing conditions favor the formation of the hydrogen bond between parallel chains, nylon 6 would crystallize to form the γ-form. Sudden cooling of nanocomposite melt crystallized to γ form[41].

The β-form has parallel and antiparallel stacking of chains which is similar to the γ-form from a crystallographic standpoint and it is closely related to the amorphous component from the standpoint of chain conformation [46, 47]. Thermal conditions, pressure, stress, atmospheric moisture, and additives influence the morphology of nylon 6 obtained by crystallized melt. The effect of crystallization time and temperature on the formation of the α-form and γ-crystalline forms has been studied before. It is reported that the crystallization for extend periods of time below 130°C leads to formation of γ-crystalline form [48-50], while above 190°C results in the α-form[39]. Temperature between 130 to 190°C is known to form a mixture of α and γ-forms. Rapid cooling or quenching of melt is known to form the γ-crystalline form[51]. Annealing of quenched samples, at 200°C for longer duration is known to transform crystal structure from the γ-form to α-form and transition is known to accelerate in the presence of high pressure[45, 52-54].

Tensile strengths of nanoclay based composites from PP, nylon-6, PMMA and PS have been compared. Among the different matrixes, nylon-6 nanoclay composite had the highest tensile stress at break compared to the rest. This high strength is due to the polar nature of nylon 6 and possible ionic bond between clay and nylon-6 chains [55,56]. Polymer chains in molten state diffuse from bulk to clay galleries. Hydroxyl groups in interlayer and surface of clay platelets act as reactive sites for nylon 6 chains[57,58]. Schematic of covalent bonding between nylon 6 and clay platelets is shown in Equation 7.

These branched lamellae are epitaxial growth (α'-form, γ-form) on the parent lamellae, which leads to shish-kebab structure, and leads enhanced mechanical properties to the nanocomposite [59]. Once the hydrogen bond formed on the platelet through nucleation, lamellar growth occurs on both sides of clay platelets, and along the sandwiched structure, branched lamellae are formed as

shown in Figure 2.7. This sandwich structure forms a rigid structure and imparts superior properties to the composite. Vanderhart et. al., concluded that the γ-crystallites reside near the polyamide-clay interface and the silicate layers promote the γ-formation in nanocomposite for both in-situ polymerization technique and melt intercalation technique[60].

Maiti et al., studied the crystallization behavior of nylon 6 nanocomposite. About 3.7 wt % of clay was enough to nucleate bulk sample. They reported 80°C higher heat of distortion temperature (HDT) of nylon 6-clay composite more than that of control nylon 6. Increase in HDT is due to psedo-hexagonal packing[59]. The nylon 6 nanocomposite exhibits very high mechanical (solid state storage modulus was ≈200-300% high) and thermal properties compared to polyolefin (≈70-80% and polyester (≈40-50%) composite[59].

Equation 7. Reaction between clay and modified nanoclay[57,58].

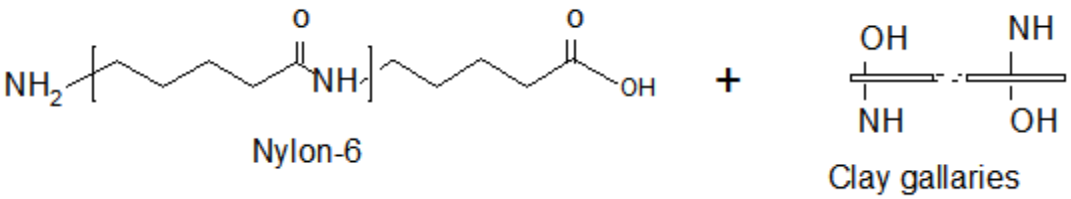

The barrier properties of the polymer films were enhanced by the incorporation of nanoclays in the polymer matrix. Schematic of the path of a diffusing gas through the polymer film with nanoclay additives is included in Figure 2.8. Total pathway of a diffusing gas given by Equation 8.

$$d' = d + d.L.\frac{V_f}{2W}$$ Equation 8

Where,

d - Thickness of the film,

L - Length of clay platelet,

W- Width of clay,

V_f- volume fraction of clay,

If nanoclay platelets are dispersed parallel in the polymer matrix, the torturous factor (τ) is given by Equation 9.

$$\tau = d'/d$$

$$\tau = 1 + (L/2W)V_f \quad \text{Equation 9}$$

Therefore, relative permeability coefficient is given by Equation 10.

$$P_c / P_p = 1/\lfloor 1 + (L/2W)V_f \rfloor \quad \text{Equation 10}$$

Equation is rough estimation of the mechanism of "tortuous path" in polymer nanocomposite films [61, 62].

2.2.1 Crystallization kinetics and melting behaviors of nylon 6 nanocomposites

It is well known that property of polymer material depends on the extent of crystallinity developed during manufacturing. Great deal of effort has been done to understand and to explain crystallization kinetics of nylon 6 and its nanocomposites[63-67]. Addition of small amounts of organoclay to each polyamide matrix results in a significant reduction in crystallization time; however, at higher percentage, clay additive retards crystallization.

Few studies reported slower crystallization of polymer nanocomposites compared to neat polymers. At lower weight concentrations, clay particles serve as nucleating agent; however, at high weight %, clay contents retard the growth process. At low concentration of clay, the distance between dispersed platelets is large so it is relatively easy for the additional nucleation sites to incorporate surrounding polymer chains.

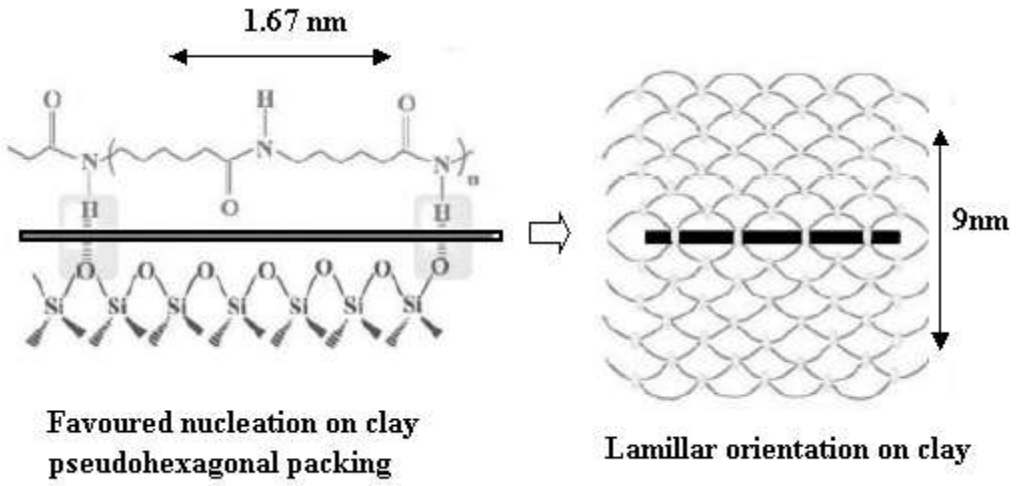

Figure 2. 7. Schematic of nucleation and growth in Nylon 6 nanocomposite [59].

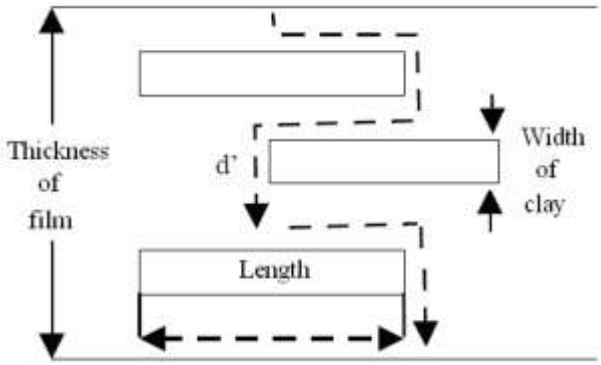

Figure 2. 8. Schematic of diffusion of gas through the polymer film with nanoclay additives.

But at high concentrations, diffusion of polymer chains to the growing crystallite is hindered by larger number of nucleation sites and limited crystal growth is expected to produce fine grain size crystals. Studies involving a variety of nucleating agents have shown that the maximum crystallization rate of nylon 6 occurs at additive concentrations in the range of 0.1–0.5 wt % [39, 68-71].

Yang et. al. reported the value of Avrami exponent (n) of 4 and 3 for neat nylon 6 and in PNC with 10% clay[72]. Hinrichsen and Lux reported a value of 3 for the Avrami exponent (n) for nylon-6 crystallization and between 1.2 and 6.0 for glass fiber reinforced composites[73]. The Avrami exponent n between 1.0 and 3.2 for the γ -form of control nylon 6 and between 0.9 and 2.6 for the γ-form in PNC, it was between 0.9 and 2.6. For the α-form of PA-6, n was between 1.0 and 2.1 and between 1.2 and 2.6 in the PNC[41].

Weng et al. studied the crystallization kinetics and melting behaviors of nylon 6/foliated graphite nanocomposites[65]. Plots of log [-ln (1-X (t))] versus log (t) for the nylon 6 samples are shown in Figure 2.9 (a) and (b). For the control nylon 6, the Avrami exponent changed progressively from 1.3 to 3.0 during the initial crystallization, but remained at about 3.2 over the range 10–75 % of the crystallization process. Beyond 75 %, exponent decreased to about 1.3, indicating a transition of mechanism of crystallization after a relative crystallinity of about 75 %. Nylon-glass fiber nanocomposite sample, did not show any secondary crystallization or roll-off at longer times, indicating that the growth of crystals in nylon 6/fiber glass nanocomposite melt is probably one dimensional, heterogeneous and simultaneous nucleation mechanism[74].

2.3 Polypropylene-nanoclay composites

Polypropylene is one of the most widely used polymers in industrial and home furnishing applications because of its low cost, high strength, toughness, low processing temperature and good chemical and fatigue resistance. Polypropylene is used for wide range of applications in the form of films, fibers, nonwovens and molded products[75].

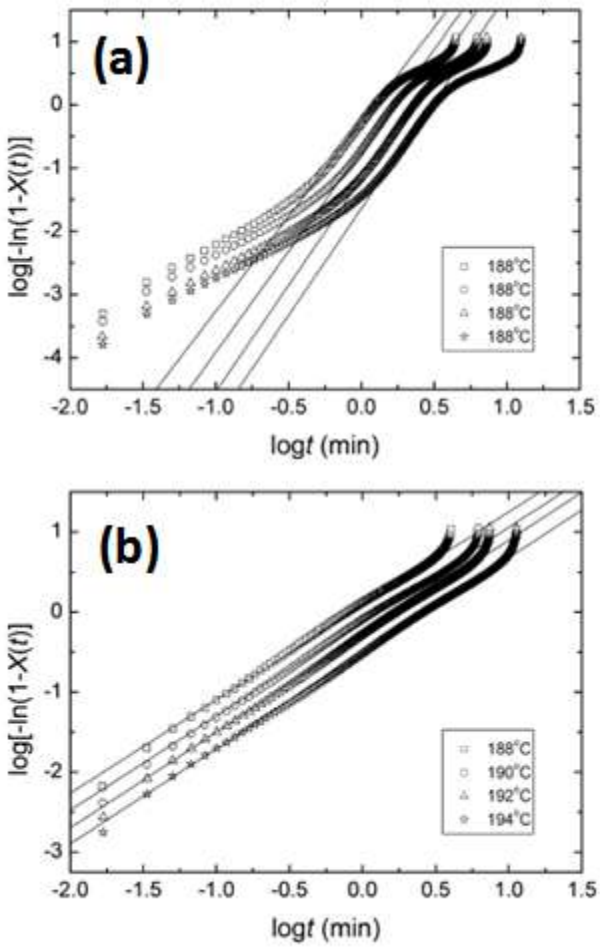

Figure 2. 9. plot of log [-ln (1-X (t))] versus log (t) for (a) neat nylon 6 (b) nylon 6/fiber glass nanocomposite [65].

Influence of clay loading on properties of polypropylene-clay nanocomposites has been studied by Liu et al., where they observed increase in tensile strength, modulus, storage modulus, and decrease in tan (δ), with 0 to 5 wt % clay additives[76]. Influence of nanoclay additive on crystallinity and crystal structure of melt compounded nylon nanocomposites has been carefully investigated by T.D Fornes et al. They found that the clay additive acts as a nucleating agent, increases crystallinity and enhances γ-crystal structure[39].

Strong interfacial interaction between the clay and polymer matrix results in increased impact strength. In the presence of clay additive, impact fracture was altered from craze initiation and propagation to microvoid-coalescence-fibrillation process[77]. It is well known that he large surface area of the fillers can give rise to improvements in properties, however high surface area and surface attraction between platelets can also result in agglomeration[78].

Yuan et al. have studied the effect of temperature and glass bead content on the brittle to ductile transition temperature (BDT) and thermo mechanical properties of glass bead reinforced polypropylene[79]. Strong interaction between the glass beads and polymer molecules was observed resulting in shift of glass transition temperature from 27.1°C to 35°C. Thermal stability/ HDT of PP was effectively increased with the incorporation of glass beads [79]. Yield strength of clay reinforced PP was higher than neat PP due to the interaction between the clay particle and polymer matrix[80].

2.3.1 Influence of clay additives on crystal structure of polypropylene

Isotactic polypropylene (i-PP) is known to develop polymorphism and contain α, β, γ and smectic psedohexagonal crystalline forms depending on the particular i-PP, and manufacturing conditions. Control PP shows pseudo hexagonal crystalline diffraction peak at 2θ of 15.02° and 21.04°.

PP/organo montmorillonite (OMMT) composite fibers exhibits different crystalline diffraction peaks. The nanocomposite fiber exhibits α- crystalline diffraction peak at 2θ of 14.26°, 17.05°, 18.70°, 21.76° and 25.59°, which appear under efficient crystallization conditions. Relative intensity of diffraction peaks for (040, 130, 111, 060) planes of composite fibers increased due to the nucleation and growth of PP crystals.

The α-crystalline form is the most frequently observed and thermodynamically stable. It has also the highest thermal and superior mechanical properties. The α-crystalline form is obtained through quiescent crystallization from the melt: as in uni-axial orientation, or melt spinning [81]. The β-(hexagonal) crystal form is favored by a number of conditions, namely, sudden quenching from the molten state [82], presence of nucleating agents[83], glass fiber reinforcement[84], ethylene co-monomers[85-87], and blending with ethyl vinyl alcohol[88]. The nanoclay additive at low concentrations is known to promote the formation of the β-structure[89]. The γ-crystalline form (triclinic) is the least frequently observed, and formed in the case of melt crystallized at high pressure or under restriction. The γ-crystalline forms were formed in PP/clay nanocomposite due to the restriction of chain movement[75, 90, 91]. The nanoclay additives is known to provides favorable sites for epitaxial growth of γ-phase because the lattice mismatch is less than10%[92].

2.3.2 Challenges involved in dispersion on nanoclay in polypropylene

In case of polypropylene nanocomposites, due to the limited to weak van der waals interactions of PP chains with the clay platelets, it is difficult for PP chains to intercalate between clay platelets. Silicate clay layers have polar hydroxyl groups, which make them incompatible with non-polar olefins. To achieve intercalation of the clay by a polyolefin requires the inclusion of a compatibilizer at the clay–polymer interface[58, 93-95]. Polypropylene-grafted-maleic anhydride (PP-*g*-MA) is one of the widely investigated compatibilizer in synthesis of blends of nylon 6-PP and melt extruded PP nanocomposite[96].

If PP-*g*-MA is used as a compatibilizer in case of nylon 6-PP blends, PP-*g*-MA reduces the interfacial tension between nylon 6 chains. The co-polymerization occurs in the melt state between amine end groups of nylon-6 chains and anhydride groups of maleated polypropylene (m-PP). These reactions occur at higher temperature of melt (t > 200 °C)[57, 58, 97, 98]. Schematic of maleated polypropylene (m-PP) dispersion on to clay galleries is shown in Equation (11) and Figure 2.10 [99].

Seo et al. compared the crystallization kinetics of i-PP and maleic anhydride grafted polypropylene (m-PP) and their blends[96]. Diffusional activation energy is lower for maleic

anhydride grafted polypropylene due to the formation of hydrogen bond between hydrolyzed maleic anhydride groups. Crystallization half time for m-PP was smaller than that of i-PP. Maleated polypropylene (m-PP) acts as nucleating agent and facilitates the crystallization kinetics. The radial growth rate of spherulite decreases due to the lower chain diffusion and thus results in formation of finer morphology [96].

In this research, linear low-density polyethylene (LLDPE) based maleated wax was used as a compatibilizer between polypropylene and Closite Na^+. Schematic of possible interaction between the clay platelet, PP chain and maleated wax is shown in Equation 12[99-101].

Baekjin et al. carefully investigated the crystallization kinetics of maleated polypropylene/clay hybrids. They found that crystallization rate of modified silicate hybrids was slower compared to natural nanoclay hybrids. Unmodified silicate platelets formed agglomerate and hence acted as nucleating agents whereas, the exfoliated modified silicate platelets acted as barrier for crystallization [102].

Influence of anhydride composition on the mechanical properties of polypropylene blends has been investigated before. Co-crystallization ability between the PP and maleated PP depends on the anhydride compatibilizer (wt% of anhydride). Blend with low-anhydride compatibilizer (0.2 wt% anhydride) facilitates finer morphology, higher fracture strains compared to high anhydride (2.7 wt% anhydride) compatibilizer.

Equation 11. Schematic of m-PP dispersion on to clay galleries [103, 104, 58.]

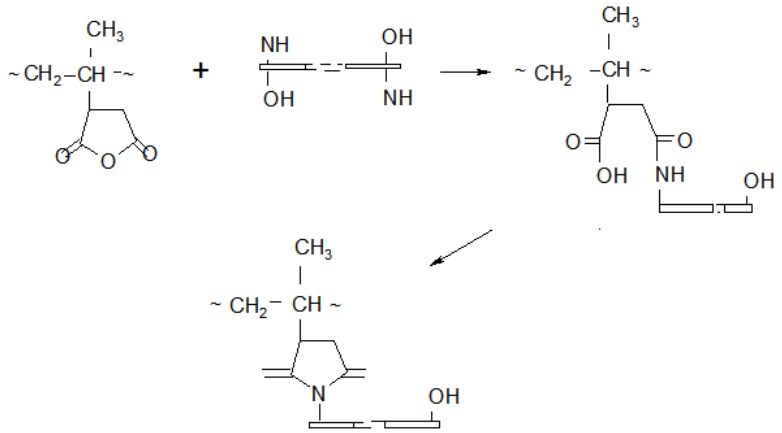

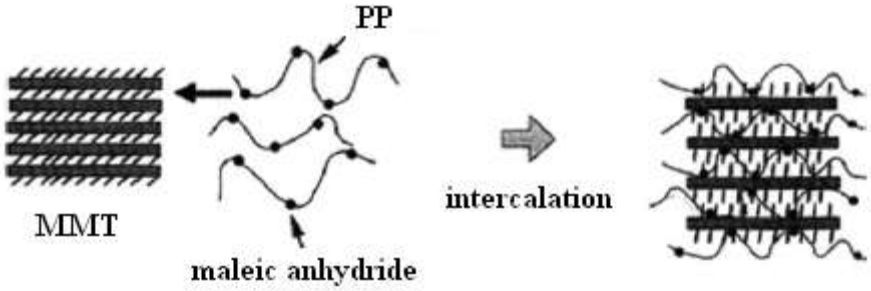

Figure 2. 10. Schematic of m-PP dispersion on to clay galleries [103].

Equation 12. Schematic of reaction between (a) maleic anhydride, LLDPE, (b) clay platelets and maleated wax and (c) clay, maleated wax, PP[100].

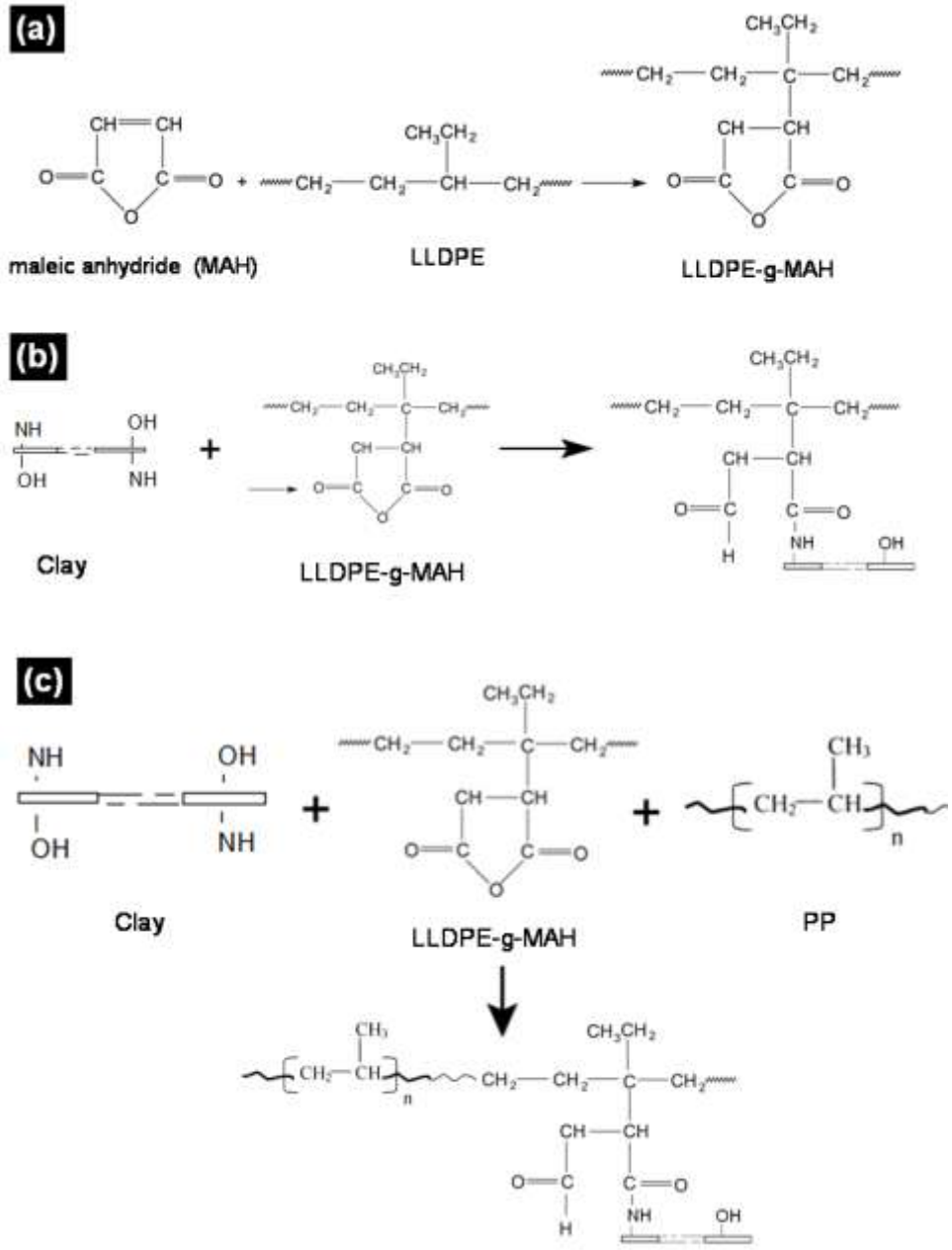

In a compression molded blend system with polypropylene and maleated polypropylene, better mechanical properties were achieved by intimate contact in melt state and subsequent cocrystallization of PP and anhydride by inter-diffusion of chains in the melt state. Higher wt% of anhydride results in phase separation at interface and decreases the adhesion strength[105]. Effect of maleated polypropylene compatibilizer on crystallization kinetics, spherulite morphology and mechanical properties needs to be explored further.

The crystallization behavior of polypropylene reinforced with conventional composites and nanocomposites has been extensively studied before[106-110]. The surface of the filler particles is known to act as nucleation site and influences the crystallization mechanism, the amount of crystallinity and crystal growth. Unit cell structure did not change from monoclinic, but the dimensions changed. This change in dimensions with the crystallization temperature (T_c) and clay content might be due to defects entering in to the lattice [111].

The extent of intercalation of polymer chains within the clay galleries depends on the duration of matrix polymer in molten state and amount of clay present in the system. Maiti et al. studied the effect of crystallization temperature and duration of molten state on the structure and morphology of PP/clay nanocomposite. They reported that by controlling the crystallization temperature, extent of intercalation, structure and morphology could be controlled[9].

At high temperatures, crystallization rate is slow; hence the polymer chains are in melt state for longer duration and have enough time to intercalate inside the galleries. Higher intercalation was observed in the case of nanocomposite with low weight % of clay because at lower wt %, most of the polymer chains were tethered to smaller amount of clay. Extent of segregation of clay particles also depend on the processing conditions. Higher segregation of clay particles is observed at higher crystallization temperatures due to the existence of molten state for longer time. At low crystallization temperatures, the system solidifies quickly and hence the diffusion of chains in between the clay galleries is minimal[9].

Few attempts have been made to explain the influence of nanoclay on the nucleation process of isotactic polypropylene [112-114]. Sarazin et al. studied the polypropylene-nanoclay interaction on the crystallization kinetics of polypropylene-nanoclay and reported that the crystallization

kinetics depend both on clay content and the interaction between polypropylene chain and clay platelets[115].

The isothermal crystallization kinetics is one of the widely used methods useful in the case of semi-crystalline polymers with additive since the study reveals important information's regarding nucleation effect, rate of crystallization and mechanism of crystallization.

2.4 Melt spun fiber with nanoclay

Even though inorganic micron size fillers in polymer matrix improve performance, most of the micron size fillers are not suitable for melt spinning as they lead to processing difficulties. Since the filler size easily approaches the fiber diameter they cause spin line failures. However in case of nanoclay additive, interaction between filler and matrix is maximized due to their very high aspect ratio. The property benefits can be achieved with less than 2 wt % nanoclay compared to that of macro composites with up to 10-30 wt% fillers[116]. Few attempts have been made to study the structure and morphology of nanoclay filled polypropylene, nylon 6 and poly ethylene terephthalate (PET) fibers[15, 116, 117]. Melt spun PP/clay composite filaments were produced and investigated for structure and properties[58, 93-95]. In melt spinning, polypropylene with higher than 1 wt % nanoclay additive imposed processing difficulties[94]. Studies report filament breakage, and reduced drawing capability due to the heterogeneity in fiber structure, which lead to overstress along the fiber axis[94].

Mlynarcikova et al., investigated the influence of spinning process on the exfoliation of additive, morphology and properties of fibers. TEM micrograph of PP/montmorillonite composite fiber showed oriented platelets along the spinning direction and also partly exfoliated very thin filler particles.

Properties also seem to depend on the molecular weight of compatibilizer. Fiber elongation decreased with increase in draw ratio and additive content for both low and high molecular weight compatibilizer. Both increase in filler content and draw ratio decrease the elongation. Fiber sample spun with high molecular weight compatibilizer could be spun at higher draw ratio due to breakage. This might be due to the lower crystallinity and orientation of fiber in the presence of a low molecular weight compatibilizer[118].

PP/nanoclay compatibilized filaments showed improved creep resistance over control PP filaments [94]. Level of exfoliation depends largely on the compatibilizer and the extent of drawing process. Tensile strength of nanocomposite fiber produced at same draw ratio and nanoclay additive for higher molecular weight compatibilizer was on the average 10 to 20 % higher than low molecular weight compatibilizer. Crystalline orientation was higher in case of compatibilized fiber samples[118].

Incorporating modified montmorillonite additive in polymer matrix was found to improve the dyeability of PP fiber. PP fibers could be dyeable by incorporating the nanoclay particles. As compared to neat PP, fibers with nanoclay additive exhibited satisfactory color-fastness [119, 120]. PP/organo-montmorillonite fibers were produced using a twin screw extruder and subsequent melt spinning. At same draw ratio, the nanocomposite fiber had increased crystallinity and low orientation. Moisture absorption increased due to the increase in surface roughness, voids and defects[15].

2.5 Injection molded polypropylene-nanoclay composite

Injection molding is a widely used method for the manufacturing of a variety of polymer products. Properties of injection-molded samples can be improved through the right combination of processing conditions, parent matrix and inclusion of additives. Process is carried out at elevated pressure of about 2 kbar.

The injection-molded bar of polymer/layered silicate nanocomposites with respect to difference in microstructure, orientation and morphology along the thickness direction of injection molded nanocomposites was also investigated. Fornes et al. reported difference in crystalline forms in core and sheath regions of nylon 6-nanocomposites with 3-5 wt % additives. The skin region was rich of γ-crystalline forms due to rapid cooling and restriction of polymer chains in skin region. Whereas the core region contained mixture of α and γ-crystalline forms[39].

Morphology and mechanical properties of injection molded PP/clay, nylon 6/clay and PET/clay nanocomposites has been investigated before[77, 121-123]. Inclusion of nanoclay in fiber matrix led to significant reduction in thermal shrinkage due to the hindrance in the molecular chain mobility in the interfacial regions. Effect of molding pressure and nanoclay on the spherulites microstructure

has been investigated before. With increase in the molding pressure and in presence of nanoclay, spherulites size decreased due to the combined effect of nucleation due to additives, and pressure induced crystallization[124]. At lower weight % (0.25- 0.5 wt %) clay loading, the higher tensile strength and elongation was observed due to the orientation of both polymer chain and uniformly distributed clay platelets[75, 92, 94].

A rounded 'cabbage-like-sheet' structure due to the extensive plastic fibrillations was observed in the fracture surface of the well-exfoliated nylon-6/montmorillonite nanocomposites[122]. Failure mechanism for nanoclay incorporated samples changes from vein type pattern to tearing of material [75, 92].

2.6 Scientific concepts of crystallization

Crystallization from melt is an important concept and extensively used for mass production of polymer products. Crystallization in particular, nucleation and growth from polymer melts have been investigated from experimental and theoretical point of view. When a polymer melt is cooled bellow its melting point, the crystallization is initiated at nuclei after certain induction time. Molecules from melt are integrated on to growing crystal at the interface. The initiation of crystallization and integration of molecules at crystal interface is called nucleation. Crystal growth rate depends on magnitude of branching and splaying of polymer chain on to growing boundary. Magnitude of branching and splaying depends on degree of undercooling which is difference between equilibrium melting temperature and crystallization temperature[125].

$$\Delta T = T_m^o - T_c \qquad \text{Equation 13}$$

There are two types of nucleation: homogeneous and heterogeneous[126]. Wunderlich et al., have studied influence of molecular weight on the crystallization kinetics. Decreasing the molecular weight results in faster crystallization since, at lower molecular weight, polymer chains have higher mobility[69].

2.6.1 Primary and Secondary crystallization

Primary crystallization proceeds through growth of spherulites with constant rate under the isothermal conditions. Secondary crystallization involves ejecting impurities from growing body and filling up of space between lamellae. If the space is not filled even after impingement, nucleation and crystal growth can take place. In the homogeneous nucleation, spherulites are formed from polymer chains below the melting point. The process is reversible up to a point where a certain crystal size is reached, and beyond this point, subsequent addition is irreversible and growth may have considered to be commenced. The distribution of spherulite is random throughout and the appearance is considered to have a first order dependence on time as per Equation 14,

$$n = Nt \qquad \text{Equation 14}$$

Where,

n- number of nuclei,

t- time,

N-nucleation constant,

Heterogeneous nucleation arises from the presence of impurities. Final size of growing bodies is inversely proportional to number of nuclei during course of crystallization. Final array of volume of induced bodies ϕ is given by total volume at the end of the process as in Equation 15,

$$\Phi = \frac{V_\infty}{N^1 V_0} \qquad \text{Equation 15}$$

Where,

V_∞- volume at end of process,

N'-number of nuclei formed per unit volume of melt,

V_o - initial melt volume,

In heterogeneous system, N' is lower at higher temperatures[127].

The rate at which growth occurs relative to the nucleation rate determines the number of nuclei formed before complete phase transformation[127]. The final volume can be given by Equation 16,

$$\Phi = \frac{4\rho L}{\rho_s \Gamma(1/4)}\left(\frac{\pi\rho_s}{\rho L}\right)^{1/4}\left(\frac{G}{N}\right)^{3/4} \qquad \text{Equation 16}$$

Where,

N-nucleate rate per unit volume,

Γ- gamma function,

Earlier studies have reported heterogeneous mechanism of crystallization in the presence of nanoclay additive in the matrix[128, 129]. Heterogonous crystallization takes place in the presence of particles with crevices. On cooling, crystallization takes place in the crevices of additives. During subsequent melting, melting point shifts to slightly higher temperature due to adherence of polymer chains in between the platelets[127].

2.6.2 Secondary nucleation theory

The temperature dependence of the spherulites linear growth rate can be best explained by the Lauritzen–Hoffman theory of secondary nucleation[130-133] as shown in Equation 17,

$$G = G_o \exp\left(-\frac{U^*}{R(T_c - T_\infty)}\right)\exp\left(-\frac{K_g}{T_c \Delta T f}\right) \quad \text{Equation 17}$$

Where,

G- Growth rate, G_o - Growth rate constant, U^*- The activation energy for polymer diffusion, R- Gas constant, T_c - Crystallization temperature, f -correction factor = $\frac{2T_c}{T_c + T^o{}_m}$, K_g - Nucleation rate constant given by Equation 18,

$$K_g = \frac{jb_o\sigma\sigma_e T_m{}^o}{k\Delta h_f} \qquad \text{Equation 18}$$

Δh_f -is the heat of fusion, j- depends on the operating regime equal to 4 for regime I, III and 2 for regime II, ΔT = (T_m-T_c) is super cooling and g- rate of lateral spreading of lamellae. In Figure 2.11,

b_o - Width of chain,

T^o_m - Equilibrium melting point,

σ - Lateral surface energy,

σ_e -Fold surface energy,

k- Boltzmann constant.

In order for these calculations to be carried out, it is necessary to estimate parameters in Equation 19.

$$K_g = \frac{jb_o\sigma\sigma_e T_m^o}{k\Delta h_f} \qquad \text{Equation 19}$$

The equilibrium melting point T^o_m can be measured by isothermal crystallization at various temperatures by carrying out a Hoffman-Weeks plot of T_m versus T_c.

The values $\sigma\sigma_e$ can be determined from the slope of the lines. σ can be calculated independently from Hoffman modification of Thomas-Stavely relation in Equation 20 [134].

$$\sigma = 0.1\Delta h_f \sqrt{a_o b_o} \quad \text{Equation 20}$$

The work done by chain (q) to form a fold can be easily calculated from;

$$q = 2a_o b_o \sigma_e \quad \text{Equation 21}$$

Lauritzen and Hoffman theory analyzes the growth data according to competition between the rate of deposition of secondary nuclei and the rate of lateral spreading of lamellae (g) deposition. Schematic of three dimensional growths of different regimes is shown in Figure 2.12(a).

Regime I occurs when the deposition rate (i) << (g) lateral spread of lamellae at very low super cooling, regime II occurs when the i ≈ g at moderate super cooling and regime III occurs when the (i) >> (g) at very high super cooling. Regime behavior varies for different polymers for example; polyethylene when crystallized shows regime I and II, polypropylene shows regime II and III [126, 135-138]. At atmospheric pressure, polypropylene shows regime I and II and the same material shows all regimes at 150 Mpa. It's been found that the developed regime is significantly governed by the crystallization condition[126, 139]. Regime II to III transition occurs when the rate of secondary nucleation is higher than the rate of surface spreading of nuclei. Surface spreading is essentially a reeling-in process dependent on the repitational ability of the polymer chain[126].

For an ideal PP, growth rate generated from the equation using following variable; T^o_m-186.1°C, T_g = -12°C, U* =1500 cal/mol, σ = 10 erg/cm2, σ_e = 100 erg/cm2, ΔH_f = 209 J/g. Three different regimes observed for the ideal polymer system is shown in Figure 2.12(b)[126].

Semi crystalline polymers exhibit different melting point based on processing condition, thermal history and composition. The melting temperature is directly related to lamellar thickness. Thicker the lamellae are, higher the melting temperature.

Equilibrium melting temperature T_m^0 is defined as melting point of infinitely large lamellae. Theoretically the melting temperature (T_m) of polymer is given by;

$$T_m = T_m^0 - \frac{2\sigma_e T_m^0}{l\Delta H_f} \quad \text{Equation 22}$$

Where, T^o_m is the equilibrium melting temperature, ΔH_f is heat of fusion, l is lamellar thickness, σ_e is fold surface energy. The equilibrium melting point T^o_m can be measured by isothermal crystallization at various temperatures by carrying out a Hoffman-Weeks plot of T_m versus T_c. Equilibrium melting pint is extrapolation to the line where T_c=T_m. Yuan et. al., have reported higher equilibrium melting point for PP/nanoclay composites[92].

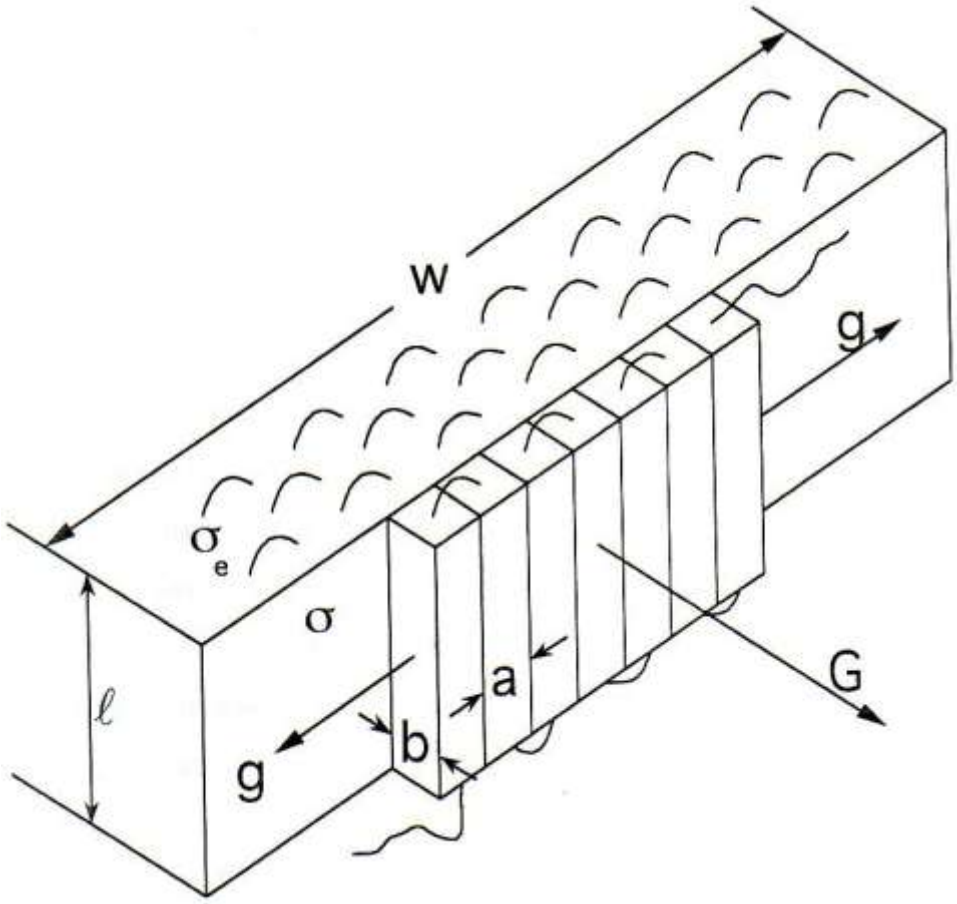

Figure 2. 11. Schematic of ideal lamellar growth front [126].

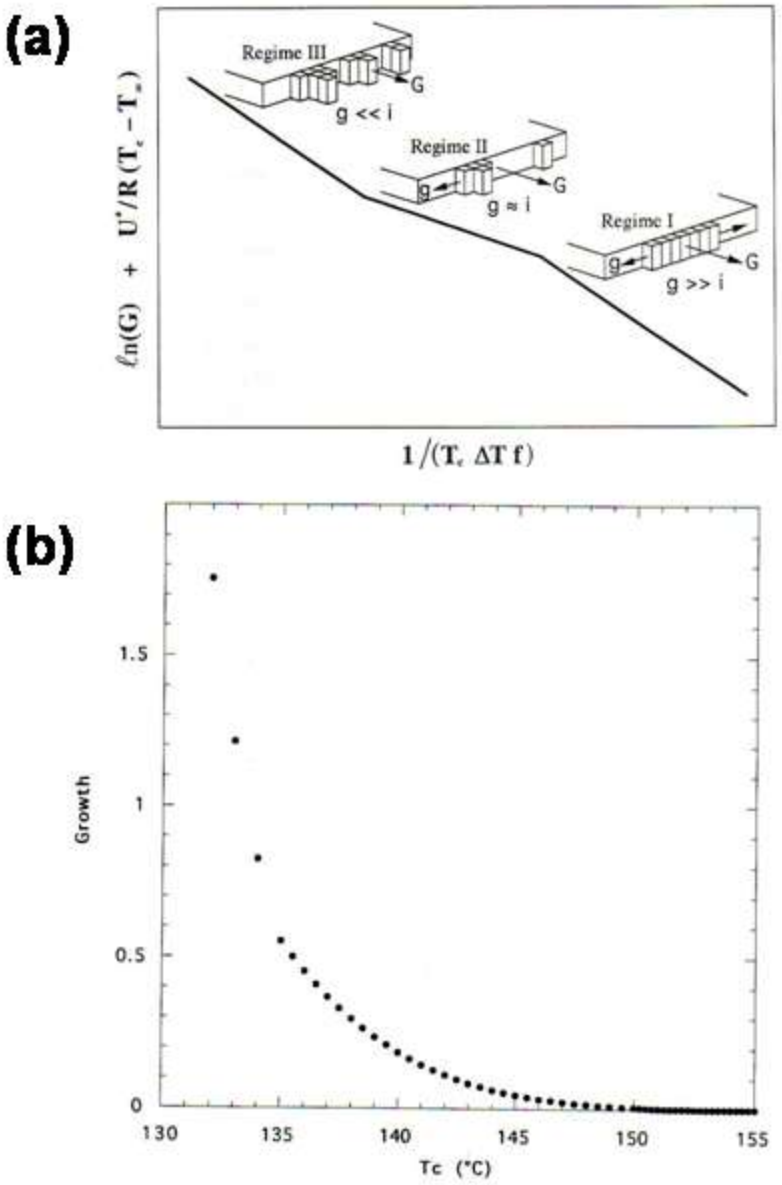

Figure 2. 12. (a) Schematic of regime analysis, (b) Growth rate versus temperature for ideal polymer [126].

2.6.3 Avrami equation

The isothermal crystallization kinetics can be analyzed by evaluating the degree of crystalline conversion as a function of time at a constant temperature. The relative crystallinity at different crystallization time $X(t)$, can be obtained from the ratio of the area of the exotherm up to time t divided by the total exotherm given by Equation 23, where Q_t and Q_∞ are the heat generated at time t and infinite time, respectively, and dh/dt is the heat flow rate [65].

Assuming that the relative crystallinity increases as a function of time, time-dependent relative crystallinity X(t) can be estimated by Avrami Equation 24[140]. Equation 24 can be re arranged in double logarithmic form as Equation 25,

$$X(t) = \frac{Q_t}{Q_\infty} = \frac{\int_0^t \left(\frac{dh}{dt}\right) dt}{\int_0^\infty \left(\frac{dh}{dt}\right) dt} \quad \text{Equation 23}$$

$$1 - X(t) = \exp(-Kt^n) \quad \text{Equation 24}$$

$$\log[-\ln(1 - X(t))] = \log K + n \log t \quad \text{Equation 25}$$

From the plot of log [-ln (1-X (t))] versus log (t), value of n (slope) and K (y- intercept) is determined. Where, n is the Avrami exponent which is nucleation and growth parameter, K is the rate constant which describes the crystallization rate and t is the crystallization time [141,142]. Theoretically n can be derived is an integer which varies between 1 and 6. Lower values of n indicate the growth in the form of sphere and disc or thick disc. Avrami constant, nucleation mode and respective crystal growth structure are summarized in Table 2.1. For spherulitic form of crystal growth, n values fall between 2 and 4 [126]. In case of i-PP with nanoclay additive, decreased induction time for crystallization (nucleation effect), has been observed [114]. Rodríguez et al. studied isothermal crystallization kinetics of iPP with 2 to 6 wt % clay additive without any compatibilizer chemicals. Avrami parameters reported in their work at 125°C and 134°C are shown in Table 2.2. They reported that at 125°C, the evolution of crystals was associated with instantaneously nucleated spheres form of growth geometry.

When the crystallization temperature was increased to 134°C, overall growth geometry remained same but the secondary crystallization decreased [114]. Better interpretation of nucleation, morphology and the mechanism of crystallization can be made by combination of data on spectroscopy, dialatometry, differential scanning calorimetry, x-ray diffraction and Avrami index [126,126].

Disadvantages of Avrami analyses are [143];

1. If there are multiple growth morphologies and or two different type of nucleation mechanisms, the Avrami exponent might take fractional value
2. The linier growth rate is not constant with time
3. During crystallization volume does not stay constant
4. The number of nuclei may not increase at same rate and reach saturation point after the completion of heterogeneous nucleation
5. The crystal morphology does not conform always to spherical or to a circular form as predicted by two dimensional approximation
6. There can be two stages of crystallization and branching
7. There can be perfection of crystals during secondary crystallization

The results of Avrami analysis can only be used for qualitative account of crystallization[143,144].

2.6.4 Crystallization half time $t_{1/2}$

The crystallization half time $t_{1/2,}$ a convenient measure of the rate of crystallization is the time at which the extent of crystallization is 50 %. The crystallization half time $t_{1/2}$ can be derived experimentally as well as theoretically. Theoretical relation between $t_{1/2}$ and crystallization rate constant K is given by;

$$t_{1/2} = \left(\frac{\ln 2}{K}\right)^{\frac{1}{n}} \qquad \text{Equation 26}$$

Where, n and K are Avrami parameters. Experimentally it can be derived from the plot of relative crystallinity X (t) versus time t.

2.6.5 Maximum rate of crystallization

Reciprocal of $t_{1/2}$, $\tau_{1/2}$ can be used as indication of the rate of crystallization, which can be written as Equation 27;

$$G = \left(t_{1/2}\right)^{-1} = \tau_{1/2} \qquad \text{Equation 27}$$

The greater the value of $t_{1/2}$, the lower the rate of the crystallization [65]. The melt temperature, molecular weight, presence of plasticizer and nucleating additive on the course of crystallization can be assessed by $t_{½}$ [127]. Additionally, the time to reach the maximum rate of crystallization t_{max} and the time to crystallize fully t_c can also be used to characterize the rate of crystallization as in Equation (28). Since t_{max} corresponds to the point at which $dq/dt = 0$,

$$t_{\max} = [(n-1)/nK]^{1/n} \qquad \text{Equation 28}$$

The value of t_{max} then can be derived from the Avrami exponent n and the parameter K obtained from the plots of log [-ln (1-X (t))] versus log (t) [65].

2.6.6 Isothermal crystallization activation energy

The crystallization is a thermally activated process. Avrami parameter K can be used to determine the energy for crystallization. The Arrhenius equation can be used to describe the crystallization rate parameter K as in Equation 29 and Equation 30 [145].

$$K^{1/n} = k_0 \exp(-\Delta E / RT_c) \qquad \text{Equation 29}$$

$$(1/n)\ln K = \ln k_0 - \Delta E / RT_c) \qquad \text{Equation 30}$$

Table 2. 1. The values of n and K for different nucleation mechanism and different crystal shapes.

Crystal Growth Shape	Nucleation mode	Avrami Exponent (n)	Avrami Constant (K)
Rod	Heterogeneous	1	NGA
	Homogeneous	2	NGA/2
Disc	Heterogeneous	2	πNG^2D
	Homogeneous	3	(π/3)NG^2D
Sphere	Heterogeneous	3	(4π/3)NG^3
	Homogeneous	4	(π/3)NG^3
Sheaf	Heterogeneous	5	-
	Homogeneous	6	-

Where, N is nucleation density, D is thickness of disc, G is linier growth rate.

Table 2. 2. Avarami parameters for iPP crystallized at (a) 125°C (b) 134°C [114].

Sample	Experimental Avrami index (a);(b) (theoretical)	Nucleation type	Growth geometry	Growth control
Homopolymer	3.1;none (3)	Instantaneous	Sphere	Interface
2% clay	3.2;3.2 (3)	Instantaneous	Sphere	Interface
4% clay	3.2;2.9 (3)	Instantaneous	Sphere	Interface
6% clay	2.9;3.2 (3)	Instantaneous	Sphere	Interface

Where k_0 is a temperature independent pre-exponential factor, ΔE is the activation energy. R is the gas constant and T_c the crystallization temperature. The activation energy for control and nanocomposites has been studied before. Transformation of the molten fluid into the crystalline state involves the release of energy and higher magnitude of energy (higher value of ΔE) has been reported for nanocomposites. Weng et al., reported crystallization activation energy of; -271 kJ/mol and a -355 kJ/mol for the neat nylon 6 and the nylon 6 nanocomposite respectively[65].

2.6.7 Non-isothermal crystallization kinetics

The non-isothermal crystallization studies of semi-crystalline polymers are of increasing technological importance since the experimental conditions are close imitation to the real industrial processing. Most of the industrial manufacturing like formation of film, fiber and molded products involve sudden non-isothermal cooling of polymer system from the molten state. So the non-isothermal crystallization kinetics gives valuable information about the end product morphology in the presence of additives.

Non-isothermal crystallization kinetics of different polymer systems; poly(ethylene oxide)-montmorillonite[110], PP-carbon nanotubes[146], nylon66-clay[147], isotactic PP-$CaCO_3$[148], polyethylene-clay[106], poly(trimethylene terephthalate)-clay [149], PP-montmorillonite[149], polyamide 6-clay[39] and polypropylene-clay[150] has been studied before. It is known that, maximum crystallization rate shifts to lower temperature with increasing cooling rate and shifts to high temperature in presence of additives[65].

Yuan et al., studied the nonisothermal crystallization behavior of PP-clay nanocomposites. They observed decrease in the half-time for crystallization due to the nucleating effect of clay nanoparticles[151]. Two mutually opposite effects, nucleating ability of clay at lower weight percentage and hindrance to secondary crystallization or growth at higher weight percentage of additive have been reported in most of these studies[151].

Rate of cooling also influences the peak crystallization temperature. At lower cooling rates, because there is more time to overcome the nucleation energy barriers, crystallization starts at

higher temperatures; while at higher cooling rate, the nuclei become active at lower temperature [152]. Relative crystallinity data can be obtained from integration of the exothermal peaks during the non-isothermal scan. In the non-isothermal crystallization studies, melting temperature, the peak crystallization temperature and the crystallization time (t) can be related by Equation (31)[153],

$$t = \frac{|T_0 - T|}{\phi} \quad \text{Equation 31}$$

Where,

t- crystallization time, which is the time required for temperature to drop from melting temperature to crystallization temperature.

T_{0-} the melting temperature,

T- peak crystallization temperature and Φ- is the cooling rate[153].

Activation energy Δ*E* of non-isothermal crystallization can be calculated using Kissinger method as in Equation (32) [154]

$$\frac{d[\ln(\lambda / T_p^2)]}{d(1/T_p)} = -\frac{\Delta E}{R} \quad \text{(K) Equation 32}$$

Where, T_p, R and λ are the peak temperature, the universal gas constant and cooling rate, respectively. Activation energy ΔE can be determined from the slopes of the least-square lines in plot of $\ln(\lambda / T_p^2)$ vs. $(1/T_p)$. Yuan et al. observed lower activation energy for PP-nanoclay composites compared to PP due to the nucleating effect of clay on PP[155,156,151].

2.6.8 Scientific concepts of spherulite

Spherulite is a birefringent entity, spherical in its symmetry and present in majority of semi-crystalline polymers. Although found in many semi-crystalline polymers, only in few cases they are large enough to be resolvable in the optical microscope. Spherulite is not a single crystal and it's an aggregate of many smaller crystallites of order 10^{-5} to 10^{-6} cm[127].

Spherulite consist of fibrous sub units. Schematic development of spherulite as proposed by Bernaueris is shown in Figure 2.13. Development starts from rod like or plate like units depending on the form of nucleus. Geometric form of the growth is different and changing with time. Spherulite development is not attained if the nucleation density is very high[127].

Schematic of overall growth front of spherulite structure is shown in Figure 2.14. It consists of 10 nm thick individual lath like crystallite stacks which are separated by non crystalline region (tie chains). Each of these ribbons like crystalline lamellae twisted for sufficiently large area (of order 1 μm^2) about the ribbon axis and create a three dimensional object: a spherulite[157].

Important process of fiber formation is that it involves broadening. It is the process by which space is filled as spherulite expands. Branching of fibrils developed often twist. In a rapidly grown structure, this twisting can produce periodic variation in refractive index[127].

Crystallization from melt can be analyzed using polarized microscope with polarizer's crossed at 90°. In the absence of crystalline region, the arrangement will not allow any light to pass through so the field appears dark. Presence of highly anisotropic material like polymer causes the plane of polarization to be rotated towards analyzer[157].

Polymer chains are intrinsically highly anisotropic and hence cause the rotation of plane-polarized light, which enables polymer spherulite structures to be analyzed using polarized microscopy[157].

Within the spherulite, long axis of the chains is oriented at right angle to the radii across the radiating fibrils. If the refractive index is greater along the chain axis spherulite is termed positive[127]. In polymer, varieties of structural features exist simultaneously. At lower nucleation density, spherulites grow and attain larger structure. Range of size of various units is included in Table 2.3 [127].

Kang et al. observed heterogeneous nucleation mechanism and decrease in spherulite size from 155 μm in neat PP to 12 μm in the case of polypropylene with 8 wt % clay additives [147]. Growth can occur in one two or three dimension to give rod, disc or sphere form to give Avrami parameter 1, 2 or 3. Complication and deviation can also occur if a nucleus gives rise to a

random array of fibrils. Values of Avrami exponent n for different type of nucleation and growth mechanism is shown in Table 2.4[127].

From the maximum attainable diameter of spherulites, nucleation density can be estimated. Nucleation density of spherulite N reported in literature is given by Equation 33,

$$N = (\frac{3}{4}\pi)(D_m / 2)^{-3} \qquad \text{Equation 33}$$

Where D_m is maximum attainable diameter of spherulite before impingement [9].

Table 2. 3. Different features in Spherulites[127].

Spherulite	$>10^{-4}$ A°
Fibril (cross-section)	$10^{-6} \times 10^{-4}$ A°
Crystallite	(5×10-7) ×(20×10-7) A°
Single crystal	$10^{-6}\times10^{-4}$ A°

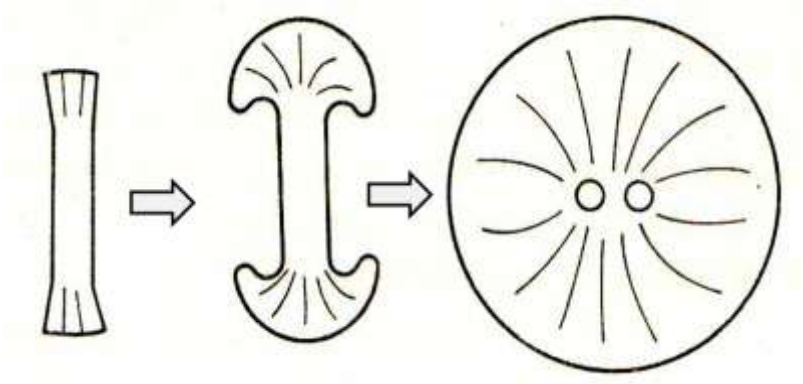

Figure 2. 13. Stages in development of spherulite, as proposed by Bernauer [127].

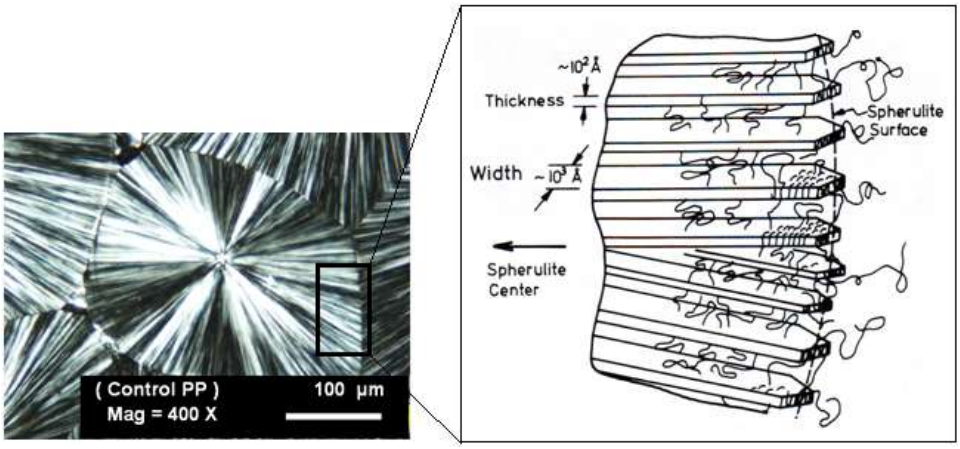

Figure 2. 14. Overall picture of growth front of a spherulite, Lathe like crystals separated by non-crystalline region [157].

Table 2. 4. Values of Avrami exponent n for different type of nucleation and growth mechanism[127].

n	
I + 0 = I	Rod like growth from instantaneous nuclei
I + I = 2	Rod-like growth from sporadic nuclei
2 + 0 = 2	Disc-like growth from instantaneous nuclei
2 + I = 3	Disc-like growth from sporadic nuclei
3 + 0 = 3	Spherulitic growth from instantaneous nuclei
3 + I = 4	Spherulitic growth from sporadic nuclei ($n \alpha t^{1.0}$)

2.7 Modeling mechanical properties of nanoclay based composites

Numbers of theoretical composite models have been developed and used for predicting the mechanical properties of nancoclay based polymer composites[35, 129, 158-162, 8, 12]. Key parameters in all these model include; filler aspect ratio, filler orientation filler/matrix stiffness ratio E_p/E_m, filler volume fraction f_p, and orientation.

From earlier studies, Halpin–Tsai equation is known to give reasonable estimates for effective stiffness and the Mori–Tanaka type model give the best results for high aspect ratio fillers[158-160].

K Hbaieb et al., have compared the accuracy of Mori–Tanaka model against Finite element method (FEM). They found that Mori–Tanaka model gave a very good prediction of elastic modulus in aligned case with weight fraction 1-5 wt%. At higher weight percentage, Mori–Tanaka gave lower value of elastic modulus since it does not account for interaction between fillers[161]. N. Sheng et al. used multiscale model to explain the hierarchical morphology, the overall elastic modulus and mechanical properties of nanoclay composites[35].

T. D. Fornes, and D. R. Paul used Halpin–Tsai equations and the Mori–Tanaka theory to evaluate nylon 6 polymer composites reinforced with glass fibers and layered aluminosilicates[129].

Luo et al. developed three-phase model which included three phases: matrix material, the exfoliated clay nanolayers and the intercalated nanoclay clusters. In their work, ellipsoidal geometry was assumed for both clay nanolayers and clusters[163].

2.7.1 Different models

Halpin and Tsai composite theory

Halpin and Tsai is well known model for predicting the stiffness of unidirectional composites as a function of filler aspect ratio, volume fraction [159, 164]. The longitudinal and transverse engineering moduli, E_{11} and E_{22}, can be expressed by;

$$\frac{E^{HT}}{E_m} = \frac{1 + \zeta \eta \Phi_f}{1 - \psi \eta \Phi_f} \qquad \text{Equation 34}$$

Where E^{HT} and E_m represent the Young's modulus of the composite and matrix, respectively, ζ is a shape parameter dependent upon filler geometry and loading direction, ψ depends on the packing volume fraction (0.601 for loose spheres)[165], φ_f is the volume fraction of filler, and η is given by;

$$\eta = \frac{\frac{E_f}{E_m} - 1}{\frac{E_f}{E_m} + \zeta} \qquad \text{Equation 35}$$

Where E_f represents the Young's modulus of the filler,

For longitudinal modulus E_{11}, ζ=2(*a*/*b*), where *a* and *b* are the length and thickness of the fiber and in transverse direction, ζ=2 [166, 167]. With ζ approaching 0, the Halpin–Tsai theory converges to the inverse rule of mixtures and can be given by;

$$\frac{1}{E} = \frac{\phi_f}{E_f} + \frac{(1 - \phi_f)}{E_m} \qquad \text{Equation 36}$$

Also, when ζ approaching ∞ the theory reduces to the rule of mixtures as in Equation 37.

$$E = \varphi_f E_f + (1 - \varphi_f) E_m \qquad \text{Equation 37}$$

When calculating elastic moduli E_{11} and E_{22} in the case of ribbons or rectangular platelets, ζ is equal to (ℓ/*t*) and (*w*/*t*), respectively, where ℓ is the length, *w* is the width, and *t* is the thickness of the dispersed particle. Schematic of fiber and disc-like platelet reinforcement and respective coordinate systems for Halpin–Tsai model and respective equations used are shown in Figure 2.15 (a) and (b) [129].

(a)

Fiber Disk shaped

(b)

Direction of Applied Load	Halpin-Tsai Composite Modulus		Shape Parameter, $\zeta^{(a)}$	
	Fibers	Platelets	Fibers	Platelets
1	$E_{11} = E_{//}$	$E_{11} = E_{//}$	$\zeta = 2(l/d)$	$\zeta = 2(l/t)$
2	$E_{22} = E_{\perp}$	$E_{22} = E_{//}$	$\zeta = 2$	$\zeta = 2(l/t)$
3	$E_{33} = E_{\perp}$	$E_{33} = E_{\perp}$	$\zeta = 2$	$\zeta = 2$

Figure 2. 15 (a) Schematic of fiber and disc-like platelet reinforcement and respective coordinate systems for Halpin–Tsai model, (b) equations used for the calculation of composite stiffness for fiber and disk-like platelet reinforcement in parallel (longitudinal) and perpendicular (transverse) to the major axis[129].

The Mori–Tanaka average stress theory

The Mori–Tanaka average stress theory was derived on the principles of Eshelby's inclusion model for predicting an elastic stress field in and around an ellipsoidal particle in an infinite matrix[168]. The longitudinal and transverse elastic moduli can be given by;

$$\frac{E_{11}}{E_m} = \frac{A}{A + \phi_f (A_1 + 2\nu_m A_2)} \qquad \text{Equation 38}$$

and

$$\frac{E_{11}}{E_m} = \frac{2A}{2A + \phi_f \left[-2\nu_0 A_3 + (1-\nu_m) A_4 + (1+\nu_m) A_5 A \right]} \qquad \text{Equation 39}$$

Where φ_f is the volume fraction of filler, ν_0 is the Poisson's ratio of the matrix, and A_1, A_2, A_3, A_4, A_5, and A are functions of the Eshelby's tensor and the properties of the filler and the matrix. The composite moduli in Equation (38) and Equation (39) are dependent upon the shape of the filler, e.g. fiber-like versus disk-like ellipsoids. Figure 2.16 (a) and (b) shows the Mori–Tanaka physical representation of glass fibers and disk-like platelets and respective equations used to calculate composite moduli along the three principle orthogonal directions[129].

(a)

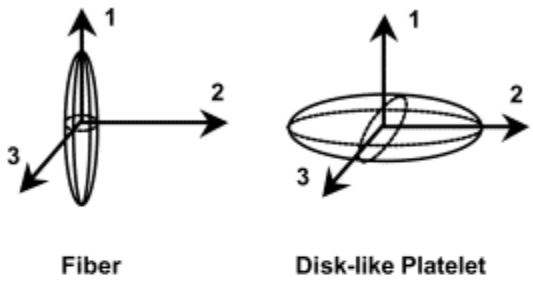

(b)

Direction of Applied Load	Mori-Tanaka Composite Modulus	
	Fibers	Platelets
1	$E_{11} = E_{//}$ (Eq. 5)	$E_{11} = E_{\perp}$ (Eq. 6)
2	$E_{22} = E_{\perp}$ (Eq. 6)	$E_{22} = E_{//}$ (Eq. 5)
3	$E_{33} = E_{\perp}$ (Eq. 6)	$E_{33} = E_{//}$ (Eq. 5)

Figure 2. 16 (a) Schematic of fiber and disc-like platelet reinforcement and respective coordinate systems for Mori–Tanaka model, (b) equations used for the calculation of composite stiffness for fiber and disk-like platelet reinforcement[129].

2.7.2 Modeling studies on nanoclay based composite

Detailed description of calculation of aspect ratio for a nylon 6/clay nanocomposite system is given by T.D Fornes et al. In their studies, TEM images were first printed on 20.3×25.4 cm^2 photographic paper. Dispersed platelets and agglomerates were traced over transparent film. Resulting transparent fill was electronically scanned and converted into a (TIFF) image file. The image analysis was used to numerically label and get information on the particle length. The histogram of all clay particle lengths and statistical data was obtained on section of nanocomposite photomicrographs from the core region of injection mold[129]. The statistical data obtained about particle length and thickness was are used to estimate the aspect ratio of the MMT particles as defined by;

$$\text{Aspect ratio} = l/t$$

Where l is the average particle length along the TD and t is the average thickness of platelets. For a perfectly exfoliated system, the average thickness of each platelet is the thickness of the MMT platelet calculated by adding the center-to-center distance between the outer oxygen atoms in the outer tetrahedral layers of sodium MMT as illustrated in Equation 40 and Figure 2.17.

$$t_{particle} = d_{001}(n-1) + t_{platelet} \qquad \text{Equation 40}$$

Where,

d_{001} is the repeat spacing of sodium as illustrated in Figure 2.17, n is the number of platelets per particle, $t_{platelet}$ is the thickness of a MMT platelet[129].

Some of the complexities in comparing composite theory to experimental composite data, for polymer-nanoclay composites is shown in Table 2.5. In addition to physical disparities between theory and experiment, the choice of composite theory will also dictate how well the predicted and observed properties agree[129]. In case of randomly oriented particles, the random distribution causes formation of clusters of nearly parallel particles with very low aspect ratio. These clusters and their respective interaction is not considered by Mori–Tanaka model[161].

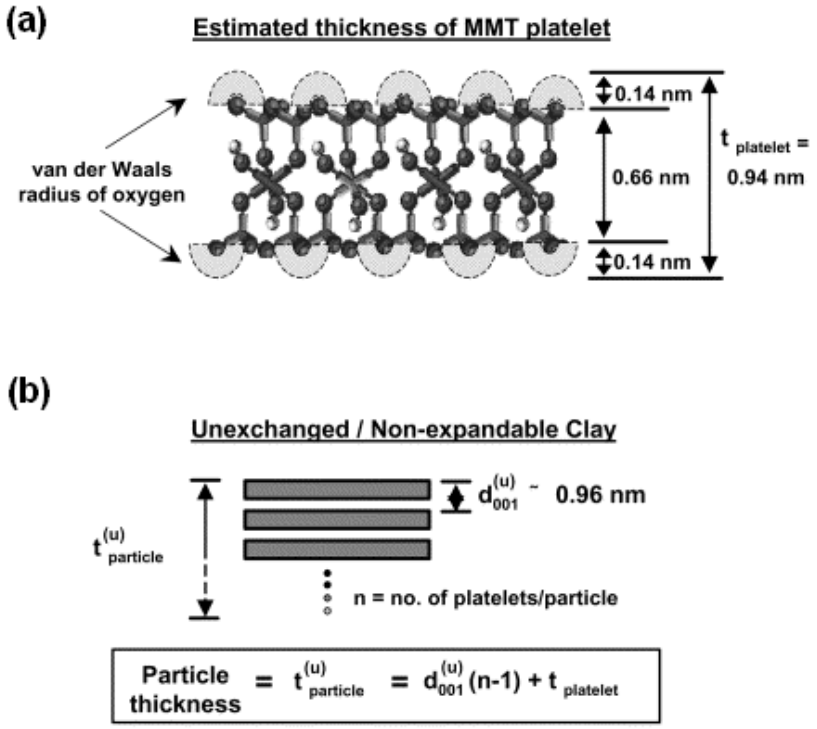

Figure 2. 17. Schematic of thickness calculation of (a) an individual MMT platelet, (b) thickness estimation of unexchanged clay stack[129].

Table 2. 5. Some important issues that limit the ability to model the stiffness properties of polymer–nanoclay nanocomposites[129].

Issue	Theory	Experimental
Filler shape and size	Uniform shape, Constant dimensions	-Non uniform shape, -Distribution of platelet size, -Imperfect exfoliation
Filler orientation	Unidirectional	Some degree of misalignment
Filler interface	The filler and matrix are well bonded	Imperfect bonding between matrix and fillers
Filler concentration	-No particle interactions, -Ignores change in viscosity, -No particle agglomeration	-Particle interaction and agglomeration, -Changes in viscosity can alter morphology during injection molding, -Changes in crystalline morphology
Matrix considerations	Assumes matrix is isotropic	-Polymer chain orientation, -Polymer crystallites

2.8 Morphology characterization of nanoclay based composites

The testing method selected for morphology characterization depends on length scale and information which is sought. Different characterization tools, wavelength range used and respective length scale measured is shown in Figure 2.18. For example, information in length scale of 0.1 to ten nanometers can be analyzed using x-ray scattering which uses wavelength in range of 0.1-0.3 nm [75].

3.8.1 Wide angle X-ray diffraction (WAXD)

Wide angle x-ray diffraction (WAXD) is ideal for analysis of nanoclay incorporated samples because of the presence of periodic structure in neat clay as well as in the clay reinforced nanocomposites[169].

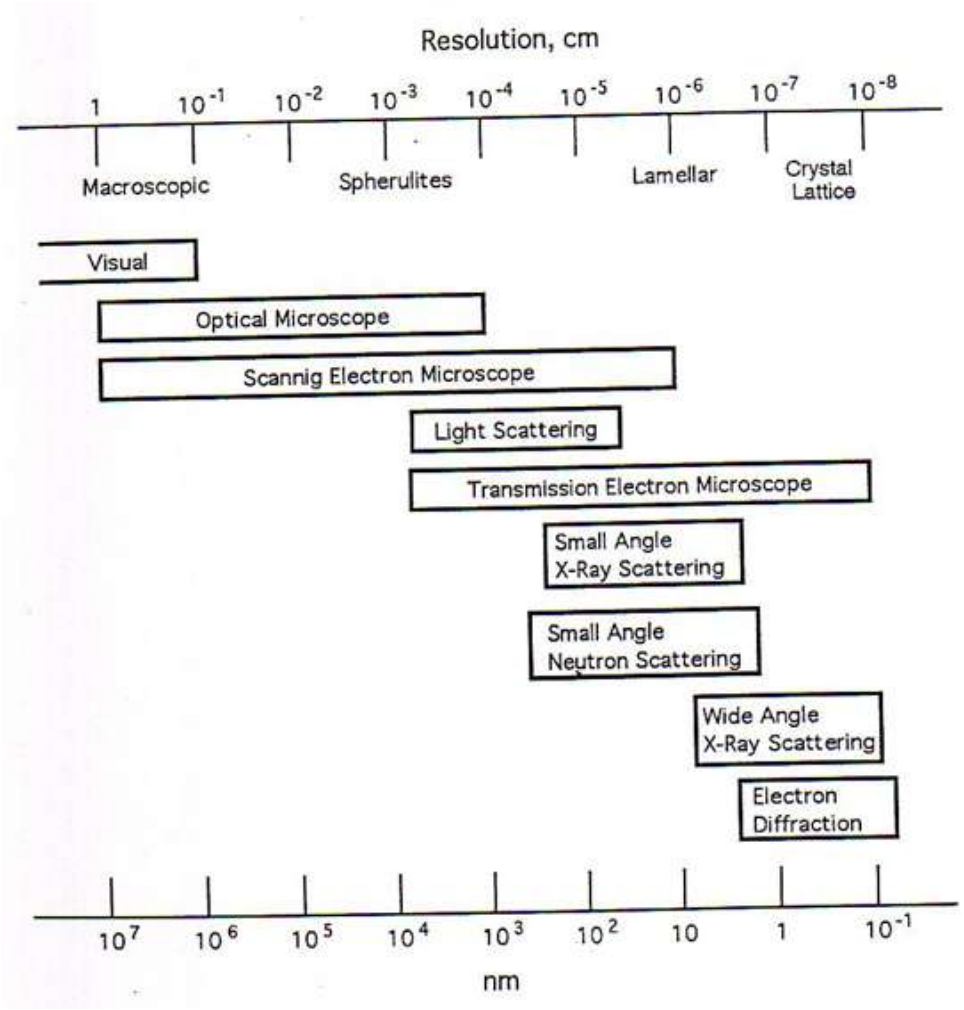

Figure 2. 18. Resolving power of structural characterization technique and length scale with respect to characterization type of structure in semicrystalline materials[75].

WAXD is based on Bragg equation (41):

$$n\lambda = 2d_{hkl}\sin\theta \qquad \text{Equation 41}$$

Where n is order of scattering, d_{hkl} specific interplanar spacing defined by indexes h,k, and θ is Bragg angle[75]. WAXD technique can be used to determine degree of crystallinity in polymeric systems from the area of amorphous and crystalline peaks;

$$X_c = \frac{A_c}{A_{total}} \times 100 \qquad \text{Equation 42}$$

Where, A_{total} is the total area between peaks and baseline. However the crystallinity index from WAXD cannot be taken as an absolute index due to errors involved in subtraction of baseline determination and delineating crystalline and amorphous scattering[75].

Wide angle x-ray diffraction data can also be used to determine global average distance between the clay platelets using Bragg's law provided the nanocomposite system processes an ordered structure[78]. Disadvantage of WAXD analysis is, it can't not be used in case of sample with completely exfoliated or delaminated morphology. Also the data cannot be used alone to interpret dispersion or distribution of additives in the samples[78].

3.8.2 Small angle x-ray scattering (SAXS)

Small-angle x-ray scattering (SAXS) is a x-ray scattering of recorded at very low angles (typically 0.1 - 10°). This angular range contains information about the in homogeneities in the nm-range, the shape and size of macromolecules, characteristic distances of partially ordered materials, pore sizes, and other data.

Lamellae are defined as ordered structures that contain polymer molecules in the form of platelets or ribbons usually in range of 20 to 500A° thick as shown in Figure 2.19 (a)[75]. Semi-crystalline polymer contains amorphous region between the crystalline lamellae as shown in Figure 2.19 (b). Stacked lamellae can be viewed as difference in electron density fluctuations due to difference in density of amorphous and crystalline phase. SAXS can be used for structural characterization in terms of periodic fluctuations in electron densities[75]. The electron density

fluctuation generates x-ray scattering at very small angles at very low angles << 1°. An important parameter often known as long period (L) which relates center-to-center distance between of stacked lamellae can be obtained by;

$$L = \frac{2\pi}{q_{peak}} \qquad \text{Equation 43}$$

Long period promotes scattering maxima or peak when measured in un-oriented samples[75].

2.8.3 Scanning Electron microscopy (SEM)

Scanning electron microscopy (SEM) is mostly used to observe morphology, structural and surface properties of polymer surfaces. SEM uses secondary electrons generated from either thermal or field emitting cathode. Condenser and an objective electromagnetic lens attenuate the generated electron beam. Electron beam is scanned by electromagnetic coils placed in the back-focal plane of the objective lens and in most cases the secondary electron signal is collected by electron detector[170].

2.8.4 Transmission Electron microscopy (TEM)

Transmission electron microscopy (TEM) is a microscopy technique whereby a beam of electrons is transmitted through an ultra thin specimen, interacting with the specimen as it passes through. An image is formed from the interaction of the electrons transmitted through the specimen. TEM consists of electron gun assembly, one condenser lens and three magnetic lens. The copper grid (400 meshes) with thin sample section is placed near the entrance to the bore of objective lens pole piece. The one condenser lens attenuates and illuminates the object. The magnified image I_1 produced by the objective is called the first intermediate image. This image I_1 serves as object for intermediate lens which produces a second intermediate image I_2. The image I_2 is further magnified by projector lens and focused onto an imaging device, such as a photographic film, or to be detected by a sensor such as a CCD camera[171].

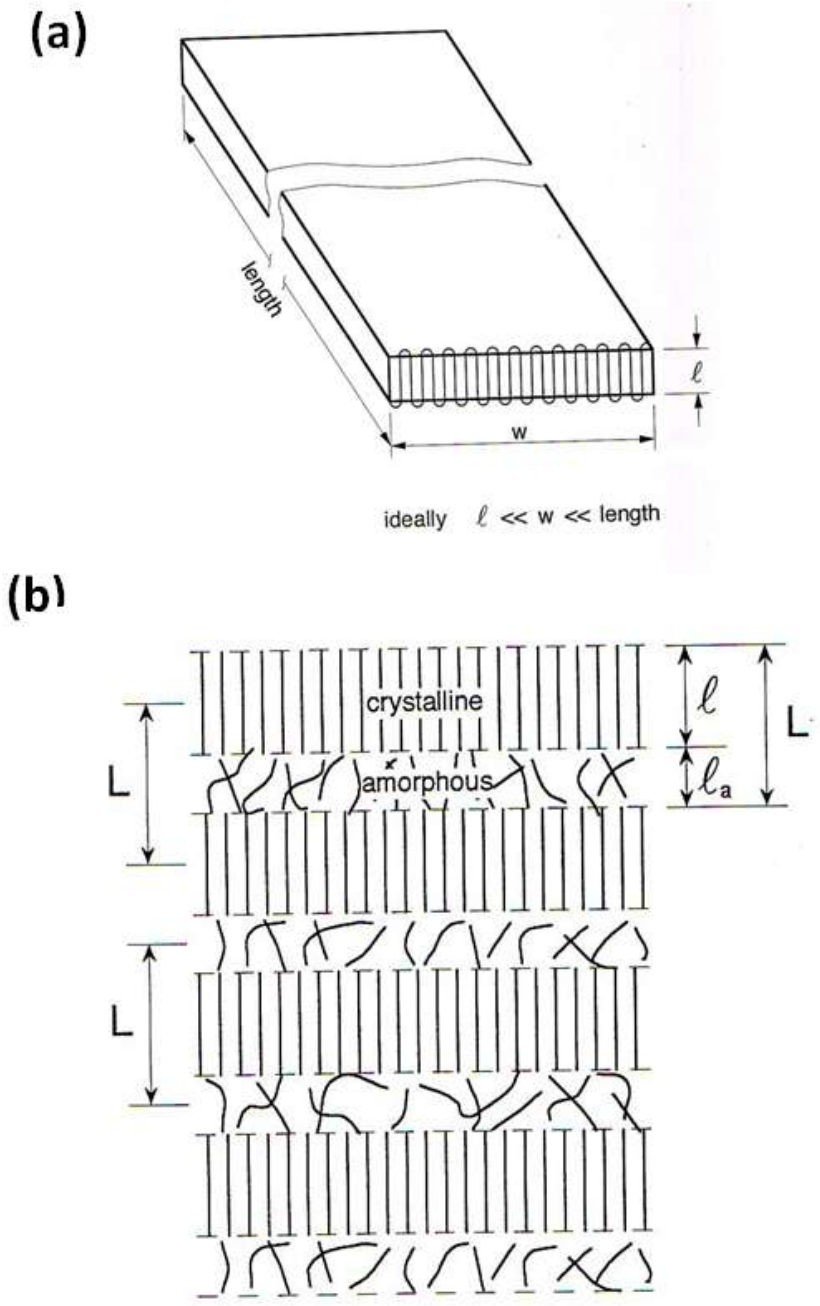

Figure 2. 19. (a) Schematic of lamellae texture, (b) model of semi crystalline materials.

TEM is one of the useful and widely used tool to determine the extent of exfoliation of clay particles in polymer matrix. The bright field mode is most common mode of operation for characterizing nanoclay based composites. In this mode, the contrast formation is formed absorption of electrons by thicker regions of the sample or regions with a higher atomic number additive. Regions with polymer matrix will appear bright – hence the term "bright field"[172].

The sample preparation for TEM is very challenging. The resolution and contrast of image obtained depends on the extent of transmission. So, sample sections have to be thin enough to get enough transmission. Electrons traveling through the sample lose energy at rate of 1eV/nm. Energy loss with thickness causes chromatic aberration and reduction in the resolution of image.
Kim et. al., reported degree of mixing of nanoalumina (Al_2O_3) nanoparticle in PET matrix using Skewness-quadrant method and Morisita's Index[78]. The Skewness quadrant method has been used in the field of ecology to determine the distribution of nests of ant lions in a sandbox, and to characterize the dispersion of small particles. Morisita's index has been used before to determine the spatial distribution of individual objects, such as plants, geographical analyses, and alloy materials. Morisita's index (I_q) gives an estimate the number of particles for the area[78].
In Skewness-Quadrat method, 720 square grids were placed on the TEM micrograph and the number of particles in each cell, (N_{qi}), was counted. Skewness (b) was used as the index from quadrant method and is given by in Equation 44;

$$\beta = \frac{q}{(q-1)(q-2)} \sum_{i=1}^{q} \left(\frac{N_{qi} - N_q^{mean}}{\sigma} \right)^3 \qquad \text{Equation 44}$$

Where,
q is the total number of cells studied,
N_{qi} is the number of particles in the ith cell,
N_q mean is the mean number of particles per cell, and
σ is the standard deviation of the N_q distribution.

Morisita's index (I_q) was determined from the particle density estimated from the TEM micrograph. For each sample; the Morisita's index is calculated from Equation 45.

$$I_\delta = Q\frac{\sum_{i=1}^{Q} n_i(n_i - 1)}{N(N-1)}$$ Equation 45

Where,

N is the total number of particles,

n_i is the number of particles found within the i^{th} section,

Q is the total number of sections. In their work, four TEM micrographs were used to estimate the distribution according to these two methods. The variation in Morisita's index and Skewness (β) was obtained by combining the number of particles from the 16 sections into a single area[78].

2.8.5 Atomic force microscopy (AFM)

AFM can be used to measure surface topology to resolution up to order of angstroms level from measuring forces order of 10^{-13} to 10^{-4} N existing between atoms [173]. Working principle is similar to STM but instead of using an electrical signal, the AFM relies on forces between the atoms in the tip and in the sample. Schematic working principle of atomic force microscopy is shown in Figure 2.20. Forces acting on the probing tip deflect the cantilever type spring. To keep the force constant, the cantilever is moves up and down. The vertical movement of cantilever is measured by detection device, usually a reflected laser beam, which corresponds to the topology of sample surface. A computer translates this vertical movement into topographical image. Lateral topology information of order of angstroms can be obtained from displacement sensor which measures deflection as small as 10^{-2} A°.

2.8.6 Surface Topology analysis using AFM

Processing conditions used, matrix and the wt % of additives have significant influence on the orientation and distribution and of nanoclay in polymer nanocomposite. Excess weight % of additives and non-uniform distribution causes surface defects. AFM has been used extensively for surface characterization of polymeric, biological samples.

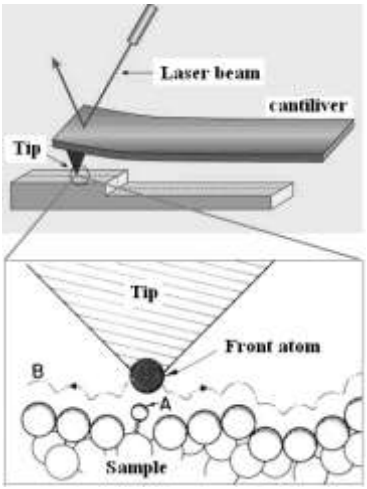

Figure 2. 20. Schematic working principle of atomic force microscopy [174].

Ganguly et al. studied the morphological mapping of Poly[styrene-b-(ethylene-co-butylene)-b-styrene] and its clay nanocomposites using AFM. They observed drastic increase in Z-range and RMS values for SEBS1 nanocomposites[175].

Section analysis

Using the cursor, cross lines were drawn across the image, and the vertical profile along that line was analyzed to make horizontal, vertical, and angular measurements. Average of n=15 sample readings was used as average RMS value.

Roughness measurements

Roughness analysis gives both RMS and Z-range. Z-range is the maximum vertical distance between the highest and lowest data points in the image. Where RMS is the root mean square of roughness. RMS can be given as Equation 46;

$$RMS = \sigma = \sqrt{\frac{\sum Z_i - Z_{ave}}{n}} \qquad \text{Equation 46}$$

Where,

Z_i -current Z value,

Z_{ave}-average of Z value between reference markers,

N-number of points between reference markers

AFM phase image can also be used to map stiffness variation of sample surface. The phase shift depends on the time-averaged surface stiffness <s> and contact radius r_c, the cantilever properties Q (quality factor) and K (spring constant) and the effective modulus E* as per Equation 47[176] :

$$\Delta\Phi \approx < s > \left(\frac{Q}{K}\right) = \varepsilon < r_c > E^* \frac{Q}{K} \qquad \text{Equation 47}$$

This equation shows that phase image could be used for stiffness mapping of sample surface, such that in phase image, stiffer region has a higher positive phase shift and hence appears brighter[177].

2.8.7 Surface energy

Fu et al., studied the influence of surface roughness on surface free energy of PP/clay nanocomposites with various clay contents. In their studies, they have reported no influence of topography on the surface free energy since average surface roughness of nanoclay based composites was less than 50 nm[178]. Kadar et al.[179] studied the surface free energy of the neat and organophilized clays. Surface energy drastically decreased from 257 mJ/m2 for neat nanoclay to 32mJ/m2 for modified clays. According to Yoshimasa et al. surface free energy for PTFE (22 mJ/m^2) decreased from 21.4 to 12.7 mJ/m^2[180].

Dharaiya and Jana reported the surface polarity of organically modified clay measured from the values of contact angle of water and diiodomethane decreased significantly due to the thermal degradation of the organic modifier of clay[181].

Hart et al. studied the influence of shear stress involved in mixing and the processing temperature on the decomposition of alkyl ammonium ions in PA6-clay nanocomposites[182]. Xei et al. used the combination of thermo gravimetric analysis and mass spectrometry to study the thermal decomposition of clays modified with a series of alkyl ammonium ions[183]. From these

studies, small molecular decomposition products, such as carbon dioxide, short chain alkanes, alkenes were observed[181].

Wetting is the ability of a liquid to maintain contact with a solid surface and is crucial in the bonding or adherence of two materials. Cohesive force causes the liquid to retain its circular shape while, liquid drop spreads on the surface due to adhesive force between interface. Contact angle of drop of liquid on the solid is the angle at which the liquid–vapor interface meets the solid-liquid surface.

Degree of wetting (wettability) is determined by a force balance between adhesive and cohesive forces. Decrease in contact angle indicates the extent of liquid drop spreading on the solid surface. So contact angle measurements can be used as an indicator of 'wettability' of surfaces[184]. The contact angle determination of a liquid–solid–vapor system satisfies Young's equation given by Equation 48. The equation is based on a 3-phase contact line, solid (s), liquid (l).

$$\sigma_s = \gamma_{sl} + \sigma_l . \cos\theta \qquad \text{Equation 48}$$

Where,

σ_{s-} Surface tension of solid,

σ_{l-} surface tension of liquid,

γ_{sl} -the interfacial tension between the solid and liquid phases,

θ-the contact angle corresponding to the angle between vectors σ_l and γ_{sl}[185].

CHAPTER III

MATERIALS AND METHODS

3.1. Materials

Influence of dispersion agent, different weight % of Closite Na^+ additives and processing conditions on the nanocomposite morphology and mechanical and thermal properties of products was studied. Commercial grade polymer pellets, films and fibers with different weight % of Closite Na^+ additives were produced at Techmer PM. Some of the samples had proprietary dispersion aids and those details are not disclosed here. All the polymers used here are commercially available materials. Specifically film grade nylon and fiber grade polypropylene were used. The natural nanoclay additive, Closite Na^+ was purchased by Techmer PM from Southern Clay Products of Gonzales, Texas.

3.1.1 Nylon 6 films and fibers

Nylon 6 blown films with 0.25, 0.5, 2, 5 and 10 wt % Closite Na+ clay additives along with control nylon 6 film were produced at Techmer PM. Melt compounding of nylon 6, maleated wax and Closite Na+ were done on counter rotating twin screw extruder (L/D= 28:1 mm). The extrusion zone temperature were in range of 238 to 243°C to produce concentrate containing clay wt % as shown in Table 3.1. Most of the film samples were in the thickness range of 600 to1520 microns. As-spun nylon 6 fibers with 1, 2 and 5 wt % Closite Na^+ clay additives along with control nylon 6 fiber were also produced at Techmer PM. The filaments were melt spun at 240°C, using Hills melt spinning unit with 41 round hole die. The spinning conditions were adjusted (speed in range of 220 mts/min to 890 mts/min, and draw ratio of 4:1) to get consistent filaments without breakage. The composition of the fibers is included in Table 3.2.

Table 3. 1. Nylon 6 film sample details.

Sample	Clay composition	Thickness (μ)	Yellowness (b)
Control	0%	860	0.16
0.25 % clay	0.25%	873	1
0.5 % clay	0.50%	691	1
2 % clay	2%	600	1
5 % clay	5%	760	3
10 % clay	10%	1520	5

Table 3. 2. Nylon 6 fiber composition.

Sample	Composition	Denier
Control Nylon 6	100 % Nylon 6	11
N6CF1	1 % clay in 5% PD1	10
N6CF2	5% clay in 5% PD1	10
N6CF3	1% clay with 0.5% PD2	9
N6CF4	2% clay with 0.5% PD2	10
N6CF5	5% clay with 0.5% PD2	9

*PD1, PD2 refer Appendix 1.

3.1.2 Spunbonding

Spunbonding is a one step integrated fabric production method consisting of filament spinning, formation of random web and bonding. The fabrics are produced by depositing extruded, spun filaments onto a collecting belt in a uniform random manner followed by bonding the fibers[186,187]. Schematic of Reicofil®-2 spunbond line based on melt spinning technique is shown in Figure 3.1. Polymer pellet is fed in to the hopper (1) by vacuum suction. Pellets are melted by the hot walls of barrel (2) and pushed forward by the flight of screw[187]. Viscous molten polymer melt then passes through the screen pack, which separates the lumps. Pressurized molten polymer is conveyed to a metering pump which regulates the quantity of melt delivered to die assembly for spinning[187]. Die block assembly consists of feed distribution and spinneret. Feed distribution manages the uniform distribution of melt all the way through the width of the die[188]. The polymer melt is forced by spin pumps (3) through special spinneret (4) which consists of single metal block with thousands of very precisely drilled orifice. The primary blow ducts (6), located below the spinneret block, continuously cool the filaments and the secondary blow ducts (7), located below the primary blow ducts, continuously supply the auxiliary room temperature air. Over the line's entire working width, ventilator-generated under pressure sucks filaments and mixed air down from the spinnerets and cooling chambers (5). The continuous filaments are sucked through a venturi (high velocity, low pressure zone) to a distributing chamber (8), which affects the entanglement of the filaments. Finally, the entangled filaments are deposited as a random web on a moving sieve belt (10). The randomness is imparted by the turbulence in the air stream, but there is a small bias in the machine direction due to some directionality imparted by the moving belt. The suction below the sieve belt (9) enhances the random lay down of the filaments[186]. Fiber web is finally thermal bonded by the nip of calender rollers. Chill roller cools the bonded web and finally fabric is wound on the winding unit[187, 188].

The polypropylenes compounded with 1-5 wt % percentages of nanoclay additive were provided by Techmer PM. SB webs were produced on Reicofil®-2 spunbonding line at the TANDEC laboratory. 5wt% maleated wax produced by Honeywell (product name AC573) was used as dispersion agent in each of the concentrate. The polypropylene, maleated wax and Closite Na^+

were melt compounded in a counter rotating twin screw extruder (L/D= 28:1 mm). The extrusion zone temperature was in range of 204 to 210°C to produce concentrate containing clay wt % as shown in Table 3.3. Spun fiber samples from the collector screen and spun bond samples after calendaring were collected for thermal analysis. Target basis weight for all the samples was 30gsm. SB run was quite normal for all formulations except for 5 wt % nanoclay for which melt filter at the end of the extruder stopped and could not be processed further. All the compositions were processed under similar conditions as shown in Table 3.4.

3.1.3 Melt blowing

Schematic of the melt blowing (MB) process is shown in Figure 3.2 is a one-step process in which high-velocity hot air blows a molten thermoplastic resin from an extruder die tip onto a conveyor or take-up screen to form a fine fibrous and self-bonding web[189]. The fiber diameters generally in the range of 2 to 4 µm.

Melt blown fabrics were produced from 1500 MFR polypropylene with 0.5 wt. % Closite Na^+ with 1.25 wt % and 2.5 wt % maleated polypropylene (mPP) compatibilizer. Webs were produced at two different air pressures 21 kN/m^2 (LP) and 41 kN/m^2 (HP) using the 15.4 cms wide research line with a single coat-hanger 60 die manufactured by Accurate products at the University of Tennessee Nonwoven Research Laboratory (UTNRL). Trial specifications are summarized in Table 3.6. Die temperatures were in the range of 216 to 288 °C. Webs were collected on rotating collector drum at die to collector distance of 38 cms at a resin throughput of 48 gms/min to achieve targeted fabric weight of 25 gsm. Different samples and respective compositions are listed in Table 3.7.

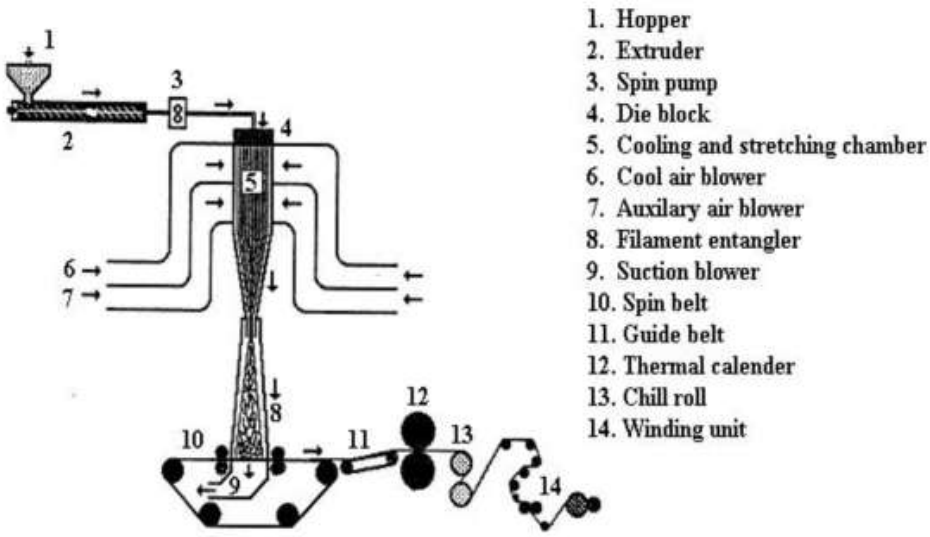

Figure 3. 1. Schematic of spunbond line[186].

Table 3. 3. Polypropylene with different additives used for the spunbond trial.

Sample	Dispersion aid	Matrix
Control PP		PP
1 % clay	5 % maleated wax	94 % PP
2 % clay	5 % maleated wax	93 % PP
5 % nanoclay	5 % maleated wax	90 % PP
5 % clay	5 % maleated wax	60 % maleated PP + 30%PP

Table 3. 4. Spunbond run conditions.

Melt temperature	240 °C
Through put	0.43 gms/hole/min
Extruder pressure	1800 PSI
Spin pump speed	9.3 rpm
Air suction / Fiber suction Speed	1490 rpm
Calendering temperature	145 ºC
Belt speed	25 mts/min

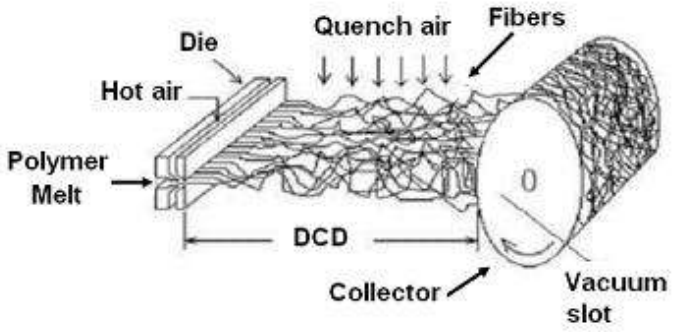

Figure 3. 2. Schematic of melt blown process[189].

Table 3. 5. SB fabric specifications.

Sample ID	Air speed	gsm	Thickness (mm)	Fiber dimension (microns)
Control 1	high air	29.5	0.328	15.20
Control 2	low air	28	0.298	15.50
1% clay	high air	30	0.313	15.85
1% clay	low air	29.5	0.312	15.50
2% clay	high air	30.5	0.305	15.91
2% clay	low air	30.5	0.304	15.50
5% clay	low air	30	0.306	16.50

Table 3. 6. Melt blown line specifications.

Die width	15.24 cms
Holes Per Die	120 holes
Die Hole size	0.045 cms
Air Gap	0.076 cms
Setback	0.076 cms
Throughput	0.4 g/(hole * min)
DCD Inch	38 cms
Collector Speed	12 meters/min
Basis Weight	25.8 grams/m^2

Table 3. 7. Sample composition.

Sample	Composition	Air Pressure
Control MB	1500 MFR PP	21 kN/m^2
1LP	0.5 % Closite Na^+ and 1.25 % mPP	21 kN/m^2
1HP	0.5 % Closite Na^+ and 1.25 % mPP	41 kN/m^2
2LP	0.5 % Closite Na^+ and 2.5 % mPP	21 kN/m^2
2HP	0.5 % Closite Na^+ and 2.5 % mPP	41 kN/m^2

3.1.4 Injection molding

Injection molded nanocomposites were prepared using the Sheffer Corp injection molding instrument. Different polypropylene-clay concentrates used for sample preparation are shown in Table 3.8. Processing conditions used for molding are included in Table 3.9. After loading the pellets in hopper, concentrates were allowed to melt in the barrel for 30 min. After injecting the melt, plunger load was maintained for 30 seconds. After retracting, injector mold was closed for 5 minutes for all the samples. The mold used for preparing the impact strength tester was rectangular[190]. All the samples were prepared under same conditions. Dimension of finished izod bars was l: w: t (63.5±0.2 mm: 12.5± 0.2 mm: 4.5±0.2 mm).

3.2. Testing and Characterization

3.2.1 Melt Index

Tinius Olsen Extrusion Plastometer MP200 was used to study the melt flow rate of the PP concentrates. The test was carried out at a temperature of 230°C, with a load of 2.6 kg recommended for PP as per ASTM standard D1238-89. The specifications of the instrument used are as under;

Table 3. 8. Polypropylene concentrates used for injection molding trial.

Sample	Additive (Wt. %)	Dispersion aid	Matrix
PP	Nil	Nil	R 230
PPN1	1	5% maleated wax	94% PP
PPN2	2	5% maleated wax	93% PP
PPN3	5	5% maleated wax	90% PP
PPN10	10	5% maleated wax	85% PP
PPN15	15	5% maleated wax	90 % PP

Table 3. 9. Processing conditions used to obtain dog bone and izod sample.

Melt loading time (sec)	Molding pressure (psi)	Mold closing time (min)	Temperature profile (°C) Plate 1/Plate2/hopper
30	100	5	49/49/204
20	80	5	33/33/211

Barrel diameter: 9.55 mm; Barrel length: 162 mm,

Capillary diameter: 2 mm; Capillary length: 8 mm,

Travel length of piston in the barrel: 25.4 mm,

Average of three measurements is reported as melt flow rate. The formulae used to calculate the melt density and MFR are as in Equation 49 and 50.

$$Melt\ Density\ \left(\frac{gm}{cc}\right) = \frac{Extrudate\ mass\ (gm)}{1.804} \qquad \text{Equation 49}$$

Where 1.804 cm^3 is the volume of the polymer that will be extruded by 25.4 mm movement of piston if the polymer melt density is 1 gm/cc.

MFR is expressed in grams/10 min is calculated using relationship;

$$MFR = \frac{426*L*d}{t} \qquad \text{Equation 50}$$

Where,

L is the length of the piston travel (cm),

d is the resin density of the polymer at test temperature (gm/cc),

t is the time (sec) of piston travel for length L,

426 is the mean of areas of piston and cylinder X 600.

3.2.2 Rheological characterization

The complex rheological properties of nanoclay incorporated polypropylene concentrates such as viscoelasticity and storage and loss modulus at different temperatures were analyzed using the Advanced Rheometric Expansion System (ARES) 2000 capillary rheometer. Tests were carried out at 240 °C at shear rates ranging from 10 to 10000 sec^{-1}. Capillary tube with length to diameter ratio of 25/1 was used. For each sample, pressure drop with temperature curve was obtained.

3.2.3 Wide angle X-ray diffraction (WAXD)

WAXD scans of the film, chopped fibers, nonwoven and molded nanocomposite samples in reflection mode were carried out using the Phillips X Pert Pro X-ray diffraction system with CuKα radiation (45 kV, 40 mA) of wavelength 1.542 A°. Samples were scanned in 2θ range of 2 to 40˚ and step size of 0.02 at 1 sec for each step. Change in crystallinity wt %, and clay dispersion was determined. Crystal size (t) was calculated using the Scherrer equation[191], from the measured full-width at half-maximum (FWHM) intensity of reflection peaks in the equatorial scans. Scherrer equation is shown in Equation (51)

$$t = \frac{0.9\lambda}{\mathrm{B}\cos\theta B} \qquad \text{Equation 51}$$

Where, λ is the wavelength in A° and B the measured FWHM intensity of (110) reflection peaks. Wide angle x-ray diffraction scan (WAXS) patterns of the blown nylon 6 films and melt spun fibers were obtained using a flat plate-type camera and with CuKα radiation (wavelength 1.542 A°). A Rigaku molecular metrology x-ray diffractometer was used to evaluate the presence of the different phases and the azimuthal scan to evaluate the orientation function.

Amorphous orientation fraction of melt spun fibers was determined by combination of optical birefringence and crystalline orientations measurements. Crystalline orientations of monoclinic γ phase were calculated as per Wilchinsky's rule explained by Ergungor et al.[116] Wilchinsky's rule for monoclinic α crystal can be given by[192]

$$\cos^2{}_{xb,z} = 1 - 1.4717 < \cos^2 \chi 200, z > -0.8721 < \cos^2 \chi 002.202 > \qquad \text{Equation 52}$$

$$\cos^2{}_{xc,z} = 1 - 1.172 < \cos^2 \chi 002, z > \qquad \text{Equation 53}$$

$$\cos^2{}_{xa,z} = 1.4717 < \cos^2 \chi 200, z > -0.8356 < \cos^2 \chi 202, z > + 0.5357 < \cos^2 \chi, 002, z > \qquad \text{Equation 54}$$

$$f_{a,z} = \frac{1}{2}(3 < \cos^2 \chi_{b,z} > -1) \qquad \text{Equation 55}$$

$$f_{b,z} = \frac{1}{2}(3 < \cos^2 \chi_{a,z} > -1) \qquad \text{Equation 56}$$

$$f_{c,z} = \frac{1}{2}(3 < \cos^2 \chi_{c,z} > -1) \qquad \text{Equation 57}$$

For the monoclinic γ form,

$$< \cos^2 \chi_{c,z} > = 1.3611 < \cos^2 \chi_{001,z} > \qquad \text{Equation 58}$$

The equatorial reflection for γ (001) monoclinic form in WAXD pinhole diffraction pattern was converted in to integrated intensity as a function of azimuthal angle 0-180° using Polar software.

Herman's orientation function produces a single number that can be used to describe the average orientation of a polymer chain[193]. From the reflection data, Herman's Stern orientation functions were calculated using Equations;

$$f_c = \frac{3}{2} < \cos^2 \phi_{c,z} > -\frac{1}{2}$$ Equation 59

$$f_c = 2.04 < \cos^2 \phi_{001,z} > -\frac{1}{2}$$ Equation 60

From f_a and f_c the orientation function along the fiber chain axis f_b is calculated

$$f_c = -2 f_c = -2 f_a$$ Equation 61

From fiber birefringence and crystallographic orientation results, the amorphous orientation is determined using Equation 62

$$\Delta n = \chi f_c \Delta_c^o + (1 - X) f_{am} \Delta_{am}^o + \Delta n_{form}$$ Equation 62

Where, Δ_n is the fiber birefringence; X is the crystalline weight fraction, values were taken from the differential scanning calorimetry (DSC). The contribution of α form to birefringence and the Δn form which is optical contrast due to nanoclay additives was assumed to be negligible[116]. $\Delta°_{am}$ and $\Delta°_c$ are intrinsic birefringence's of amorphous and crystalline regions which were taken as $\Delta°_{am}$=0.064, $\Delta°_c$=0.078 from literatures[116].

3.2.4 Small angle x-ray scattering (SAXS)

Small angle x-ray scattering (SAXS) profiles were obtained on Rigaku molecular metrology x-ray diffractometer with CuCα radiation operating at 45kV and 24mA. Distance between sample and detector was 550 mm.

3.2.5 Differential Scanning Calorimetry (DSC)

Thermal analysis was carried out using the Mettler Toledo DSC 822e. Samples were heated in the temperature range of 25° to 300°C at heating and cooling rates of 10°C per minute in the N_2

atmosphere. Crystallinity $X_c\%$, of nanoclay incorporated samples were calculated from enthalpies of crystallization using Equation 63

$$X_c(\%) = \frac{\Delta H}{(1-\varphi)\Delta H_{100\%}} \times 100 \qquad \text{Equation 63}$$

Where, ΔH is the measured heat of fusion of the sample, φ is the weight fraction of nanoclay additive, $\Delta H_{100\%}$ is the heat of fusion of the 100 % crystalline polymer which is taken as 190 J/g for nylon 6 and polypropylene[194,195].

3.2.6 Isothermal and non-isothermal crystallization kinetics

For isothermal crystallization kinetics, samples were cooled at -65°C to the desired crystallization temperature for different polymer systems (PP, nylon 6, and nanocomposite samples) and held for 20 minuits. Each run was performed under 80 ml/min nitrogen purge. For $t_{1/2}$ and t_{max} calculation, induction time t_i is subtracted from the t.

The non-isothermal crystallization behavior of control nylon 6 and nylon 6-clay composites were studied as follows: the samples were initially held at 40˚C for 5 min, heated from 40 to 250 °C, about 20 °C above the melting temperature of nylon 6, at a rate of 10 °C/min. The samples were kept at 250°C for 5 min to erase the processing history before cooling at a specified cooling rate. The samples were then cooled to 40 °C at cooling rates of 5, 10, 20, 50, 65 and 85 °C/min. Variation in crystallization behavior and nature of exotherm for different samples with clay additive was studied. Each run was performed under 80 ml/min nitrogen purge.

3.2.7 Thermo Mechanical Analyses (TMA)

Thermo mechanical analysis of the samples in compression mode was carried out using the TMA/SDTA 840. In compression mode, samples were placed between the fused silica discs and heated in the temperature range from 30 °C to 150 °C at a heating rate of 10°C / min. Tests were carried out at varying probe forces of 0.02 N to 0.90N and constant probe force of 0.02N. Analyses in elongational mode were carried out using copper clamp method. Samples were

mounted in probe using the copper clamps as shown in Figure 3.3 and the sttandard 13 mm clamping distance in the sample press was used[196].

3.2.8 Thermo Gravimetric Analysis (TGA)

Thermo gravimetric analysis of the samples was carried out using the TGA/ SDTA 851. Samples were placed in 70µl Aluminum oxide crucible and heated from room temperature to high temperature above decomposition temperature of the polymer. In this research, TGA scans of Closite Na^+ and nanocomposite samples is scanned from 50 to 500°C at a heating rate of 10°C/min. Each scan was performed under 80-ml/min nitrogen purge. Indium/Aluminum was used to calibrate over the whole temperature range. Change in thermal transition, onset, loss temperature and decomposition behavior of sample was analyzed.

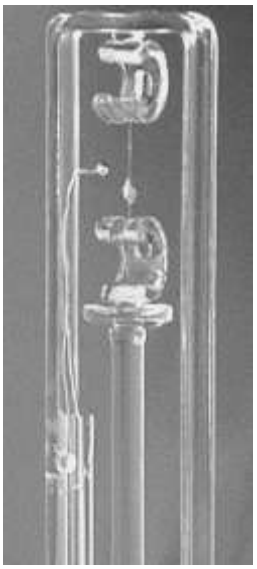

Figure 3. 3. Schematic of TMA copper clamp probe from METTLER TOLEDO TMA SDTA 840e [196].

3.2.9 The Dynamic mechanical analysis (DMA)

The Dynamic mechanical analysis (DMA) of center portion of dog bone samples was analyzed using TA instruments DMA Q800. Three point bending test was carried out in case of each sample covering frequency of 0.1, 1, 3, 10 Hz and 0.08 % strain. Rectangular bar from center portion of the mold was used for test. Dimension of sample in each case was, length = 35± 0.2 mm and width 7 ± 0.2 mm. Two point bending test was carried out for each sample in the temperature range of -50°C to 150°C at a heating rate of 10 °C/min.

DMA tests dependence of molecular properties on the temperature and frequency. Important property which can be determined from results which relate temperature and frequency of tests is activation energy from Arrhenius equation (Equation 64)[197, 198]. Activation energy can be determined from the semi-log plot of Arrhenius equation (as included in Equation 65)

$$Frequency = Ae^{\frac{-Ea}{RT}} \qquad \text{Equation 64}$$

$$\ln(Frequency) = \ln A - \frac{Ea}{Rt} \qquad \text{Equation 65}$$

The temperature and frequency values of DMA results are plotted on semi log plot, from the slope, activation energy can be calculated by multiplying slope with –R (8.314 J K^{-1} mol^{-1}).

3.2.10 Nonwoven testing

Samples of spun fiber and spunbond fabrics produced in the experiments were conditioned for 24 hours under standard textile laboratory conditions and analyzed for physical properties and structure according to ASTM D1117-97 - Standard Test Methods for nonwoven fabrics [199]. Thicknesses of film and fabric samples were measured using the TMI thickness tester as per ASTM D5729-97.

Fabric stiffness was estimated by measuring the bending length using the cantilever bending test method as per ASTM D5732-95. Bending length is the length of fabric at which, nonwoven web bends under its own weight which is taken as a means to account for nonwoven web stiffness. In

this method, rectangular fabric strip of 15 × 2.5 mm is selected in each case. Sample is placed on the horizontal platform with the engraved scale and slid at constant rate along with template. Length is noted down when the sample bends under its own weight and makes an angle of 41.5° with the horizontal platform. Each sample was tested four times on both sides (top, bottom) and by turning (right, left). Tear strength was determined as per ASTM D5734-95 using the Elmendorf tear tester. Burst strength was tested using the B F Perkins, Mullen burst tester as per ASTM D3786-87[199]. Extent of color change in film and web samples due to nanoclay additives was determined using Miniscan XE hunter colorimeter.

3.2.11 Tensile test

Single fiber tensile test was carried as per ASTM 8322. Fibers were pasted on cardboard template as shown in Figure 3.4. After curing epoxy drop for 24 hours at room temperature, tab was placed in grip of tensile tester and tab was cut. The single fiber was tested at gauge length of 2.5 cm at speed of 2.5 cm/min.

Tensile properties of nonwoven web were determined using the United tensile tester as per ASTM D3822-07. Sample dimension of 25mm width and 75mm gage length were used for tensile test and stretched to break at a uniform strain rate of 0.0034 cm/min. For fiber samples, a bundle of 20 filaments was tested using 25 mm gauge length.

Tensile test of injection molded dog bone samples was conducted as per ASTM-D638 using Instron Inc model 5567 computer controlled tensile tester equipped with extensometer. Five specimens (dimension width 7.5 ± 0.2 mm, thickness 3.5 ±0.2 mm) of each concentrate were tested. The crosshead speed was kept at 5 mm/min and test was carried out at room temperature.

3.2.12 Izod impact strength test

Impact strength is analyzed using Tinius Olsen Model 892 tester as per ASTM D256-04. Rectangular test specimens of length 63.5±0.2 mm, width 6.5±0.2 mm and depth 12.5± 0.02 mm for izod impact strength test was prepared using injection molding. Notching was done using Tinius Olsen milling machine. Cutting speed and feed speed was constant throughout the cutting. Angle of notch was 45±1° with radius of curvature at apex of 0.25±0.05 mm. After cutting the

notch, depth of plastic material remaining under the notch was 10.16 ± 0.05 mm. The energy absorbed per unit of specimen cross-sectional area under the notch is reported[200].

3.2.13 Nanoindentation

Nanoindentation technique was used to investigate the mechanical properties of nanoclay incorporated nylon 6 films. Nanoindentation experiment was carried out using Nanoindenter X.P MTS tester with Berkovich hp tip, 2 nm for continuous stiffness at strain rates of 0.02, 0.05, 0.1, 0.2 sec^{-1}. Each indent was separated by 150μm to avoid overlapping of plastic deformation between neighboring indents.

Experiment involved following steps;

1. Careful approach of indenter to surface
2. Loading to peak load (mN)
3. Holding of indenter at peak load
4. Unloading 90% of peak load for 50's
5. Holding the indenter after 90% unloading for 100 s
6. Completely unloading

As the indenter penetrates in to sample, both elastic and plastic deformations occur in the sample. Only elastic portion of displacement is recovered. Hardness (H) and elastic modulus (E) were calculated from load-displacement data as in Equation 66;

$$H = \frac{P_{\max}}{A} \qquad \text{Equation 66}$$

Where $P_{\max}$ is the load measured at maximum depth at the point of penetration (h) during indentation, A-projected contact area ($24.5\ h_c^2$) and h_c is contact depth of indent. Elastic modulus of the sample can be inferred from the initial unloading contact stiffness (S), i.e., the slope $\left(\frac{dp}{dh}\right)$

of the initial portion of unloading curve. The relation between contact stiffness, contact area and elastic modulus are given by Equation 67;

$$S = 2\beta\sqrt{\frac{A}{\pi}}E_r \qquad \text{Equation 67}$$

Where β is a constant that depends on the geometry of the indenter (β=1.034 for Berkovich indenter) and E_r is the reduced elastic modulus which accounts for the fact that elastic modulus occurs in both the sample and the indenter. The sample elastic modulus (E_s) can be given as in Equation 68;

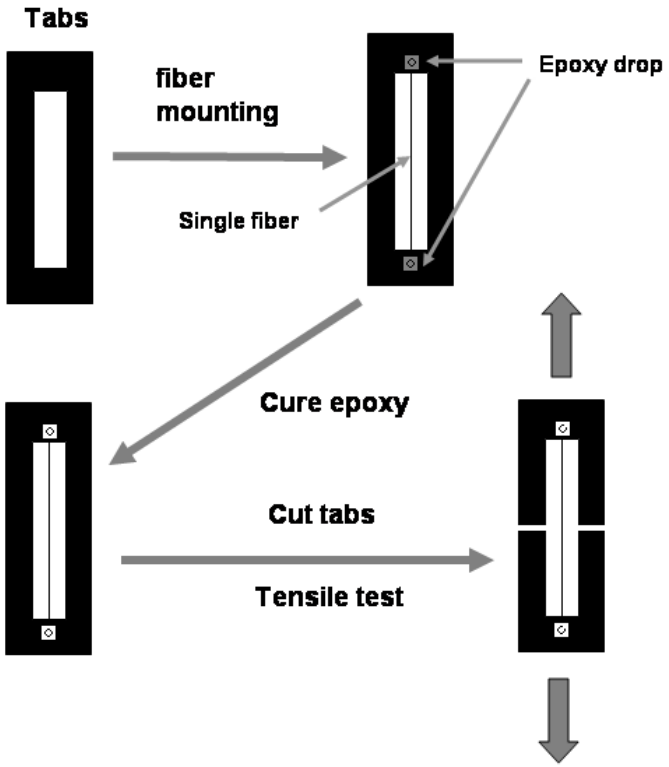

Figure 3. 4. Single fiber tensile test template.

$$E_s = (1-\nu_s^2)\left(\frac{1}{E_r} - \frac{1-\nu_i^2}{E_i}\right)^{-1} \qquad \text{Equation 68}$$

Where, v_s and v_i are the poissons ratios of specimen and indenter respectively, while E_i is the modulus of the Berkovich indenter (1141 Gpa)[201]. In this research, near surface hardness and elastic modulus of nylon 6-clay nanocomposites films were evaluated using the nanoindentation technique.

3.2.14 Energy dispersive spectrometers (EDS)

EDS has a small solid state device cooled by liquid nitrogen which produces the voltage pulse with energy equivalent to incident photons. These pulses are sorted, counted and displayed as spectrum on cathode ray tube by an analyzer. An advantage of EDS over WAXD is the large collection angle which makes it suitable for the quick analysis of rough surfaces. Its disadvantages are low resolution and error in the results due to peak overlaps. These spectral overlaps lead to inaccurate determinations [202]. In this research, Oxford Pentafet EDS system was used to evaluate chemical composition in failure spots of nanocomposite. ZAF Quantitative method: ZAF (3 iterations) with the system resolution of 127 eV and running Link ISIS software was used for data analysis.

3.2.15 Polarized light Microscopy (PLM) analysis of spherulite

For spherulite microstructure analysis, small section of PP pellets were kept in between the glass plate and cover slide. Samples were isothermally melted at 205°C using a hot press and kept in molten state for 10 min to ensure complete melting. The hot press was then switched off and the samples were allowed to cool on the heated plate of the hot press. Average thickness of the crystallized film was less than 200μm. Spherulite images were analyzed using Olympus BX51 polarized optical microscope. Maximum diameter of spherulite for each sample was determined from average of n = 30 spherulite measurements. Experimental conditions used for isothermal crystallization kinetics of polypropylene concentrates were simulated using the combination of hot stage and polarized optical microscope. The spherulite micrographs of different PP

concentrates at 125 and 135°C were analyzed using METTLER FP82HT hot stage controlled by FP90 Processor. Two separate hot stages were used for this analysis. Small samples were first placed on glass slide on the hot stage, which was maintained at 250°C. After complete melting, the glass slide was shifted to the second hot stage, which was maintained at the crystallization temperature of 125°C and 135° C. Spherulite micrographs were taken at 300, 600, and 900 seconds using Olympus BX51 polarized optical microscope in transmission mode.

3.2.16 Birefringence

The birefringence can be thought of as a direct measure of the orientation of polymer chains along the fiber axis. An increase in the birefringence value usually indicates a more oriented sample[193]. The optical retardation of as spun nylon 6 fibers and spunbond fibers (fibers in the SB web) was determined using Olympus BX51 polarized optical microscope equipped with a 20X analyzer eyepiece and tilting compensator B. From the optical retardation (R) birefringence (Δn) is estimated using Equation (69) given by

$$\Delta n = \frac{R}{t} \quad \text{Equation 69}$$

Control nylon 6 and nanocomposite fiber birefringence measurement was used to gain insight into polymer orientation with respect to fiber axis.

3.2.17 Electron microscopy

Scanning Electron Microscopy (SEM) images of the MB web surface, SB web failure structure and tensile failed injection molded samples were taken using the Leo 1215 Field emission gun. The samples were coated for 10 seconds using the SPI sputter coater. Image magnification was in the range of 100 to 1700X.

To count the interspherulite region between the different concentrates, Image J and Image Pro Plus software's were used. Figure 3.5 (a), (b), (c), (d) and (e) shows example of SEM micrograph of PP with 1 wt % clay analyzed suing the Image pro plus count size tool. RMC Power tome CRX microtome equipped with diamond knife is used for sectioning of samples for TEM. The injection molded nanocomposites, 1 mm thick rectangular blocks from surface of

mold was used as sample for sectioning. Thin sections were directly cut from rectangular piece as shown in Figure 3.6 (a). In the case of fiber and nonwoven webs they were embedded within epoxy block and the thin sections were cut from the composite block as shown in Figure 3.6 (b). Specimen temperature was –100°C and Glass knife temperature was set to –103°C. Thin sections of thickness less than 70 nm perpendicular to machine direction (MD) were cut from the samples. Sections were stained for 48 hours using Osmium tetroxide (OsO4).

The stained sections were mounted on standard 400 mesh Cu grids and TEM images were taken using the Hitachi H-800 electron microscope operated at 200 kV. Neat clay samples were held on the Cu grids coated with film. Scanning Transmission Electron Microscopy (STEM) is a high-resolution imaging technique, used to get chemical and structural characterization of samples. It is a special TEM technique in which finely focused electron beam is bombarded on to the samples and transmitted beam, back-scattered electrons and even characteristic x-ray spectrum of the samples can be obtained [203]. Convergent electron beam is scanned on selected area of the sample. The back-scattered electrons are gathered and converted into an image. Transmitted beam is used in analytical TEM and also x-ray spectroscopy [204]. High-energy beam has very high depth of penetration into the sample.

There is no chromatic aberration in the case of STEM because there is no lens below the sample. Sample thickness of up to 5μ can be analyzed using the STEM technique. In this research, nylon 6 film sections were characterized using STEM facility at CNMS. Surface topology of nylon 6 blown films was analyzed using an AFM in taping mode. Surface roughness was calculated for the blown film sample from AFM height image size.

Phase and height images were captured in tapping mode using Antimony (n) doped silicon probe tips (Veeeco TESP7), with a spring constant in the range of 20-80 N/m. Dimension of probe used was: thickness: 3.5-4.5 μm, Length: 110-140 μm and width: 25-35μm. Five images were taken for each blown film sample. The cantilever was oscillated in resonance frequency range of F-280-341kHz.

3.2.18 Contact angle measurements

Influence of nanoclay additive in the surface wettability of nylon 6 films was measured using sessile drop technique. The contact angles of sessile drops of water on the nylon 6 films were measured using Easy drop device from KRUSS. The water was dispensed from the syringe at a constant rate of 5 μl/min. The contact angles were measured on the digitized optical image of the drop on both the edges using the software. Average of n-20 readings is taken as contact angle data for each of the blown film sample. Earlier studies have shown that the contact angle exhibits hysteresis for advancing and receding liquids due to the surface roughness and heterogeneity[95]. So the surface topology results from AFM were used along with the contact angle results to interpret the data.

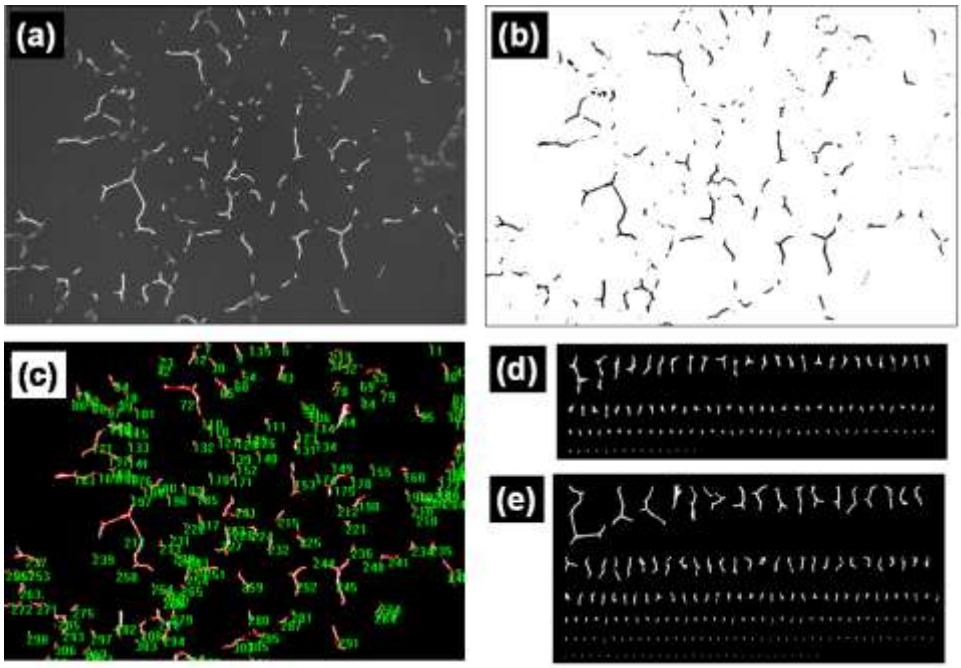

Figure 3. 5. (a) SEM micrograph of concentrate with 1% clay additive (b) Micrograph processed with Image J software, (c) Image Pro plus count size tool, (d) inter spherulite region objects in control PP arranged according to size (e) inter spherulite region objects in concentrate with 10% clay additive arranged according to size.

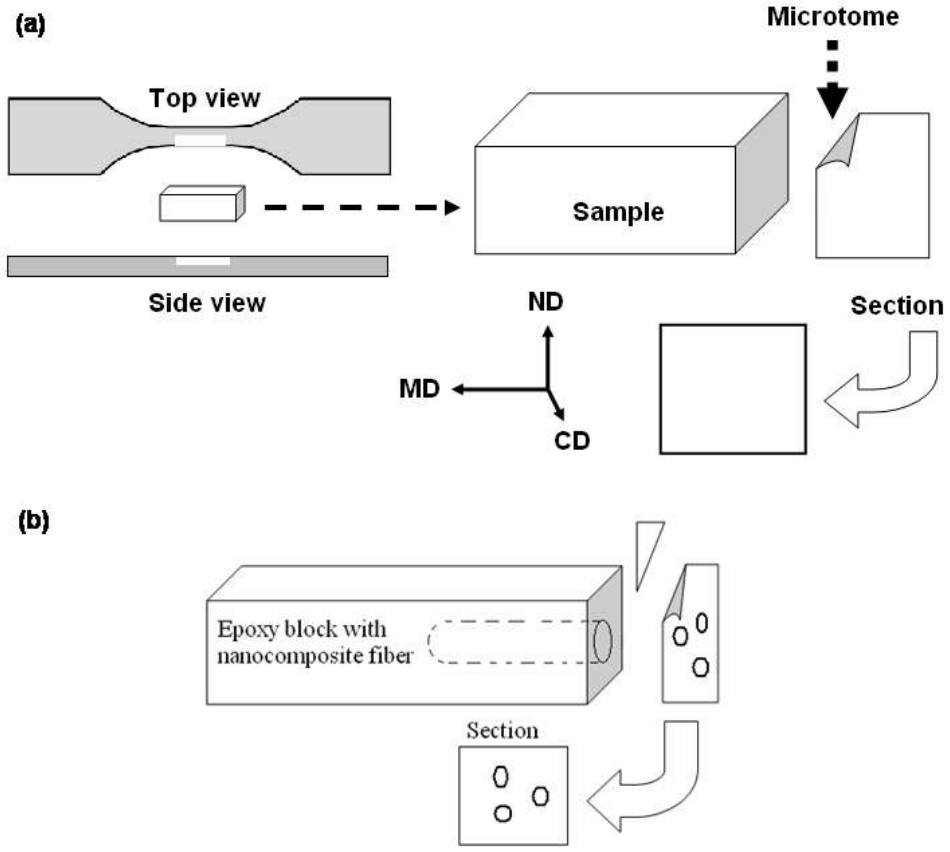

Figure 3. 6. TEM sample sectioning schematic of (a)-injection molded dog-bone samples, (b)-fiber and nonwoven web nanocomposites.

CHAPTER IV

RESULTS AND DISCUSSION

4.1. Nylon 6 nanoclay blown films

4.1.1 Nanocomposite morphology

WAXD scans of films with different weight % of nanoclay additive are included in Figure 4.1.1. Diffraction peak corresponding to (001) plane of neat clay (occurs at 2θ of 6.07°) increased for sample with increase in wt % of additive in film. This peak intensity decreases with intercalation/exfoliation and completely disappears for fully exfoliated samples. Also, sharpness and intensity of peak corresponding to crystalline segment increased with additives indicating increase in crystal size and percentage crystallinity. Films with 0.25 and 0.5 wt % clay have the lowest peak intensity corresponding to (001) plane of nanoclay, which is an indication of good dispersion in film samples.

Crystallinity and crystal size are not estimated from the WAXD scans due to complications and possible errors involved in measurements. One of the complications is the center peak consisting of superimposition of reflections from crystalline and amorphous portions. Center peak includes reflections from α_1, γ and α_2-forms at 2θ of 20°, 21.3° and 23.7° respectively. Subtraction of baseline from the peak is also not accurate. 2D WAXS patterns in the CD direction of films are shown in Figure 4.1.2. Patterns do not show change in orientation for samples with additives.

SEM micrograph of neat Closite Na^+ samples is shown in Figure 4.1.3 (a). The micrographs revealed fine particles of dimension in the range of 2 to 20μm. TEM image of neat nanoclay is shown in Figure 4.1.3 (b). Dark shady lines in the image represent the cross-section of layered clay platelets, each of thickness less than 10A°. TEM images of film sample with 0.25, 0.5, 2, 5 and 10-wt % nanoclay additive are included in Figures 4.1.4 to 4.1.8.

Images revealed clay platelets of thickness less than 5 nm uniformly dispersed in sample. Sections of film samples with 0.25 to 2 wt % clay (Figure 4.1.4, 4.1.5) show better exfoliation of clay in the matrix.

Good dispersion of additive in the matrix is due to the polar nature of nylon 6 and ionic bond formation between clay and the nylon 6 chains [27]. Extent of chain intercalation within small agglomerate was analyzed using STEM (scanning transmission electron microscope) analysis. High magnification STEM micrograph (Figure 4.1.6) shows significant polymer chain intercalation. In the case of film sample with 5 wt % additive (Figure 4.1.7), slightly large well dispersed tactoids were observed. Low magnification micrographs also revealed better dispersion of clay platelets through the samples along the direction of melt flow. At high magnification, image shows significant intercalation of polymer chains within the clay platelets.

TEM micrographs also reveal the influence of processing conditions on the additive orientation, and distribution of particle in the sample. Overall sample had clay platelets oriented along the MD direction of film. The platelet surfaces were oriented parallel to the thickness direction. Similar orientation and distribution of platelets has been reported in earlier studies[205-207], which reconfirms the influence of processing conditions on additive orientation and distribution.

In the case of sample with high weight percentage clay, highly aggregated and intercalated morphology was observed. Image of section with 10-wt % clay additives (Figure 4.1.8) shows large amount of clay particles through the sample. Presence of large aggregates and tactoids were observed in the case of sample with 10-wt % clay additive.

The section of aggregates in film with 10-wt % clay, where though there is enough polymer chain intercalation, the agglomerates have some void in between the platelets. Delamination of clay platelets with large clay agglomerates caused micro-voids in the samples. Most of the voids nucleated between the clay layers because, the electrostatic interaction between the clay platelets is weak compared to strong interaction between the clay platelets and nylon 6 matrix[128].

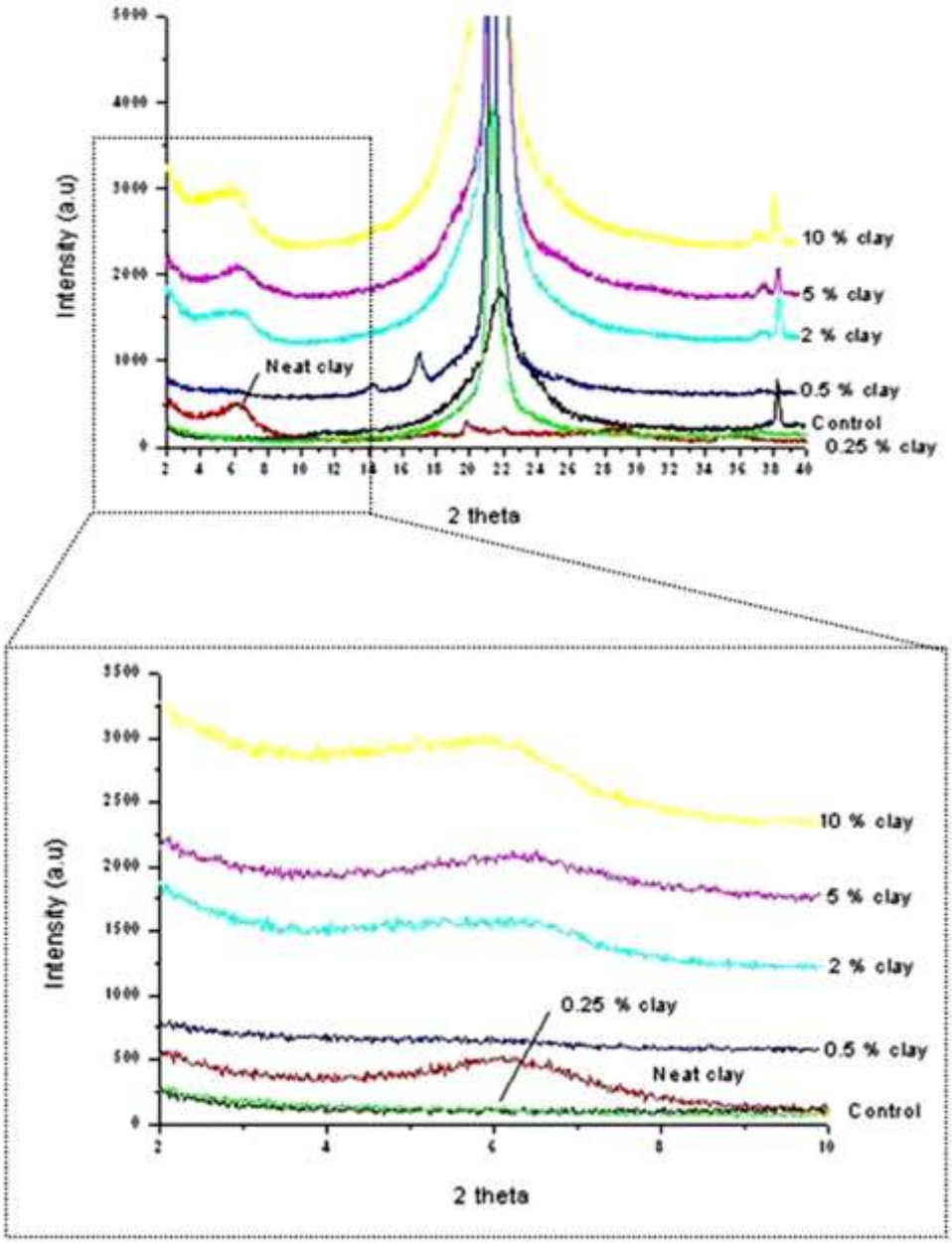

Figure 4.1. 1. WAXD scans of nylon-6 with different wt % of nanoclay.

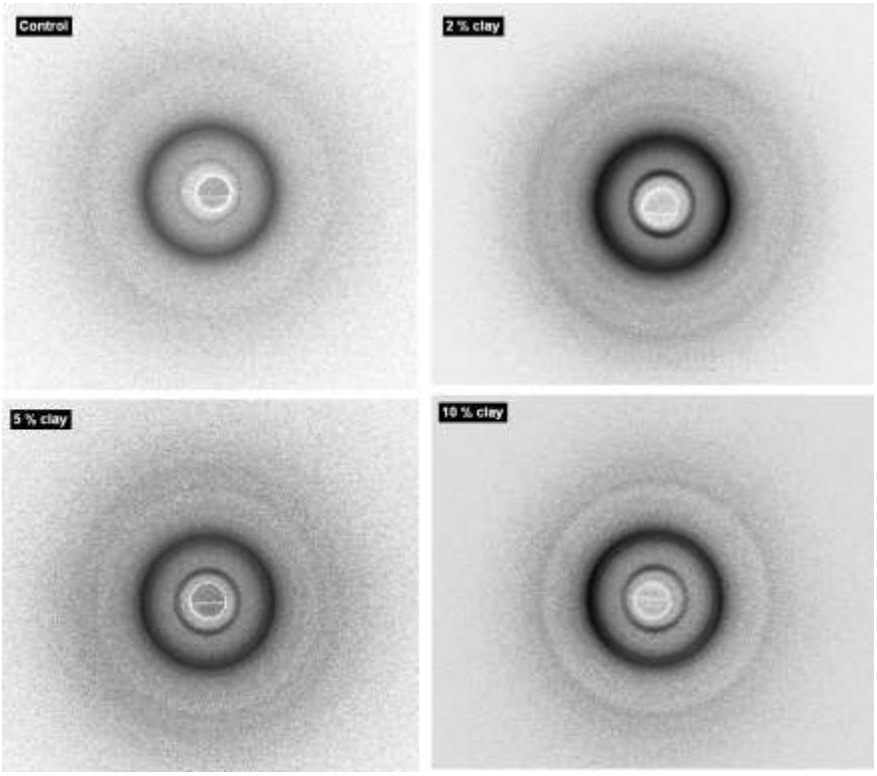

Figure 4.1. 2. 2D WAXS pattern in the CD direction of films.

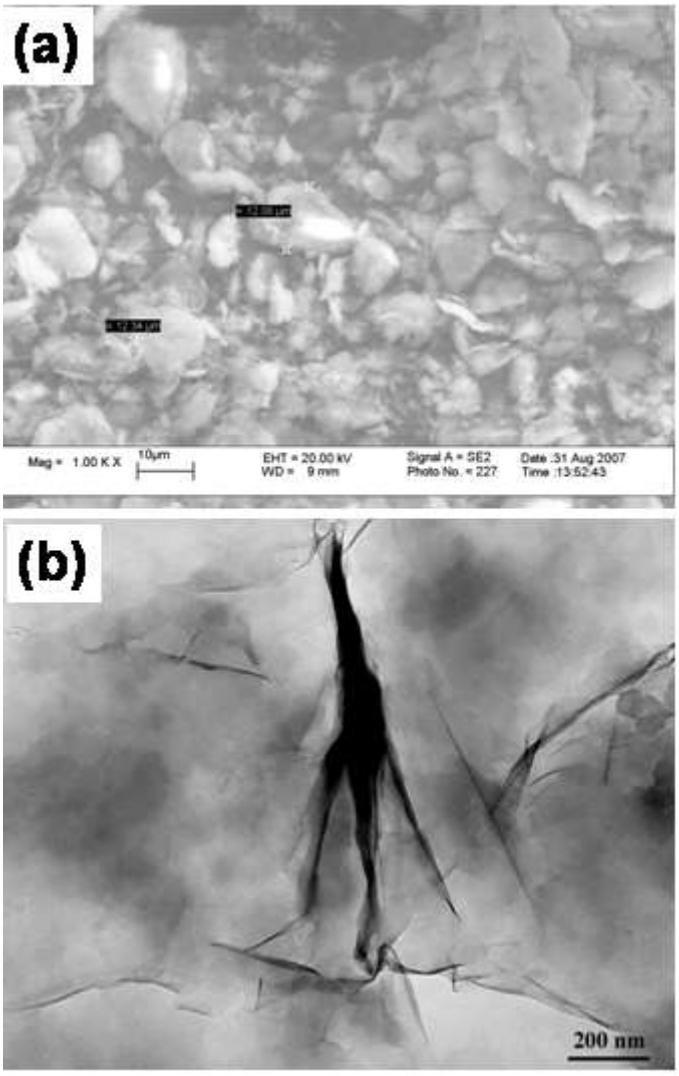

Figure 4.1. 3. (a)SEM micrograph of neat clay powder, (b) Transmission electron microscopy image of neat nanoclay.

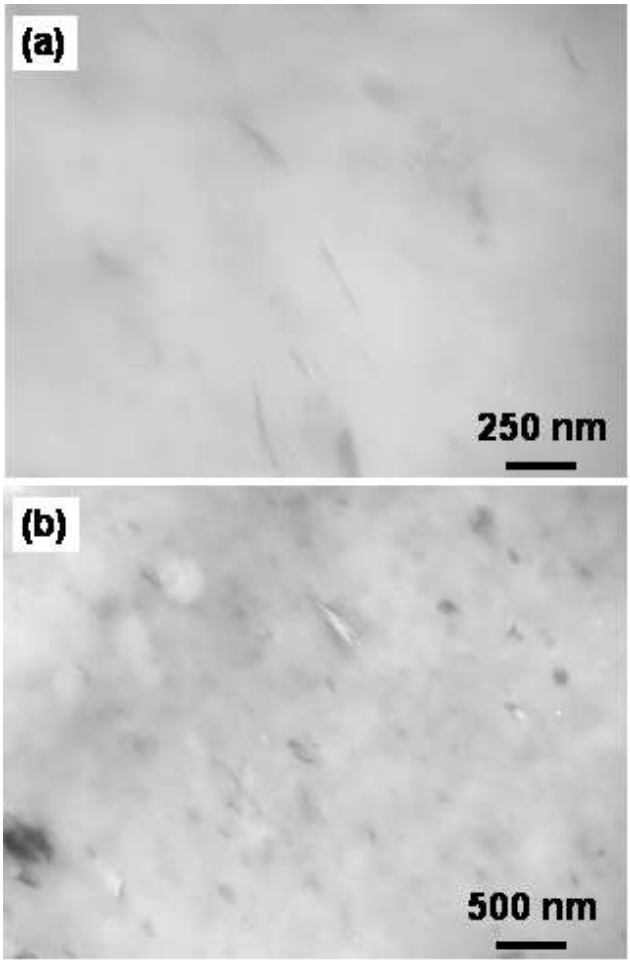

Figure 4.1. 4. TEM micrographs of (a) nylon-6 film with 0.25 wt % nanoclay, (b) film with 0.5 wt % clay.

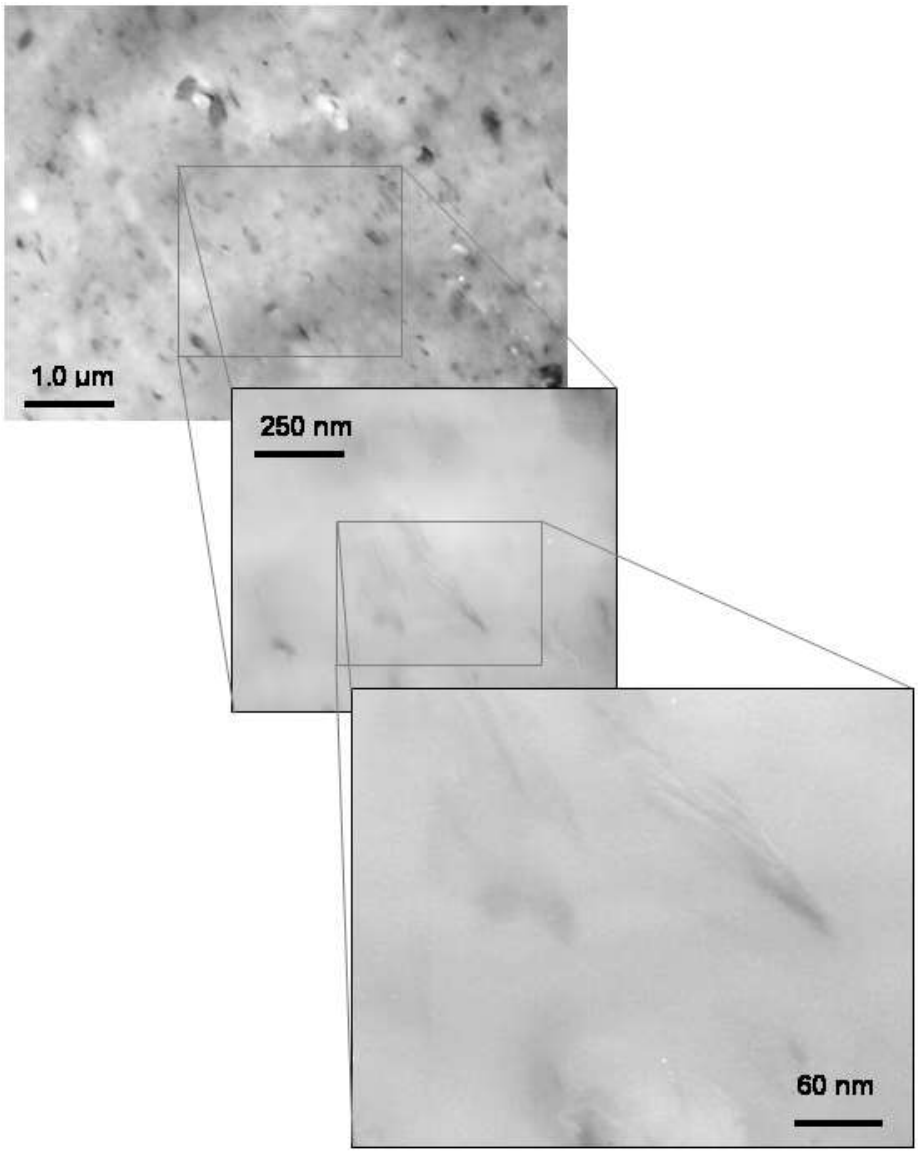

Figure 4.1. 5. TEM micrographs of nylon-6 film with 2 wt % nanoclay.

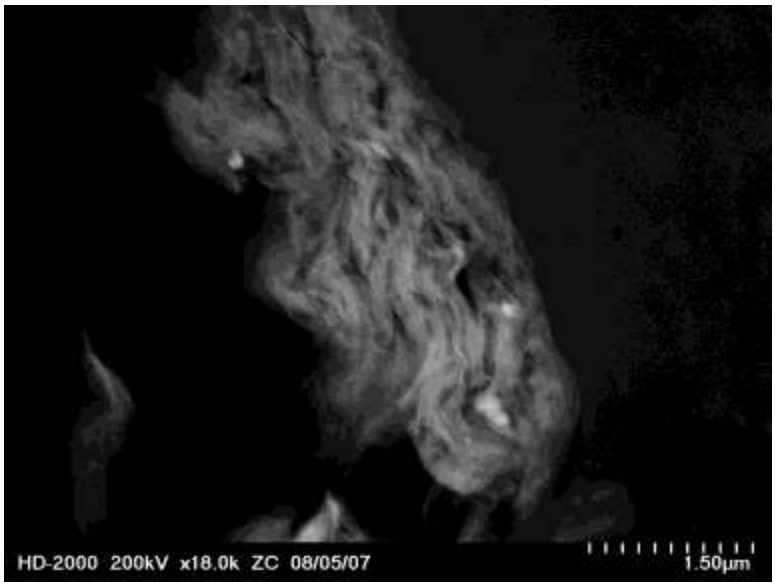

Figure 4.1. 6. Dark field TEM micrograph of small particulate of film with 2 wt % clay additives.

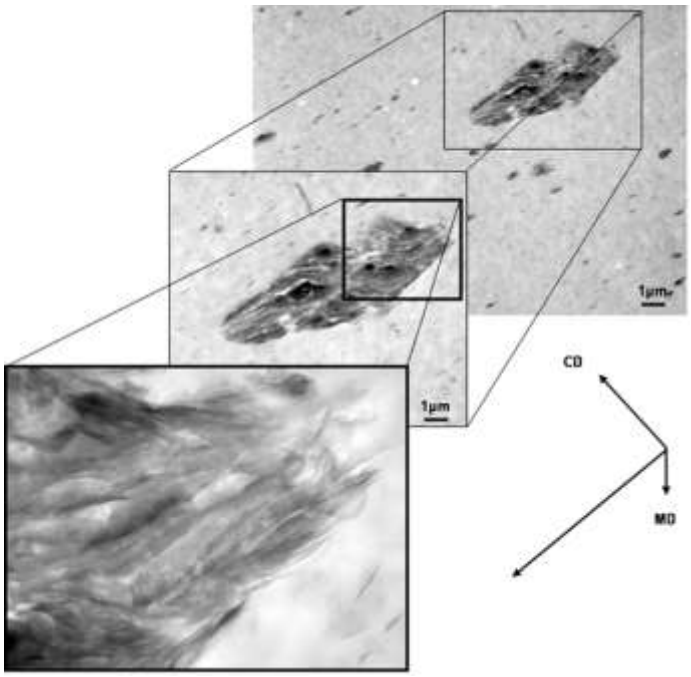

Figure 4.1. 7. TEM image of nylon-6 film with 5 wt % nanoclay.

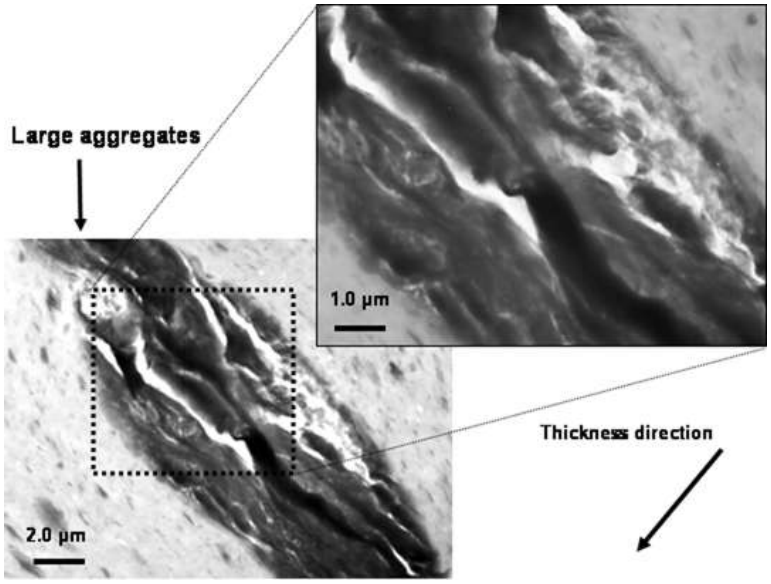

Figure 4.1. 8. TEM image of nylon-6 film with 10 wt % nanoclay.

4.1.2 Thermal analysis

Thermal analysis results obtained from DSC cooling segments are included in Table 4.1.1. All the films with nano additives show higher crystallization temperatures than that of control indicating nucleating effect of additives. All the samples with nanoclay additives have higher onset of crystallization temperature, which is due to the nucleating effect of additives. However this increase shows a tendency of going up till 2% clay and then the level of increase drops off with further increase in clay platelet. Also, there is some shift in peak melting temperature and change in the shape of the melting peak, indicating differences in crystallinity or crystal size distribution.

Isothermal and non-isothermal crystallization kinetics studies were carried out using DSC. Relative crystallinity versus time for different film samples is shown in Figure 4.1.9. Results show sigmoid shape response with two different stages of crystallization. For all the samples with clay additives, primary crystallization was completed before control film. Relative crystallinity for film with 10 wt% at different times was almost similar to that of control nylon 6. Results of isothermal crystallization parameters are presented in Table 4.1.2. The parameter "n"

varies within the range 3 to 4 which indicates spherulitic form of crystal growth[126]. Results indicate that presence of just 0.25% clay additive is enough for nucleation of nylon 6 matrix. Crystallization occurs in two stages; primary crystallization via nucleation and secondary crystallization that involves growth of nucleates in lateral direction. In the case of samples with lower weight percentage clay, well dispersed clay platelets act as nucleating sites and facilitate crystallization [208]. Whereas for the sample with 10 wt % clay, presence of large nucleation sites hinders the polymer chain diffusion and crystallization process.

Results of non-isothermal crystallization scans obtained from DSC are shown in Figures 4.1.10 (a) and (b). The non-isothermal crystallization parameters are shown in Table 4.1.3. With increase in cooling rate, the half time for crystallization ($t_{1/2}$) increases. For the nanocomposite films, half time for crystallization ($t_{1/2}$) is less than that of control nylon 6 film. With increase in cooling rate, the peak crystallization temperature shifts to lower temperature. At lower cooling rate, crystallization starts at higher temperature because there is more time available for the system to overcome nucleation barrier[150]. Also presence of clay leads to slight increase in crystallization temperature for the films with clay additives. In non-isothermal crystallization results, film with 10-wt % clay did not show significant difference compared to control or rest of the films with additives. These observations are consistent with the results seen in isothermal crystallization studies.

Table 4.1. 1. Nylon 6 film DSC results.

Sample	Control	0.25%	0.5 %	2%	5%	10%
Clay (wt %)	0	0.25	0.5	2	5	10
Onset	132	138	147	147	136	133
Peak	121	131	140	140	129	126
Endpoint	109	120	127	128	118	115
ΔHC (J/g)	56	60	60	55	52	48
Cooling rate	-65	-65	-65	-65	-65	-65
Crystallinity wt %	29	32	32	30	29	28

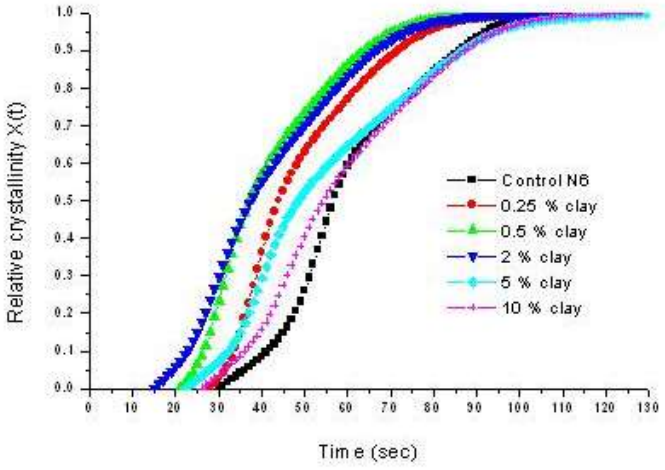

Figure 4.1. 9. Relative crystallinity for nylon 6 film with different percentage of clay.

Table 4.1. 2. Crystallization parameters for different film samples.

Sample	Control	0.25 % clay	0.5 % clay	2 % clay	5 % clay	10 % clay
n	4.3	3.6	3.3	2.4	3.2	2.8
K	1.2	2.9	4.6	1.5	1.9	1.2
$t_{1/2}$ (min)	1.0	0.7	0.6	0.6	0.8	0.8
t_{max} (min)	1.9	1.8	1.6	1.1	2.1	2.1
G(1/min)-exp	1.1	1.4	1.6	1.6	1.2	1.2
G(1/min)-theory	1.1	1.5	1.8	1.4	1.4	1.2
H_f (J/g)	89	75	72	65	72	67

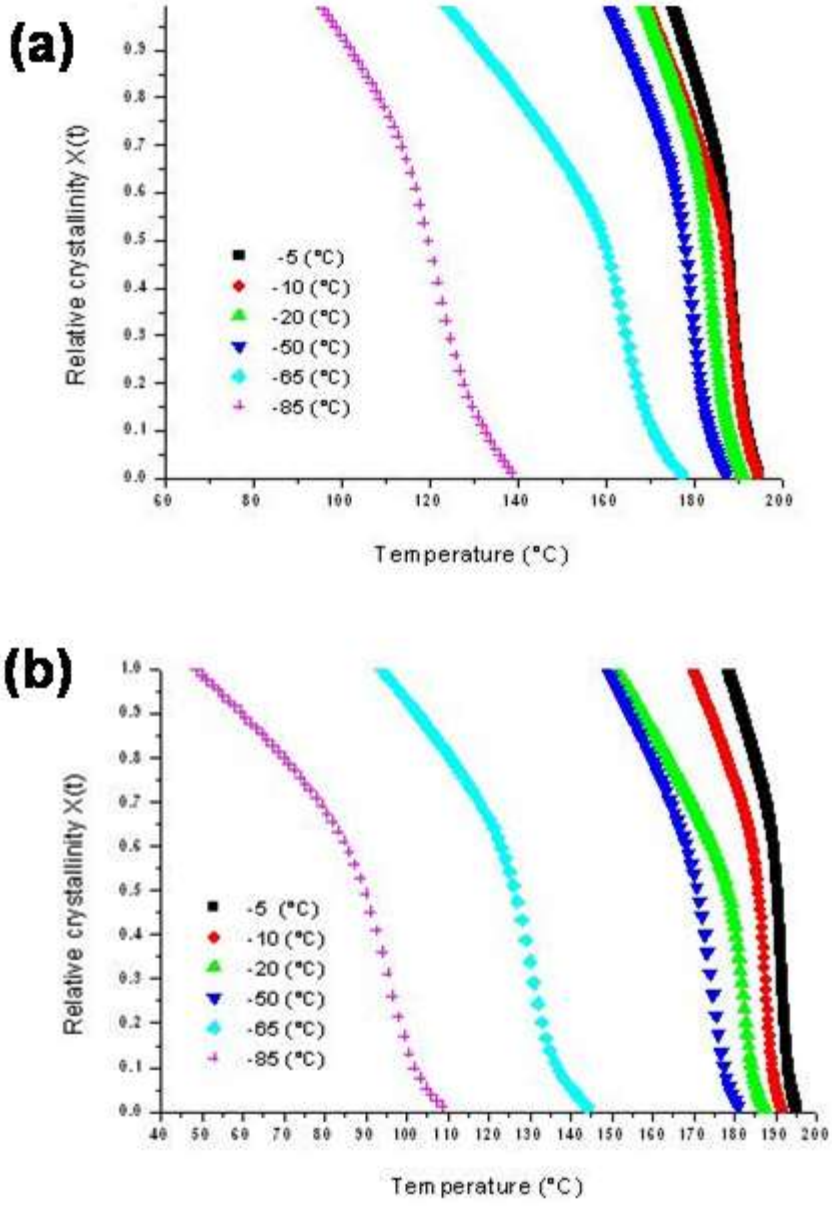

Figure 4.1. 10. (a) Control nylon 6 film, (b) nylon 6 film with 0.25 % clay.

Table 4.1. 3. The crystallization onset temperature, (T onset) and peak crystallization temperature (T peak) and half time crystallization (t1/2) for different film samples.

			Control nylon 6 film			
Cooling rate (°C)	5	10	20	50	65	85
onset (°C)	194	194	191	187	177	139
peak (°C)	175	169	168	160	123	95
t1/2 (min)	0.3	0.5	0.5	0.9	1.5	1.6
			0.25% clay			
Cooling rate (°C)	5	10	20	50	65	85
onset (°C)	195	192	187	181	144	109
peak (°C)	178	170	151	149	94	50
t1/2 (min)	0.23	0.30	0.25	0.47	0.57	0.98
			0.50% clay			
Cooling rate (°C)	5	10	20	50	65	85
onset (°C)	241	234	221	195	150	102
peak (°C)	238	226	210	183	110	42
t1/2 (min)	0.23	0.25	0.25	0.45	0.65	0.80
			2% clay			
Cooling rate (°C)	5	10	20	50	65	85
onset (°C)	198	197	191	187	173	113
peak (°C)	167	146	157	143	100	42
t1/2 (min)	0.30	0.32	0.40	0.55	0.60	1.60
			5 % clay			
Cooling rate (°C)	5	10	20	50	65	85
onset (°C)	196	193	189	181	141	114
peak (°C)	182	171	168	147	96	42
t1/2 (min)	0.17	0.30	0.32	0.37	0.65	1.08
			10% clay			
Cooling rate (°C)	5	10	20	50	65	85
onset (°C)	196	192	188	178	139	138
peak (°C)	185	170	158	147	98	41
t1/2 (min)	0.32	0.32	0.45	0.77	1.05	1.07

TGA scans of neat Closite Na^+ and nylon-6 nanocomposite films are shown in Figure 4.1.11. Scans showed slight shift in thermal decomposition temperature for films with 2 and 10 wt % clay additives. This might be due to char formation and un-availability of polymer chains for decomposition [209]. 5 % of weight loss observed in the temperature range of 90 °C to 100 °C in case of Closite Na^+ is due to the evaporation of moisture which is in agreement with the moisture content reported by Southern clay products[210].

Results of ash content at 500 °C at the end of the experiment included in Table 4.1.4 reconfirmed the presence of clay as used in the sample. Ash residue increased with weight % of clays (0.25 %< 0.5 %< 2 % < 5 % < 10 %) in films. Influence of clay additive on thermal stability has been reported before [211]. Nanoclay platelets are known to act as blocking agents and reduce surface oxidation of released condensed phase species [211]. Lower amount of heat and CO_2 are released for samples reinforced with clay.

TMA scans of samples (Figure 4.1.11-c) show significant difference in dimensional change for nanocomposites. Thermal expansion of control initiates at 92°C, whereas expansion for film with 5 % clay occurs at 130°C. Films with 2 and 10 % clay do not show any swift expansion with temperature. This shift in thermal transition for nanocomposites is due to restricted thermal motion of chains due to presence of nanoclays. Also films with additives showed elongational behavior. It has been shown that the addition of nanoclay facilitates the formation of γ-crystalline forms[212] and γ-crystalline forms acquire higher draw capability of nylon 6 in the temperature range of 110 to 180 °C [213].

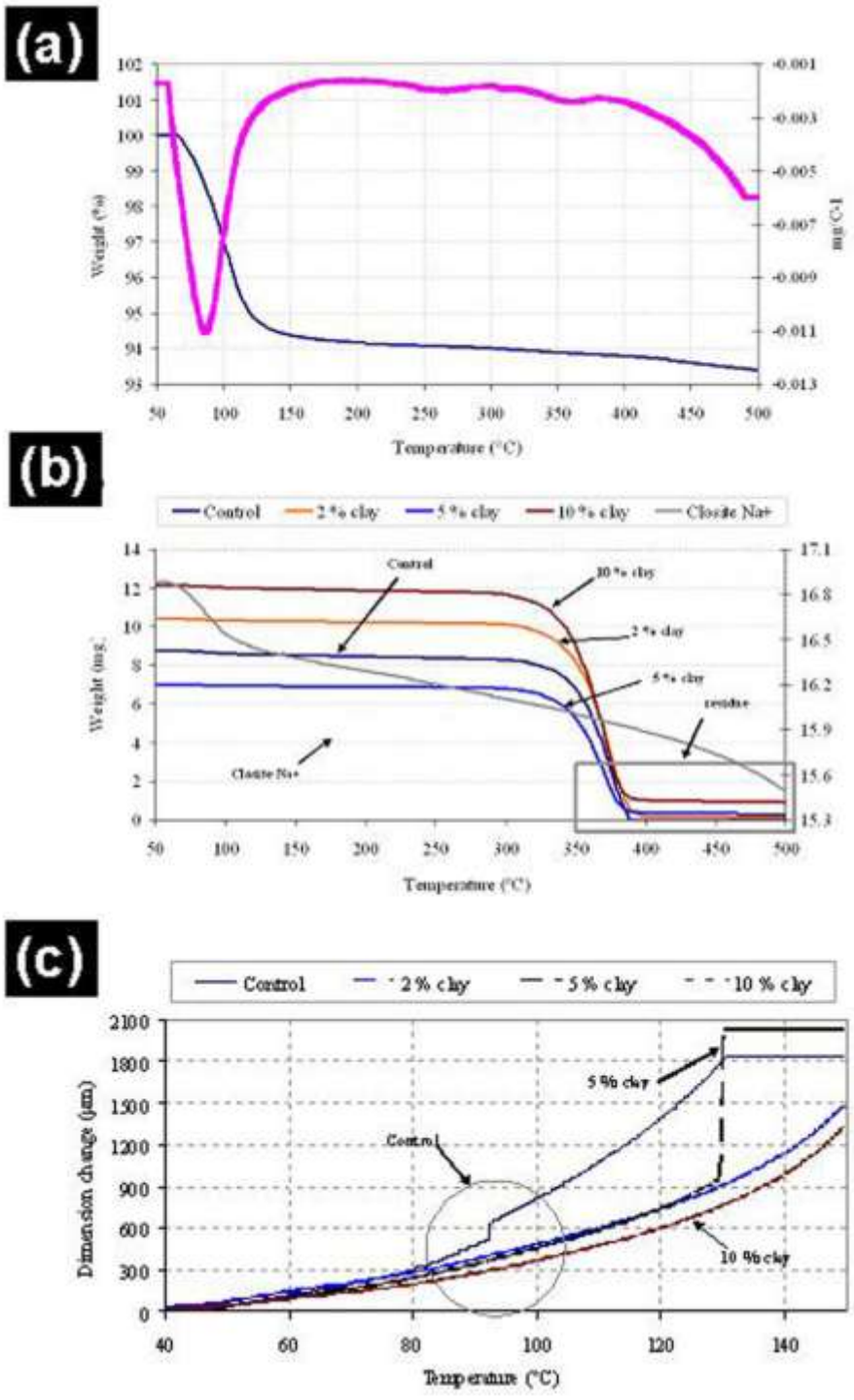

Figure 4.1. 11. TGA scans of (a) neat Closite Na^+ (b) nylon-6 nanocomposite film samples and (c) TMA results of nylon-6 nanocomposite film samples.

Table 4.1. 4. Nylon 6 film TGA, Tear strength and burst strength results.

Sample	Ash % by TGA	Clay composition (Wt %)	Tear strength (cN)	Burst strength (Mpa)
Control	0	0%	95	0.26
0.25 % clay	0.2	0.3	68	0.30
0.5 % clay	0.4	0.5	57	0.28
2 % clay	1.5	2%	88	0.31
5 % clay	4.5	5%	76	0.35
10 % clay	7.7	10%	73	0.21

4.1.3 Mechanical properties

Results of tensile test are shown in Figure 4.1.12 and Table 4.1.5. Peak force increased for the sample with clay additives. Samples with 2 and 5 wt % additives show strain hardening after the natural drawdown before failure like the control. This indicates completeness in molecular network between different crystalline segments. The sample with 10 wt% fails without any natural drawdown and fails at low percentage strain. Sample shows toughening effect and increase in hardness till 5 wt % clay additive and sample with 10 wt% becomes hard and brittle. Further, it can be noticed that there are no added benefits by increasing the clay additive level from 2 wt % to 5 wt %. Results are in accord with the earlier observations by Maiti et. al, [9].

Film burst strength and CD direction tear strength are shown in Figure 4.1.13 (a) and (b). Though results show increasing trend, results are not significantly different (statistical analysis is included in appendix). Slightly improved burst strength and increased toughness of films is due to combined effect of reinforcement in the amorphous region and non-homogeneous distribution of high modulus clay platelets. Tear strength does not show any increase with clay loading.

It is well known that there exists strong hydrogen bond between nylon 6 chain and clay platelets due to polar nature of nylon 6 chains[214]. The strong interaction between the polymer matrix and clay platelets acts as crosslink points and reinforces the molecular network. At higher wt %, these physical crosslink's reinforce the molecular network and restricts the motion of molecules.

Schematic of load-hold-unloading curves of control nylon 6 films and films with different percentage of clay are shown in Figure 4.1.14 (a). The initial slope of unloading curve (dp/dh) which indicates the unloading stiffness together with contact area (A) increases with concentration of clay. Maximum depth of indentation decrease for the films with clay additives, which indicates the increase in the near surface hardness for nanocomposite films. Modulus was determined by the initial slope of the unloading curve. Overall load for nanocomposite film is higher than that of neat nylon 6 film as the addition of high modulus (≈400 Gpa) clay platelet increases the stiffness of material[201,35]. Schematic of near surface hardness and modulus profiles of nylon 6 blown films with different percentage of clay loading are shown in Figure 4.1.14 (b) and (c).

Figure 4.1.15 compares the modulus and hardness for different samples at different strain rates. Surface hardness and modulus slightly increase with increasing strain rate for control nylon6 and sample with 2 and 10 wt % clay additives which indicates increase in resistance of film surface to indentation.

The standard deviation and coefficient of variation C.V (tabulated in Table 4.1.5) of results are high for the sample with 10 wt % clay which is due to the change of morphology from dispersed, intercalated for 2 wt% to agglomerated clay with increased percentage of additives. In some samples even at 5% clay loading, C.V was higher indicating possible mixed morphology.

Modulus values obtained from tensile and nanoindentation analysis were fitted with the modulus values reported by Fornes et. al for nylon 6-MMT composites[129]. Schematic of the graph with modulus values is shown in Figure 4.1.16. Modulus values obtained from tensile and nanoindentation are almost close to each other. However, the modulus values do not fit with the theoretical modulus values predicted by any of the models. Reason for this might be due to the discrepancy between the theoretical and experimental modulus values discussed in literature section.

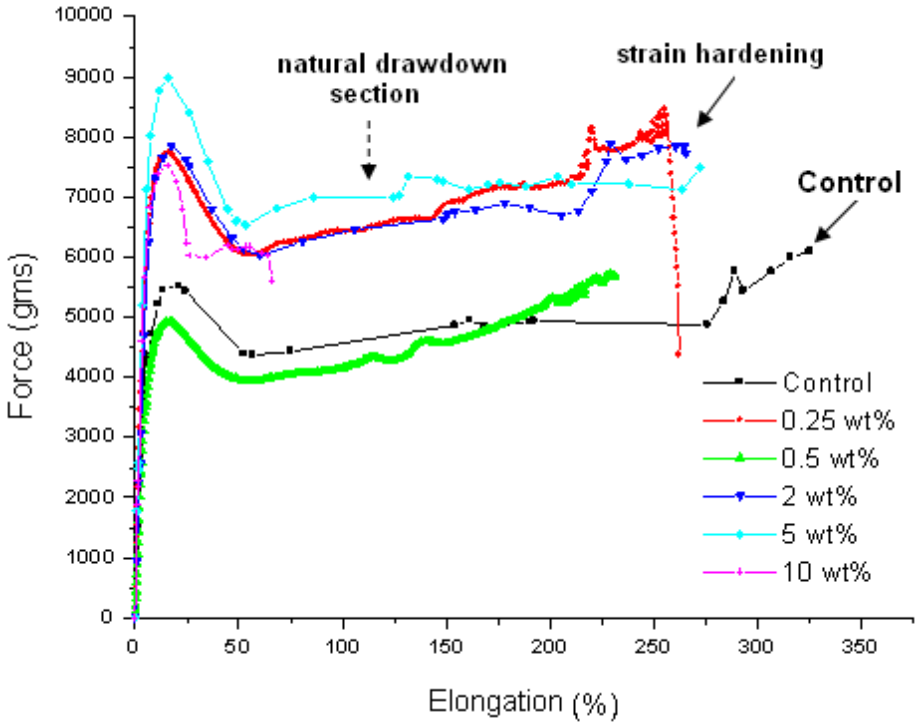

Figure 4.1. 12. Tensile strength results of nylon-6 nanocomposite films.

Table 4.1. 5. Tensile strength results of nylon-6 nanocomposite films.

Sample	Peak force (gms)	Peak elongation (%)	Modulus (GPa)
Control	6155	323	2.0
0.25 % clay	6668	255	2.8
0.5 % clay	6305	231	2.3
2 % clay	7879	230	2.4
5 % clay	8972	16	2.9
10 % clay	7539	14	2.8

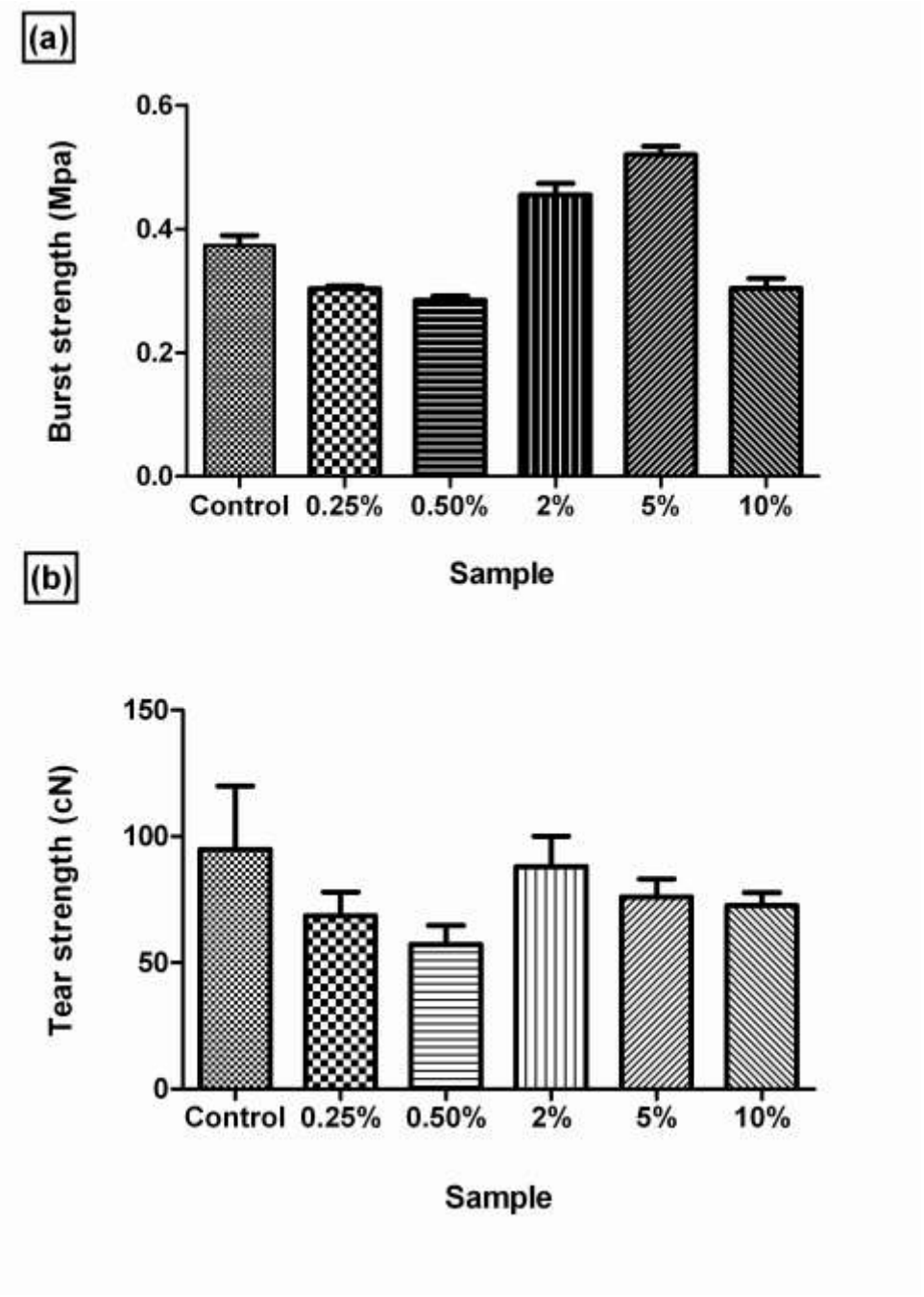

Figure 4.1. 13. Burst and CD tear strength results for nylon-6 nanocomposite films.

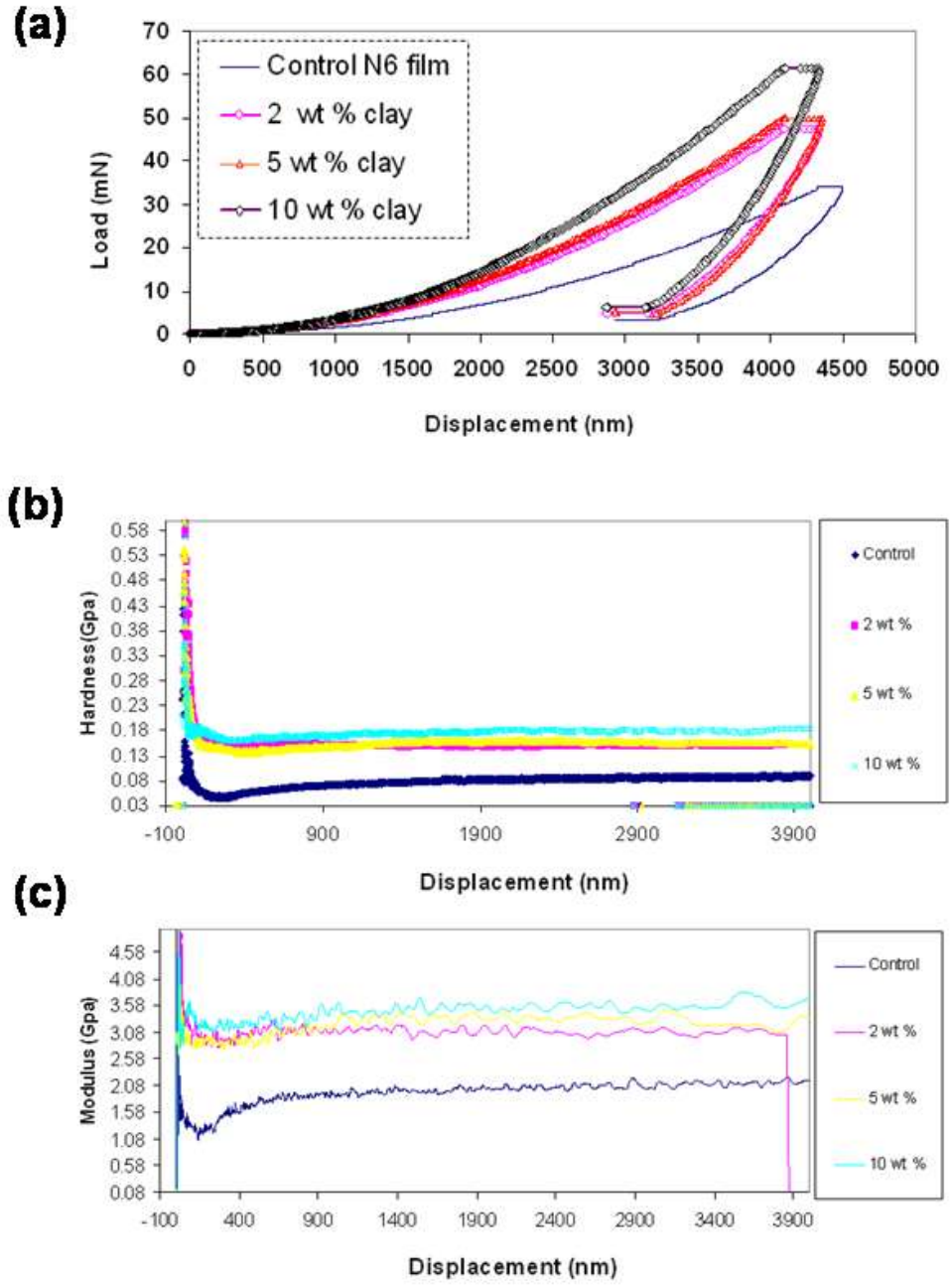

Figure 4.1. 14. (a) Load-hold-unloading curves of control nylon 6 films and films with different percentage of clay (b) Hardness and (c) modulus profiles of nylon 6 blown films with different percentage of clay loading..

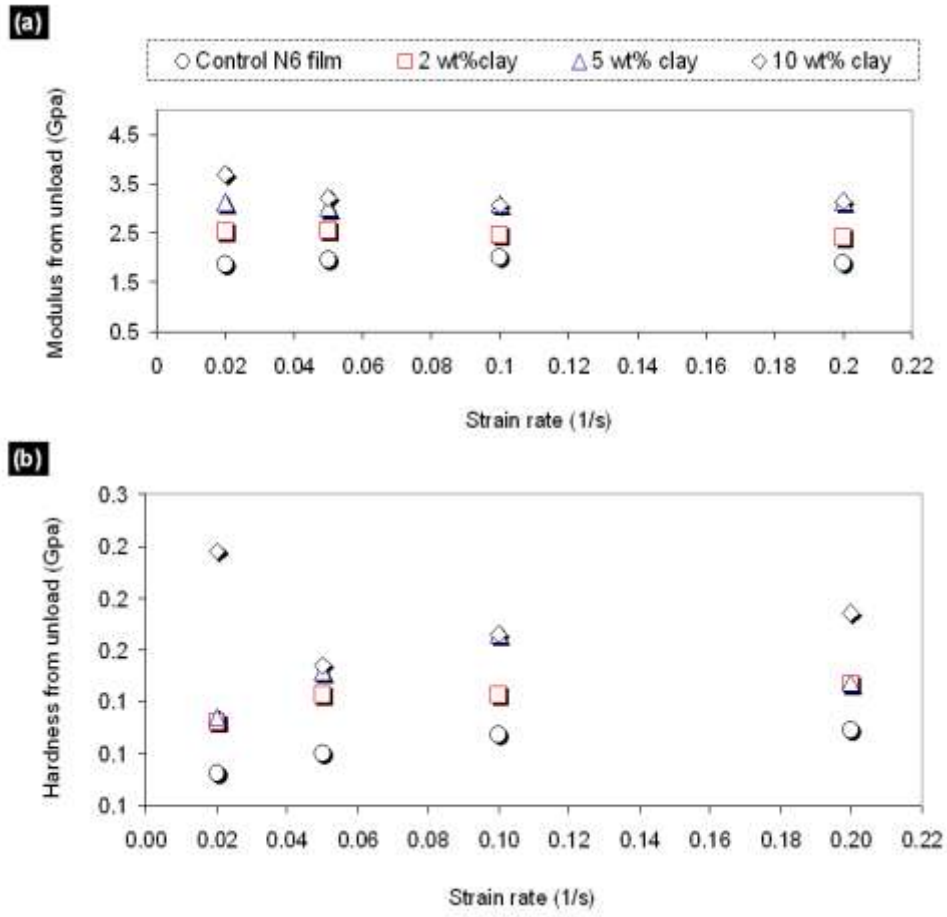

Figure 4.1. 15. Surface modulus and hardness for sample with 2, 5 and 10 wt % clay additives.

Table 4.1. 6. Nanoindentation results for Nylon 6 films.

Strain Rate (1/s)	0.02					
	Modulus From Unload			Hardness From Unload		
Sample Name	GPa	Std. Dev.	% COV	GPa	Std. Dev.	% COV
Control	1.86	0.05	2.59	0.09	0.00	3.22
2 %	2.55	0.05	2.09	0.12	0.00	3.12
5 %	3.11	0.36	45.79	0.12	0.02	14.61
10 %	3.23	0.07	91.32	0.128	0.005	4.06
Strain Rate (1/s)	0.05					
Control	1.95	0.04	2.25	0.10	0.00	3.78
2 %	2.57	0.00	0.16	0.13	0.00	1.51
5 %	3.01	0.43	43.15	0.15	0.04	24.36
10 %	3.23	1.77	91.32	0.15	0.01	3.86
Strain Rate (1/s)	0.1					
Control	2.02	0.04	1.77	0.11	0.01	4.45
2 %	2.45	0.05	2.12	0.13	0.01	3.59
5 %	3.09	0.34	42.01	0.17	0.03	17.99
10 %	3.06	0.66	54.18	0.17	0.06	36.24
Strain Rate (1/s)	0.2					
Control	1.89	0.07	3.60	0.11	0.01	5.09
2 %	2.41	0.01	0.24	0.14	0.00	0.04
5 %	2.89	0.20	6.91	0.14	0.02	11.82
10 %	3.13	0.37	11.71	0.18	0.03	14.45

Most of these model predictions are based on the two-component system and assume uniform dispersion of fillers along flow direction. However, the mixture of intercalated and agglomerated morphology was observed beyond 2 wt% additive. Also interface properties in the presence of dispersion agents are different from the two-phase system.

4.1.4 Surface morphology

SEM images of control nylon 6 film and films with 2, 5 and 10 wt % clay additives are shown in Figure 4.1.17. Control surface is relatively smoother compared to films with additives. Films with 2 and 10 wt % clay revealed increase in flaws and grooves on surface. SEM micrographs show micron size particle on surface ever for film with 2 wt% additive level, which indicates presence of agglomerates even at 2 wt% add on level. SEM micrographs of film show 20 to 104 μm size particles on the surface especially at higher clay loadings, due to non-uniform dispersion or agglomeration of clay platelets and protrusion from surface.

Spherulite micrographs obtained from polarized light optical microscope are shown in Figure 4.1.18. Maximum attainable diameter of spherulite in case of control nylon 6 was found to be 55μm (average of n=15 spherulites). The spherulite domain dimensions for samples with additives are considerably smaller. Average maximum attainable diameter of spherulite in case of sample with nanoclay additives could not be calculated because of very high nucleation density and decrease in spherulite size.

This decrease in spherulite size is due to the combination of increased nucleation and, hindrance to polymer chain diffusion on to growing crystallite. Since $\Delta\phi$ clay > $\Delta\phi$ nylon 6, AFM phase image can be used to map stiffness difference on the surface. The phase contrast images for control and nanocomposite films for scan size of 1μm are shown in Figure 4.1.19. Figure 4.1.19-(a) shows only small differences in phase difference. Bright region for nanoclay incorporated films is due to the high surface energy of additive than matrix. Surface energy of neat clay is extremely high (257 mJ/m^2) compared to nylon 6 (46.5 mJ/m^2)[178].

Bright hills in the height image (Figure 4.1.20) correspond to high modulus nanoclay (E≈400 Gpa) and the darker valley region is from nylon 6 matrix. The repulsive force between the tip and the brighter clay platelets and the attractive force between the tip and darker nylon matrix give the extent of difference in phase image[175]. Phase contrast image of sample with 10 wt % clay is significantly different from the rest, which is due to the increase in surface stiffness due to presence of higher wt % of additives.

Schematic of section analysis for control and nanocomposite films is shown in Figure 4.1.21. Sectional analysis of for film samples was carried out using cross-sectional lines across the phase image. Lines were drawn in all directions for each sample and average of n=15 readings were taken to determine the topology of each film sample. Large numbers of sharp valleys with width of about 19 nm were observed on control surface. Compared to control, the width of hills and valleys increased for the nanocomposite films. The average widths of hilly clay phase observed were 46, 50 and 74 nm respectively for 2wt %, 5 wt % and 10wt % films. These increases in width of clay phase are due to agglomeration as revealed by SEM micrograph of film surface. Distance between clay phases decreased in the case of nanocomposite films with higher wt% of clay additives.

Results of section and roughness analysis are shown in Table 4.1.7. Compared to neat nylon 6 film, slightly higher Z-range, RMS and roughness values were observed for the nanoclay incorporated films. It is worthy of mention that Ganguly et. al. studied the morphological mapping of Poly[styrene-b-(ethylene-co-butylene)-b-styrene] and its clay nanocomposites using AFM. They observed drastic increase in Z-range and RMS values for SEBS1 nanocomposites[175].

So non-uniform dispersion of nanoclay additive has significant influence on the nanoscale surface topology. Increase in the area of high surface energy clay platelets on the film surface also influences the wetting behavior of films. Increased wettability or decrease in contact angle is observed for samples with clay additives. Schematic of sessile drop technique, and decrease in contact angle for nanoclay-incorporated films is shown in Figure 4.1.22-(a). Results of contact angle measurements are shown in Figure 4.22-(b). At higher wt % clay loading, it's difficult to disperse the additive through sample and additive forms larger size tactoids. TEM image in Figure 4.1.8 revealed increased agglomerate formation for sample with 10 weight % clay.

Interaction between the clay platelets is weak compared to interaction between clay and nylon-6 chains. So, during tensile and tear testing, these tactoids with voids act as weak spots and initiate craze causing overall decrease in elongation to break.

At higher weight percentage, high modulus clay agglomerates act as stress concentrates due to difference in their elastic properties compared to matrix. The differences in particle size distribution in matrix lead to stress concentration. The stress concentration leads to tri-axial stress concentration around the agglomerate leading to debonding at particle-polymer interface. Voids resulting within the agglomerate and de-bonding due to stress concentration lead to shear yielding. For efficient toughening, the filler has to be uniformly dispersed and particle dimension should be less than 5 μm otherwise voids created would act as crack initiation sites[215].

Adverse effect of clay agglomerate is more prominent in tear strength results. Tear strength test is carried out on the sample, which has the slit to start with. In earlier studies, decrease in fracture resistance has been reported. High nucleation density and small spherulite size and exclusion of additives from spherulite induce lots of week spots in films. So the tear strength did not improve for the films with additives.

TEM image (Figure 4.1.8) reconfirms the presence of these voids between platelets. Crystallization kinetics studies showed significant enhancement in kinetics due to presence of even at 0.25 wt% additives. Thermo mechanical behaviors of nanoclay incorporated nylon 6 fibers were different than that of control nylon 6 fibers at 100°C. Kojima et. al reported, increase in γ-crystalline forms for nylon-6 clay hybrids[212]. The γ-crystalline forms acquire higher draw capability for nylon 6 in the temperature range of 110 to 180°C [213]. The extensional behavior is due to the change in morphology of the fibers and slight increase in the γ-crystalline forms, which is evident from WAXD, scans.

Initial uncertainty in hardness and modulus profiles is due to the indentation size effect[216,217,] or uncertainties in surface topology of films which is also evident in SEM micrographs. Nanoindentation results showed increase in near surface hardness at nanolevel.

Thus, beyond 5 wt %, clay loading, nanocomposite morphology can be compared to conventional composite morphology due to agglomeration of platelets and insufficient interfacial adhesion between platelets and matrix[17, 218].

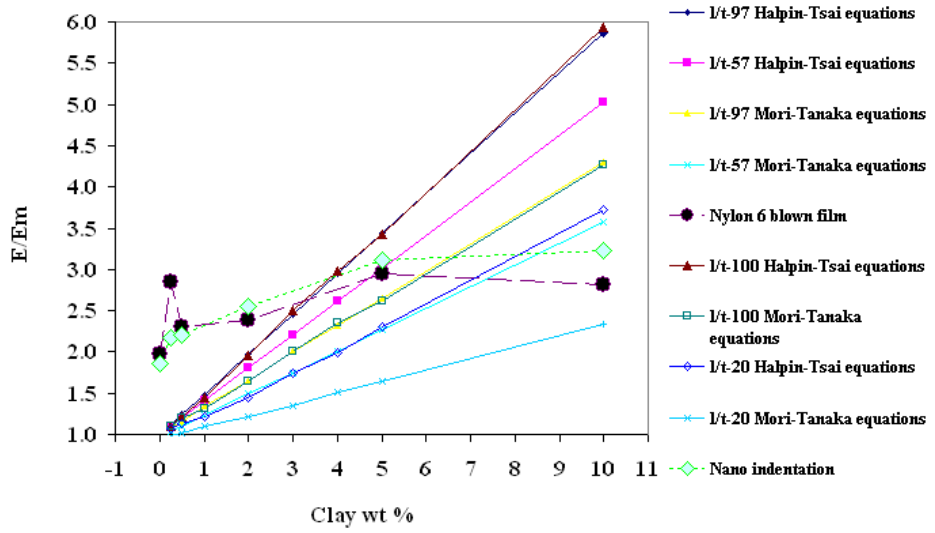

Figure 4.1. 16. Modulus values obtained from tensile and nano indentation[129].

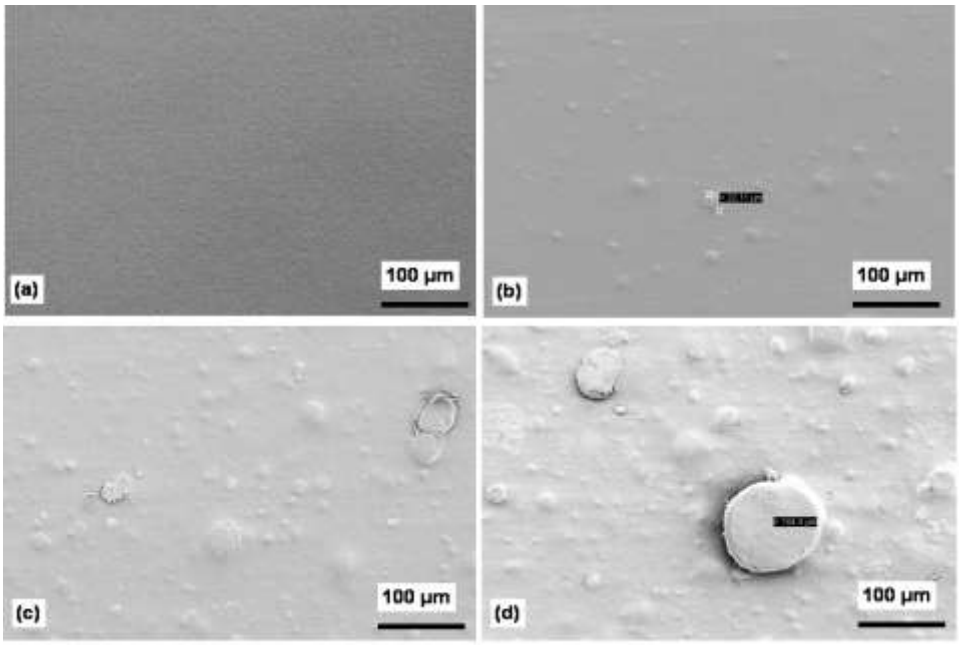

Figure 4.1. 17. SEM micrograph of (a) Control nylon 6 film (b) Nylon 6 film with 2 % clay (c) Nylon 6 film surface with 5% clay (d) Nylon 6 film surface with 5% clay.

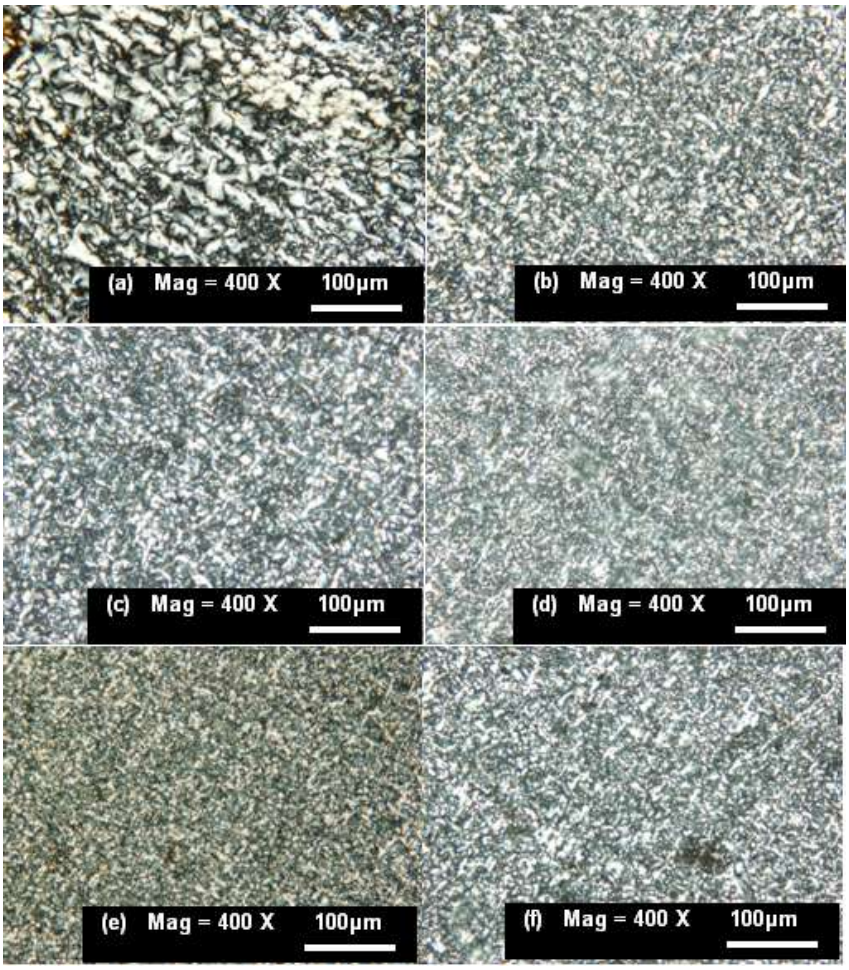

Figure 4.1. 18. Polarized light micrographs of (a) Control nylon 6 film (b) 0.25 % nanoclay (c) 0.5 % nanoclay, (d) 2 % nanoclay, (e) 5 % nanoclay, (f) 10 % nanoclay.

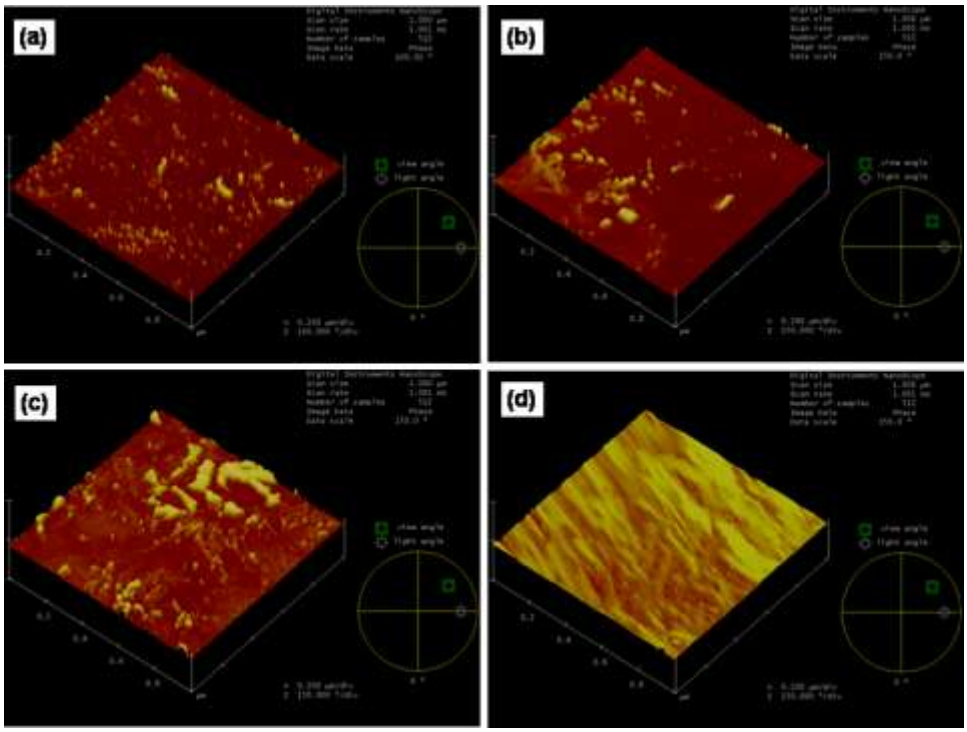

Figure 4.1. 19. AFM image of (a) control nylon 6 film, (b) film with 2 wt % clay, (c) film with 5 wt% clay and (d) film with 10 wt % clay.

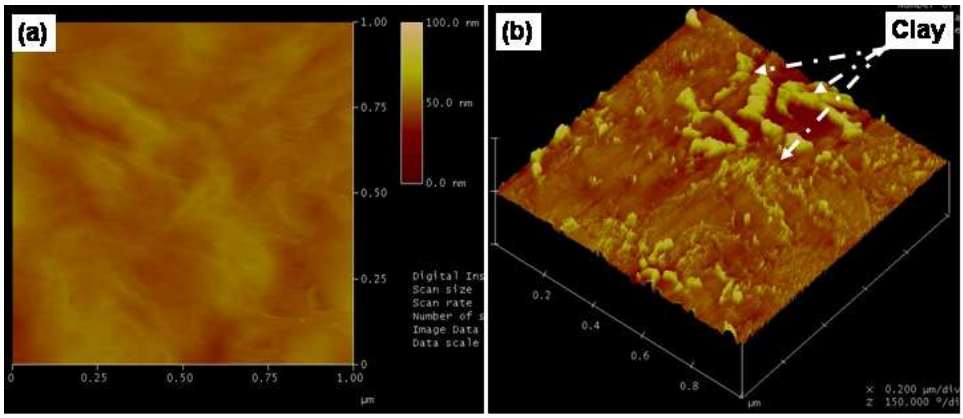

Figure 4.1. 20. Tapping mode height image and phase morphology of the nylon 6 film with 5 wt% nanoclay.

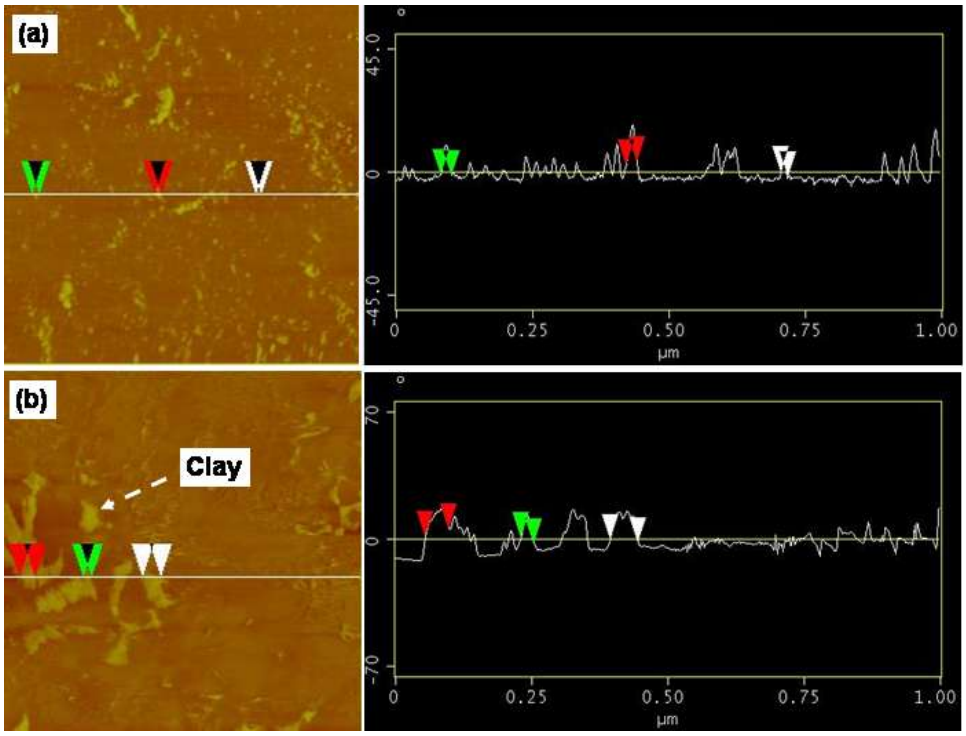

Figure 4.1. 21. Sectional analysis and width determination of (a) control film, (b) nylon 6 film with 2 wt% clay.

Table 4.1. 7. Roughness and section analysis for control and nanoclay incorporated films.

Sample	RMS (nm)	Z range- (nm)	Roughness (nm)
Control	1.4	16.4	1.2
2 % clay	2.5	20.9	2.5
5 % clay	3.1	22.9	2.6
10 % clay	3.5	21.0	3.2

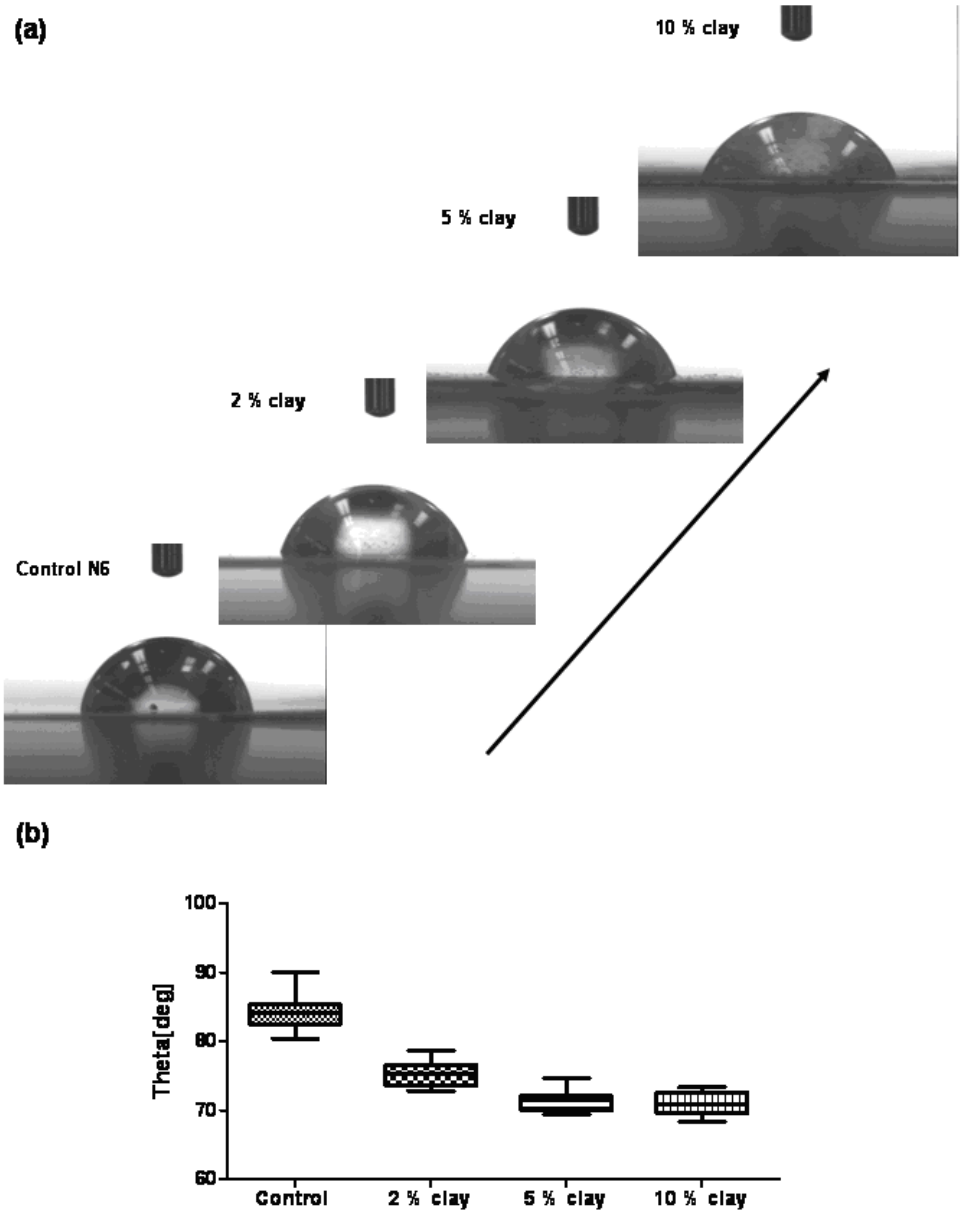

Figure 4.1. 22. (a) Schematic of water drop shape on film surface observed from sessile drop technique (b) results of contact angle measurements for nylon 6 film samples.

4.1.5 Nylon 6 melt spun fibers with nanoclay

WAXD scan of fiber samples are shown in Figure 4.1.23. Sharpness and intensity of peak corresponding to γ-crystalline form increased with nanoclay additives. Peaks at 2θ of 13.5°, 14° and 16.7° for fiber with nanoclay are due to the presence of maleated wax. There is no sharp significant peak at 2θ of 6.07° corresponding to (001) plane of clay which indicates the delaminated structure[191]. WAXS diffraction patterns and equatorial intensity profiles for melt spun fibers is shown in Figure 4.1.24. These patterns do not show any significant orientation change among these fibers.

Small angle x-ray scattering (SAXS) patterns obtained with x-ray beam perpendicular to fiber direction are shown in Figure 4.1.25. Patterns do not exhibit discrete scattering maxima corresponding to long spacing. Patterns show a clear uniform scattering from crystal lamellae along meridian. Sample N6C2 and N6C5 (shown in Figure 4.1.25 (c) and (f)) show much stronger scattering along meridian attributed to presence of clay tactoids.

Fiber diameter and birefringence results for spun fibers are included in Table 4.1.8. Slightly higher orientation was observed for control nylon 6 fiber-compared to rest of the fibers with nanoclay. Hermans-Stein orientation function and the amorphous orientation factor $f_{amorphous}$ were measured from the birefringence, crystalline orientation of monoclinic γ form as discussed detail in experimental section. The results for the Hermans-Stein orientation function and amorphous orientation (shown in Table 4.1.8) do not show any significant difference.

The TEM micrographs of fiber N6C5 is shown in Figure 4.1.26. The section shows presence of tactoids within the fiber cross-section. So the absence of peak corresponding to (001) plane in WAXD scans might be due to combination of lower quantity of clay platelets in scanned area and also loss of ordered structure during melt processing.

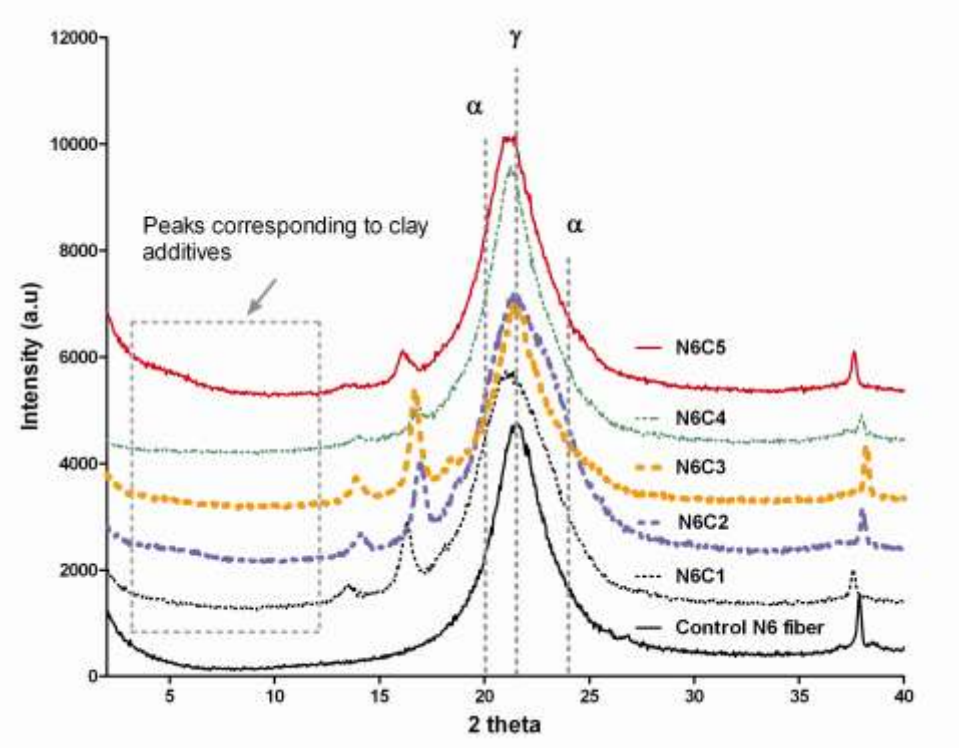

Figure 4.1. 23. WAXD scan of different nylon 6 nanocomposite fibers.

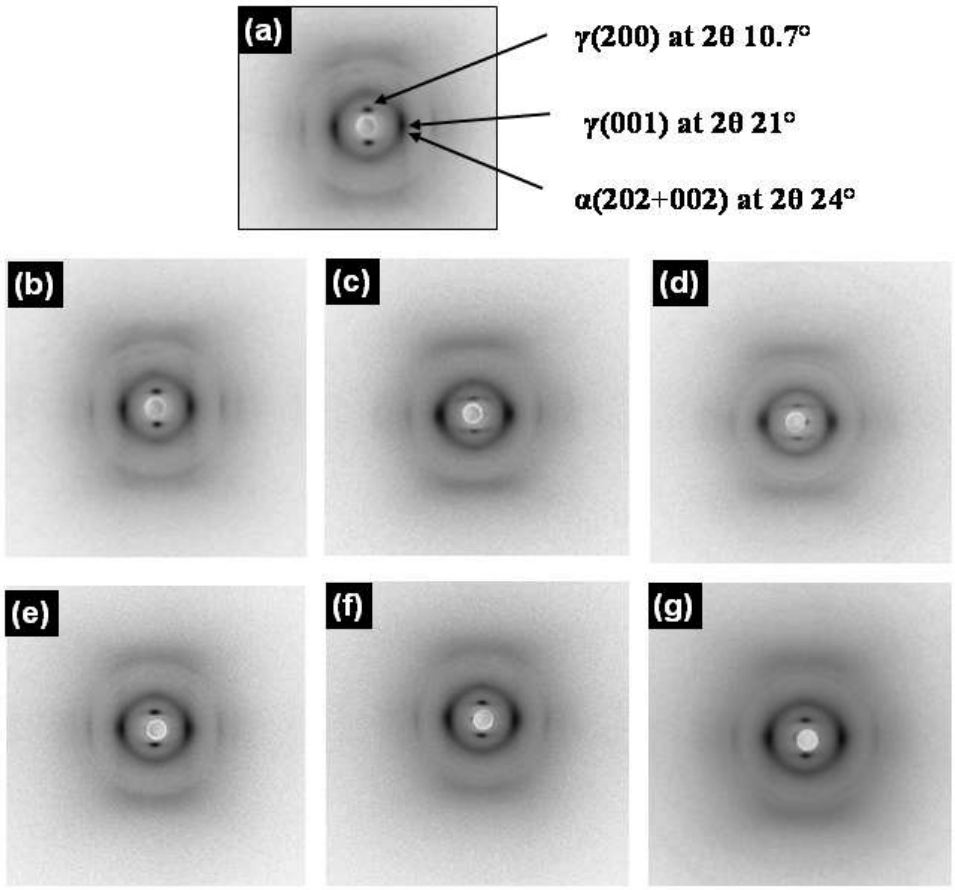

Figure 4.1. 24. WAXS diffraction patterns of α and γ forms of nylon 6 (b) Control nylon 6 fiber (c) N6C1 (d) N6C2 (e) N6C3 (f) N6C4 (g) N6C5.

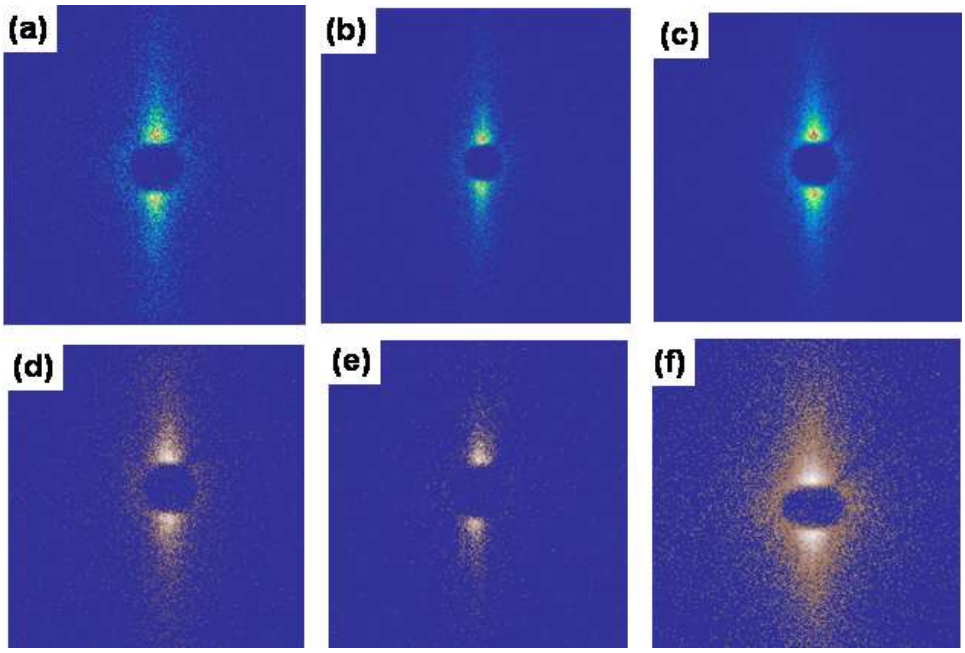

Figure 4.1. 25. SAXS pattern's of (a)Control nylon 6 fiber (b)N6C1 (c)N6C2 (d)N6C3 (e)N6C4 (f)N6C5.

Table 4.1. 8. Properties of control and nanocomposite nylon 6 fibers.

Sample	Fiber diameter (microns)	Birefringence	f_b	$f_{amorphous}$
Control Nylon 6	26	0.08	0.91	0.41
N6C1	15	0.07	0.85	0.32
N6C2	14	0.06	0.96	0.34
N6C3	22	0.04	0.88	0.38
N6C4	15	0.06	0.91	0.38
N6C5	18	0.05	0.95	0.35

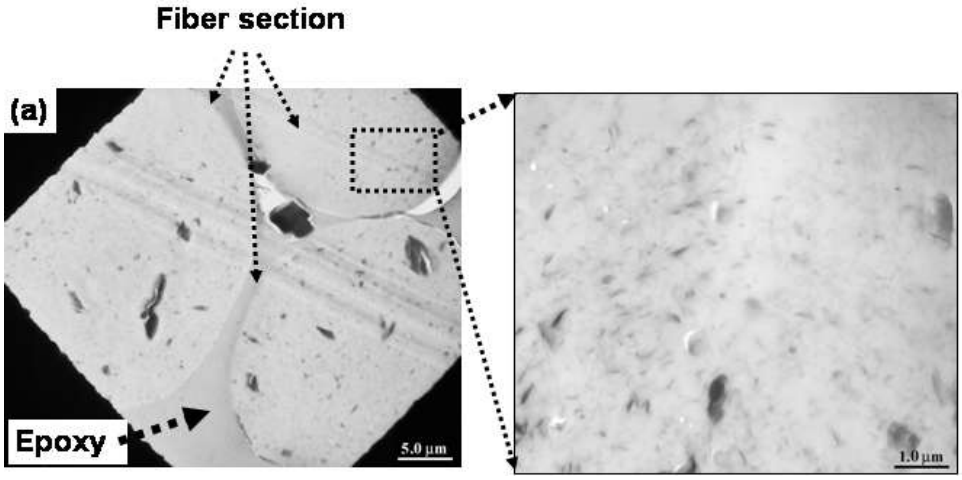

Figure 4.1. 26. TEM micrograph of film with N6C5 (5 wt % clay) fiber embedded in epoxy.

Thermal analysis results obtained from DSC cooling segments are included in Table 4.1.9. All the films with nano additives show higher onset of crystallization temperatures than that of control indicating nucleating effect of additives. However this increase shows a tendency of going up till 2% clay and then the level of increase drops off with further increase in clay wt%.

From the DSC scan results (Figure 4.1.27) it is evident that, the onset of melting peak is shifted to higher temperatures. Also the melting endotherm is sharp compared to control nylon 6, which indicates perfection of crystals. The endothermic and exothermic transition of nanocomposites is significantly different compared to control nylon 6. Samples NC1, NC4 and NC5 show melting and subsequent re-crystallization at higher temperatures. This double melting endotherm is due to α and γ-phases of nylon 6, with lower temperature peak corresponding to melting of γ phase[116], polymer crystal perfection and melting at higher temperature[219]. Presence of endotherm at temperature higher than melting point 240°C is due to melting of stable γ-phase trapped between the silicate aggregates at very high temperature as shown in Figure 4.1.28[116].

Table 4.1. 9. Results of DSC thermal analysis in cooling cycle.

Sample	Control	NC1	NC2	NC3	NC4	NC5
Clay (wt %)	0	1	5	1	2	5
Onset (°C)	183	181	184	216	183	183
Peak (°C)	174	175	178	223	176	175
Endpoint (°C)	158	158	165	228	161	161
ΔHC (J/g)	65	56	53	62	61	55
Cooling rate (°C)	-60	-60	-60	-60	-60	-60
Crystallinity wt %	34	29	28	33	32	29

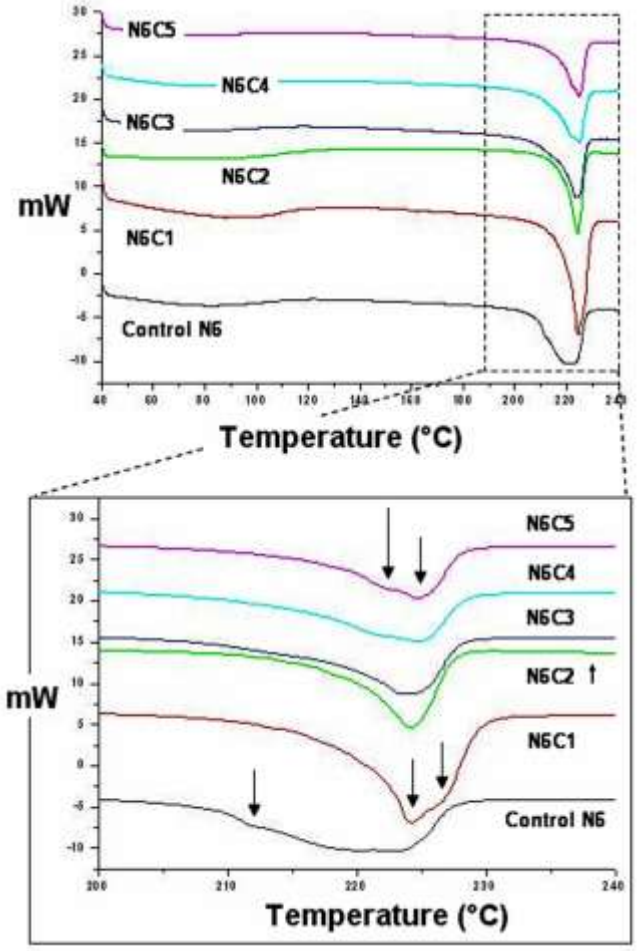

Figure 4.1. 27. DSC scans of nylon 6 fiber composites.

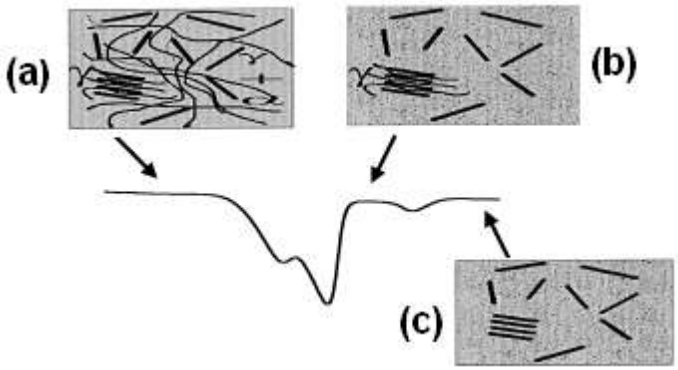

Figure 4.1. 28.Thermal behavior of nylon 6 fiber nanocomposite (a) below main melting point, small portion of γ -phase is trapped between the silicate aggregates (b) small portion of stable γ phase stable between the platelets and (c) completely molten system[116].

Results of thermo mechanical analysis (TMA) scan of samples are shown in Figure 4.1.29. The scans show significant difference in dimensional change for nanocomposite fibers with increment in temperature. For control fiber, thermal shrinkage initiates at 120°C, whereas fiber with clay showed slower rate of shrinkage and sample N6C3 showed expansion.

Results of single fiber tensile tests are shown in Figures 4.1.30, 4.1.31 and Table 4.1.10. Tensile properties on nanoclay-incorporated fibers did not show any improvement compared to control nylon 6 fibers. Among different nanocomposite fibers, sample N6C2 with 5 % clay in 5% maleated wax gave better strength, compared to control nylon 6 fibers.

Mechanical property benefits were not observed from nanoclay additives in as spun nylon 6 fibers. The structure and morphology of semi crystalline fiber is developed due to the stress-induced crystallization in semi molten state immediately after extrusion of melt from orifice just before complete solidification. Semi crystalline polymer fibers or products in molecular level consist of highly ordered crystalline segment, relatively unstable incomplete crystalline regions, transition segments between relatively unstable crystalline and the amorphous regions, and unstable oriented amorphous fractions[220].

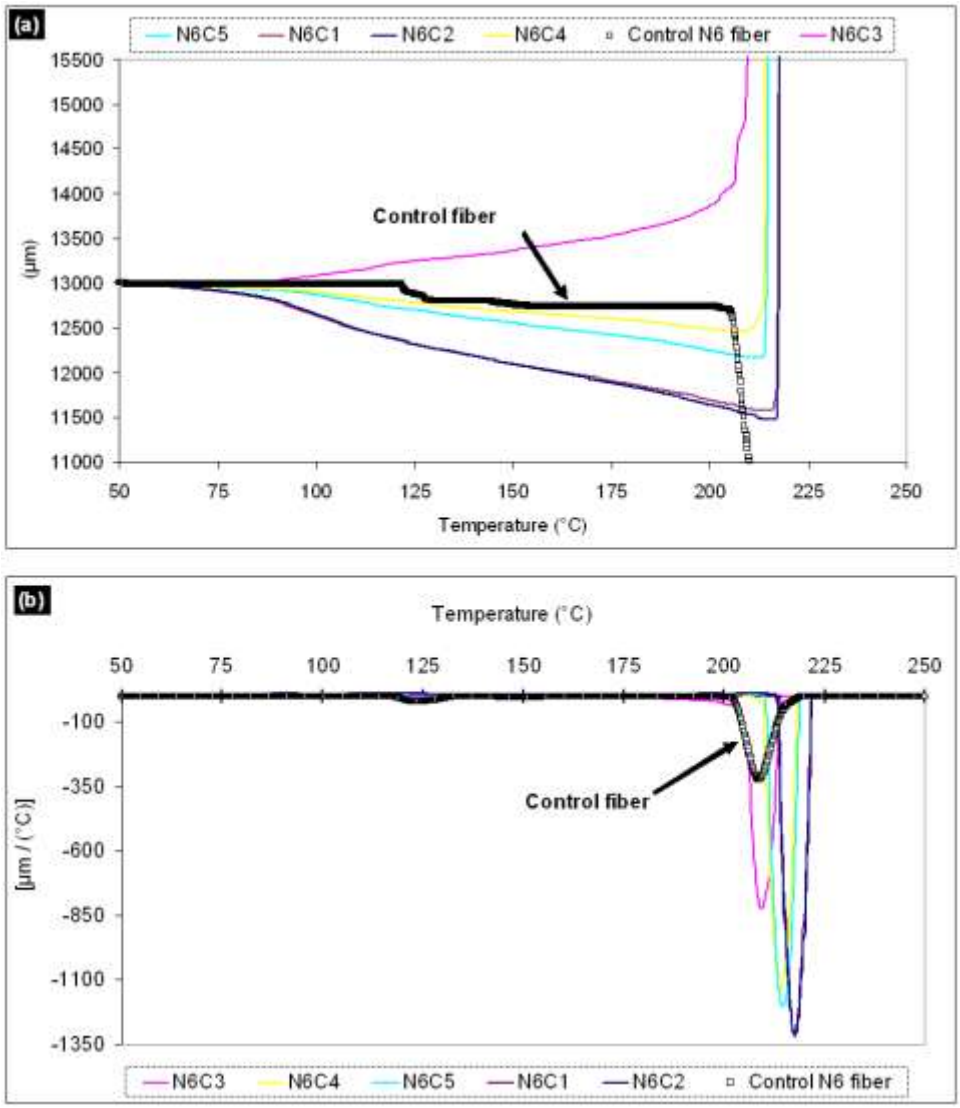

Figure 4.1. 29. TMA (copper clamp) analysis of nylon 6 fibers, (a) dimension change with increase in temperature, (b) first derivative dimension change with temperature.

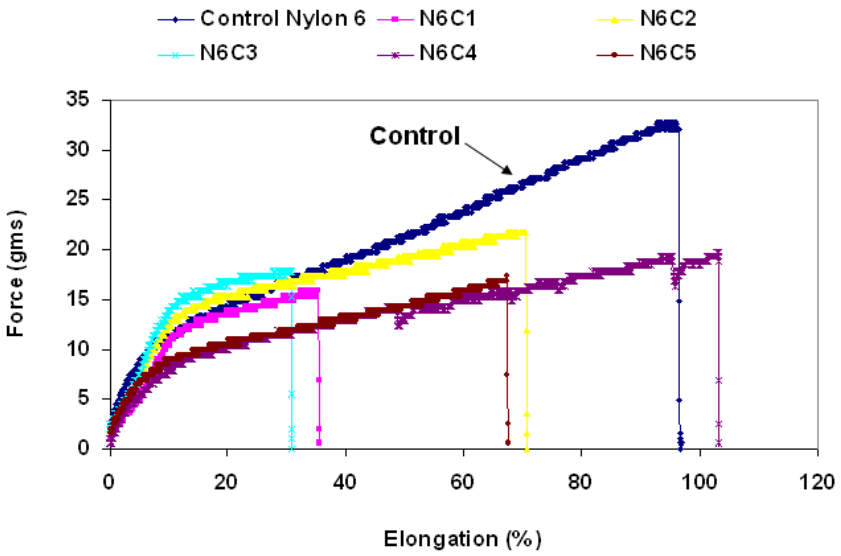

Figure 4.1. 30. Single fiber tensile strength results.

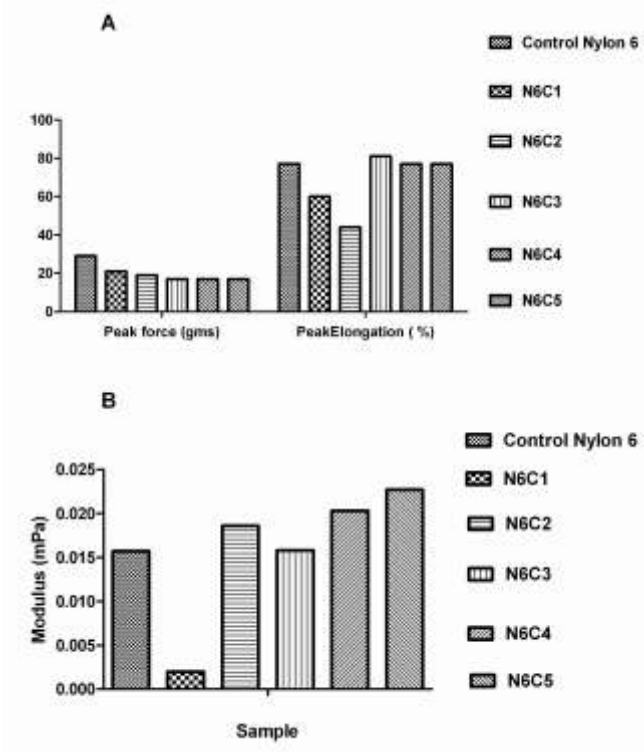

Figure 4.1. 31. Mechanical properties of Nylon 6 fibers: A-peak force and elongation, B-fiber modulus.

Table 4.1. 10. Mechanical properties of Nylon 6 fibers.

Sample	Peak load (gms)	Peak elongation (%)	Tenacity (gms/den)
Control	29	77	3
N6C1	21	60	2
N6C2	19	44	2
N6C3	17	81	2
N6C4	17	77	2
N6C5	17	77	2

Mechanical properties like stiffness, strength and elongation exhibited by the fiber relies on the completeness and continuity between these four molecular network segments[221]. Transition in different molecular segments in a melt spun fiber during tensile test is illustrated in Figure 4.1.32 (a) to (d) [220].

In the melt spun fibers, additive agglomerate in fiber easily reaches order of fiber magnitude[116]. Uniform dispersion of platelets is the key to achieve tensile property improvement. At lower weight percentage add on levels, as shown in Figure 4.1.32 (e), clay platelets are well dispersed in matrix, and there will be good load transfer between the filler and matrix, which leads to increase in tensile strength. Also stiffness of fiber increases due to reinforcement in molecular network by high modulus of nanoclay additives[21].

At higher weight percentage (Figure 4.1.33-f), continuity in molecular network is lost because of generation of voids and/or agglomerates, which act as stress concentrates and lead to brittle failure[222].

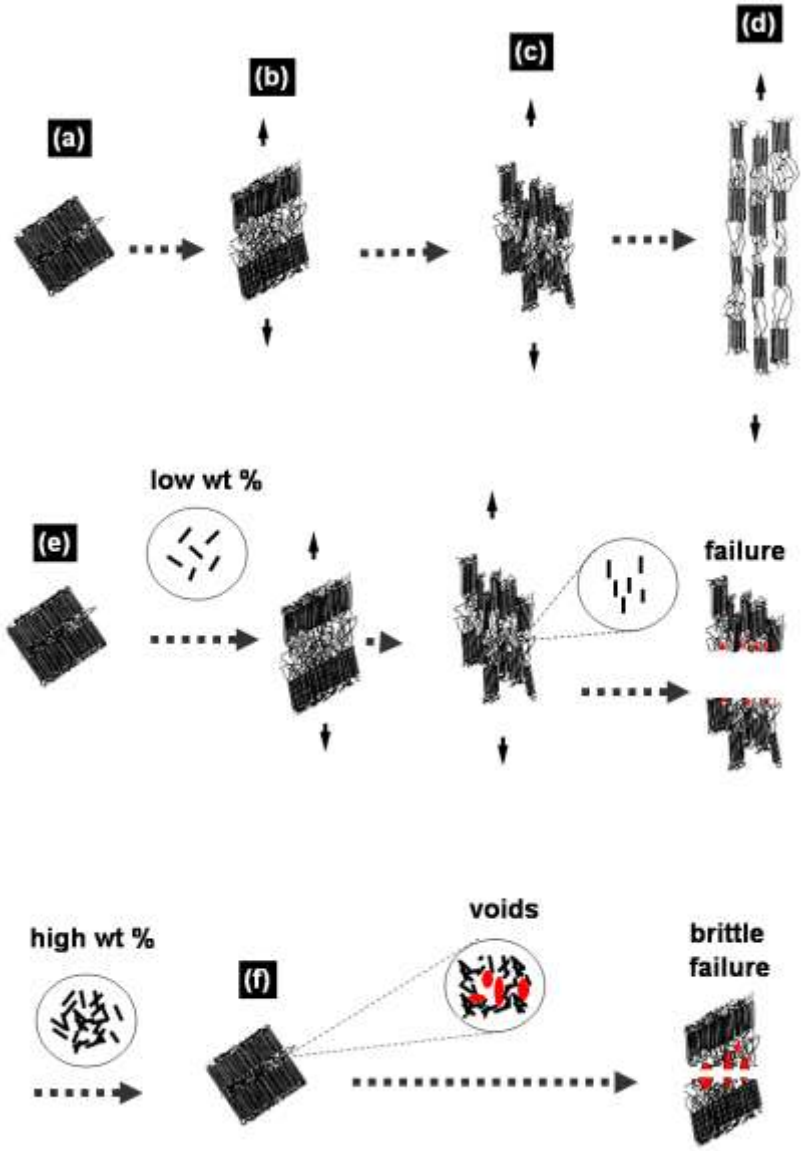

Figure 4.1. 32. Schematic of morphology and transition in different molecular segments in a melt spun fiber during tensile test, (a) stretching of amorphous segment, (b) shear yielding in crystalline, (c) void formation (d) re-crystallization with orientation (e) at lower weight percentage loading, there is reorientation of platelets in matrix (f) at higher weight percentage reinforcement, agglomerates lead to amplification of voids and brittle failure.

4.2 Polypropylene spunbond web with nanoclay

Variation in shear viscosity at different shear rates for resins with different percentage of clay is shown in Figure 4.2.1. Overall shear viscosity for resin with clay in low shear range of 100 sec^{-1} is higher than that of control. At higher shear rate of beyond 100 sec^{-1} samples with clay additive show shear thinning behavior. Difference in shear viscosity is due to difference in dispersion of nanoclay additives in each of these concentrates.

Shear viscosity decreases and levels off at extremely high shear rates of the order of 10000 sec^{-1}. Results of melt flow rate (MFR) summarized in Table 4.2.1 are in accord with the shear viscosity results. Concentrates with clay additive had slightly higher MFR, which is beneficial from processing point of view. Higher shear viscosity for resin with clay in low shear range of 100 sec^{-1} is due to the hindrance caused by the nano additive particles. Sample with 5 % clay shows thixotropic behavior of increasing shear viscosity at lower shear rates. However, resin with 5 % clay in maleated polypropylene (m-PP) had opposite effect at low initial shear rates and slight increase in shear viscosity at shear rate of 100 sec^{-1} and final reduction. The sample could not be processed due to high viscosity, pressure rise and filter clogging.

The increase in shear viscosity is due to formation of loop like conformations between polypropylene chains, maleated polypropylene and clay platelets. At higher shear rates (of order 10000 sec^{-1}), shear viscosity decreases and levels off due to the disentanglement of nanoclay platelets and the polymer chain[218, 223, 224]. Critical shear rate is lower for PP with nanoclay additives. The shear thinning behavior at higher shear rates is due to alignment of clay platelets parallel to the applied load as illustrated in Figure 2.8[225,226].

WAXD scans of different SB fabric samples and natural nanoclay are included in Figure 4.2.2. WAXD scans do not show any peaks corresponding to natural nanoclay (around 2θ of 6.07°) which is due to very high levels of extrusion involved during spunbond process and delamination of the clay platelets beyond 100 A° [103]. In this case, TEM is the best technique which reveals information about presence and extent dispersion of clay within the polymer sample[218].

The peak positions and respective reflection indices are labeled as shown in Figure 4.2.2. Reflection indices are similar for all the samples except for 5 wt % clay in maleated

polypropylene. The decrease in (040) peak for sample with clay is due to slightly larger size clay tactoids which hinder the growth in (040) direction[102].

Results of fiber crystallinity (%) and crystal size (A°) are shown in Table 4.2.1 Crystallinity and crystal size are higher for the samples with nano-additive and increase with increase in percentage of clay additive. This increase in crystal size might be due to segregation of clay platelets at the spherulite boundary as reported by Maiti et. al. in case of their studies on polypropylene/clay hybrids[9]. Crystallinity wt (%) was lower for fibers with additives. This lower crystallinity (%) might be due to hindrance to crystallization by well dispersed clay tactoids.

TEM micrograph of neat nanoclay is shown in Figure 4.2.3 (a). Dark shady lines (50 nm) in the image represent the multiple layers of clay platelets, each of thickness less than 10A°. TEM micrographs of concentrates used to produce the SB samples are included in Figures 4.2.3 (b), (c) and (d). Micrographs revealed intercalated and flocculated morphology for all the concentrates.

Table 4.2. 1. Properties of the polypropylene concentrate.

Sample ID	Flow rate gms/10 min	Crystal size (A°)	Crystallinity wt%	
			WAXD	DSC
Control	32	91	57	53
1 % clay	55	104	52	49
2 % clay	44	159	59	50
5 % clay	55	127	57	49

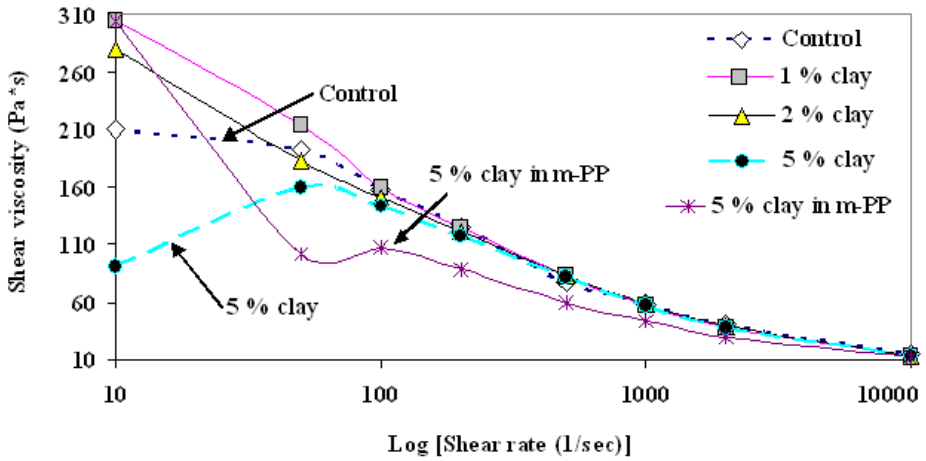

Figure 4.2. 1. The capillary rheometry results.

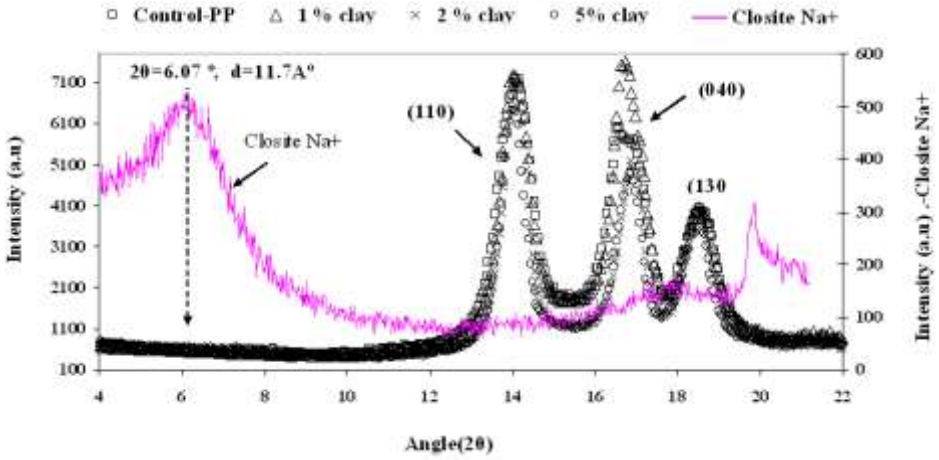

Figure 4.2. 2. WAXD scans of spun fiber samples.

TEM micrographs of SB web samples are shown in Figure 4.2.4, 4.2.5 and 4.2.6. Micrographs contain sections of fiber within epoxy matrix. Dark shady lines within the fiber represent nanoclay stacks. Good dispersion was observed for concentrates with 1 and 2 wt % clay in the polypropylene matrix (Figures 4.2.4 and 4.2.5). Mixtures of intercalated and exfoliated morphology were observed in the case of sample with 5 wt % clay (shown in Figure 4.2.6). Stacks have significant chain intercalation. Similar dispersion and morphology has been reported for PP/clay nanocomposites in earlier literatures[27, 227].

Presence of clay stacks near the fiber surface and protrusion of clay stacks from the fiber surface lead to significant difference in fiber surface topology as indicated in Figure 4.2.6 (a). Micrographs also reveal difference in the additive distribution along the fiber cross-section. Additive particles near the fiber diameter are smaller fragments and oriented along the spinning direction, but the additives at center portion of fiber are larger and randomly oriented. Also, the particles near fiber diameter have higher polymer chain intercalation compared to ones at the center. This difference in the additive distribution is due to the "wall effect" a phenomena, which leads to reduction in concentration of suspension adjacent to the solid wall of the flow channel. Higher shear rate is created near the fiber diameter and the additive particles migrate to the center[228]. Effect is more prominent in case of sample with 5 wt % additives as shown in Figure 4.2.6.

The nature of dispersion and clay stack morphology observed in concentrates was also present in fiber webs. This demonstrates immiscibility of PP matrix and need for better dispersion in master batch to get higher dispersion in the end product.

Properties of SB webs with nanoclay additives are shown in Table 4.2.2. Most of the SB web sample basis weight was 30 grams/square meter; fiber diameter was 15 μ and the web thickness was in the range of 300 microns. Sample with 5 wt% clay had high b value (yellowness), which is due to maleated wax and higher light scattering by clay platelets.

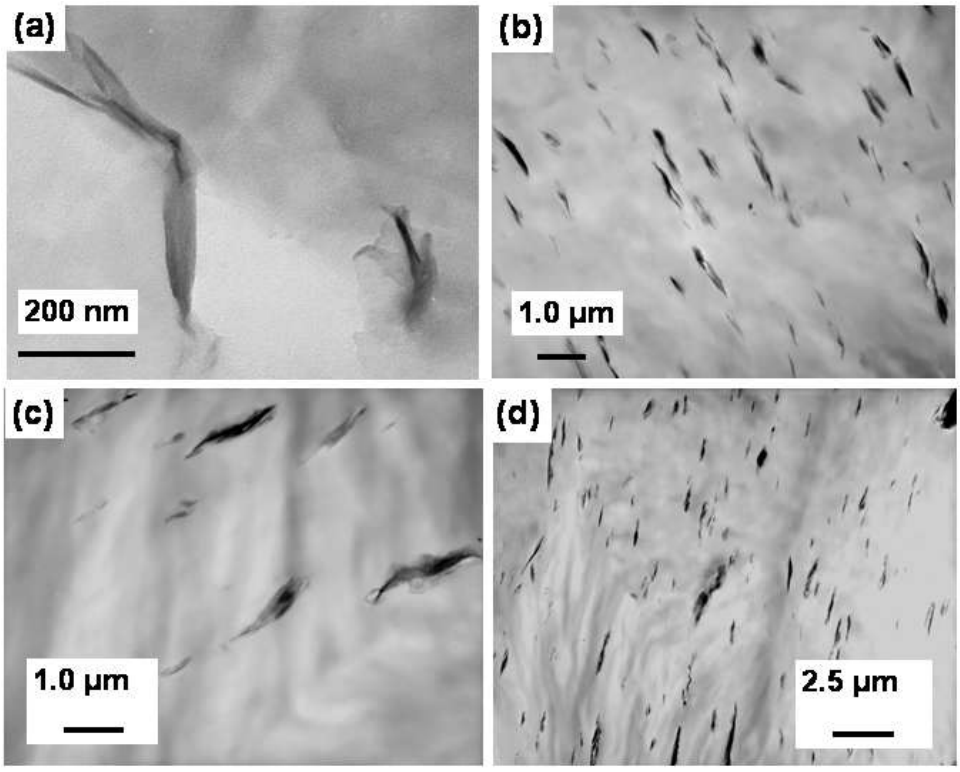

Figure 4.2. 3. TEM micrographs of concentrates (a) neat clay Closite Na^+ (b) with 1 wt % clay, (c) with 2 wt % clay, (d) with 5 wt % clay.

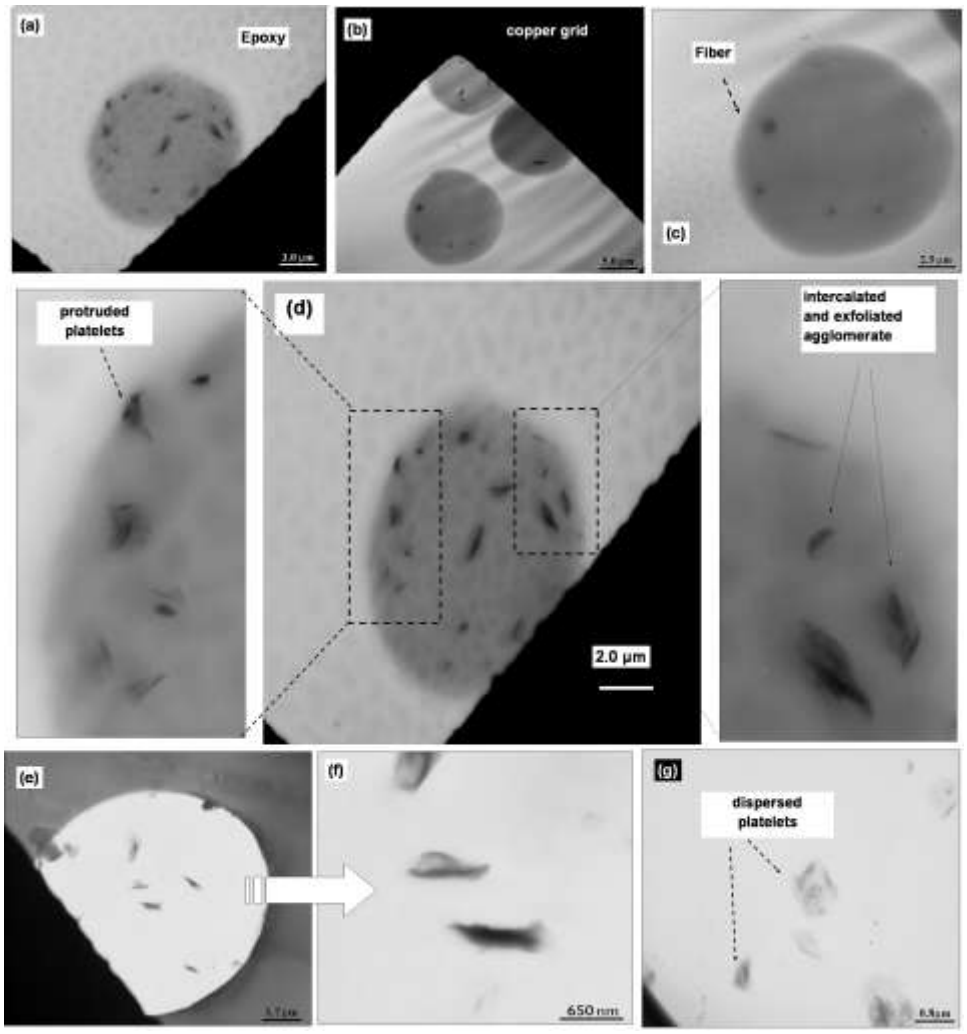

Figure 4.2. 4. (a), (b), (c) TEM micrographs of concentrate with 1 wt % clay (d) magnified micrograph showing particles at high magnification, (e) micrograph of fiber embedded in epoxy, (f) magnified micrograph at center of fiber with intercalated tactoids (g) dispersed platelets.

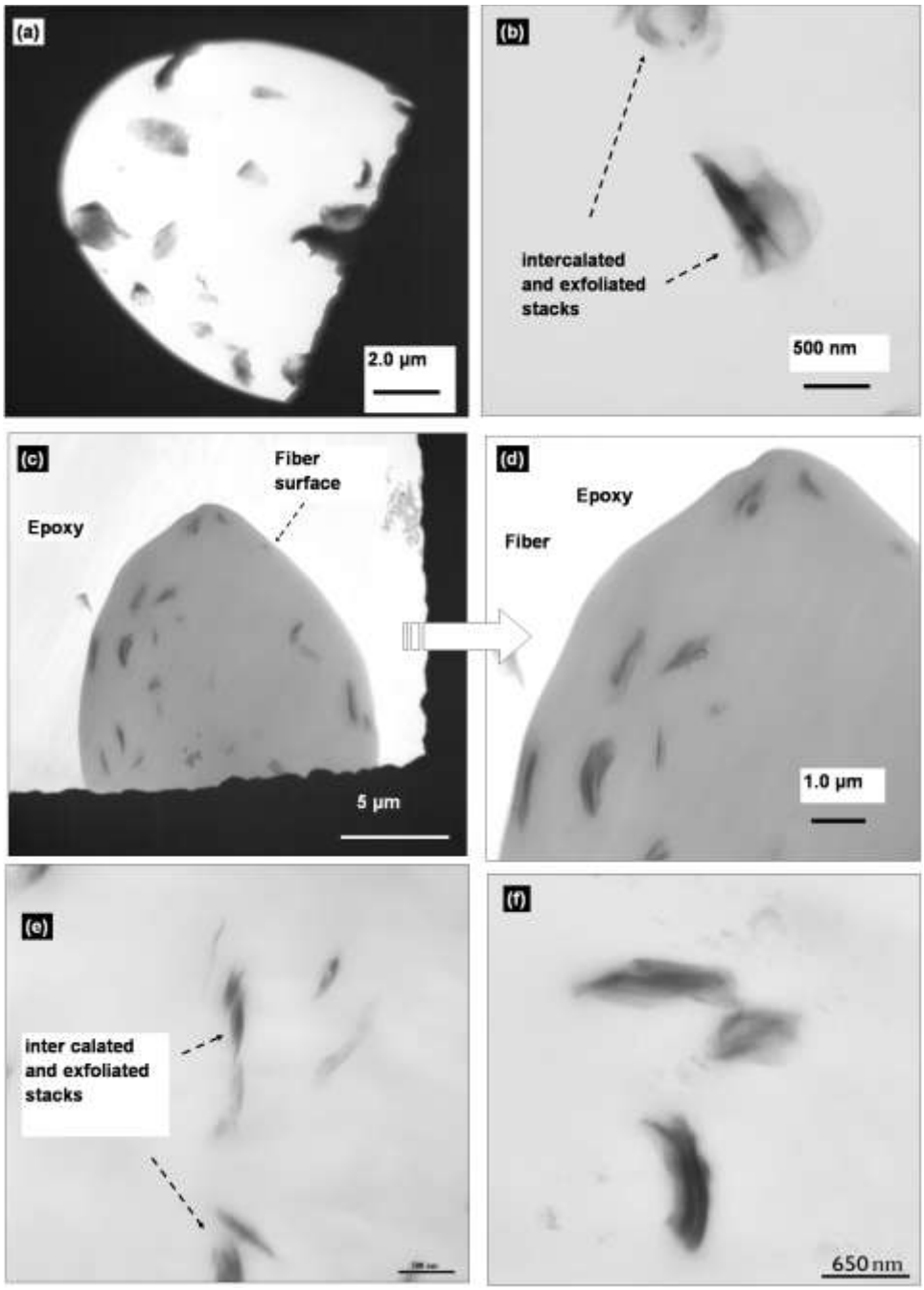

Figure 4.2. 5. TEM micrograph of film with 2 wt % clay (a), (c) micrograph of fiber with 2 % clay embedded in epoxy magnified micrograph showing particles at high magnification, (b) micrograph of fiber embedded in epoxy (d) magnified micrograph (e) micrograph at higher magnification showing significant polymer chain intercalation (f) tactoids with significant polymer chain intercalation.

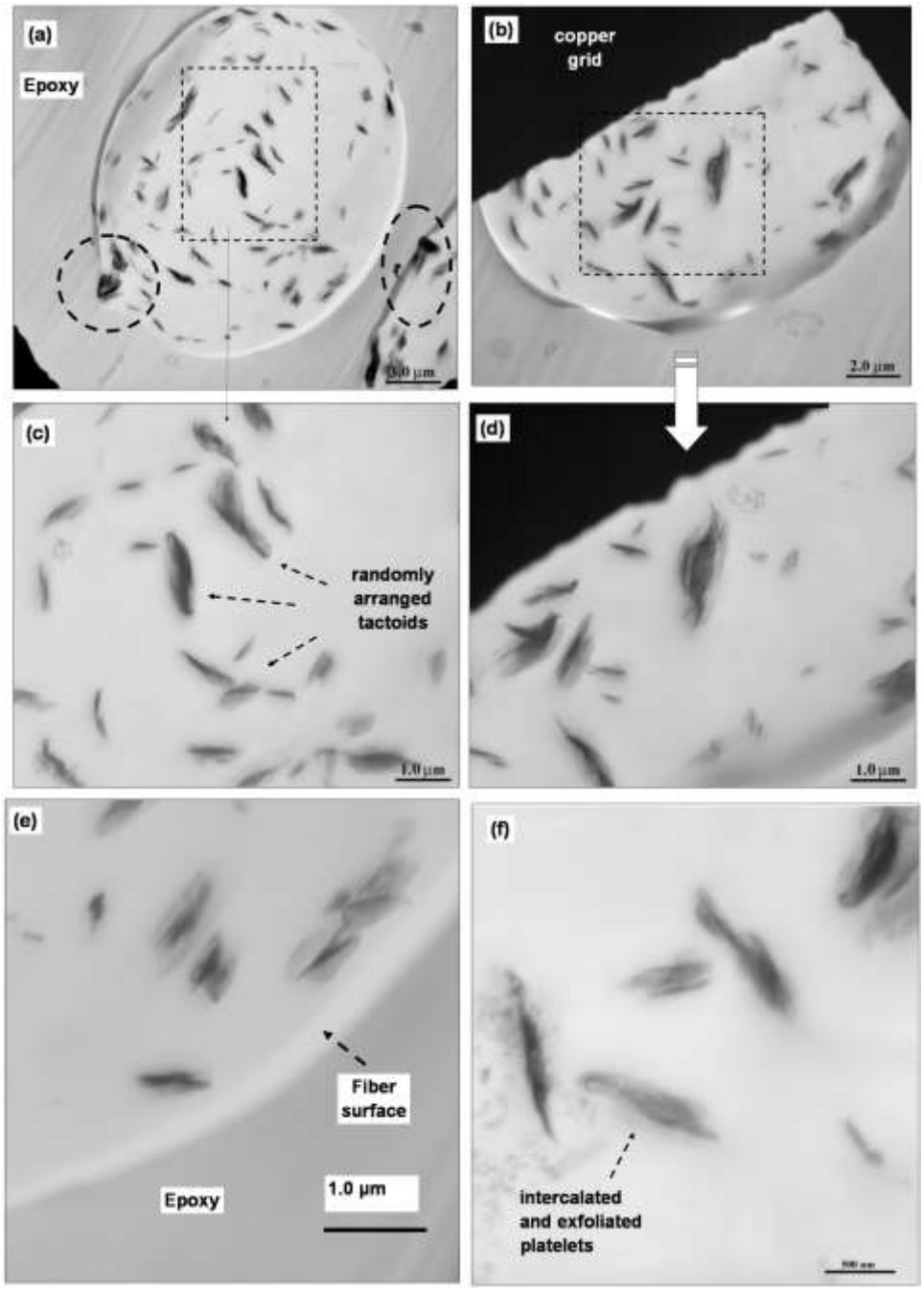

Figure 4.2. 6.TEM micrographs of film sample with 5% clay (a) two fiber micrographs at their surface show protruding clay agglomerates, also compared to fiber edge, at the fiber center, slightly large tactoids are observed, (b) micrograph of fiber with 5 % clay (c) micrograph at the center of fiber showing randomly oriented particles, (d) tactoids with significant chain intercalation (e) platelets near the fiber surface with slightly higher intercalation (f) tactoids with significant chain intercalation.

Machine direction (MD) tensile strength data is summarized in Figure 4.2.7-(a) and (b). Even though MD tensile strength shows decreasing tend with additives, drop in strength is not significant. However at higher level add on (5% clay), the strength drop was significant. Results of nonwoven web tear strength and stiffness are shown in Figure 4.2.7-(c). About 25 to 30 % increase in cross direction (CD) tear strength was observed for 1 to 2 wt % clay loading. Beyond 2 wt % clay loading, tear strength shows decreasing trend but the difference is not significant. Nonwoven web stiffness significantly increased in presence of additives. Observed discrepancy in mechanical properties is due to inherent uncertainty in dispersion of additives in these SB trials with additives.

However increasing trend is observed only up to 2 wt % additives. Increase in additive wt% beyond 2% did not bring any stiffness improvements. Increase in web stiffness is due to the presence of high modulus (≈400Gpa[35]) clay stacks as observed in TEM micrographs. These fabric properties are due to reinforcing effect of high modulus clay and change in morphology of constituent fibers.

Table 4.2. 2. Properties of Spunbond web with nanoclay additives.

Sample	(gsm)	Thickness (mm)	Fiber diameter (μ)	Birefringence (Δn)	Yellowness (b)
Control	30	0.3	15.8	0.015	0.7
1 % clay	30	0.3	15.3	0.019	2.6
2 % clay	30	0.3	16.7	0.017	3.5
5 % clay	30	0.3	18.9	0.013	5.2

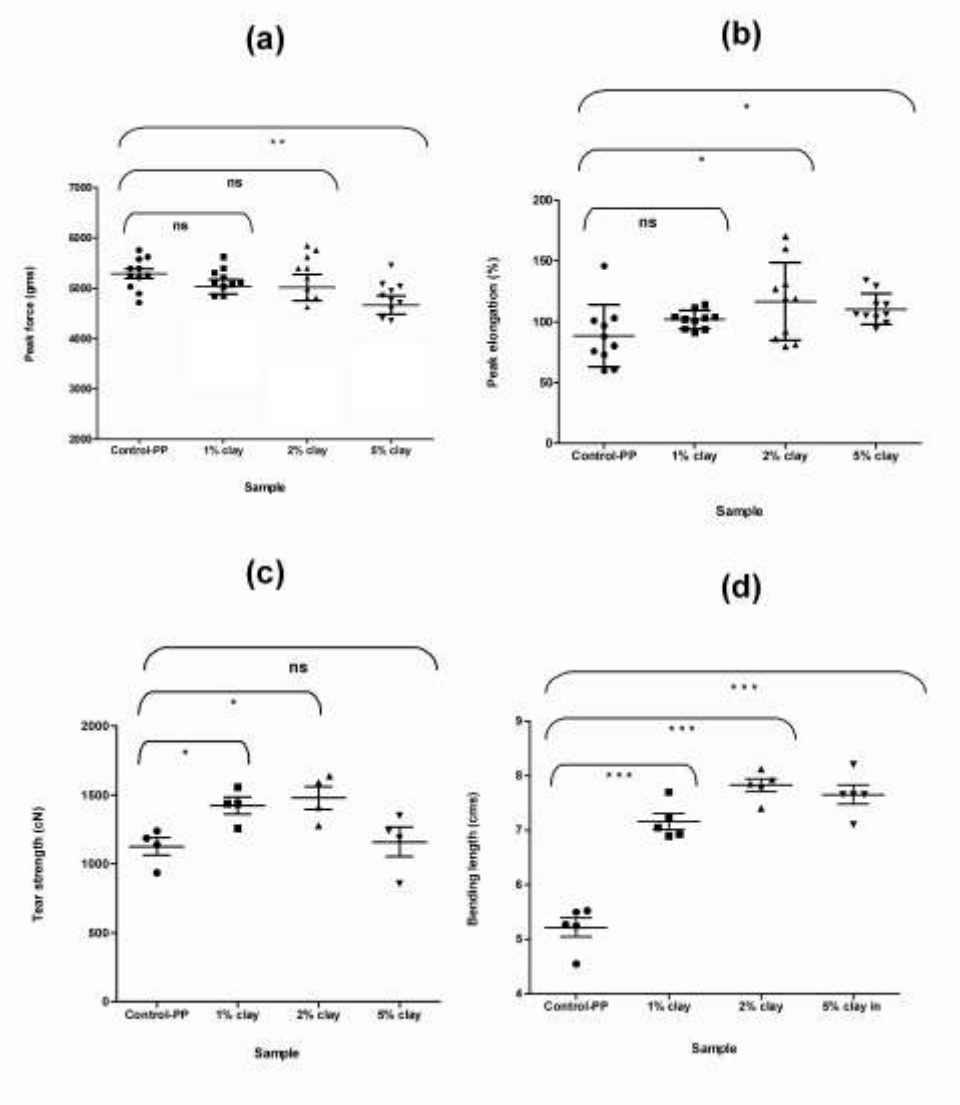

Figure 4.2. 7. Tensile strength (a) Machine direction (MD) tensile strength, (b) Elongation properties of web samples, (c) CD direction tears strength and (d) MD direction bending length of spunbond webs.

The thermal bonding conditions were same for all spun fiber webs and bonding temperature was not optimized. However, careful examination of several bond points revealed difference in bond point, failure mode and surface microstructure. SEM micrographs of bond point of control and fiber with 1 wt% clay are shown in Figure 4.2.8 (a) and (b). Fibers with even as low as 1 wt % clay retain their morphology and integrity in bond points better after calendering. Under same processing conditions, fibers with additives retained their structural integrity after thermal calendering. Similar results were observed in our earlier studies of spunbond trial with incorporation of Closite 15A and Closite Na^{+}[218].

SEM micrographs of spunbond web failure structure at bond point for control and webs with 1 wt% clay are shown in Figure 4.2.8 (c) and (d). Micrographs depict difference in failure mechanism between the samples. Most of the failures in the case of control webs were due to fiber breakage at bond edge, whereas the web failure in case of nanoclay reinforced spunbond webs were due to fiber pull off (Figure 4.2.8-d) from bond point.

Increased clay loading had adverse effect on the surface topology. SEM micrograph of fiber surface with 1 wt% clay is shown in Figure 4.2.8 (f). The micrograph shows 0.5 to 1.76 μ particle on surface for sample with higher level of clay. These are due to non-uniform dispersion, agglomeration of clay platelets, and protrusion of tactoids from surface. These protrusion and agglomerates are clearly shown in TEM micrograph in Figure 4.2.6-(a).

Statistical analysis (student t test showed $p<<0.05$) showed significant decrease in mechanical properties for sample with 2 and 5% clay additives. These mechanical property differences are due to change in polymer microstructure due to presence of additives. To understand this difference, an investigation on spherulite microstructure was performed using polarized light microscope.

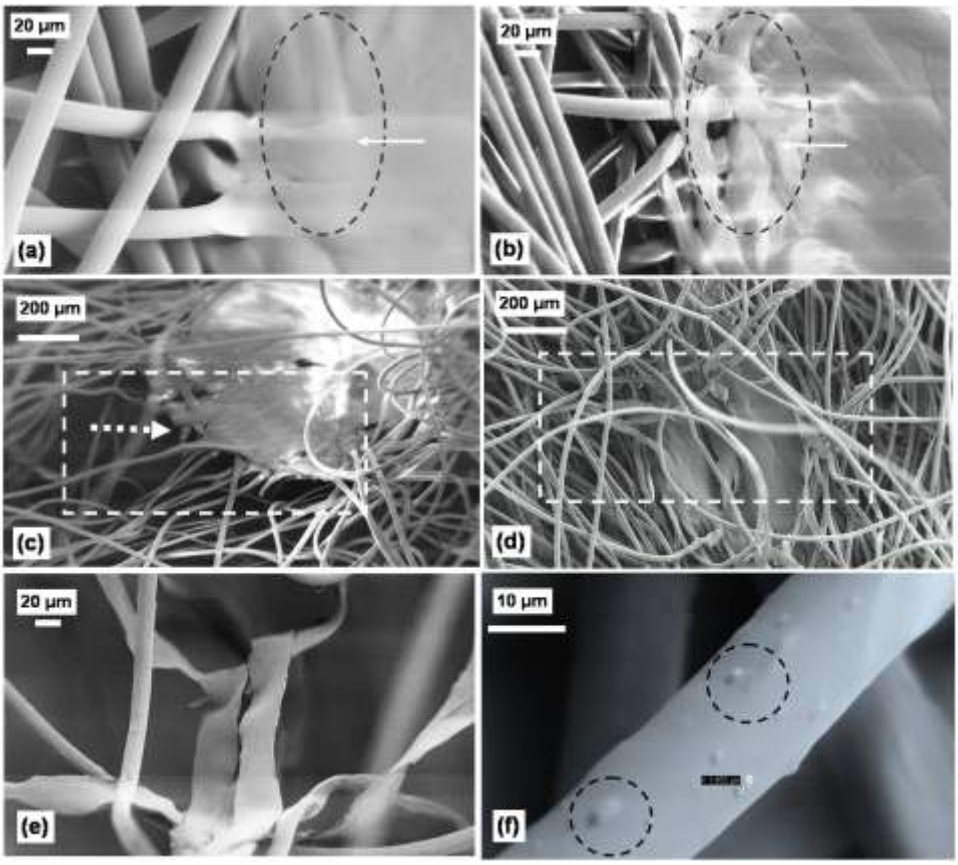

Figure 4.2. 8. SEM micrograph of (a) bond point of control SB web, (b) bond point with 1 % clay fibers retain their structure, (c) Control SB bond failure point which indicates most of failure at bond edge, (d) failed bond point of web with 1 % clay which is full of pulled off fibers, (e) pulled off fiber strip with 1 % clay and (f) agglomerates on fiber surface with 2 % clay.

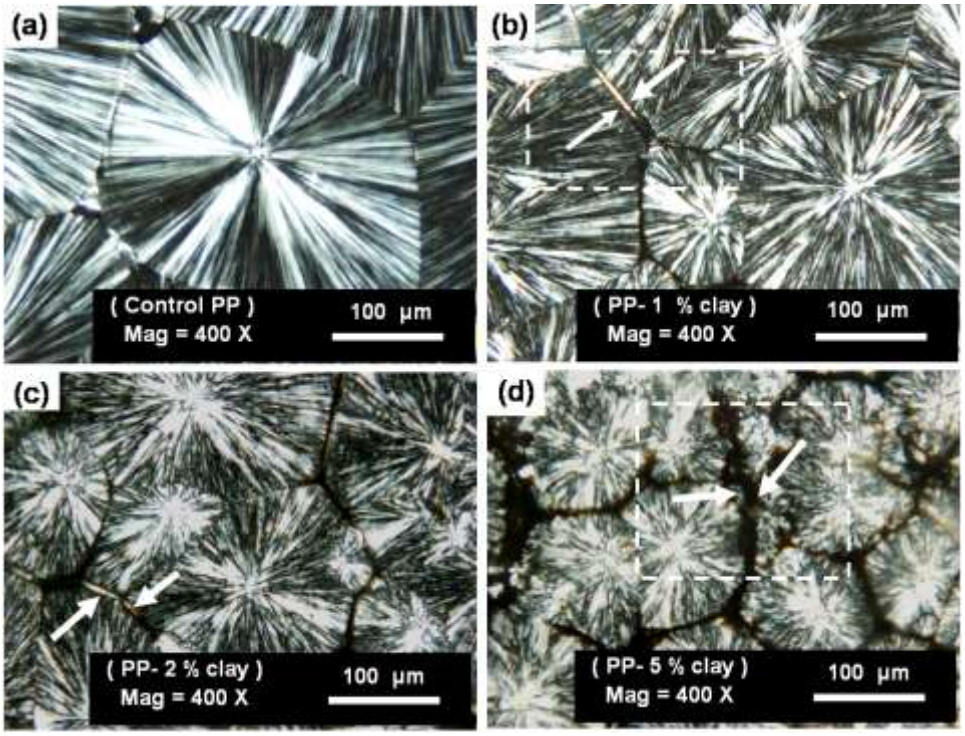

Figure 4.2. 9. Polarized light micrographs of (a) control PP (b) PP with 1 wt % clay (1% clay+5 % maleated wax + 94 % PP) (c) PP with 2 wt % clay (d) PP with 5 wt % clay.

Spherulite micrograph's for different samples are shown in Figure 4.2.9. The number of spherulites per unit area, maximum attainable diameter D_m and nucleation density N are shown in Figure 4.2.10 (a), (b) and Table 4.2.3. At higher concentration of nanoclay, nucleation density is very high. Incorporation of nanoclay additive significantly changes the microstructure.

Although the concentrates were crystallized in static condition and could not be directly related to spunbond process, the spherulite micrographs give clear representations of the difference in polymer microstructure and change in morphology in the presence of additives.

With the increase in clay weight %, segregation, and hence reinforcement in interspherulitic region was observed as shown in Figure 4.2.9 (b), (c) and (d). The area of interspherulitic region was 377 μm^2 for PP and 580 μm^2 for PPN1 respectively. This segregated mass may consist of compatibilizer maleated wax along with excluded clay agglomerate.

To investigate the composition of interspherulite region, combination of EDS and SEM was used. SEM micrograph of interspherulitic region and EDS scan of sample with 1% clay are shown in Figure 4.2.11. EDS scans revealed clay chemistry in the interspherulite regions. The segregation at the interspherulitic region is due to the exclusion of clay platelets from the growing boundaries of the spherulites. During the solidification, the clay platelets from the agglomerated mass are excluded out of crystal boundary.

Sample with 5 wt% maleated PP could not be processed due to rise in pressure. At low shear rates, shear viscosity increased for all the concentrates. This increase in viscosity is due to the agglomeration, entanglement of polymer chains and clay platelets. Entanglements between nano clay additives and the polymer chains resist the free motion of melt and increases melt viscosity. WAXD scans do not show any peaks corresponding to natural nanoclay in fiber webs due to very high levels of extrusion involved during spunbonding process and loss of ordered structure.

These differences in mechanical properties might also be due to change in microstructure and mechanical properties of the fibers. In our earlier studies, 15-75% increase in single fiber strength was observed[218]. At higher weight percentage, the MD tensile strength drops because of large agglomerates and exclusion of excess clay platelets at spherulite boundaries.

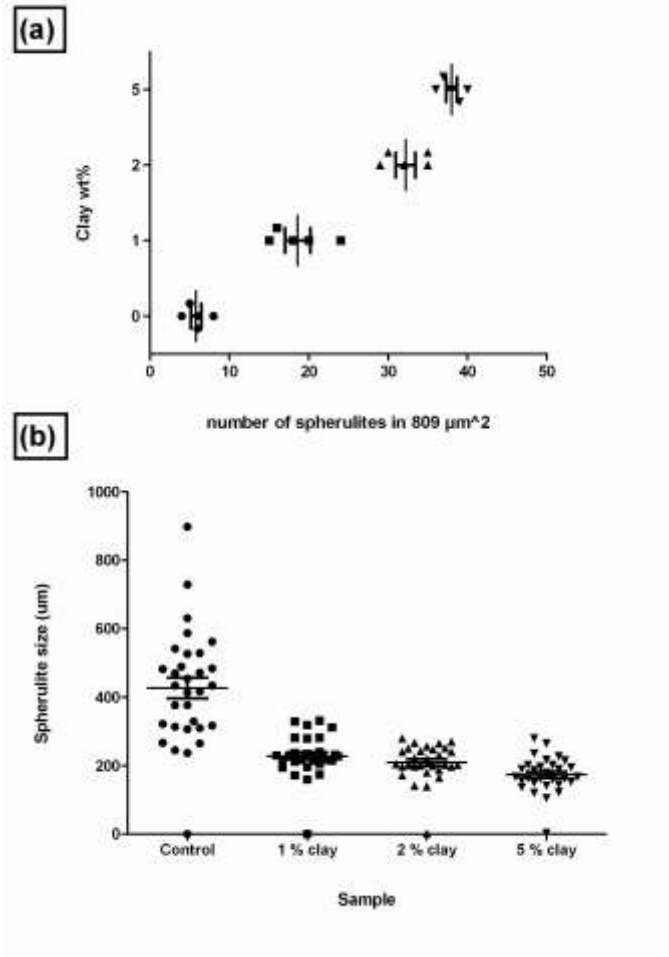

Figure 4.2. 10. (a) Number of spherulite in area, (b) Average diameter of spherulite in different PP samples.

Table 4.2. 3. Maximum attainable diameter, Nucleation density and average number of spherulites per 809 µm^2 area.

Sample	maximum diameter of spherulite (µm)	N (µm^-3)	Average no of spherulites in 809 µm^2
Control	441	2E-07	6
1 % clay	236	1E-06	19
2 % clay	216	2E-06	32
5 % clay	179	3E-06	38

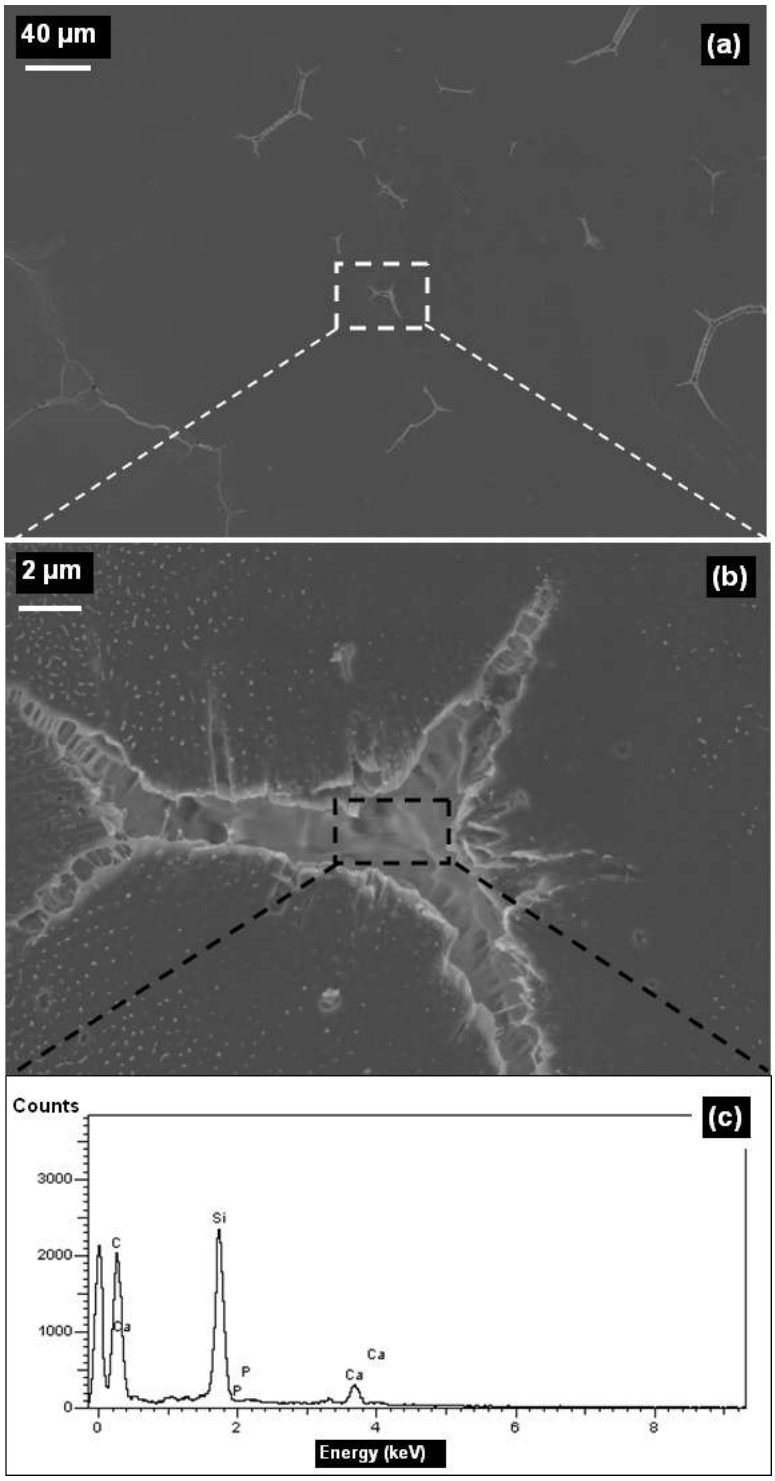

Figure 4.2. 11. SEM micrograph of interspherulitic region (a) lower magnification, (b) higher magnification, (c) EDS of interspherulitic region of PP with 1 wt% clay.

Difference in failure mode and retaining of fiber integrity in webs with additives might be due to the change in polymer microstructure.

Two different effects might involve during extrusion of polymer melt with additive as it is extruded from the spinneret. First, cooling rate and kinematics are totally different due to presence of additives and webs with additives cool at faster rate[229]. Since the fibers cool faster, extent of stress induced orientation might be different in case of fibers with additives. Significant difference in birefringence (shown in Table 4.2.2) was observed for SB fiber with 5 % clay (statistical analysis). The difference might be due to scattering from large amount of clay platelets. Second, clay additives acts as nucleating agent and increases the crystallization kinetics and fiber crystallinity[102, 230]. However, thermal analysis of fibers showed lower crystallinity wt % for all samples with additives.

From spherulite microstructure analysis, it is clear that there is significant change in polymer microstructure. Failures in semicrystalline products initiate and propagate at spherulite boundaries and along spherulite[231]. With increase in clay add on level, number of spherulites per unit area increases and impurity rich spherulite boundaries are formed by exclusion of clay platelets. At higher weight percentage, there is increase in overall weak spots in a given unit area. These weak spots decrease the web tear strength. However, increase in nonwoven web stiffness of is due to the reinforcement effect of high modulus clay stacks (≈ 400 Gpa[35]) in matrix and exclusion of excess clay platelets in the interspherulite regions. The reinforcement in the amorphous region makes the molecular network more compact and restricts the motion of molecules.

The key findings from SB webs with nanoclay additives are:

1. The intercalated and flocculated morphology of PP concentrates with 1 to 5 wt% clay subsist in the SB webs,
2. SB nonwoven web stiffness significantly improved in presence of 2 wt% natural nanoclay additives,
3. In case of polypropylene, at higher wt %, even in the presence of compatibilizers, it's difficult to evenly distribute the clay platelets and avoid clay tactoids in the matrix.

4. Clay additive has significant influence on the fiber surface topology,
5. Improvements in mechanical (tensile) properties observed in our previous SB trial could not be reproduced which demonstrate possible statistical variation in end product.

4.3 Polypropylene melt blown web with nanoclay

Some of the physical properties of the meltblown webs are summarized in Table 4.3.1. Presence of nanoclay additives did not improve any of these properties in meltblown webs. Compared to control, air permeability of web with additives was 10 to 75 % higher. Results of web bending length and air permeability prove the formation of stiffer webs with open web structure. Results of fiber diameter measured using optical microscope are shown in Figure 4.3.1. Average fiber diameter, coefficient of variation and standard deviation were high for melt blown web samples with clay, especially the 1LP. Fiber diameter for 1LP was significantly different from control MB web (from one way anova analysis results). This is expected since the presence of clay affects processing, and in turn, variability in melt blowing. Web with open structure is the result of overall increase in fiber diameter. Tensile strength and elongation in machine direction (Figure 4.3.2) were poor in the presence of additives. The sample 1LP (produced at low air pressure) showed low mechanical properties and higher variability in structure compared to rest of samples. These changes in properties of webs result from change in polymer microstructure due to well-dispersed clay additive.

The WAXD scans of different melt blown web samples are shown in Figure 4.3.3. The scans do not show any peaks corresponding to natural nanoclay which occurs around 2θ of 6.07° reconfirming good dispersion or delamination of the clay platelets beyond 100 A°. The delaminated structure or loss of ordered structure is probably due to higher level of shear involved in the extruder.

Cooling of polypropylene melt in the melt blowing process is non-isothermal and hence produces mesophase of low order known as smectic state[232]. As evident from the WAXD scans, compared to control melt blown web, samples produced with clay additive have well developed monoclinic crystalline peaks which are due to nucleating effect of nano additives. Results of crystallinity wt. % and crystal size measured by WAXD are summarized in Figure 4.3.4. Results do not show any specific trend with most of the samples having similar values.

Table 4.3. 1. Properties of melt blown webs.

Sample	Thickness (mm)	gms/m2	Air permeability (cm3/cm2/sec)	Bending length (cm)	Yellowness (b)
Control MB	0.5	25	73	4	0.5
1LP	0.4	26	295	6	0.9
1HP	0.4	25	96	5	0.9
2LP	0.4	25	83	7	0.6
2HP	0.4	25	88	7	0.5

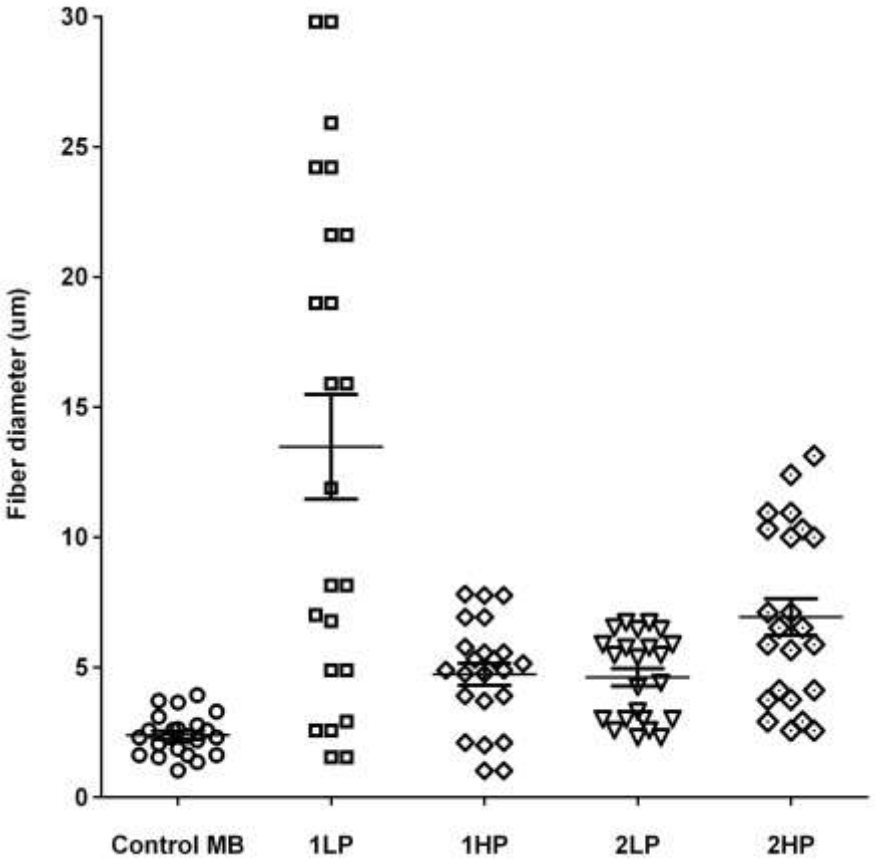

Figure 4.3. 1. Meltblown web fiber diameter measurements.

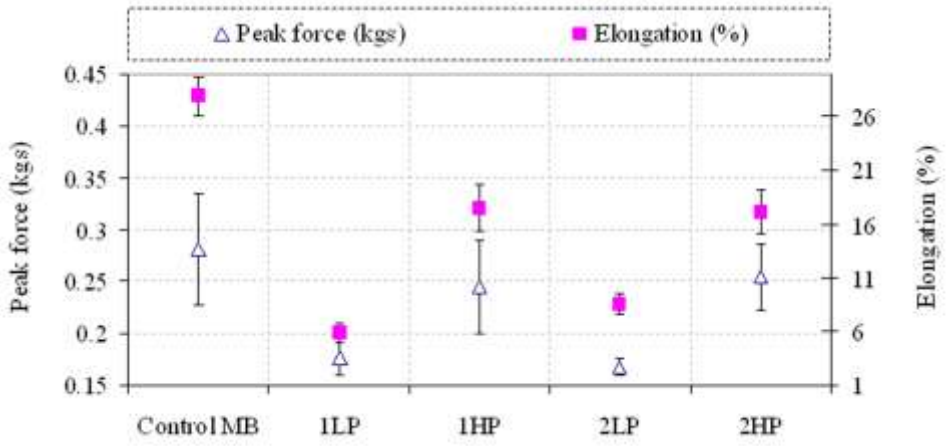

Figure 4.3. 2. Tensile properties of web.

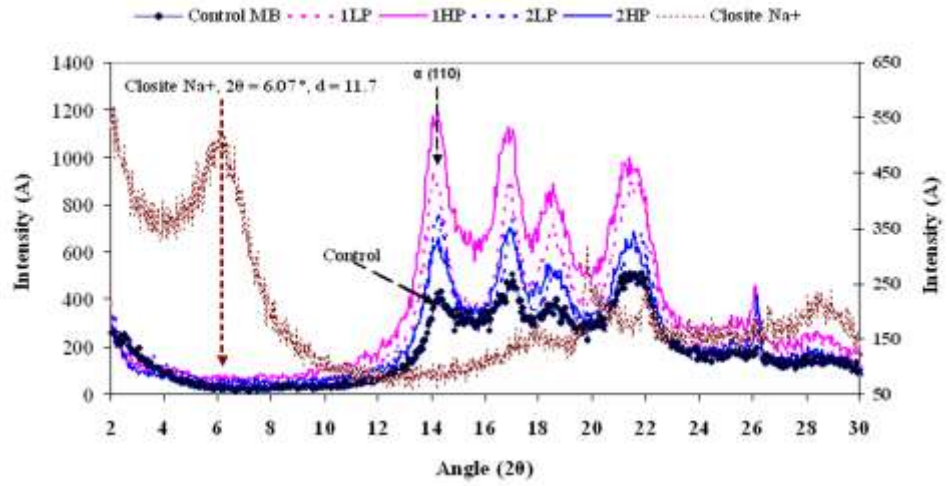

Figure 4.3. 3. WAXD scans of melt blown web samples.

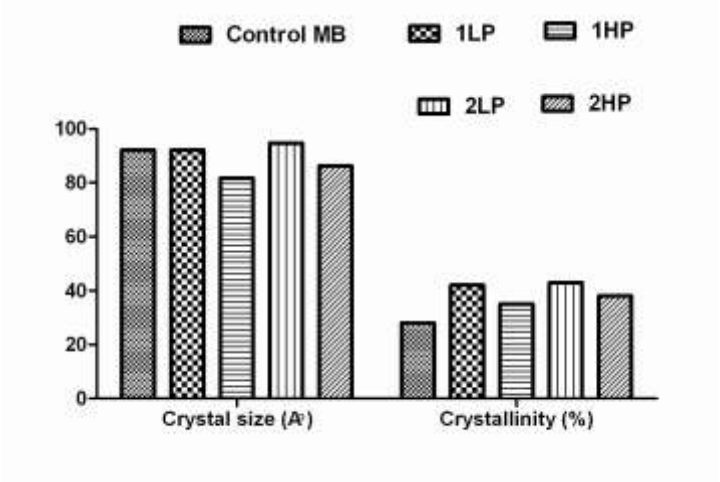

Figure 4.3. 4. Results of fiber crystallinity (%) and crystal size (A°) of melt blown samples.

TEM micrographs of MB web samples with additives are shown in Figures 4.3.5 to 4.3.8. Micrographs reveal significant dispersion and delamination of clay platelets, which is due to high melt flow rate (MFR) of polypropylene resin and also higher shear rate experienced by concentrates in the extruder. Clay platelets in case of sample 1LP (Figure 4.3.5) show complete dispersion of clay additives through fiber section. Small delaminated stacks and intercalated tactoids were observed in 1HP, 2LP and 2HP (shown in Figures 4.3.6, 4.3.7 and 4.3.8). TEM micrographs also reveal loss of ordered clay platelet structure in all the fiber web samples, which explains the reason for absence of peak corresponding to clay stacks in WAXD analysis.

The small agglomerates and intercalated stacks present during compounding might have been changed to delaminated structure due to high extrusion involved in MB processing. Additionally lower molecular weight of the resin in melt blowing will also make the intercalation easier. The delaminated structure is the reason for disappearance of peaks corresponding to nanoclay.

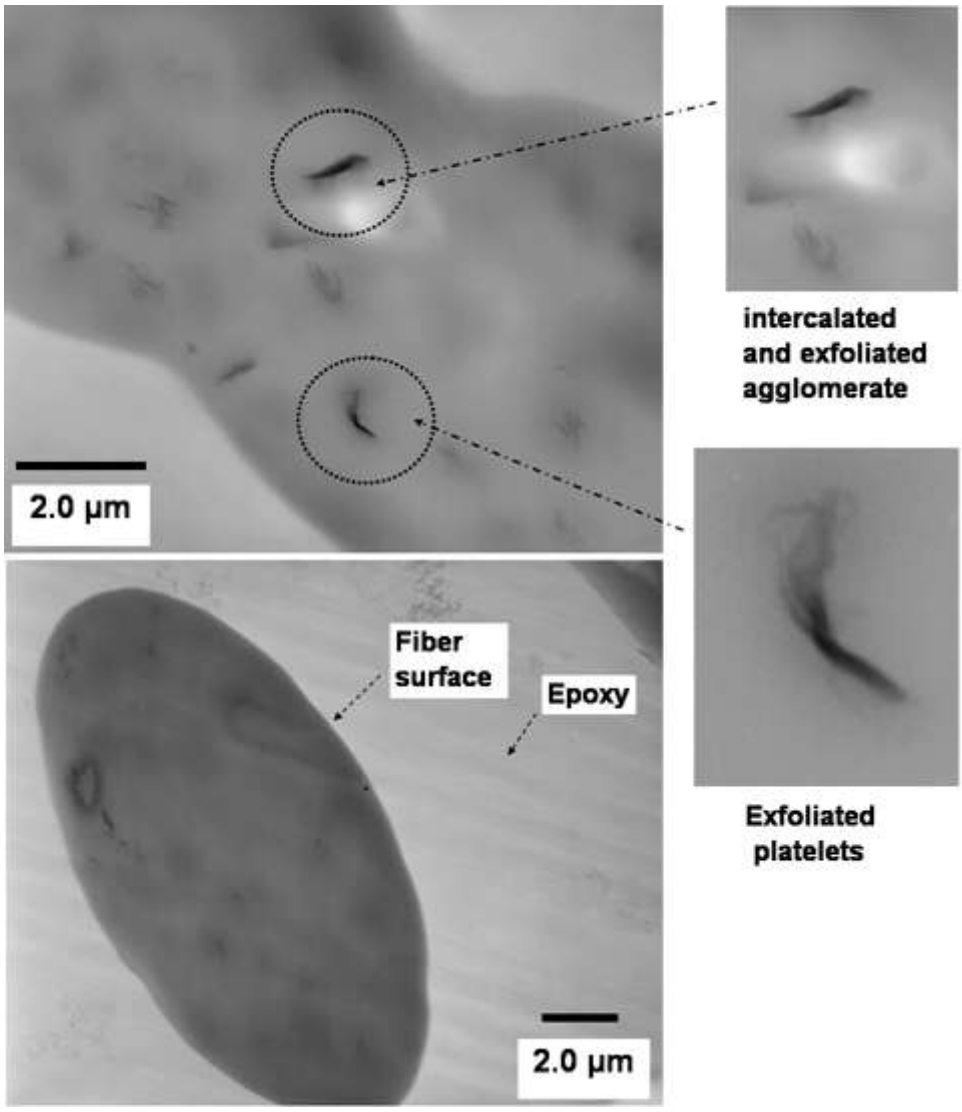

Figure 4.3. 5. TEM image of MB web 1LP with 0.5 wt % nano clay.

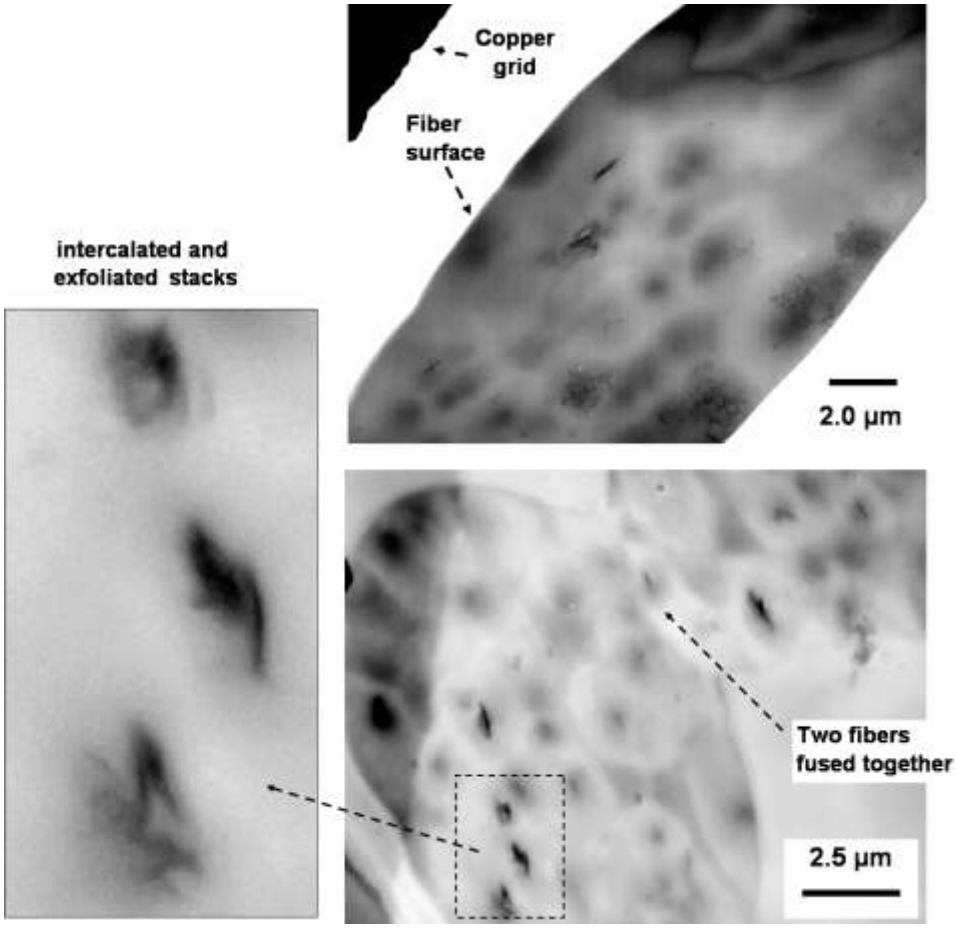

Figure 4.3. 6. TEM image of 1HP MB web with 0.5 wt % nano clay.

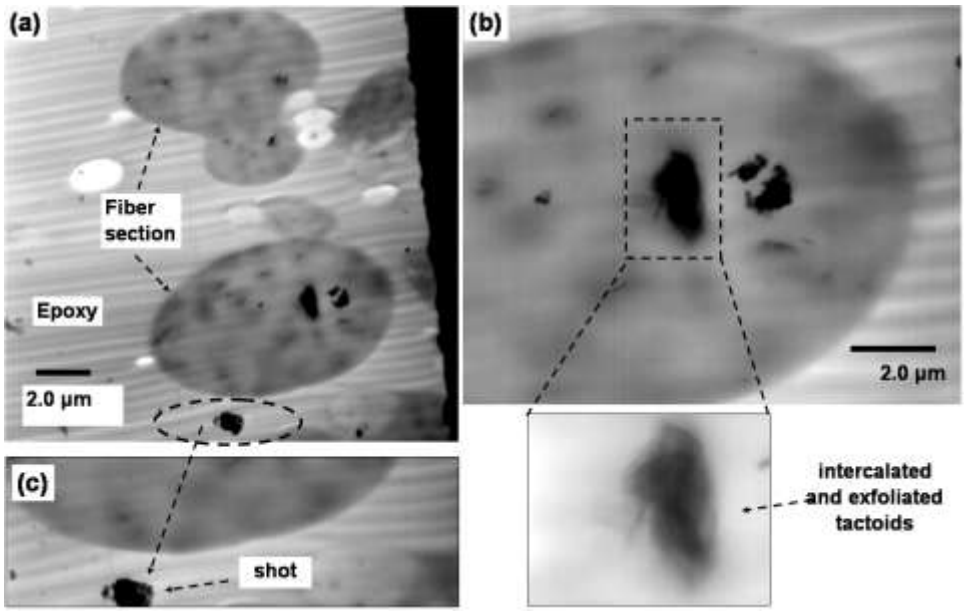

Figure 4.3. 7. TEM micrograph of 2LP with 0.5 wt % nano clay, (a) section with 3 fibers, (b) magnified image of fiber section with clay agglomerate and (c) section of shot.

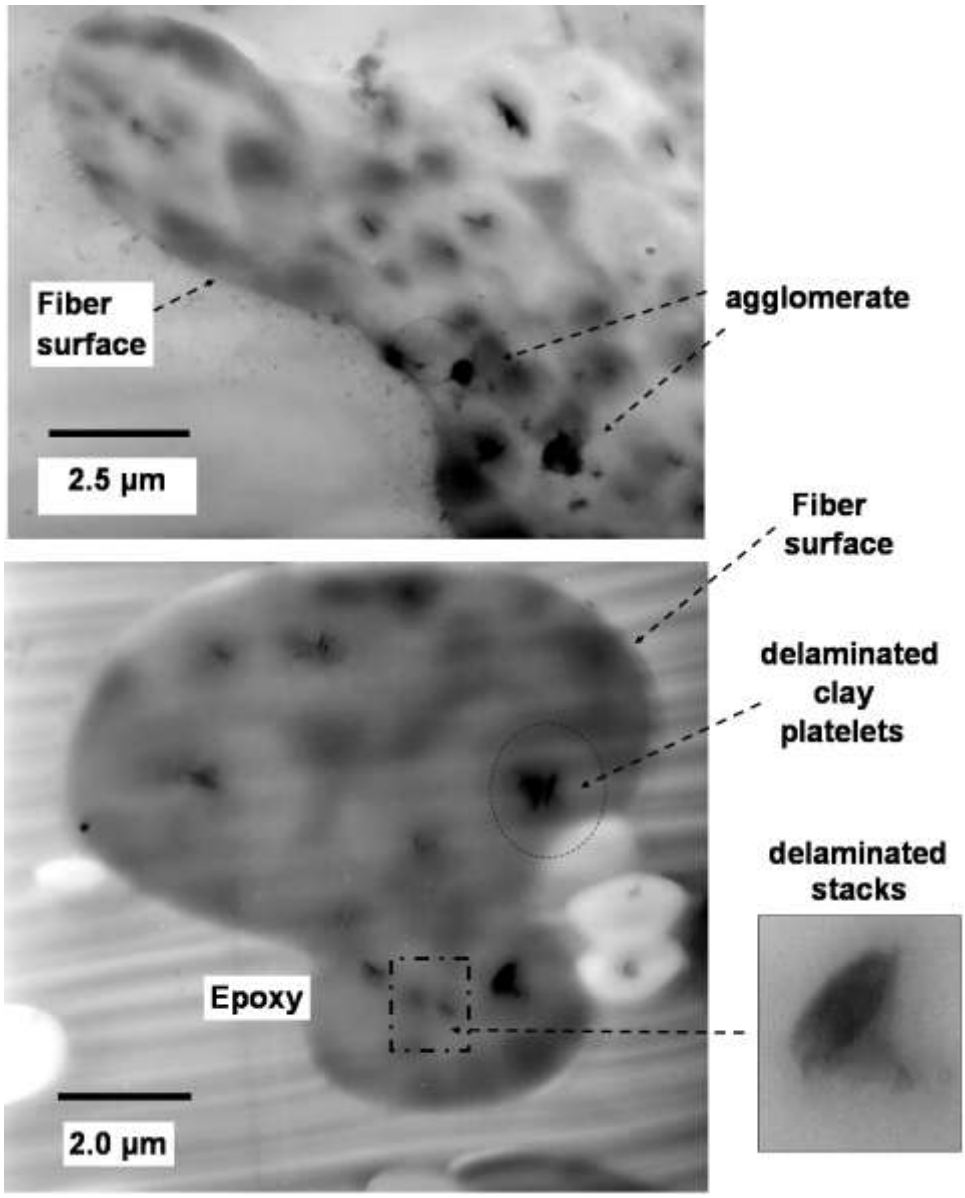

Figure 4.3. 8. TEM micrograph of 2HP with 0.5 wt % nano clay.

Thermal analysis results obtained from the DSC cooling scans are summarized in Table 4.3.2. Results do not show any specific trend. Crystallinity % of web with 2.5 wt % compatibilizer is slightly lower. Sample 1LP has higher crystallinity compared to rest of the fiber webs, which might be due to the very high exfoliated fiber morphology evident from the TEM micrographs. Results of relative crystallinity X (t) versus time for different web samples estimated from the iso-thermal crystallization kinetics are included in Figure 4.3.9. From the relative crystallinity results, it is evident that mechanism of crystallization is different for webs with nanoclay additives. Sigmoid shape is observed for all the samples except difference in saturation times. Sigmoid shape represents initial rate of phase change followed by subsequent slowing down as growing bodies impinge. Samples with additives attain saturation before the control polypropylene.

Results of isothermal crystallization parameters obtained from Avrami analysis are summarized in Table 4.3.3. Avrami exponent 'n' for nanocomposites and control PP varied from 1 to 2 which indicates spherulitic form of crystal growth. Sample 2HP has n of 1.4, which according to literature represents rod like growth from instantaneous nuclei[144]. Also fractional value of n indicates presence of multiple growth morphologies and two different types of nucleation mechanisms[233]. Total time for crystallization (t-max) for sample 1LP was 57 % lower compared to control PP. Overall, total time for crystallization (t-max) for samples with additives was 33-57 % lower compared to control MB.

In the presence of the clay additive, rate of crystallization, mechanism of heat transfer, cooling rate and kinematics are different. Having additives facilitate the web to cool at faster rate compared to control polypropylene web. Increased crystallization kinetics and higher cooling rate causes the individual fibers to solidify faster compared to neat resin, which minimizes the extent of interfacial bonding between the fibers. Hence the elongation and strength of meltblown webs in the presence of additive are lower compared to that of control[229]. These differences contribute to the difference in the observed web structure. Optimization of process conditions might help bring the property benefits.

Table 4.3. 2. DSC cooling segment results for MB web.

Sample	Control MB	1LP	1HP	2LP	2HP
Clay wt (%)	0	0.5	0.5	0.5	0.5
Onset (°C)	125	124	124	121	124
Peak (°C)	119	120	120	116	118
End set (°C)	115	113	114	111	110.4
integral (J/g)	737	840	825	725	803
normalized (mJ)	98	104	101	91	96
Crystallinity (%)	52	55	53	48	51

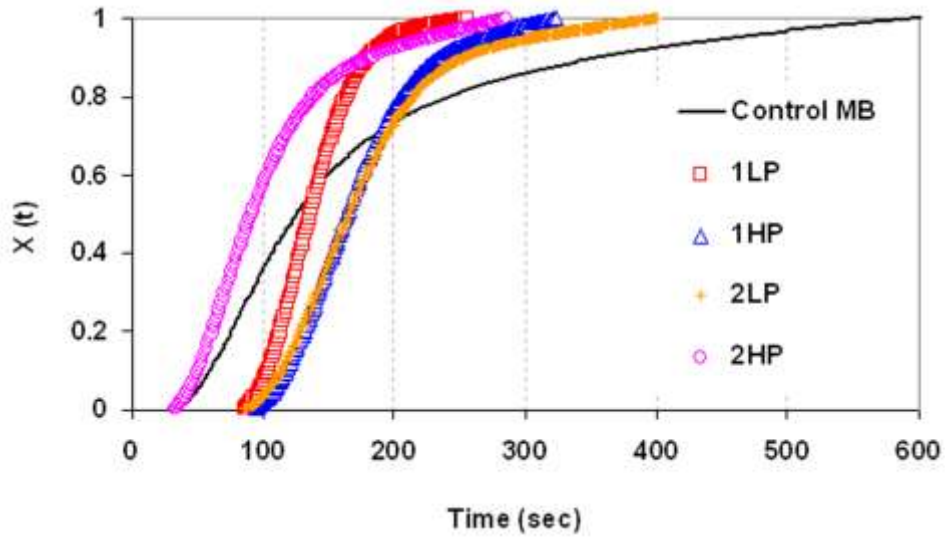

Figure 4.3. 9. Relative crystallinity versus crystallization time of different MB web samples from DSC thermograms.

Table 4.3. 3. Avrami parameters for different MB web samples.

Sample	n	K	t 1/2 (min)	t-max (min)	Hf (j/g)
Control PP	1.5	0.33	120	600	61
1LP	1.8	0.59	120	240	87
1HP	1.5	0.28	180	300	81
2LP	1.7	0.28	180	420	89
2HP	1.4	0.35	120	300	69

Polarized light micrographs and number of spherulite in unit area for different polypropylene samples are shown in Figure 4.3.10 (a)-(d). The pronounced Maltese cross extinction pattern is observed for neat PP as shown in Figure 4.56 (a) whereas, smeared four leaf-clove pattern is observed for sample 1 and 2 with 0.5 % clay[9]. Kang X et al. observed heterogeneous nucleation mechanism and decrease in spherulite size from 155 μm in neat PP to 12 μm for the case of polypropylene with 8 wt % clay additives[234].

Micrographs show well-developed spherulites size of ≈ 100 μm for control PP. The spherulites size of control PP is larger than that of concentrates with nanoclay additives. Average number of spherulites per area (volume fraction) of material studied is shown in Figure 4.3.10 (d). Results confirm nucleating effect of additives even at 0.5 % add on level. The C.V of number of spherulites in unit area observed is very high for sample with additives, which indicates variation of microstructure in sample (Figure 4.3.10-d). Acceleration of crystallization and decrease in crystal size are due to the large number of spherulites per unit area[9, 235-238].

The maximum attainable diameter (D_m) of spherulite and nucleation density (N) for different concentrates is included in Figure 4.3.11(a) and (b). The maximum attainable diameter further decreased for sample with nanoclay additives, which indicates significant change in microstructure in presence of additives. High nucleation density explains the differences in the relative crystallinity results. C.V for the sample 1 is higher compared to control MB and sample 2, which might be due to the variation in dispersion of clay stacks obtained in TEM micrographs.

Slightly higher secondary crystallization time for sample with additives is due to the time involved in growth and to fill the interspaces between the spherulites[51]. The maximum spherulite diameter of control PP observed in this study is ≈125 μm which is less than the spherulite diameters of polypropylene reported in literatures (≈150-800 μm) [9, 239]
which is due to high MFR (1500 MFR) PP used in this study.

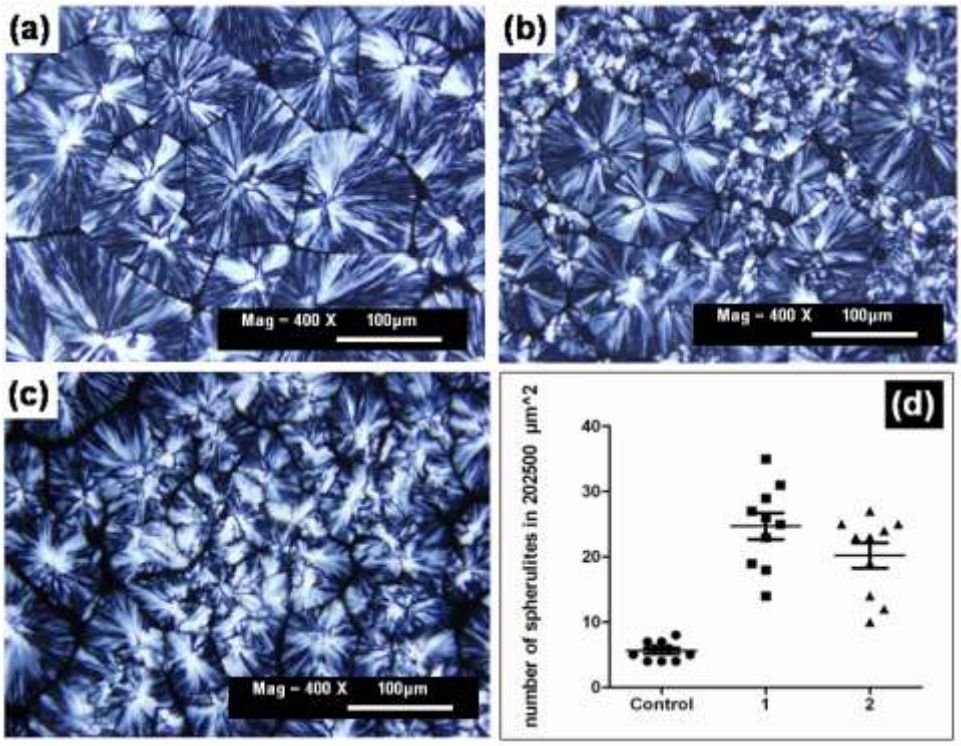

Figure 4.3. 10. Polarized light micrographs of (a) Control polypropylene, (b) sample 1 with 0.5 wt. % nanoclay additive, (c) sample 2 with 0.5 wt. % nanoclay additive and (d) number of spherulite in unit area for different polypropylene samples.

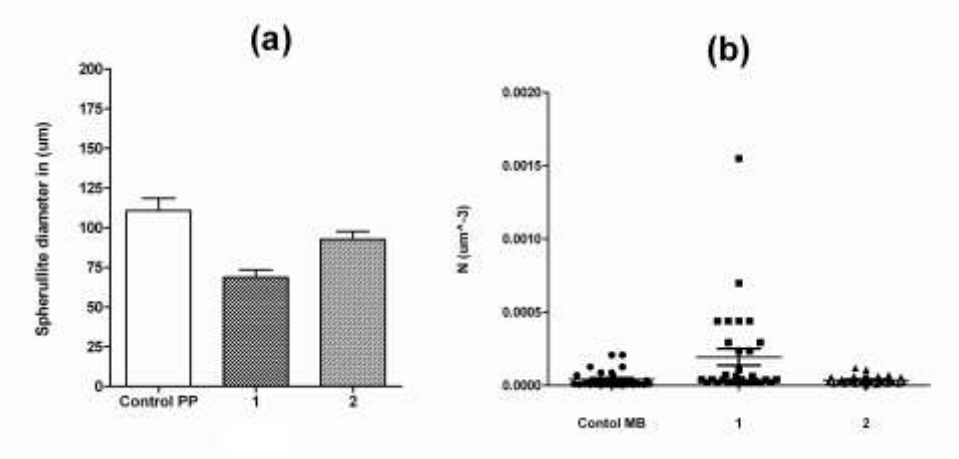

Figure 4.3. 11. (a) Average maximum attainable diameter of spherulite in different polypropylene samples (b) Nucleation density for different polypropylene samples.

SEM micrographs of control and 1LP surface (Figure 4.3.12 a, b, c and d) clearly show increase in fiber diameter variation and shot formation for samples with clay. Figure 4.3.12 (e) shows the SEM micrograph of section of shots found on the 1LP web sample. Some of these shots had clay agglomerates in them as reconfirmed by EDS elemental composition results. Fiber diameter shows much higher variability for webs with additives. In our previous studies, increase in shear viscosity has been observed for polypropylene-clay concentrates[218, 240]. Increase in viscosity leads to increase in the fiber diameter variation.

Control resin formed better melt blown webs with fine fiber diameters and lower coefficient of variation. Web produced at high air pressure had lower fiber diameter variation in the final web compared to that of webs produced at lower air pressure indicating formation of fine fibers with increase in primary air speed. Bressee et al. have reported similar results of fiber diameter variation with different air pressure for neat PP resins[240].

In the meltblown process, fiber orientation and attenuation take place in semi-molten state. Fibers remain hot even after lay down on collector and continue to crystallize on the collector. Some fibers fuse and form attenuated webs by contact in hot condition. Final web structure is developed after lay down in fused state on collector drum.

In this situation, increase in shot content is due to the increased melt viscosity in the presence of clays. Increased melt viscosity increases the fiber diameter and causes web variation. In earlier studies, it has been proved that fine fibers cool faster; orient and stick together to form better melt blown webs. Fiber webs with increased fiber diameter and diameter variation cool at a slower rate. Irregularity and increase in cooling rate also result in the melt fusion and number of shots[52, 34].

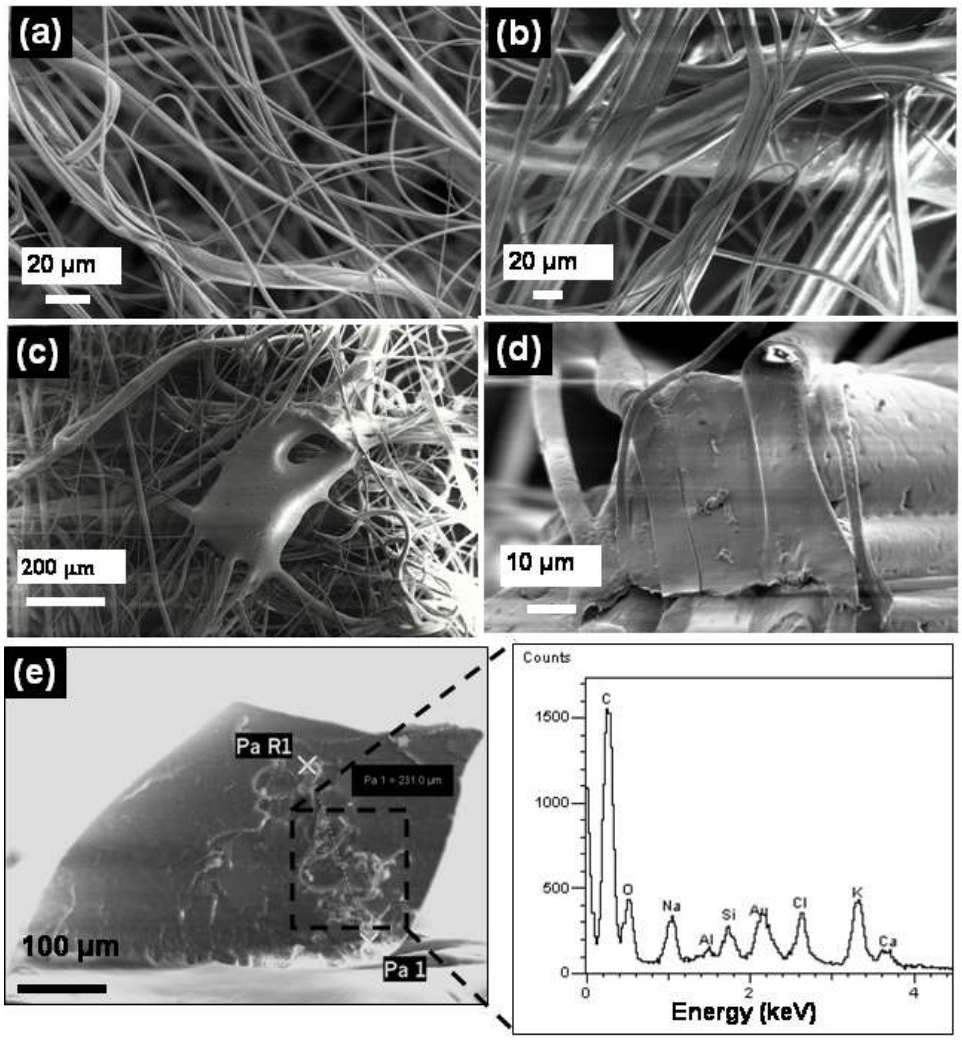

Figure 4.3. 12. SEM micrograph of (a) Control MB web, (b) Web 1LP, (c) Shots on 1LP, (d) Cross-section of fiber web1LP, (e) SEM micrograph of cross section of shots of 1LP web sample (nanoclay platelet clusters within agglomeration is reconfirmed).

4.4 Injection molded polypropylene-nanoclay composite

WAXD scans of Closite Na^+ additive and different molded bars are shown in Figure 4.4.1 (a) and (b). Peak corresponding to (001) plane of clay platelet occurs at 2θ of 6.07° which correspond to d-spacing of 1.5 nm. Peak corresponding to γ-crystalline form of PP was only observed for PPN15. Crystal thickness was calculated using Scherrer equation from FWHM of peak corresponding to (110) plane.

Results of d-spacing (A°) and crystal size (A°) are summarized in Figure 4.4.2 and Table 4.4.1. With increase in clay wt. %, peak corresponding to (001) plane shifts to higher 2θ angle, which indicates the decrease in d-spacing of clay. This decrease in d-spacing is due to the molding pressure or degradation of surface modifiers[13]. Similar increase in lamellar thickness results which is also reported in the literature is due to the segregation of clay platelets in the inter-lamellar regions[111].

TEM micrographs of PP with 1 to 15 wt. % clay are included in Figure 4.4.3 (a), (b), (c) and (d). Micrographs revealed intercalated and flocculated morphology observed in all the samples[103]. Sections revealed preferential orientation of platelets for sample with low wt. % of additives (Figure 4.4.3 (a), (b) and (c). Shear induced preferential orientation of clay platelets parallel to the surface of mold has been investigated before[241].

Also low degree of preferential orientation can be observed in case of PPN15. Observed orientation behavior in case of PPN15 is due to the sensitive response of layered nanoparticle to shear deformation and the structural recovery of clay networks by the electrostatic attraction existing between adjacent nanoplatelets[242]. Samples with 1 % clay additive have higher modulus and extension properties.

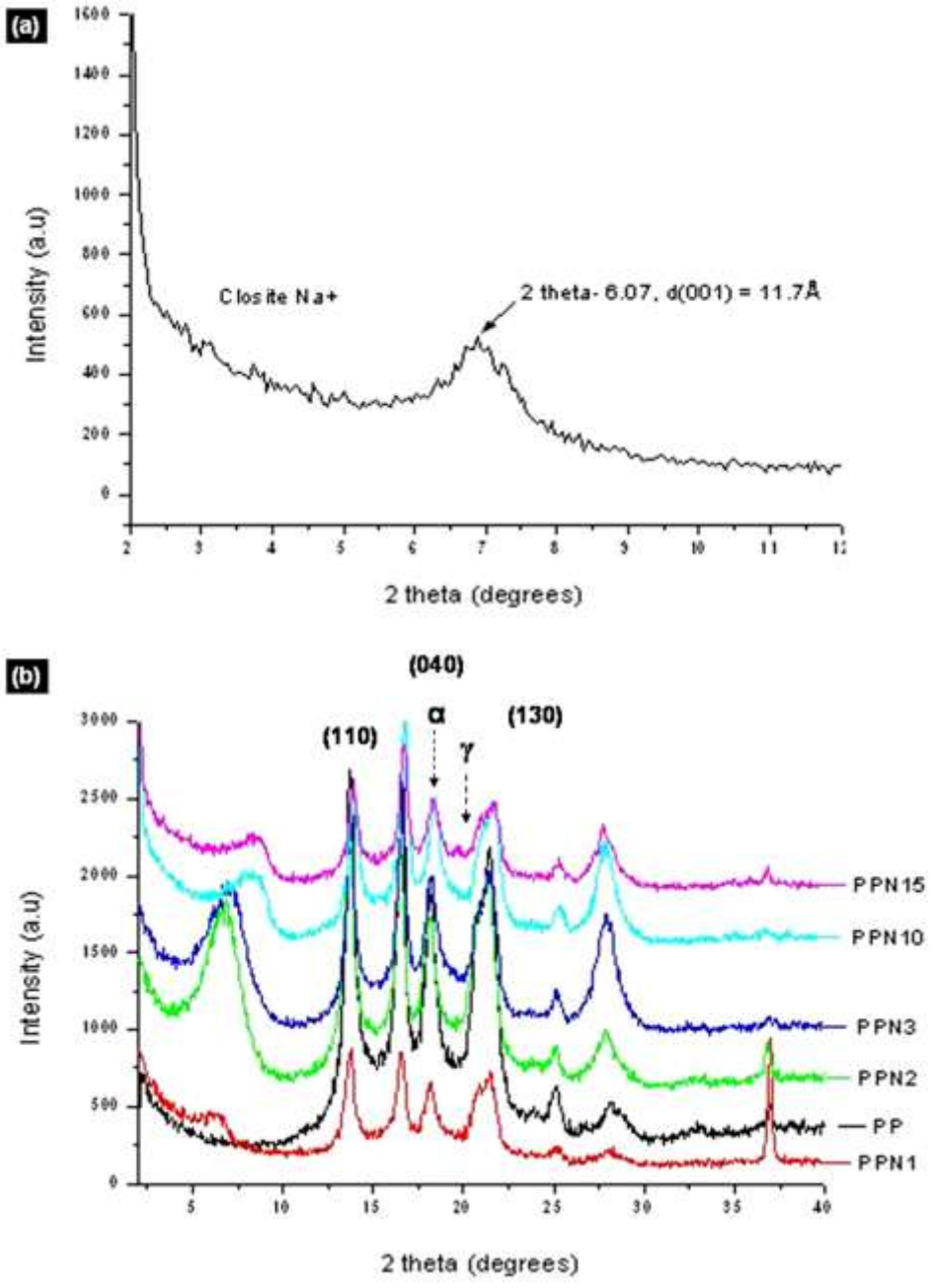

Figure 4.4. 1. XRD scans of (a) Closite NA+, (b) injection molded polypropylene composite bar samples.

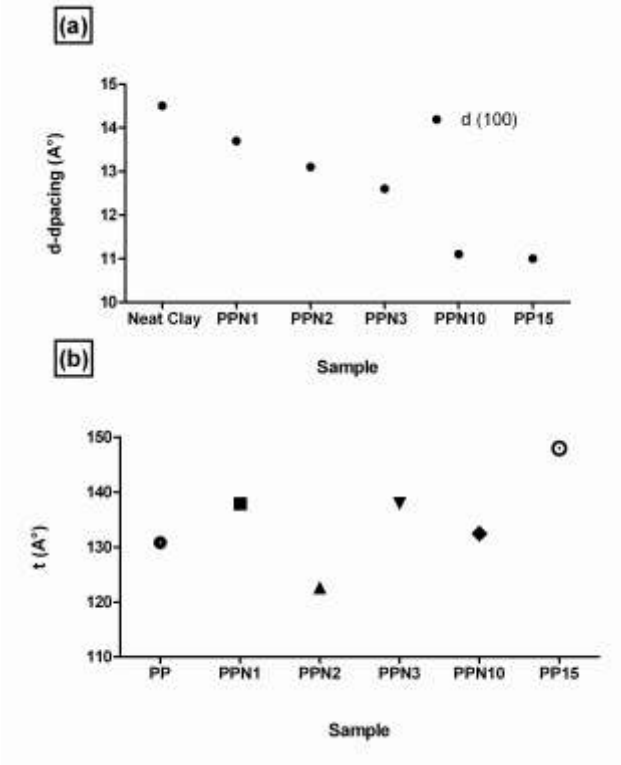

Figure 4.4. 2. WAXD results (a) d-spacing (A°) of (100) plane of clay platelets and (b) crystal size (A°) calculated from Scherrer equation from peak corresponding to (110) plane.

Table 4.4. 1. WAXD results of crystal size and d spacing of (100) plane of clay platelets.

Sample	Crystallinity Wt %	t (A°)	D spacing (100)
Neat Clay		131	15
PPN1	52	138	14
PPN2	59	123	13
PPN3	57	138	13
PPN10	51	133	11
PPN15	38	148	11

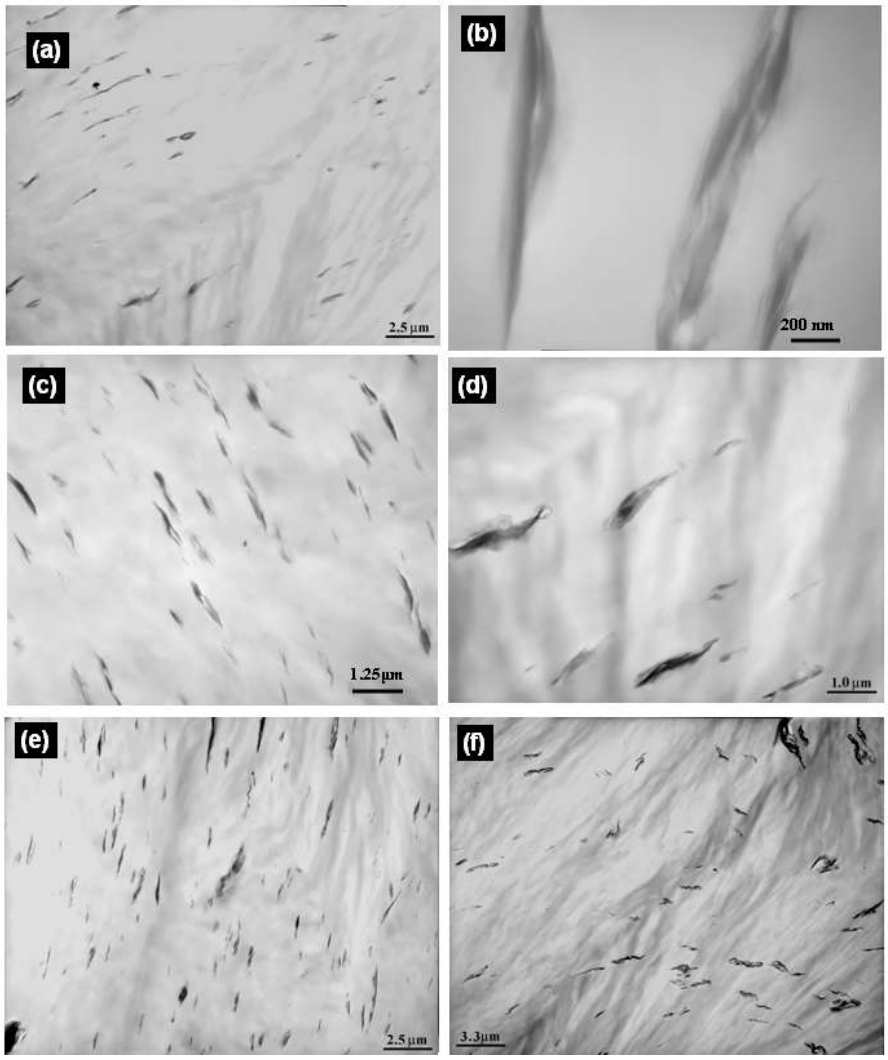

Figure 4.4. 3. TEM micrographs of (a) PPN1, (b) PPN1 at high magnification, (c) PPN3, (d) PPN3, (e) PPN10, (f) PPN15.

Exact filler weight percentage in the concentrates was determined from TGA analysis and summarized in Figure 4.4.4 (a) and (b). Slightly lower rate of weight loss was observed for concentrates with clay. Standard deviation of weight percentage is high for sample with 15 wt. % clay additive compared to rest of the concentrates.

DSC results (Table 4.4.2) showed slight decrease in crystallinity compared to control polypropylene. DSC scan results from cooling segments are shown in Figure 4.4.5 (b). The peak crystallization temperature was 10°C higher for sample with PPN10 and PPN15, which indicates the nucleating effect of clay. Thermal analysis results showed slight decrease in crystallinity weight %, which might be due to hindrance to polymer chain mobility due to the presence of large amount of clay in the matrix.

Effect of crystallization temperature on isothermal crystallization thermograms of PP and PPN15 is shown in Figure 4.4.6 (a) and (b). For both the sample, with increasing crystallization temperature (T_c), the crystallization shifts to longer time and crystallization peak becomes flatter. For PPN15, at each crystallization temperature, rate is higher than that of control PP.

Effect of different wt. % of nanoclay additives on the relative crystallization kinetics at 125°C is shown in Figure 4.4.6 (c). Sigmoid shape is observed for all the samples. Sigmoid shape represents initial rate of phase change followed by subsequent slowing down as growing bodies impinge. Concentrates PPN1, PPN2, PPN3 reach saturation after control PP. However sample PPN10 and PPN15 attain saturation before control polypropylene. These differences in crystallization will be explained in further discussions.

Results of crystallization kinetics are shown in Figure 4.4.7. The "n" varies within the range of 1 to 3 which is due to spherulitic form of crystal growth[126]. The rate constant showed a decreasing trend for PPN1, PPN2 and PPN3. However for PPN10 and PPN15, even at high temperature of 135C, the rate constant was higher than rest of samples. The half time of crystallization $t_{1/2}$ increased with crystallization temperature, which indicates the decrease in crystallization rate.

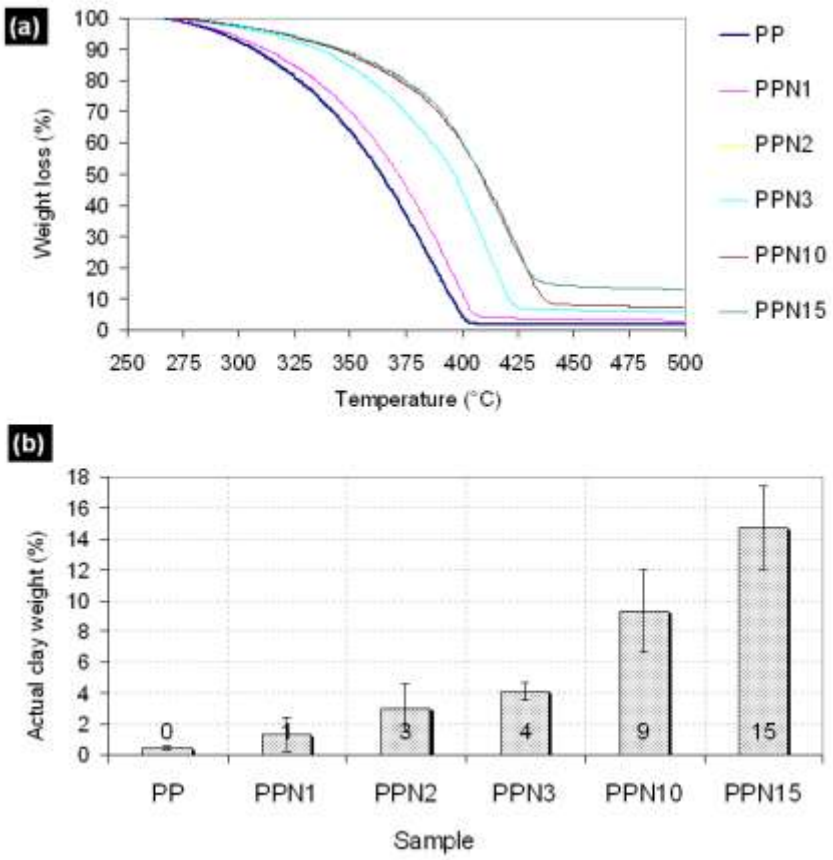

Figure 4.4. 4. (a) TGA scans of different concentrates with different percentage of clay additive, (b) Actual filler content at 500°C.

Table 4.4. 2. Thermal analysis results for different concentrates.

Sample	Clay wt %	Onset	Crystallinity (%)	Integral (mJ)	Normalized (J/g)
PP	0	120	49	1180	102
PPN1	1	114	45	886	94
PPN2	2	118	46	948	95
PPN3	2	117	46	861	93
PPN10	10	123	46	795	91
PPN15	15	124	47	645	87

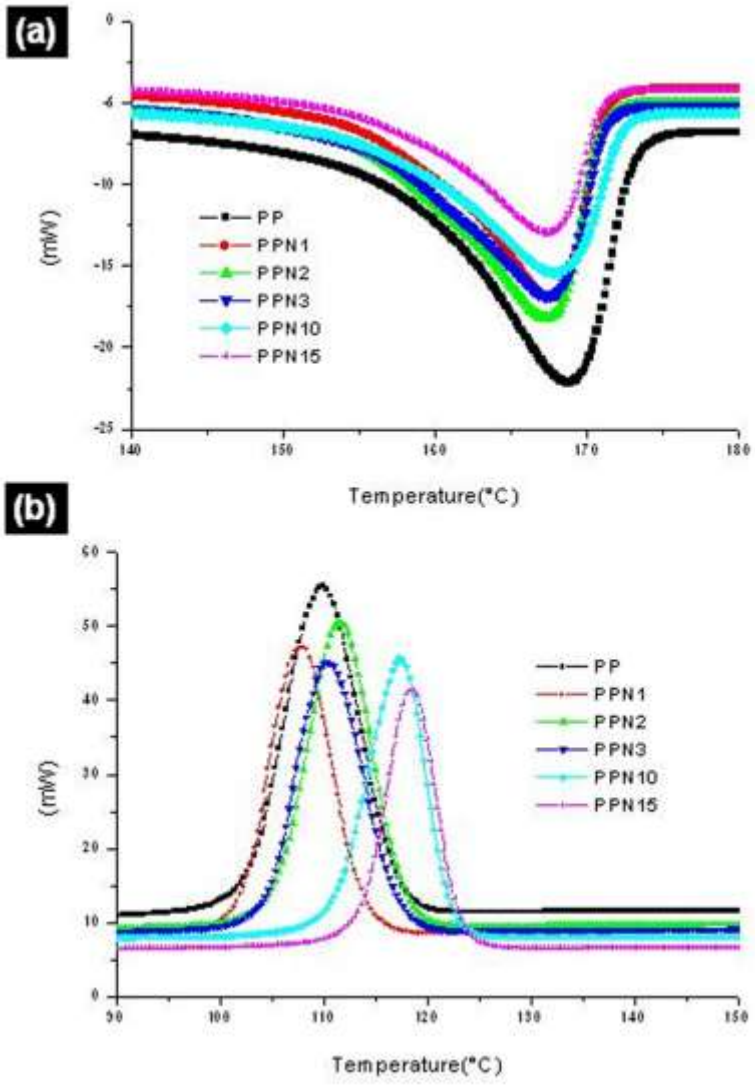

Figure 4.4. 5. DSC scans of different samples in (a) heating cycle, (b) cooling segment.

Tensile properties are summarized in Table 4.4.3 and Figure 4.4.8. As expected the sample with clay showed higher peak stress and higher modulus due to reinforcing effect of high aspect ratio Closite Na^+ additives.

Only modulus showed significant improvement. From the statistical analysis results (included in section 5), it is evident that differences in tensile stress and strain values are not significant. Slight improvement in mechanical properties at lower weight percentage of clay additives is due to good dispersion of high aspect ratio clay platelets in the matrix. Since the individual platelets are well dispersed, there is a greater area of interaction between the filler and the matrix. As the percentage increases beyond 5 wt %, extent of agglomeration increases. During tensile testing, there is greater chance of de-bonding between the stacks and matrix, which results in reduced elongation to break.

The dynamic mechanical spectra as a function of temperature and wt. % nanoclay additives are included in Figure 4.4.9 and 4.4.10. McCrum and colleagues have shown that PP exhibits (T_g) at 10°C [76, 243]. Values of (E') and T_g at different temperatures for different samples are included in Table 4.4.4 and 4.4.5. The results clearly show a remarkable increase in stiffness and decrease in tan δ values for PP-nanoclay concentrates. The E" scans (Figure 4.4.9-b) for nanoclay concentrates display a slight increase in rubbery plateau, which is due to reinforcement effect. At temperature close to room temperature range of 30°C, the values of E′ of PP-clay concentrates are 4-10 wt. % higher than that of PP. This enhancement in the storage modulus above T_g is due to the possible three dimensional network of interconnected high aspect ratio clay platelets in the matrix[27].

T_g (β-relaxation) decreases slightly for all the nanocomposite samples, which is due to the plasticizing effect of nanoclay stacks. Earlier studies in case of nylon 11/organoclay nanocomposites report about 12 °C decrease in T_g for 8 wt % organoclay additive loading [244]. The values of T_g in Table 4.20 are derived from E″ and tan δ scans carried out at 1Hz are slightly lower. At 10 Hz the storage modulus E″ and tan δ scans revealed well-defined peaks for T_g. Control PP has T_g of 13°C and the nanoclay incorporated concentrates have T_g in range of 10 to 11 °C.

Activation energy for the glass transition temperature was calculated as per method discussed in chapter II. Results of activation energy of glass transition (T_g) for control and nanocomposite samples are shown in Table 4.4.6. Activation energy observed is slightly lower for nanocomposite samples.

Notched impact strength for samples with different percentage of clay are shown in Figure 4.4.11. Results show significant increase in breaking energy for PPN1 and PPN2. However, at higher wt%, the impact strength showed decreasing trend. Improvement in impact strength at lower weight percentage of nanoclay has been reported before[227, 245]. However at higher weight percentage, reason for drop in impact strength is not yet addressed. One of the objective of this research was to investigate and understand change in microstructure, which drives such change.

Failure mode of injection-molded composites in tensile and impact strength tests was investigated. SEM micrographs revealed brittle fracture in case nanoclay reinforced samples. SEM micrographs of tensile failed surfaces at failure spot are summarized in Figure 4.4.12 (A)-(E). Failure mechanics in case of impact force is included in Figure 4.4.13 (A)-(D).

The control PP (Figure 4.4.12-A) and 4.4.13-A) clearly shows the flatter fracture features along with river-like marks typical of relatively fast fracture. Control PP also shows micro-voids and sharp edge structure at the crack surface. The PPN1 (Figure 4.4.12-B), 4.4.13-B) shows slightly widespread voids and sharp fibrous edge structure.

The PPN1 also indicate undulations, rough terrains and white plastic deformations spots in fracture surface. Such features are typical of relatively slow fracture propagation and hence larger energy absorption. Hence the PPN1 is expected to provide better fracture toughness (energy absorption) compared to control PP. With increase in clay wt % the failure mode shifted from ductile pull off to brittle failure (Figure 4.4.12-C) and 4.4.13-E). Sample PPN3 with 5% clay (Figure 4.4.12-D) revealed pull off of the fibrils at crack surface. With further increase in clay weight percentage, as in the case of PPN10, particles and micro voids were observed in the failure structure (Figure 4.4.12).

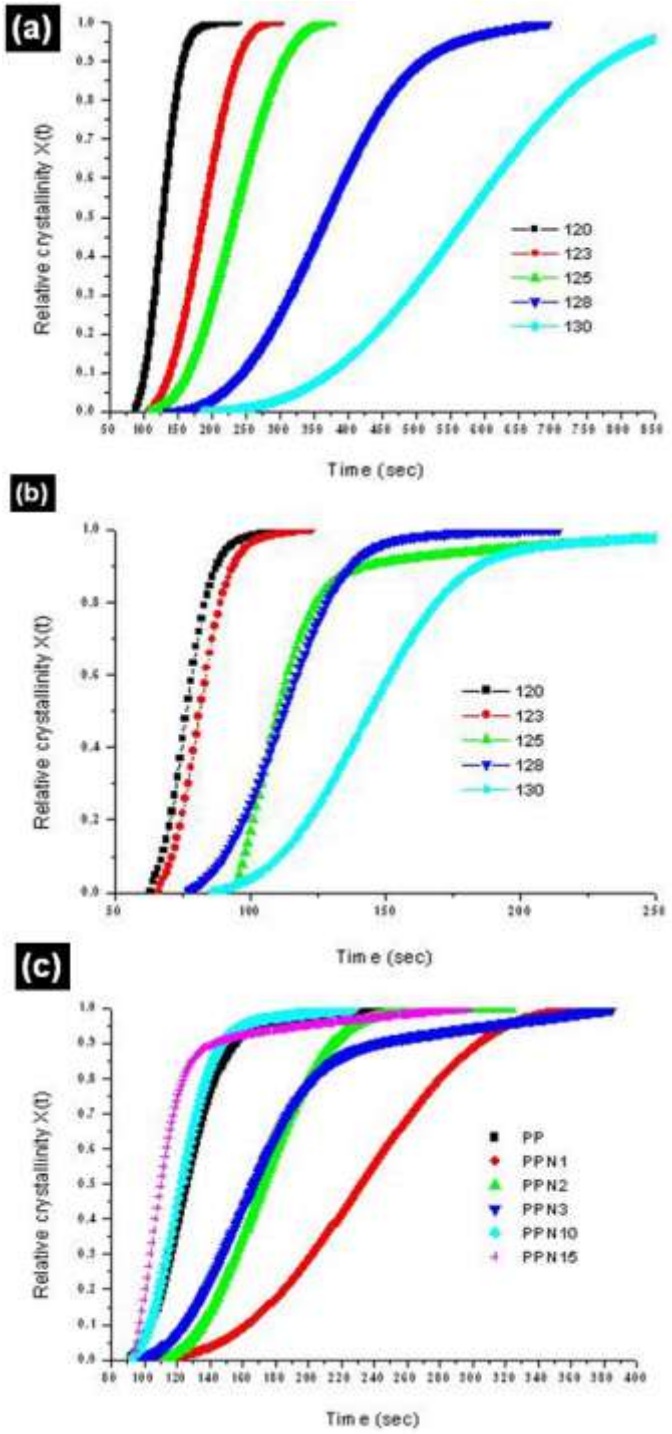

Figure 4.4. 6. DSC isothermal crystallization of (a) effect of temperature on crystallization kinetics of control PP, (b) effect of temperature on crystallization kinetics of PPN15 and (c) relative crystallinity versus time for different polypropylene (PP) concentrates at 125°C measured using DSC.

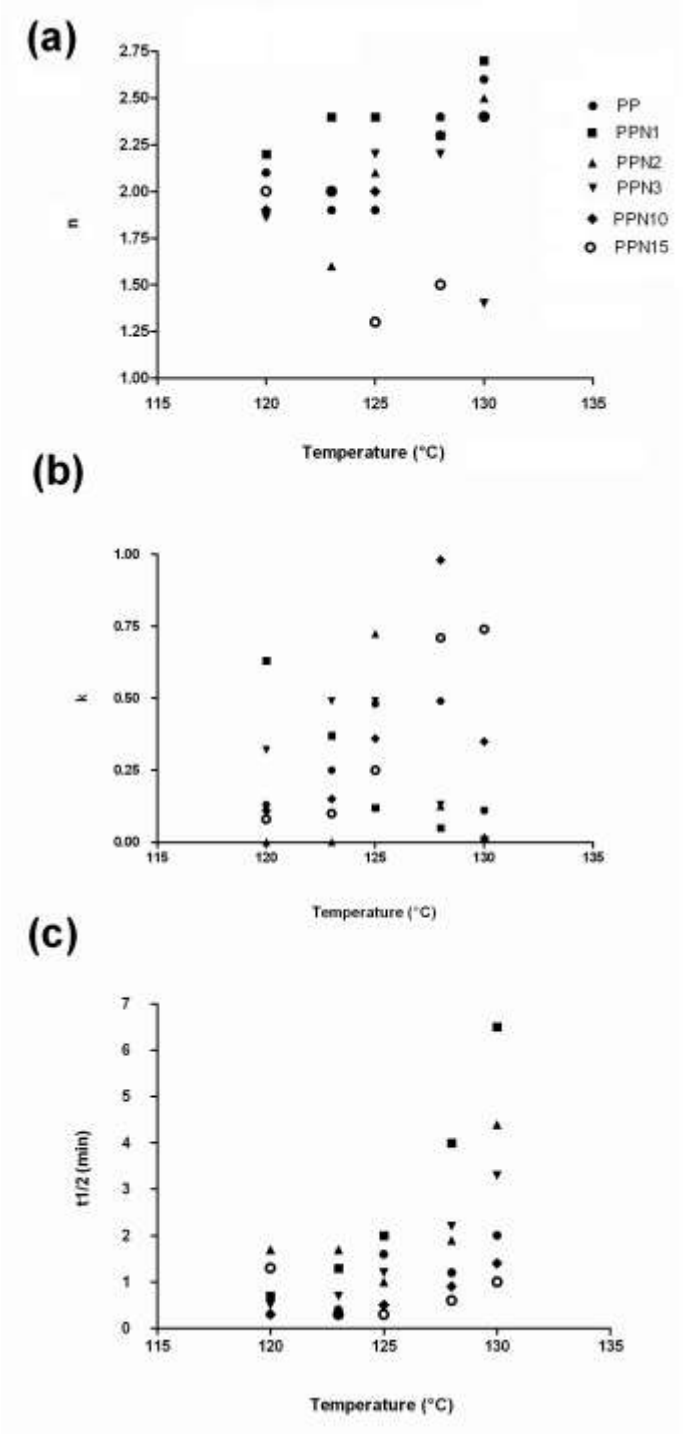

Figure 4.4. 7. Crystallization parameters (a) Avrami exponent “n”, (b) Avrami rate constant “K”, and (c) half time of crystallization vs. temperature.

Table 4.4. 3. Tensile properties of injection molded samples.

Sample	Additive Wt. %	Modulus (Mpa)	Tensile stress (Mpa)	Tensile strain (mm/mm)	Extension (mm)
PP	0	1255	21	0.33	5
PPN1	1	1267	22	0.17	7
PPN2	2	1310	21	0.19	4
PPN3	5	1581	24	0.12	4
PPN10	10	1893	15	0.12	4
PPN15	10	2090	20	0.07	3

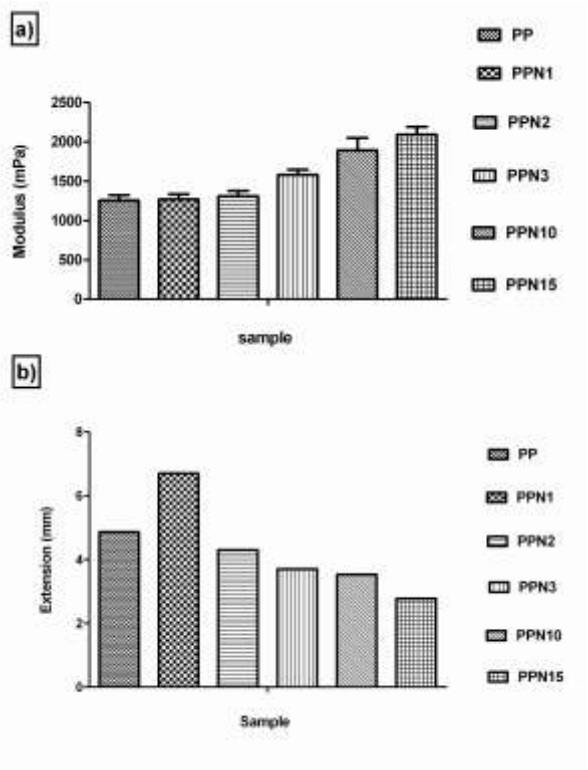

Figure 4.4. 8. Tensile modulus and strain of injection molded samples with different clay content.

Table 4.4. 4. Dynamic storage modulus (E') at different temperature and glass transition temperature for PP concentrates at 1Hz.

		Storage modulus E' (MPa)		
	t_g (°C)	-40(°C)	30(°C)	130(°C)
PP	8	3944	1590	176
PPN1	7	3960	1488	163
PPN2	9	4234	1654	173
PPN3	9	4408	1725	178
PPN10	7	4120	1765	220
PPN15	7	4122	1731	247

Table 4.4. 5. Dynamic storage modulus (E') at different temperature and glass transition temperature for PP concentrates at 10Hz.

		Storage modulus E' (MPa)		
	t_g (°C)	-40(°C)	30(°C)	130(°C)
PP	13	4050	1677	208
PPN1	11	4067	1697	193
PPN2	12	4350	1815	185
PPN3	11	3990	1619	188
PPN10	11	4242	1982	259
PPN15	10	4245	1965	289

Table 4.4. 6. Activation energy for Tg of different samples.

Sample	Activation energy ($kJ\ mol^{-1}$)
PP	549
PPN1	477
PPN2	508
PPN3	480
PPN10	381
PPN15	480

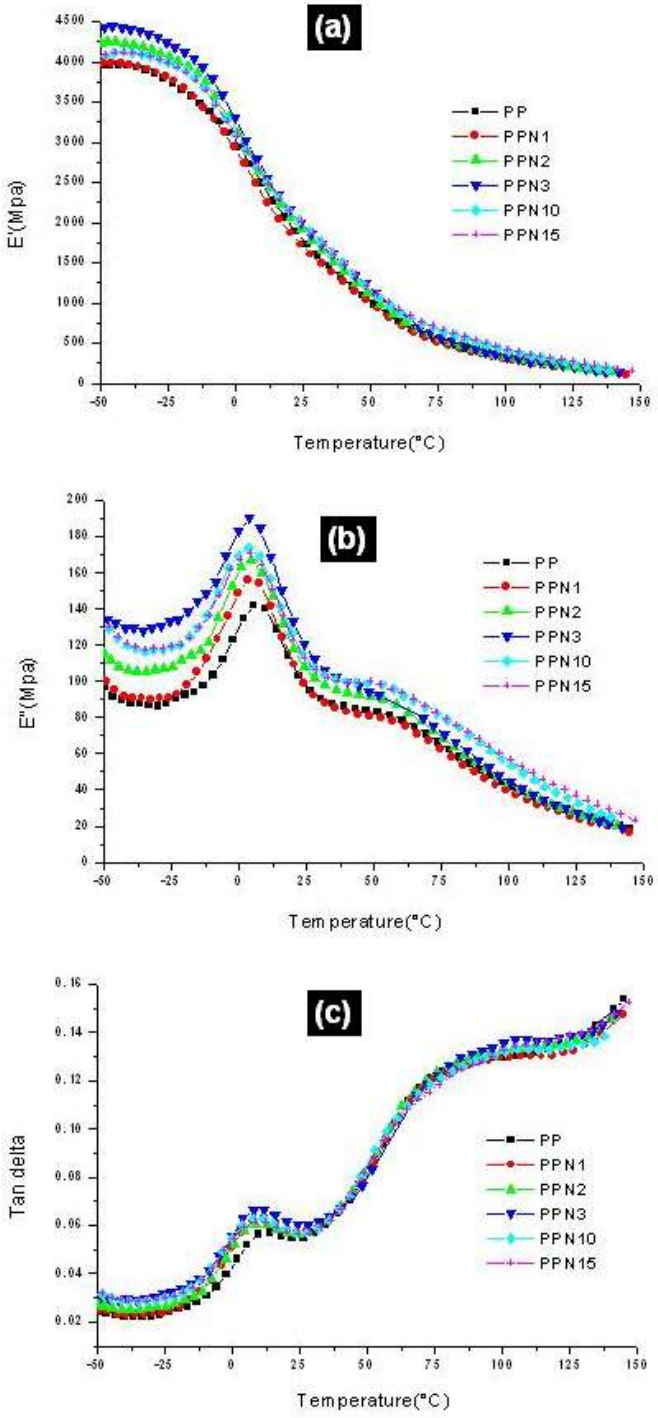

Figure 4.4. 9. DMA spectra (a) storage modulus E', (b) loss modulus, E'' (c) tan delta as function of temperature for different PP concentrates at frequency of 1 Hz.

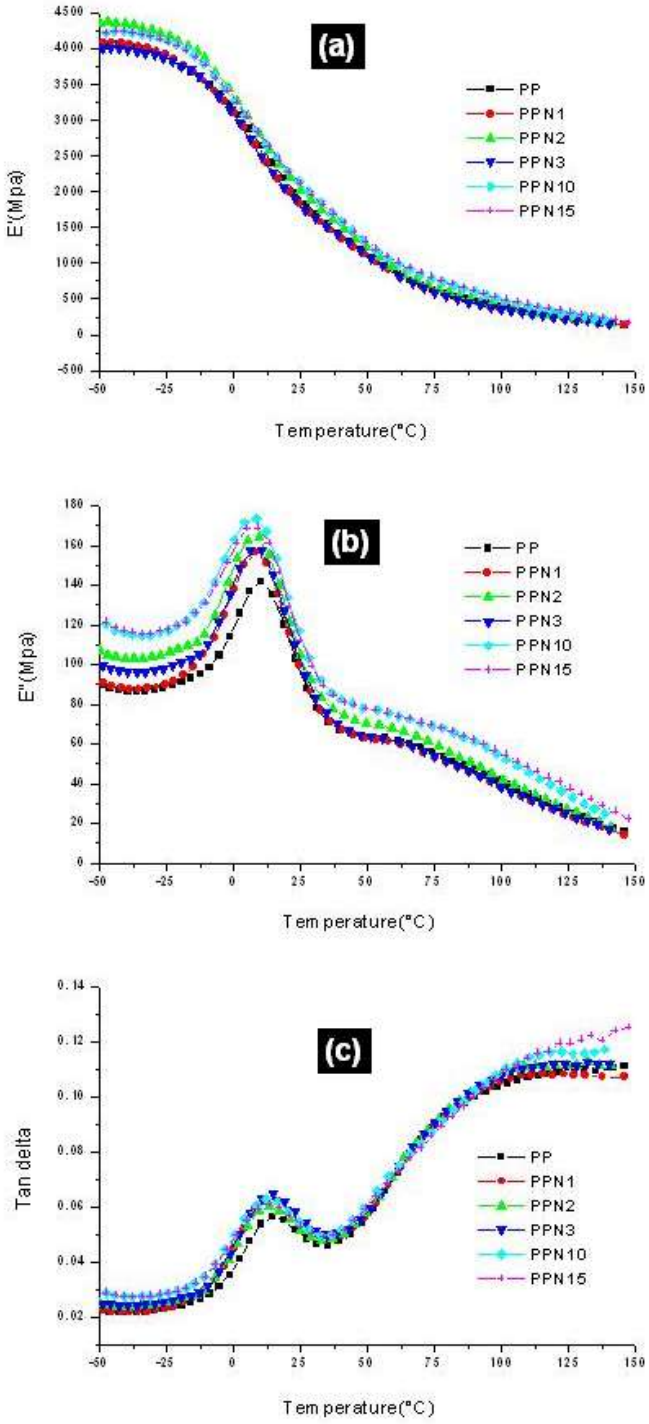

Figure 4.4. 10. DMA spectra (a) storage modulus E', (b) loss modulus, E" (c) tan delta as function of temperature for different PP concentrates at frequency of 10 Hz.

SEM image revealed presence of 20-50μ size tactoids at failure spot (as shown in Figure 4.4.12-(E). The EDS analysis of these spots revealed presence of high concentrates of clay in them (as shown in Figure 4.4.12-(F). These large agglomerates also influence the failure mechanism as shown in Figure 4.4.14. For such samples the failure surface revealed decreased sharp edges and increase in fine particulate at crack surface which indicates less matrix available for bridging cracks[246].

Polarized light micrographs show well-developed spherulites with maximum attainable diameter of about 400 to 450 μm for control polypropylene. Spherulites in case of nanoclay exhibit negative birefringence. The maximum attainable diameter D_m and number of spherulites per unit area are summarized in Table 4.4.7, Figure 4.4.15 (a) and (b). Data shows that the overall crystallization rate is high for PP concentrates with nanoclay. It is clearly seen in Figure 4.4.15-(a), as the spherulites in case of control PP are larger than concentrates with nanoclay additives. The number of spherulites per area increases for PP with additives.

Also, C.V of D_m (maximum diameter) are very high for PPN10 which indicates broader distribution of unit size. Incorporation of nanoclay additive significantly changes the microstructure. These concentrates were crystallized in static condition. In injection molding, same concentrate crystallizes under shear. At higher concentration of nanoclay, nucleation density (N) is very high for PP concentrate as shown in Table 4.4.7.

To understand the crystallization mechanism for different concentrates, the spherulite analysis was carried out at 125 and 135°C. The polarized optical micrograph image of molten phase of each concentrates is shown in Figure 4.4.17. PP and PPN1 showed homogenous featureless melt. Whereas, appearance of small features was observed in case of PPN2 and PPN3, micron size agglomerates were observed in case of PPN10 and PPN15. Sequence of photographs at 300, 600 and 900 seconds for the different concentrates at 125°C is shown in Figure 4.4.18. Control has a large number of spherulites. But the concentrates with 1, 2 and 5 wt % additives have well-developed spherulites.

Micrographs of PPN1, PPN2, and PPN3 reveal slower growth and less impingement compared to control PP. In case of PPN10 and PPN15, complete area of the micrographs is full of fine spherulites. At higher add on level, the nucleation dominates the slow diffusion of chains and

results in slow growth rate. These results are in complete agreement with the isothermal crystallization kinetics results at 125°C, shown in Figure 4.4.6(c). The delayed sigmoid shape for PPN1, PPN2 and PPN3 compared to control PP are due to hindrance to polymer chain diffusion. Sequence of photographs at 300, 600 and 900 seconds for the different concentrates at 135°C is shown in Figure 4.4.19. The crystallization kinetics studies did not show any crystallinity at this temperature except for PPN15. The results confirm presence of significant nucleation sites at high temperature for samples with clay additives.

Interspherulite region and exclusion of clay platelets at spherulite boundaries for PP, PPN1 and PPN3 (PP concentrate with 1, 2 and 5 wt% clay) was discussed in SB web section. SEM micrographs of interspherulite region and EDS scan of PPN10 are shown in Figure 4.4.20. With the increase in clay weight %, higher segregation and hence reinforcement in interspherulitic region was observed. The area of interspherulitic region was 377 μm^2 for control PP, 580 μm^2 for PPN1 and 743 μm^2 for PPN10. This segregation at the interspherulitic region is due to the exclusion of clay platelets from the growing crystal.

As shown in Figure 4.4.21 (a), at higher wt% add on level, two different spherulites conform in to a single spherulite. Also in between large spherulites, there are smaller spherulites (4.4.21-b). These smaller spherulites are result of crystallization of more difficultly crystallizable compounds and crystallization of impurities, which are rejected from growing fibrils during spherulite development[127].

Table 4.4. 7. Maximum attainable diameter, nucleation density and average number of spherulites per 809 µm^2 area.

Sample	maximum diameter of spherulite (µm)	N (µm^-3)	Average no of spherulites in 809 µm^2
PP	441	2E-07	6
PPN1	236	1E-06	19
PPN2	216	2E-06	32
PPN3	179	3E-06	38
PPN10	111	1E-05	87
PPN15	67	6E-05	110

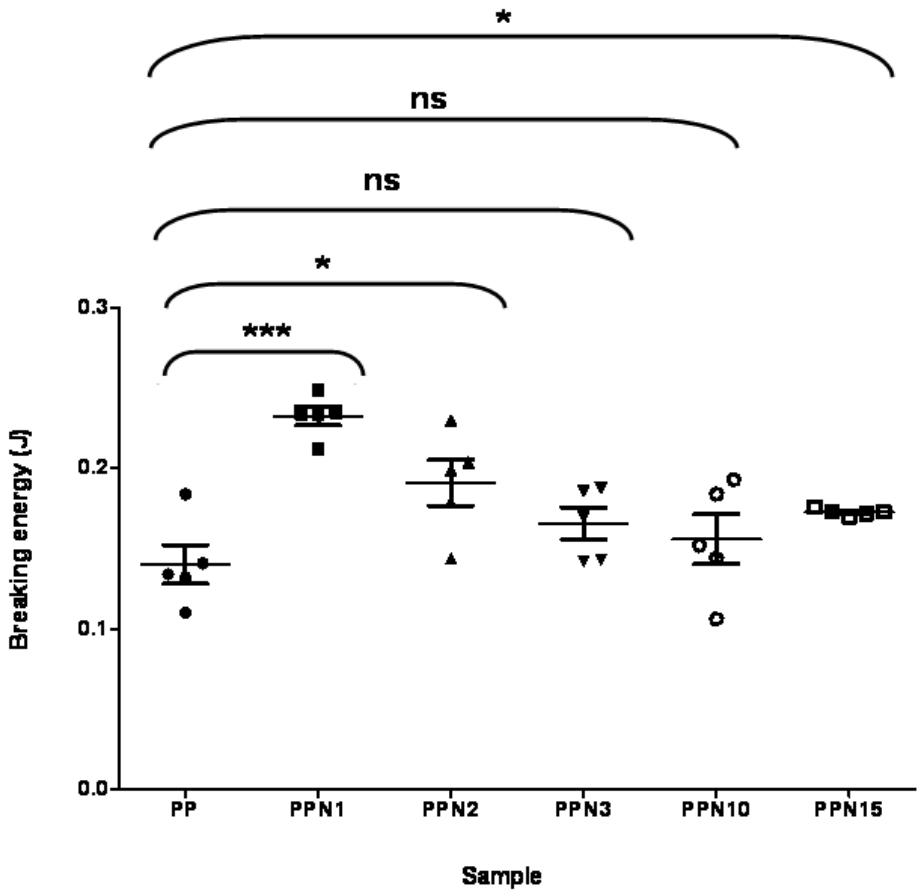

Figure 4.4. 11. Breaking energy observed from notched impact strength of different injection molded PP nanocomposites.

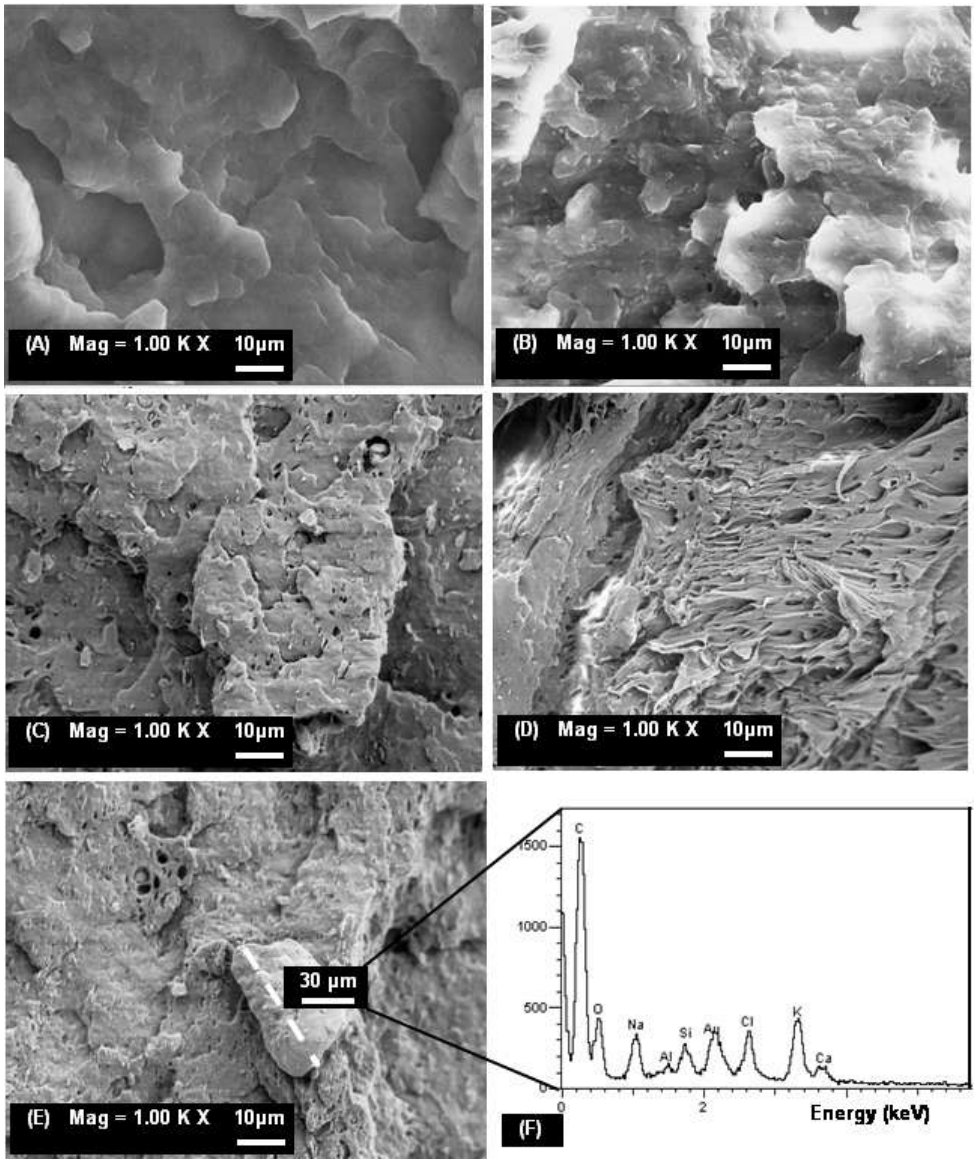

Figure 4.4. 12. SEM micrograph of tensile failed injection molded (A) Control PP- 0 wt %, (B) PPN1-1wt %, (C) PPN2- 2 wt %, (D) PPN3- 5 wt % clay, (E) PPN10- 10 wt %, and (F) EDS of particle at tensile failure spot of PPN5.

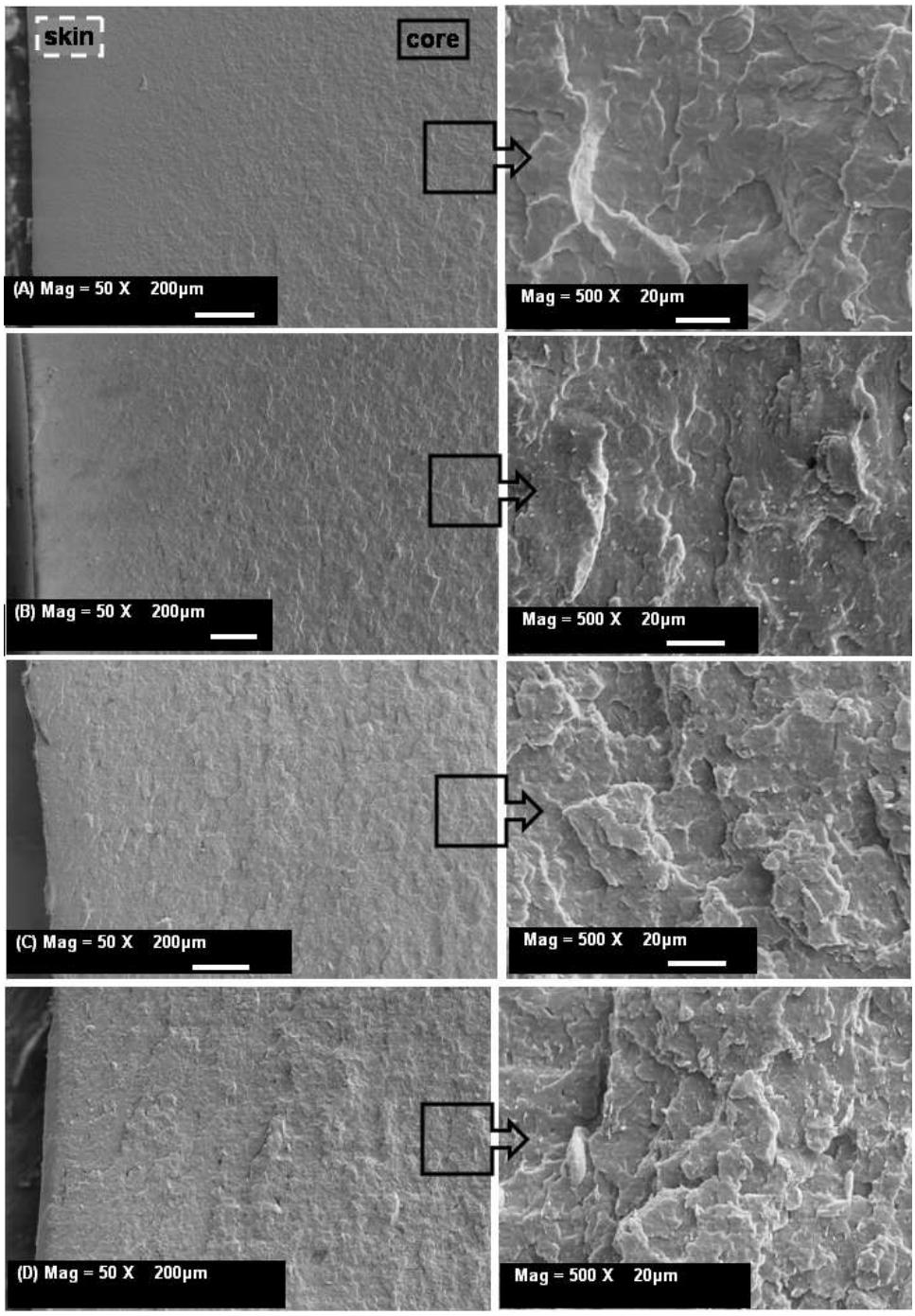

Figure 4.4. 13. SEM micrograph of impact failed injection molded (A) Control PP- 0 wt %, (B) PPN1-1wt %, (C) PPN10- 10 wt % clay, (D) PPN15- 15 wt % clay.

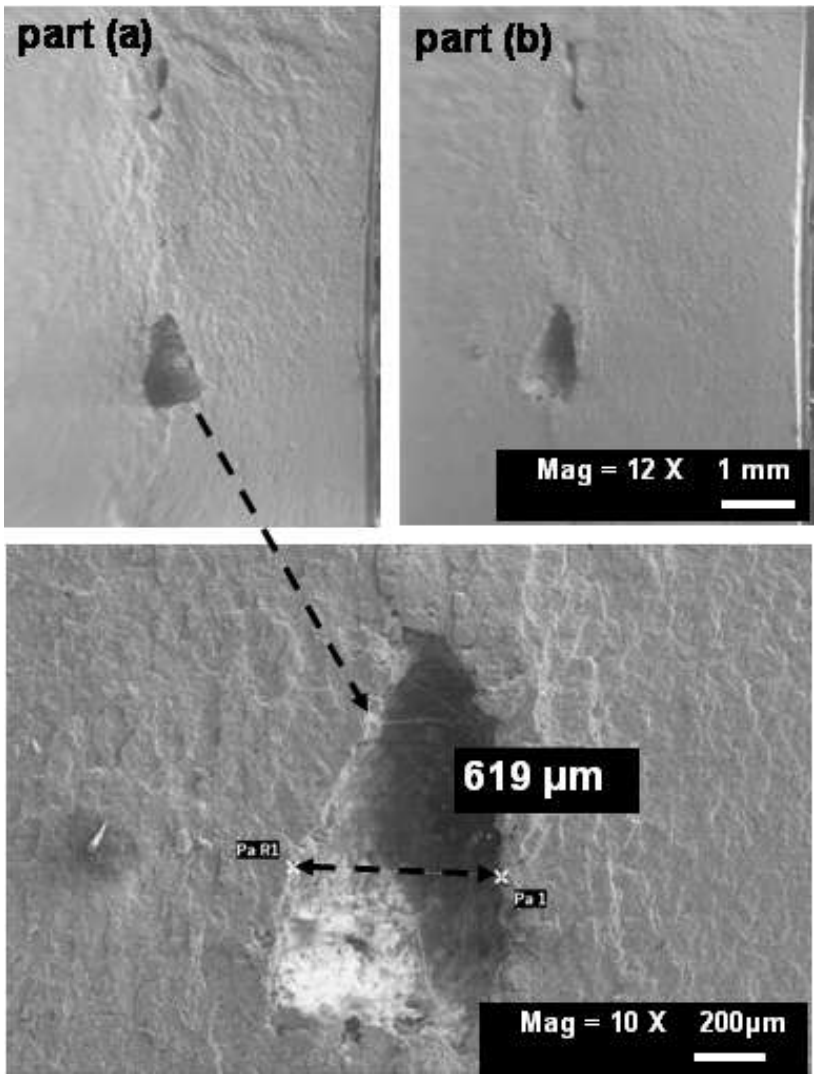

Figure 4.4. 14. Impact failed cross section of PPN10.

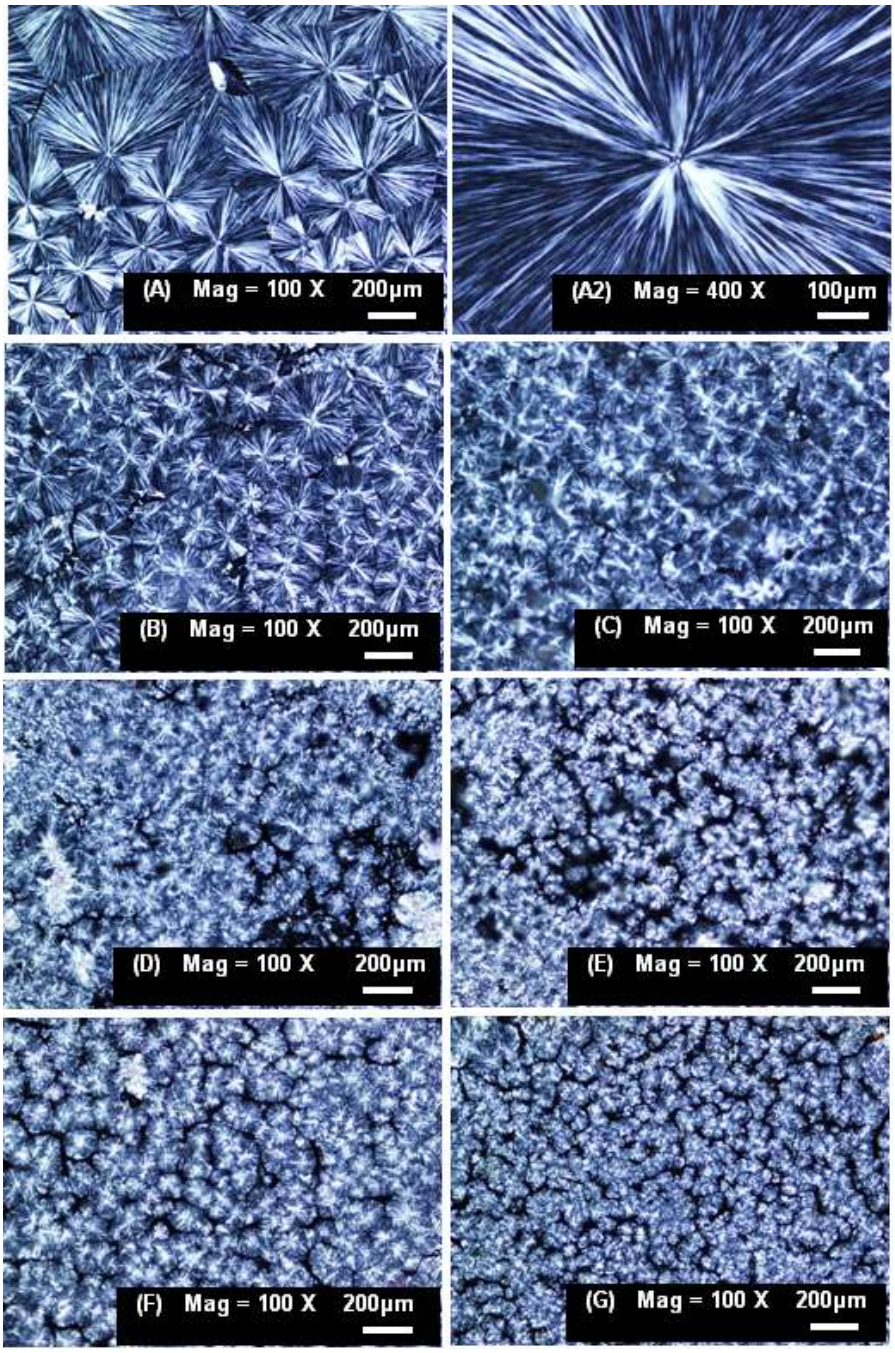

Figure 4.4. 15. Polarized light micrographs of (A) control PP, (B) PPN1-1wt %, (C) PPN2- 2 wt %, (D) PPN3- 5 wt % in mPP, (E) PPN5- 5 wt %, and (F) PPN5- 10 wt %, and (G) PPN5- 15 wt % nanoclay additive.

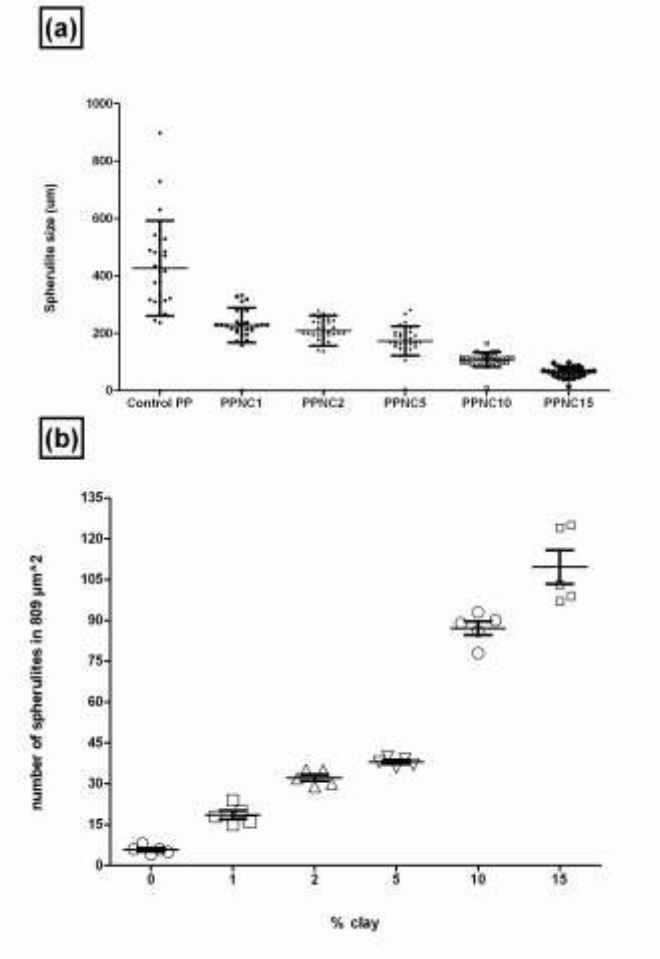

Figure 4.4. 16. (a) Average diameter of spherulite in different PP samples (b) number of spherulite in area.

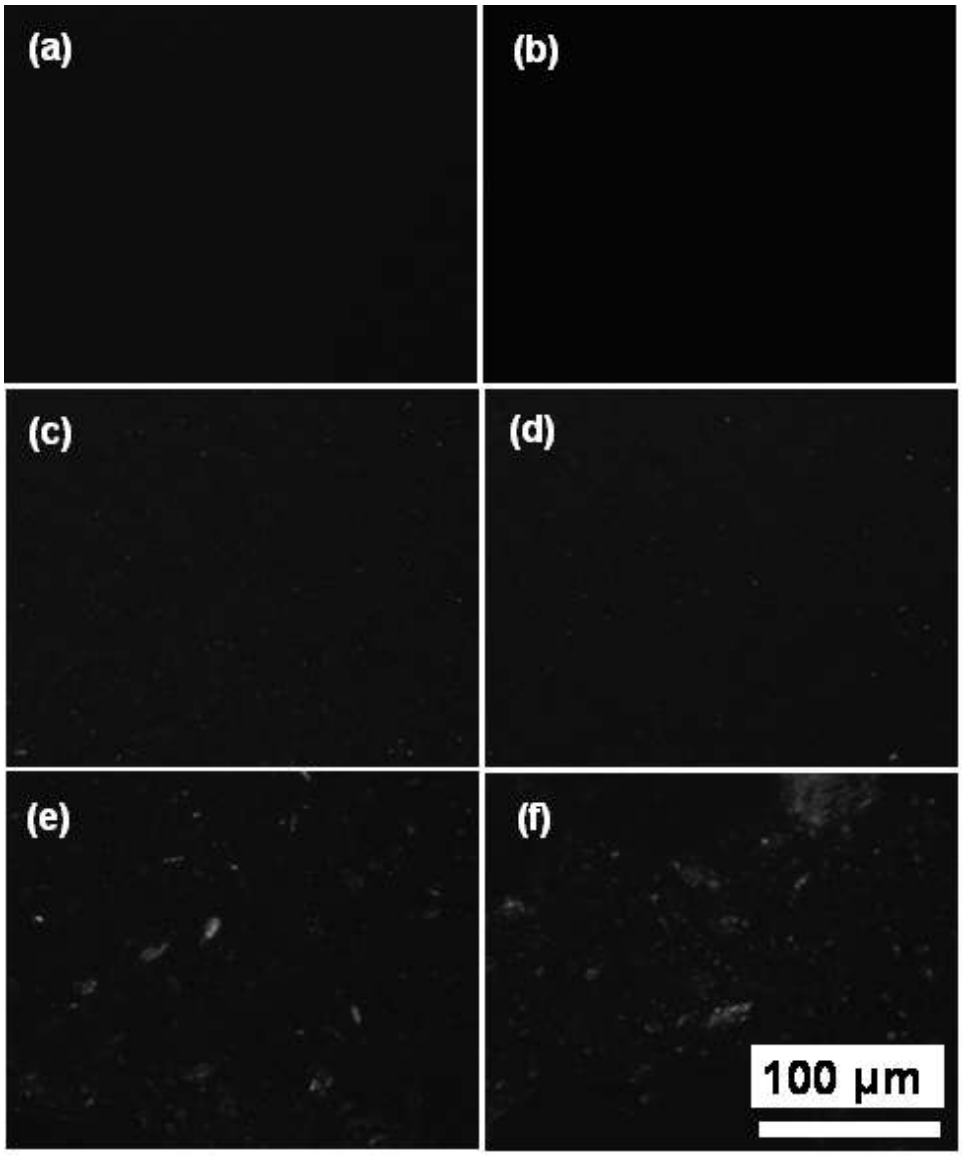

Figure 4.4. 17. Photographs of concentrates at (a) PP, (b) PPN1, (c) PPN2, (d) PPN3, (e) PPN10, (f) PPN15 250°C, bright areas indicate the existence of clay tactoids, and the dark areas indicate the molten PP matrix.

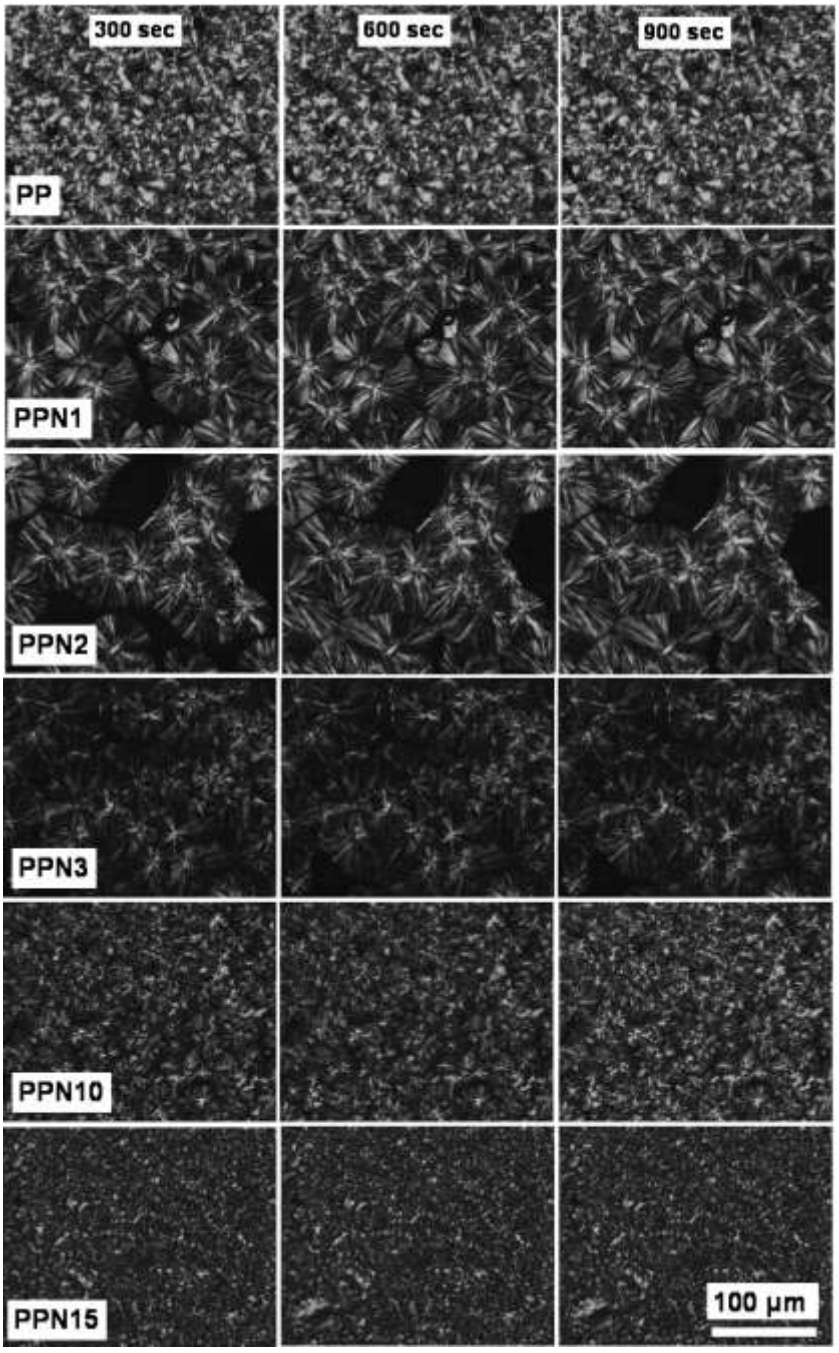

Figure 4.4. 18. Sequence of photographs of different concentrates at 125°C at 300, 600 and 900 seconds.

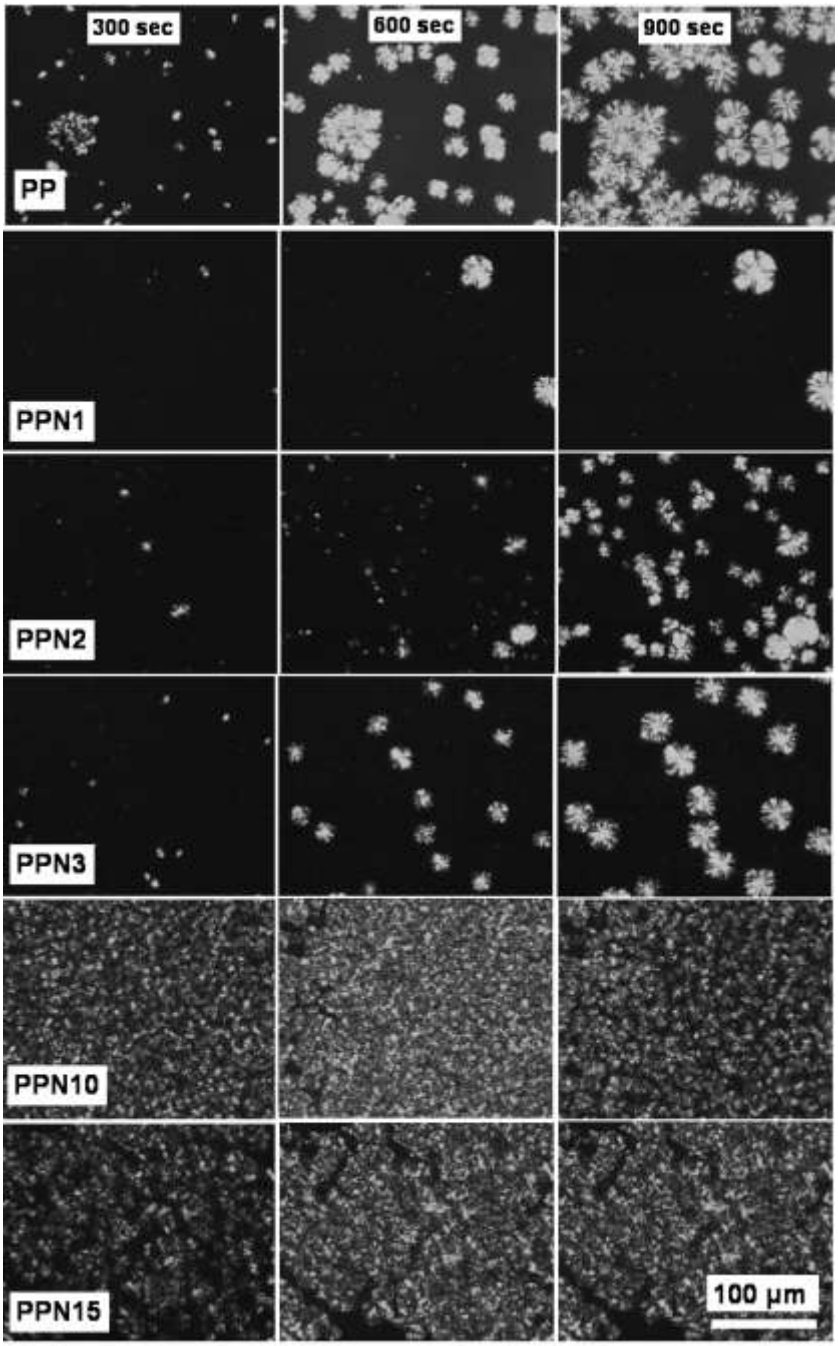

Figure 4.4. 19. Sequence of photographs of different concentrates at 135°C at 300, 600 and 900 seconds.

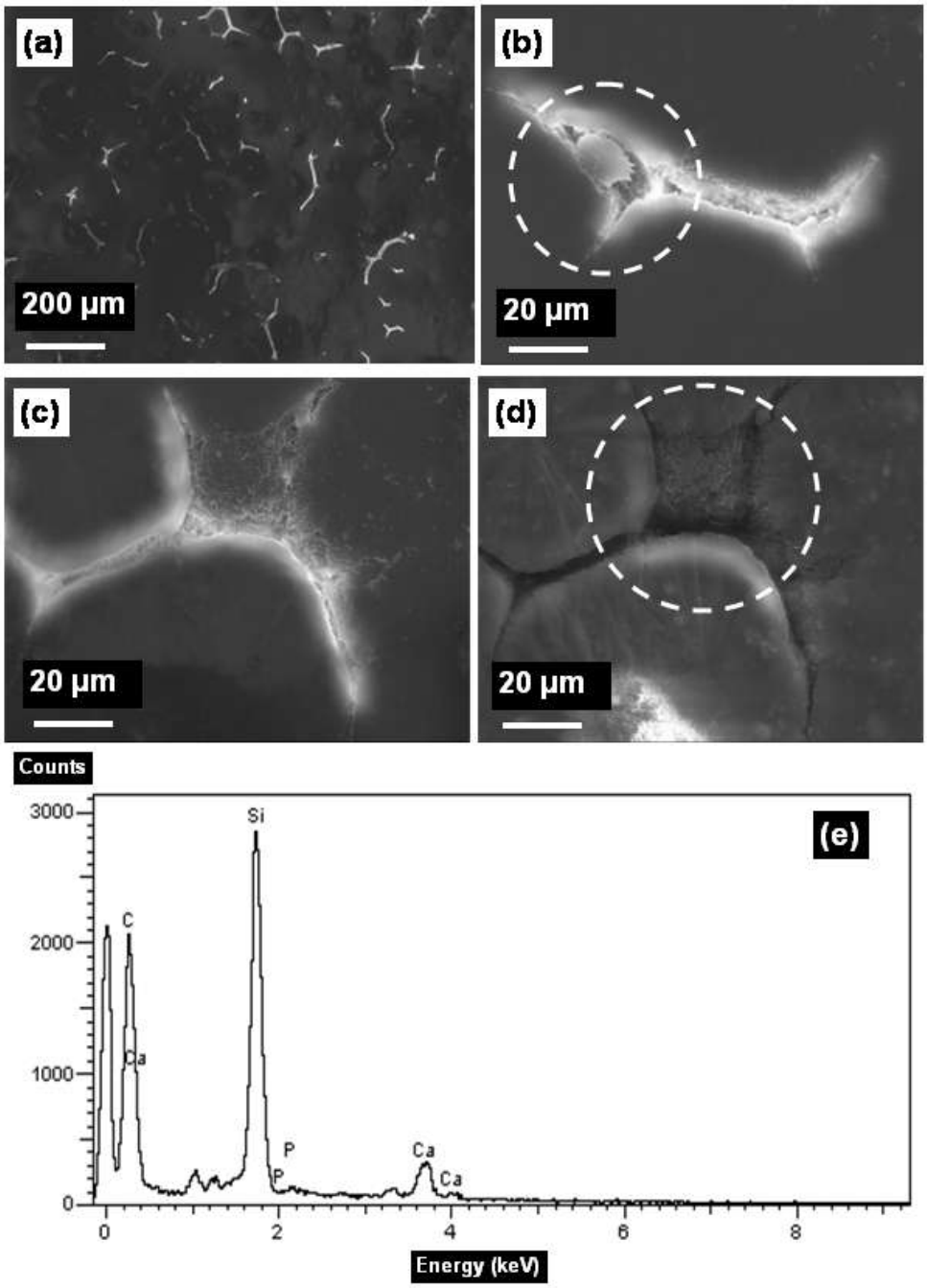

Figure 4.4. 20. SEM micrograph of interspherulitic region (a) lower magnification, (b) crystallized species in the interspherulitic region (c) agglomerates in the interspherulitic region, (d) agglomerates in the interspherulitic region (e) EDS of interspherulitic region of PPN10.

Spherulite growth velocity decreases with increase in concentration of the non-crystallizing species[157, 247-250]. When the molecular mobility is small, the molecular movements will be local and gradient of density can be formed. At the crystal/melt interface, if solute diffusion is faster, the interface becomes geometrically unstable. The instantaneous solute concentration near any protrusion from interface is lower than the rest of the interface. The growth velocity is greater at protrusion than spherical interface because concentration of crystallizable species is higher at that point [157].

Schematic development of possible mechanism of spherulite nucleation is shown in Figure 4.4.21(c, d, e and f). Development starts from rod like or plate like units between the clay stacks. Geometric form of the growth is different and changes with time[127]. Maximum attainable diameter after time x, depends on the amount of material d_{ws} which have not been converted to $dw_{s;}$

$$\frac{dw_s}{dw_{S^1}} = 1 - \frac{W_s}{W_o} \quad \text{Equation 70}$$

onsidering the presence of micron size agglomerate in molten state at 250°C (as shown in Figure 4.4.17), mechanism of clay exclusion from the polypropylene chains can be compared to zone refining [251].

During the solidification, the clay platelets from the agglomerated mass, which are not included in spherulite, are excluded out of crystal boundary. Maiti et. al. carefully studied the influence of crystallization temperature on the segregation of dispersed clay platelets in the interspherulitic region. They reported higher density of clay platelets at spherulite boundary at higher crystallization temperature[9]. The nucleation may also initiate between clay stacks. Exact mechanism of exclusion and crystallization mechanism in between clay stacks need to be studied further.

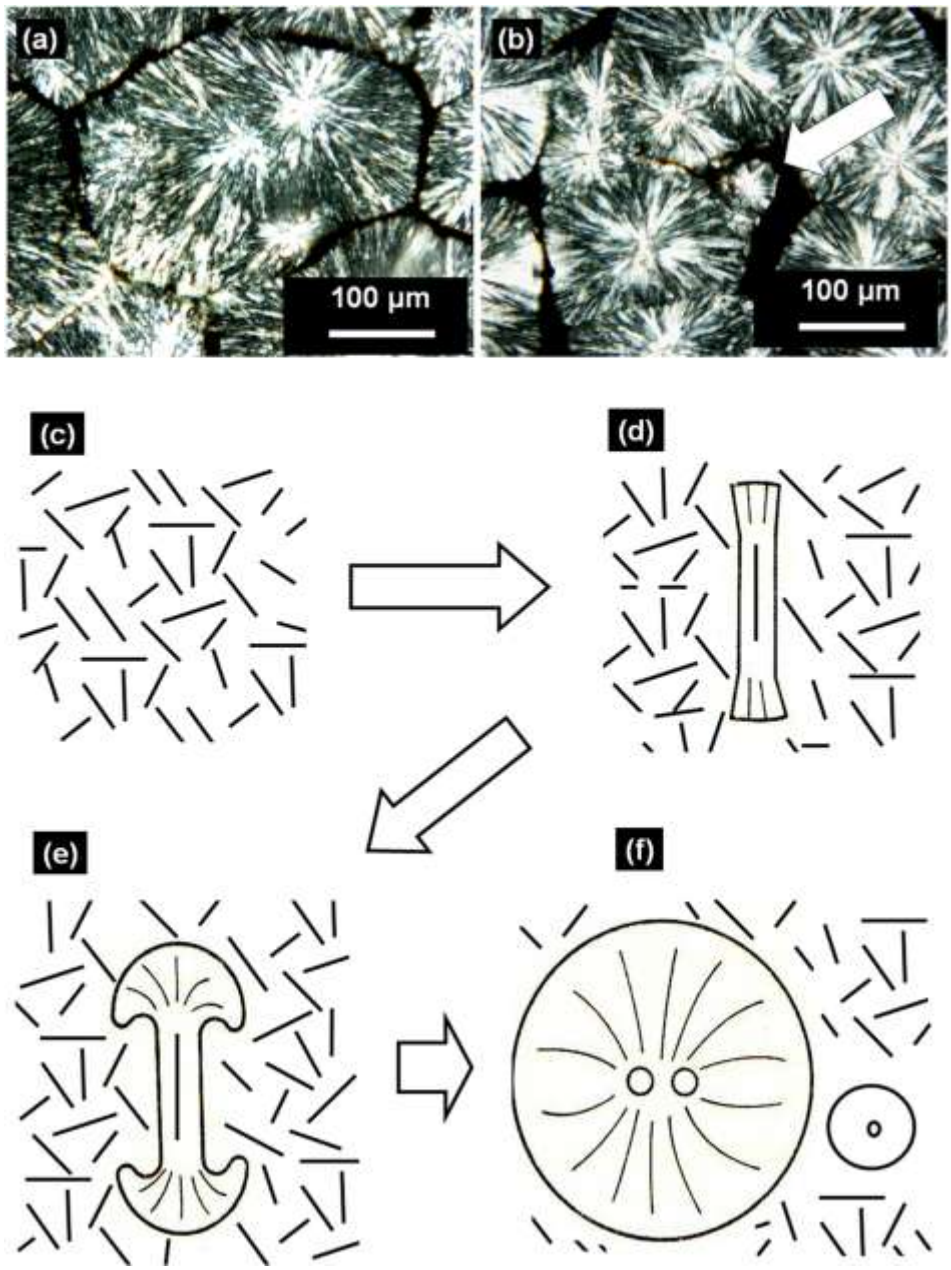

Figure 4.4. 21. (a) Polarized light micrographs of PPN10 (b) small size spherulite in between large spherulites, (c) clay platelets in molten polymer matrix, (d) on cooling, spherulite nucleation between clay stacks, (e) growth of large spherulite, (f) formation of smaller spherulites as result polymer chain deficiency and also crystallization of more difficultly crystallizable compounds.

The slight increase in trend observed for mechanical properties is due to the reinforcing effect of additive rather than increase in crystallinity [39, 252]. Standard deviation of weight percentage remained from TGA analysis was high for sample with 15 wt. % clay additive compared to rest of the concentrates. This is due to increased tendency for agglomeration due to mutual electrostatic attraction between the presence of higher amount of additives.

Activation energy of glass transition temperature for nanocomposites was less than that of control PP. The glass transition, T_g is a property of amorphous segment. The glass transition of isotactic component is higher than that of the atactic component[253]. With increase in percentage of clay, the segregation increases[9,254] which is evident from the SEM micrograph shown in Figures 4.4.20. With exclusion of non polymer species from the crystalline segment, composition of amorphous segment changes and the peak corresponding to T_g falls[255,256].

With increasing crystallization temperature (T_c) the crystallization shifts to longer time and crystallization peak becomes flatter. Observed results of increase in the crystallization time, decrease in crystallization rate at higher crystallization temperature (Tc), are in complete agreement with the kinetic theory of crystallization. Increase in the crystallization temperature will result in a decrease in supercooling (ΔT) and lower the growth rate [257].

According to the definition of the Avrami's exponent, when the value of "n" is around of 2.0, the nucleation process is instantaneous and the growth of crystals is probably two-dimensional under the experimental conditions [143]. Avrami's exponent "n" showed decreasing trend with increase in crystallization temperature (T_c) as shown in Figure 4.65. This results from the fact that, the number of athermal nuclei is found to increase tremendously with decreasing crystallization temperature causing the nucleation mechanism to be more instantaneous in time, which, in turn, decreases the values of Avrami exponent "n" [125, 258, 259].

The behavior observed in the curves in Figure 4.4.6 (c) is due to the increase in nucleation density due to presence of high wt. % clay. Increase in nucleation density causes decrease in spherulite size (which is also evident from width at half height of crystallization peak in Figure 4.4.5). Secondary crystallization involves collision between spherulites and growth. Large number of smaller spherulites in unit area reduces the time required to fill the interstices. Results are in complete agreement with the spherulite micrograph results obtained from polarized optical

micrograph shown in Figure 4.4.16. Large number of smaller spherulites is reconfirmed by POM images. Similar behavior is reported by other researchers, such as Albano et. al. [259] for PP/talc blends, Patel and Spruiell in case of nylon 6,[260] and Krolikowski [140] in case of PP with different additives[259].

Significant increase in notched impact strength was observed for PPN1 and PPN2. However, with further increase in additive wt%, the impact strength showed decreasing trend. Failure mode shifts from ductile to brittle. The brittle failure with increase in weight percentage of clay is due to limitation imposed by excessive clay agglomerates to intrinsic polymer chain deformation and also discontinuity in the network. These differences in failure mode can be explained by the change in spherulitic microstructure observed from POM results.

Crystalline microstructure has pronounced influence on the craze formation and fracture behavior of semicrystalline polymers [231]. Craze and micro cracks during failure run along spherulitic boundaries as well as along the radial trans-spherulitic pathways lying perpendicular to applied load as both are considered as weaker spots of spherulitic structure[261,262]. During melt crystallization, additives, impurities, low molecular weight polymer and non-crystallizable chains are partly pushed away from growing spherulite fronts[9,254]. This process in the fully crystallized sample provides impurity-rich spherulite boundaries which are much weaker and more brittle than the highly crystalline and harder, interior zones of the spherulites[220, 231, 254]. With higher nanoclay additives and fine spherulite structure, amount of potential craze nucleation spots increases[9, 235-239]. So at higher wt%, the sample shows decrease in impact strength.

In case of polymer nanoclay composites PPN10 and PPN15, crazes formed in one of these regions have enough strength to cause further crazing in their neighborhood before they break down, and thus a dense craze bundle is formed in front of the crack which can absorb much energy before complete fracture. Similar structure property results were also observed for SB webs with more than 2 wt% additives. Property benefits could not be achieved beyond certain volume fraction because, reinforcing effect is minimized due to exclusion and agglomeration.

Having nanoclay additive cools the mold faster compared to control PP due to quenching effect[229]. Hence, PP-clay composite molds have lower crystallinity compared to control PP. Crystallinity wt % from DSC, Half time $t_{1/2,}$ and total time t_{max} for crystallization observed in this research are in complete agreement with these findings.

The property benefits are not realized from additives beyond 2 wt % clay additives. At higher wt % , even in the presence of compatibilizer it's difficult to evenly distribute or exfoliate the clay platelets in the matrix. The reinforcement in the amorphous region makes the molecular network more complete, restricts the motion of molecules, which significantly increases the modulus of composites.

CHAPTER V

5. Conclusions

Influence of different percentage of nanoclay and different dispersion agents on the microstructure, morphology and mechanical properties of nylon 6 and polypropylene nanocomposites products was investigated. Compared to polypropylene, slightly better dispersion of platelets was observed in nylon 6. Nylon 6 blown films and fibers could be processed with nanoclay additives. Different nanocomposite morphologies were observed for different matrix (nylon 6 and polypropylene) and process (film, fiber, nonwovens and injection molded composites).

Increase in clay level from 2 to 5 wt % did not bring any significant mechanical property benefits for nylon 6 blown films. Presence of nanoclay additive even at 0.25% caused significant nucleating effect. Higher wt % clay loading caused adverse effect on the film tensile, tear strength. Film elongation decreased with increase in additive wt %. In case of nylon 6 films, good dispersion and significant exfoliation was seen for samples with up to 2-wt % clay loading. Nanoindentation results showed increase in near surface hardness at nanolevel. This increase in modulus and hardness was observed for all levels of loading. However, such performance improvement is not translated to macro scale.

There is no significant difference or mechanical property benefits by incorporating Closite Na^+ nylon 6 blown films. The non-uniform dispersion of nanoclay additive in blown film showed significant influence on the nanoscale surface topology. Increase in the area of high surface energy clay platelets influences the wetting behavior of films. Increased wettability or decrease in contact angle was observed for sample with clay additives.

Nylon 6-clay nanocomposite fibers did not show any improvement in fiber mechanical properties. Fiber thermo mechanical properties were slightly different due presence of γ-crystalline forms and entrapment of polymer chains between platelets.

In case of polypropylene concentrates, TEM micrographs revealed intercalated and flocculated morphology for all the concentrates. Nanoclay additives could be incorporated in to spunbond

and melt blown nonwoven fabrics using the existing processing equipments. At higher wt% nanoclay additives lead to processing difficulties.

The morphology observed in the PP concentrates is preserved in spunbond fibers also. MD tensile strength showed slight decreasing trend and CD tear strength showed increasing trend. Fibers with as low as 1 % clay retain their morphology and integrity in bond point after thermal bonding. Incorporating the nanoclay additives can regulate SB web stiffness, however the difference in tensile and tear property benefits is not significant. WAXD and TEM micrographs showed good dispersion of additives in the MB webs. However, nanoclay additive did not result in property benefits in the case of polypropylene melt blown webs. Compared to control MB web, stiff, open and weak web structure was obtained for samples with clay additives.

Different crystallization mechanisms were observed at lower weight % (1-3 wt %) compared to higher wt% (10, 15 wt %) of nanoclay in PP. Half time of crystallization ($t_{1/2}$) and maximum time for crystallization (t_{max}) increased for sample with 1 to 5 wt % clay additives due to large number of nucleation sites. $t_{1/2}$ and t_{max} decreased for sample with 10 and 15 wt % clay additives. At the higher wt %, the growth rate overrides the slow diffusion rate.

As seen with films and fibers, in the case of injection molded PP samples also, 1 wt. % clay additive was enough to get modulus and mechanical property benefits. Significant improvement in breaking energy (BE) was observed for sample with 1-wt % nanoclay and at higher wt %, failure mode shifted from ductile to brittle.

Polarized light micrographs revealed increase in nucleation density and decrease in spherulite size for concentrates with nanoclay additives. In case of sample with higher weight percentage of nanoclay additives, segregation of additives was observed in the interspherulite region.

Overall, nanoclay affects processing to a limited extent at loadings up to 1%, and at higher loadings lead to processing difficulties. The property benefits observed are better till 1-2 wt% of clay and beyond that, the gain is minimal. The changes in crystallization behavior and developed morphology have an impact on the properties, and the morphological changes are different at lower (up to 2%) and higher (25%) Nanoclay loadings. Combination of WAXD & TEM techniques is useful in determining the intercalation/exfoliation of nanoclay in polymers.

However, the effects on physical properties are dependent on factors other than intercalation & exfoliation, especially an uniform dispersion in the matrix.

5.1 Recommendations for further work

- In case of spunbonding and melt blowing, there was no effort to optimize the processing conditions. It is with studying processing conditions as properties may improve with nanoclay additives.
- Effect of compatibilizers on the mechanical properties need to be studied further.
- Exact mechanism of crystallization between stacks and exclusion of the clay agglomerates need to be studied further.
- Influence on nanoclay and compatibilizers on the surface energy need to be explored further.

LIST OF REFERENCES

1. D. S. Mathur KK. J. Vinyl. Technol 1982**,** 4, 81.
2. Z. Bartczak.; A.S. Argon; R. E. Cohen; M. Weinberg. Polymer 1999**,** 40, 2347.
3. M. Wilbrink; A.S. Argon; R.E. Cohen; M. Weinberg. Polymer 2001**,** 42, 10155.
4. Q. Yuan.; C. Deshmane.; T. C. Pesacreta.; R. D. K. Misra. Materials Science and Engineering: A 2008**,** 480, (1-2), 181-188.
5. Yuan Q; Jiang W; An LJ; Li RKY; Jiang ZH. J. Appl. Polym. Sci. 2003**,** 89, 2102.
6. Yuan Q; Jiang W; Zhang HX; Yin JH; An LJ; L. RKY. J. Polym. Sci. Part B: Polym. Phys. 2001**,** 39, 1855.
7. F. Hussain; M. Hojjati; M. Okamoto; R. E. Gorga. Journal of Composite Materials 2006**,** 40, (17), 1511-1575.
8. B. K. G. Theng., In *The Chemistry of clay organic reactions*, Wiley: New York, 1974.
9. P. Maiti; P. H. Nam; M. Okamoto; N. Hasegawa; A. Usuki. Macromolecules 2002**,** 35, (6), 2042-2049.
10. E. Picard; A. Vermogen; J. F. Gérard; E. Espuche. Journal of Membrane Science 2007**,** 292, (1-2), 133-144.
11. R. A. Vaia; G. Price; P. N. Ruth; N. T. Hieu; and; L. Joseph. Applied Clay Science 1999**,** 15, (1-2), 67-92.
12. L. S. Loo; K. Gleason; And; K. K. Polymer 2004**,** 45, (17), 5933-5939.
13. R. J. Opalko. Evaluation of effects of nanofil nanoclays in the blending of polypropylene and polystyrene. Akron, 2008.
14. P. Persico; C. Carfagna, and ; P. Musto. Macromolecular Symposia 2006**,** 234, (1), 147-155.
15. X. Zhang; M. Yang; Y. Zhao; S. Zhang; X. Dong; X. Liu; D. Wang; D. Xu. Journal of Applied Polymer Science 2004**,** 92, (1), 552-558.
16. N. R. Savvas G. Hatzikiriakos., Edward B. Muliawan. Polymer Engineering & Science 2005**,** 45, (8), 1098-1107.
17. X. Zhang; M. Yang ; Y. Zhao ; S. Zhang ; X. Dong ; X. Liu; D. Wang; and; D. Xu. Journal of Applied Polymer Science 2004**,** 92, (1), 552-558.
18. A. G. Cairns-smith, In *Introducing clay in Clay minerals and origin of life*, Hartman, A. G. C.-s. a. H., Ed. Cambridge university press: Vol. 19, p 16.
19. G.W. Brindley; G. Brown, Crystal Structures of Clay Minerals and Their X-ray Identifications. Mineralogical Society: London, 1980; p 1-123.
20. D. M. Moore; R. C. Reynolds, X-ray Diffraction and the Identification and Analysis of Clay Analysis of Clay Minerals. Oxford University Press: Oxford 1997; p 104–120
21. S. C. Tjong. Materials Science and Engineering R 53, 73–197.
22. L. Douglas. MRS bulletin 2007**,** 32, 323-325.
23. D. Carroll, Clay Minerals: A Guide to Their X-ray Identification. The geological society of America, Inc: 1970.
24. A. G. Cairns-smith, Clay minerals and origin of life. 1986.
25. S. W. Brindly.; G. Brown, Crystal structure of clay minerals and their X-ray diffraction. London, 1980.
26. Commercial. http://www.nanocor.com/nanoclays.asp
27. M. Alexandre; P. Dubois. Materials Science and Engineering 2000**,** 28, 1-63.
28. P. Aranda.; R. E. Hitzky. Chem Mater 1992**,** 4, 1395-403.

29. D. J. Greenland. J Colloid Sci 1963**,** 18, 647-664.
30. P. Diwan; A. Bharadwaj. Pentagon press 2006**,** 1, (69).
31. G. Lagaly. Solid state electronics 1986**,** 22, 43-51.
32. T. Lan, P. D. Kaviratna & T. J. Pinnavaia. Chem. Mater 1995**,** 7, (11), 2144-50
33. T.D. Fornes; D.R. Paul. Polímeros: Ciência e Tecnologia 2003**,** 13, (4), 212-217.
34. P. H. Nam; P. Maiti; M. Okamoto; T. Kotaka; N. Hasegawa; A. Usuki. Polymer 2001**,** 42, (23), 9633-9640.
35. N. Sheng; M. C. Boyce; D. M. Parks; G. C. Rutledge; J. I. Abes; R. E. Cohen. Polymer 2004**,** 45, (2), 487-506.
36. M. Okamoto. Nano letters 2001**,** 1, (6), 295-298.
37. S. G. Hatzikiriakos.; N. Rathod.; E. B. Muliawan. Polymer Engineering & Science 2005**,** 45, (8), 1098-1107.
38. Y. Ke; J. Lu; X. Yi; J. Zhao; and; Z. Qi. J. Appl. Polym. Sci. 2000**,** 78, 808-815.
39. T. D. Fornes; D. R. Paul. Polymer 2003**,** 44, (14), 3945-3961.
40. S. M. Aharoni. John Wiley & Sons Ltd 1997, 3844.
41. M. R. Kamal; N. K. Borse; A. Garcia-Rejon. Polymer Engineering & Science 2002**,** 42, (9), 1883-1896.
42. Polyamide PA66 and PA6 structure, nylon. http://commons.wikimedia.org/wiki/Image:PA6-PA66.png. August 20.
43. H. Arimoto; M. Ishibashi; M. Hirai; and; Y. Chatani. J. Polym. Sci. Part B: Polym. Phys. Part. A 1965**,** 3, (15), 317.
44. M. Kyotani; and; S. Mitsuhashi. J Polym Sci Part A-2 1971**,** 10, 1497.
45. N. Hiramatsu; and; S. Hirakawa. Polym. J. 1982**,** 14, (165).
46. L. Panel-Pierron; C. Depecker; R. Seguela.; and; J. M. Lefebvre. J. Polym Sci: Part B: Polym Phys 2001**,** 39, (484).
47. L. Sandermann; and; A. Keller. J. Polym Sci 1956**,** 19, (401).
48. H. H. Illers KH. Makromol Chem 1971**,** 142, 31-67.
49. M. S. Kyotani M; 1497–508. J Polym Sci, Part A-2 1972**,** 10, (8).
50. F. A. Gurato G, Grandi FZ, Zannetti R, Canal P. Makromol Chem Mater 1974**,** 175, (3), 953–75.
51. A. Okada; M. Kawasumi; I. Tajima; T. K. and; O. Kamigaito. J Appl Polym Sci 1989**,** 37, (5), 1363-1371.
52. G. Gurato; A. Fichera; F. Z. Grandi; R. Zannetti; P. Canal. Makromol Chem 1974**,** 175, (3), 953–75.
53. S. Gogolewski; and; A. J. Pennings. Polymer 1975**,** 16, (673).
54. Y. Kojima; T. Matsuoka; T. H.; and; K. T. J. AppL Polym Sci 1994**,** 51, (683).
55. Y. Kojima; A. Usuki; M. Kawasumi; A. Okada; T. Kurauchi; O. Kamigaito. J. Polym. Sci. Part A: Polym. Chem 1993**,** 31, 983-986.
56. Y. Kojima; A. Usuki; M. Kawasumi; A. Okada; T. Kurauchi; O. Kamigaito. J. Polym. Sci Part A: Polym. Chem 1993**,** 31, 1755-1758.
57. K. S. Hynn; and; M. A. Splding. Polym. Eng. Sci. 1959**,** 30, (10), 571.
58. N. O. Hasegawa, H.; Kato, M.; Tsukigase, A.; Usuki, A. . Macromol. Mater. Eng 2000**,** 76, 280/281.
59. P. Maiti; M. Okamoto. Macromol. Mater. Eng 2003**,** 288, (5).
60. D.L. VanderHart; A. Asano; and; J. W. Gilman. Chem Mater 2001**,** 13, (10), 3781-3795.

61. K. Yano; A.Usuki; A. Okada; T. Kurauchi; and; O. Kamigato. J. Polym. Sci., Part A, Polym. Chem. 1993**,** 31, 2493-2498.
62. B. Singh. Polymner Clay Nanocomposite http://www.scribd.com/doc/518847/Polymner-Clay-Nanocomposite#document_metadata.
63. S. C. Di Lorenzo ML. Prog Polym Sci 1999**,** 24, (917).
64. X. F. Lu; and; H. J. N. 2001**,** 42, (19), 8055-8067

65. G. C. Wengui Weng, Dajun Wu. Polymer 2003**,** 44, 8119–8132.
66. T. M. Y. Kojima, H.Takahashi. andT. Kurauchi. J. AppL Polym Sci 1994**,** 51, (683).
67. D. R. Mathias LJ, Jarret WL. . Macromolecules 1999;32:7958 1999**,** 32, (23), 7958-7960.
68. M. Inoue. J Polymer Sci Pt A 1963**,** 1, 2013–20

69. B. Wanderlich, New York: Academic Press: 1973; Vol. 2.
70. G. D. Gurato G, Zannetti R. . Makromol Chem 1978;179(1): 231–45 1978**,** 179, (1), 231-45.
71. B. G. Mudra I. J Therm Anal Calorim 1998;52(2):355–61 1998**,** 52, (2), 235-61.
72. F. Yang; Y. Ou; and; Z. Yu. Journal of Applied Polymer Science 1998**,** 69, (2), 355-361.
73. G. Hinrichsen.; and; F. Lux. J. AppL Polym Sci 1998**,** 69, (355).
74. B. Wanderlich, Thermal characterization of polymeric materials, 2nd ed. . New York: Academic Press: 1997.
75. K. Mazhani. Studies of the Gamma form of isotactic Polypropylene at Atmospheric and Elevated pressures 1996.
76. X. Liu; Q. Wu. Polymer 2001**,** 42, (25), 10013-10019.
77. Q. Yuan; R.D.K Misra. Polymer 2006**,** 47, (12), 4421-4433.
78. Dongsik Kim; Jun S. Lee; Carol M. F. Barry; J. L. Mead. Microscopy Research and Technique 2007**,** 70, (6), 539-546.
79. Q. Yuan. Polym. Adv. Technol 2004**,** 15, 409-413.
80. D. Shah. Advanced Materials 2004**,** 16, (14), 1173-1177.
81. S. Bru¨ckner; S.V. Meille; V. Petraccone; and; B. Pirozzi. Prog. Polym. Sci 1991**,** 16, (361).
82. A.J. Turner-Jones; J.M. Aizlewood; and; D. R. Beckett. Macromol.Chem. 1964**,** 75, (134).
83. J. Varga; I. Mudra; and; G. W. Ehrenstein. J. Therm. Anal.Calorimetry 1999**,** 56, (1047).
84. H. Tai; W.Y. Chiu; L.W. Chen; and; L. H. Chu. J. Appl.Polym. Sci. 1991**,** 42, (3111).
85. S.H. Ryu; C.G. Gogos; and; M. Xanthos. Polymer 1991**,** 32, (13), 2449-2455.
86. K. Yamada; S. Matsumoto; K. Tagashira; and; M. Hikosaka. Polymer 1998**,** 39, 5327.
87. K. Mezghani; and; P. J. Phillips. Polymer 1995**,** 36, 2407.
88. E. Ramı´rez-Vargas; F. J. Medellı´n-Rodrı´guez; D. Navarro-Rodrı´guez; C. A. A. Orta.; S. G. Solı´s-Rosales.; and; S. Lin. Polym. Eng. Sci. 2002**,** 42, 1350.
89. W. Zheng; X. Lu; C.L. Toh; T.H. Zheng; and; C. He. J. Polym. Sci., Part B: Polym. Phys. 2004**,** 42, 1810.
90. R.A. Campbell; P.J. Phillips; and; J.S. Lin. Polymer, 1993**,** 34,, 4809
91. S.V. Meille; P.J. Phillips; K. Mezghani; and; S. Bru¨ckner. Macromolecules 1996**,** 29, 795.

92. Q. Yuan; C. Deshmane; T. C. Pesacreta; R. D. K. Misra. Materials Science and Engineering: A 2008**,** 480, (1-2), 181-188.
93. P. H. Nam; P. Maiti; M. Okamoto; T. Kotaka; N. Hasegawa; A. Usuki. Polymer 2001**,** 42, 9633.
94. M. Joshi; V. Viswanathan. Journal of Applied Polymer Science 2006**,** 102, (3), 2164-2174.
95. K. Rogers; E. Takacs; M. R. Thompson. Polymer Testing 2005**,** 24, (4), 423-427.
96. Y. Seo; J. Kim; K. U. Kim; Y. C. Kim. Polymer 2000**,** 41, (7), 2639-2646.
97. D. Godshall. Production and structure/properties of Nylon-6 core/isotactic polypropylene sheath bi-component fibers suitable for use in carpeting applications. Masters Thesis, blacksburgh VA, 1999.
98. A. L. Malaika., Reactive modifiers for Polymers,. Chapman and Hall: London, 1997.
99. S.H.P. Bettini; J.A.M Agnelli. Polymer Testing, Elsevier 2000**,** 19, (1), 3-15.
100. R. Jeziórska. Pigment & Resin Technology 2006**,** 35, (1), 3-11.
101. W. S. Chow; Z. A. Mohd Ishak; J. Karger-Kocsis; A. A. Apostolov; U. S. Ishiaku. Polymer 2003**,** 44, (24), 7427-7440.
102. B. Kim; S.-H. Lee; D. Lee; B. Ha; J. Park; K. Char. Industrial & Engineering Chemistry Research 2004**,** 43, (19), 6082-6089.
103. S. Sinha Ray; M. Okamoto. Prog. Polym. Sci 2003**,** 28, 1539-1641.
104. H. N. Kawasumi M, Kato M, Usuki A, Okada A. Macromolecules 1997**,** 30, 6333–8.
105. J. Duvall; C. Sellitti; C. Myers; A. Hiltner; a. E. Baer. Journal of Applied Polymer Science 1994**,** 52, (2), 207-216.
106. Xu JT; Wang Q; and; F. Z. Q. Eur Polym J 2005**,** 41, 3010.
107. M. Avella; S. Cosco; D.i Lorenzo; D.i Pace; M. E. Errico. J Therm Anal Calorim 2005**,** 80, (131).
108. Y.M. Wang; C. Y. Shen; H.M. Li; Q. Li; J. B. Chen. J Appl Polym Sci 2004**,** 91, (308).
109. C.A. Mitchell; R. Krishnamoorti. Polymer 2005**,** 46, (8796).
110. D. Homminga; B. Goderis; I. Dolbnya; H. Reynaers; G. Groeninckx. Polymer 2005**,** 46, (11359).
111. P. Maiti. Polymer Engineering & Science 2002**,** 42, (9), 1864-1871.
112. X. Liu; and; Q. Wu. Polymer 2001**,** 42, 10013.
113. M. G. W. Xu, and P. He. J. Polym. Sci., Part B: Polym. Phys. 2002**,** 40, (408).
114. F. J. Medellín-Rodríguez. Polymer Engineering & Science 2007**,** 47, (11), 1889 – 1897.
115. T.-T. M. Perrin-Sarazin F, Bureau MN, Denault J. Polymer 2005**,** 46, (11624).
116. Z. Ergungor; M. Cakmak; C. Batur. Macromolecular Symposia 2002**,** 185, (1), 259-276.
117. W. Xiao; H. Yu; K. Han; and; M. Yu. Journal of Applied Polymer Science 2005**,** 96, 2247–2252.
118. Z. Mlynarcikova ; D. Kaempfer ; R. Thomann; R. Mulhaupt; E. Borsig; A. Marcincin. Polymers for Advanced Technologies 2005**,** 16, (5), 362-369.
119. Q. F. Lalit Toshniwal, Samuel C. Ugbolue. Journal of applied polymer science 2007**,** 106, 706-711.
120. G. Mani; Q. Fan; S. C. Ugbolue; I. M. Eiff In AATCC, 2003; 2003.
121. K.E. Wang. Polymer 2006**,** 47, 7103-7110.
122. S. Xie; B. Z. S. Zhang; H. Qin; F. Wang; and; M. Yang. Polymer International 2005**,** 54, (12), 1673-1680.

123. M. Yuan; L. Sheng; T. Shaoqin; G. Daniel; C. Chris; H. R. Spindler. Polymer Engineering and Science 2004**,** 44, (4), 673-686.
124. K. Friedrich. Adv. Polym. Sci. 1983, 52-53.
125. P. Supaphol; and; J. E. Spruiell. Polymer 2001**,** 42, (2), 699-712.
126. K. Mazhani. Isothermal crystallization and melting of deuterated isotactic polypropylene. 1995.
127. A. Sharples, Introduction to polymer crystallization. St Martin's Press: New York, 1966.
128. A. Dasari; Z. Yu; Y. Wing; G. Hua; V. Joël. Composites Science and Technology 2005**,** 65, (15-16), 2314-2328.
129. T. D. Fornes; and; D. R. Paul. Polymer 2003**,** 44, (17), 4993-5013.
130. J.I. Lauritzen; J. D. Hoffman. J. Appl. Phys 1973**,** 44, (4340).
131. G. Natta; P. Corradini. Suppl. Nuovo Cimento 1960**,** 15, (40).
132. M.J. Avrami. J Chem Phys 1939**,** 7, (1103).
133. J.D. Hoffman; G. T. Davis; J. I. Lauritzen.; N. B. Hanny., Treatise on solid state chemistry. New York: Plenum Press: 1976; Vol. 3.
134. Hoffman JD; Davis GT; L. J. In:; Hanny NB, Treatise on solid state chemistry. New York: Plenum Press: 1976; Vol. 3.
135. B. Monnasse; J. M. Handin. Coloid and Poly. Sci 1985**,** 263, (822).
136. S.Z.D. Cheng; J. J. Janimak; A. Zhang. Makromolecules 1990**,** 23, (298).
137. P. J. Phillips, M. Dosiere, ed., Kluewer. The Netherlands 1983.
138. E.J. Clark; J. D. Hoffman. Macromolecules 1984**,** 17, (878).
139. R. A. Campbell. University of Tennessee, , 1991.
140. M. Mucha; and; Z. Królikowski. J. Therm. Anal. Cal. 2003**,** 74.
141. M.J. Avrami. J Chem Phys 1940, (8), 212.
142. M.J. Avrami. J Chem Phys 7 1939, 1103.
143. B. Wanderlich., Academic press inc: New York, 1976; Vol. 2.
144. A. Fukada. Crystallization kinetics and annealing behavior of a thermotropic liquid crystalline polymer. Master's thesis, The university of Tennessee, 1991.
145. H. S. Cebe P. Polymer 1986**,** 27, (183).
146. W. Leelapornpisit; M.N. Ton-That; F. Perrin-Sarazin; K.C. Cole; J. Denault; and; B. Simard. J Polym Sci Part B: Polym Phys 2005**,** 43, 2445.
147. Kang X; He SQ; Zhu CS; Wang LY; L. LY. J Appl Polym Sci 2004**,** 95, (756).
148. Avella M; Cosco S; Di Lorenzo ML; Di Pace E; E. ME. J Therm Anal Calorim 2005**,** 80, (131).
149. Z. Liu; K. Chen; D. Yan. European Polymer Journal 2003**,** 39, (12), 2359-2366.
150. Q.Yuan; S. Awate; and; R.D.K. Misra. European Polymer Journal 2006**,** 42, (9), 1994-2003.
151. Q. Yuan; S. Awate; R. D. K. Misra. European Polymer Journal 2006**,** 42, (9), 1994-2003.
152. M.L. Di Lorenzo and C. Silvestre. Prog Polym Sci 1999**,** 24, 917.
153. S. Pitt. J Appl Polym Sci 2000**,** 78, 338–354v.
154. K. HE. J Res Natl Stand 1956**,** 57, (217).
155. R. Hadal; Q. Yuan; J. P. Jog; and; R.D.K. Misra. Mater Sci Eng A 2006**,** 418, 268.
156. R. Rao; A. Mudaliar; Q. Yuan; J. P. Jog; and; R.D.K. Misra. Mater Sci Eng A 2006**,** 418 292.
157. J. M. Schultz, Polymer Crystallization. Oxford University Press: Washington, D.C, 2001.

158. J. C. Halpin Affdl; and; J. L. Kardos. Polymer Engineering & Science 1976**,** 16, (5), 344-352.
159. J. C. Halpin. J Compos Mater 1969**,** 3, 732.
160. C. L. Tucker Iii; E. Liang. Composites Science and Technology 1999**,** 59, (5), 655-671.
161. K. Hbaieb; Q. X. Wang; Y. H. J. Chia; B. Cotterell. Polymer 2007**,** 48, (3), 901-909.
162. Jyi-Jiin Luo; I. M. Daniel. Composites Science and Technology 2003**,** 63, 1607–1616.
163. J. J. Luo; I. M. Daniel. Composites Science and Technology 2003**,** 63, 1607–1616.
164. J. C. Halpin; and; J. L. Kardos. Polym Engng Sci 1976**,** 16, (5), 344-352.
165. J. R. Fred, Polymer Science and Technology. Printice Hall PTR: New Jersey, 1995.
166. D. Adams; and; D. Doner. J Compos Mater 1967**,** 14, 152.
167. R. Hill. J Mech Phys Solids 1964**,** 12, 119.
168. J. D. Eshelby. Proceedings of the Royal Society of London. Series A. Mathematical and Physical Sciences 1957**,** 241, (1226), 376-396.
169. R. J. Opalko. Evaluation of the effects of nanofil nanoclays in the blending of polypropylene and polystyrene. 2008.
170. H. Bilge. Mechanical properties of Indevidual polymeric micro and nano fibers using Atomic Force Microscopy (AFM). North Corolina State University, Raleigh, North Carolina, 2006.
171. Transmission electron microscopy. http://en.wikipedia.org/wiki/Transmission_electron_microscopy. 30 June 2009
172. Transmission Electron Microscopy and Diffractometry of Materials. Springer: 2007.
173. G. Binnig; C. F. Quate; C. Gerber. Physical Review Letters 1986**,** 56, (9), 930.
174. Nise. Seeing Atoms. http://www.nisenet.org/publicbeta/articles/seeing_atoms/seeing_atoms_print.html. 2008.
175. A. Ganguly; De. M. Sarkar; and; A. K. Bhowmick. Journal of Polymer Science Part B: Polymer Physics 2007**,** 45, (1), 52-66.
176. S.N. Magonov; V. Elings; M. H. Whangbo. Surface Science 1997**,** 375, L385-L391.
177. J. F. Lubben. Journal of Physics: Conference series 2007**,** 61, 735-739.
178. H. K. Fu; C. F. Huang; S. W. Kuo; H. L. Ding-Ru; and; Y. F. C. Chang. Macromolecular Rapid Communications 2008**,** 29, (14), 1216-1220.
179. F. Kadar; L. Szazdi; E. Fekete; B. Pukanszky; Langmuir. 2006**,** 22, (7848).
180. U. Yoshimasa; N. Takashi; Langmuir. 2005**,** 21, (2614).
181. D. Dharaiya; S. C. Jana. Polymer 2005**,** 46, (23), 10139-10147.
182. A. A. Vanderhart DL, Gilman JW. Chem Mater 2001**,** 13, 3796–809.
183. Xei W; Xei R; Pan W; Hunter D; Koene B; and; Tan L. Chem Mater 2002**,** 14, 4837-45.
184. E. Sharfrin. The Journal of Physical Chemistry 1960**,** 64, (5), 519-524.
185. KRÜSS, Contact angle measurement – a theoretical approach. In 2005.
186. R. Kotra; H. Rong; A. Dahiya; M. G. Kamath; R. R. Hegde. Spunbond Technology. http://www.engr.utk.edu/mse/Textiles/Spunbond%20Technology.htm. February 2009.
187. S. R. Malkan; L. C. Wadsworth. Nonwovens 1992**,** 4, 24-33.
188. R. R. Hegde. Influence of Material Variables in Thermal Bonding of Nonwovens. Tennessee, Knoxville, 2006.
189. R. Kotra; H. Rong; A. Dahiya; M. G. Kamath; R. R. Hegde. Melt blown Technology. http://web.utk.edu/~mse/Textiles/Melt%20Blown%20Technology.htm. February 2009.

190. K. Kit; R. Ramachandra, Operating Procedure of Pneumatic Injection Molding. In The University of Tennessee: Knoxville, 2005.
191. B.D. Cullity; S.R. Stock, Elements of X-Ray Diffraction. 3rd edition ed.; 2001; p 556-557.
192. B. Yalcin; D. Valladares; M. Cakmak. Polymer 2003**,** 44, (22), 6913-6925.
193. D. R. Steinmetz. Texture Evolution in Processing of Polystyrene-Clay Nanocomposites. Drexel University, 2007.
194. DSC 822e Thermal analysis user manual. In METTLER TOLEDO
195. METTLER TOLEDO DSC 822e STARe Software user manual DSC evaluations.
196. R. Riesen. J. Therm. Anal. Cal 2000**,** 59.
197. F. Rodriguez, Principles of Polymer Systems. Fourth ed.; Ithica, NY, 1996.
198. C. P. Stephens; R. S. Benson, Dynamic mechanical thermal analysis of Honeywell nylon nanocomposites. In 2003.
199. Standard Test Methods for Nonwoven fabrics. In *ASTM D1117-97*.
200. Standard test methods for determining the izod impact resistance of plastics. In *ASTM D 256-04*, ASTM: 2004.
201. P. G. Oliver WC. J Mater Res 1992**,** 7, (6), 1564-83.
202. M. J. Wilson, Clay mineralogy: Spectroscopic and chemical determinative Methods. first edition ed.; Chapman & Hall: 1994.
203. IUPAC Compendium of Chemical Terminology; 1997.
204. Scanning Transmission Electron Microscopy. http://www.microscopy.ethz.ch/STEM-home.htm.
205. L. S. Loo; K. K. Gleason. Polymer 2004**,** 45, 5933-5939.
206. R. Zbinden, Infrared spectroscopy of high polymers. In New York Academic Press,: New York, 1964.
207. P. J. Yoon; Fornes T. D.; &; Paul D. R. Polymer 2002**,** 43, (25), 6727-6741.
208. D.M. Lincoln; R.A. Vaia; Z.-G. Wang; and; B. S. Hsiao. Polymer 2001**,** 42, (4), 1621–1631.
209. S. Zhang. Polymer degradation and stability 2007**,** 92, 727-732.
210. Cloisite® Nanoclays. http://www.nanoclay.com/benefits2.asp.
211. W. M. Pitts. Prog Energy Combust Sci 1995**,** 21, 197-237.
212. Y. Kojima; A. Usuki; M. Kawasumi; A. Okada; Y. Fukushima; T. Kurauchi; and; T. Kamigaito. J Mater Res 1993**,** 85, 1185–1189.
213. M. Ito; K. Mizuochi; and; T. Kanamoto. Polymer 1998**,** 39, (19), 4593–4598.
214. X. Bai; Y. Wang; J. Zhengzhou. Univ (Eng Sci) 2002**,** 23, (91).
215. S. C. Tjong. Materials Science and Engineering: R: Reports 2006**,** 53, (3-4), 73-197.
216. L. Shen; I. Y. Phang; L. Chen; T. Liu; K. Zeng. Polymer 2004**,** 45, (10), 3341-3349.
217. G. H. J. Nix W D. J Mech Phys Solids 1998**,** 46, 411-25.
218. G. S. Bhat; R. R. Hegde; M. G. Kamath; and; B. Deshpande. Journal of Engineered Fibers and Fabrics 2008**,** 3, (3).
219. T. K. M. Todki. Journal of Polymer Science., Polymer Physics 1977**,** 15, 1067.
220. K. Friedrich; U. A. Karsch. J. Mater. Sci 1981**,** 16, (2167).
221. Z. X. Chen, Q.; Li, J.; Cheng, S.; Zhang, Y.; Wei, Y.; Ma, R. Acta Polym Sinica 1997**,** 5, (530).

222. H. Y. Weizhen Xiao, Keqing Han, Muhuo Yu. Journal of Applied Polymer Science 2005**,** 96, 2247–2252.
223. N. A. Memon. Journal of applied Polymer Science 1994**,** 54, 1059-1069.
224. S. G. Hatzikiriakos; N. Rathod; and; E. B. Muliawan. Polymer Engineering & Science 2005**,** 45, (8), 1098-1107.
225. R. Krishnamoorti; R. A. Vaia; E. P. Giannelis. Chemistry of Materials 1996**,** 8, (8), 1728-1734.
226. T. D. Fornes; P. J. Yoon; H. Keskkula; D. R. Paul. Polymer 2001**,** 42, (25), 09929-09940.
227. P. Svoboda; C. Zeng; H. Wang; L. James; L. David; L. Tomasko. Journal of Applied Polymer Science 2002**,** 85, (7), 1562-1570.
228. H. A. Barnes; J.F. Hutton; and; K. Walters., An introduction to Rheology. First edition ed.; Elsevier Science Publishers: 1989.
229. L. M. Amish. In Benefits of Inorganic additives in Meltblown Polypropylene, INTC, Texas, September 8-11, 2008; Texas, 2008.
230. J. Yu; J. He. Polymer 2000**,** 41, (3), 891-898.
231. K. Friedrich. Advances in Polymer Science 1983**,** 52/53.
232. P. J. Hendra. Polymer 1984**,** 25, 785-790.
233. B. Wunderlich., Macromolecular physics. Academic press inc: New York, 1976; Vol. 2.
234. X. Kang; S.Q. He; C. S. Zhu; L.Y. Wang; and; L. Y. Lu. J Appl Polym Sci 2004**,** 95, (756).
235. S. Hambir; N. Bulakhm; J. P. Jog. Polym Engng Sci 2002**,** 42, (1800).
236. P. Svoboda; C. Zeng; H. Wang; L. James; L. David; and; L. Tomasko. Journal of Applied Polymer Science 2002**,** 85, (7), 1562-1570.
237. J. Ma; S. Zhang; Z. Qi; G. Li; and; Y. Hu. J Appl Polym Sci 2002**,** 83, (1978).
238. A. Pozsgay; T. Frater; L. Papp; I. Sajo; and; B. Pukanszky. J Macromol Sci, Part B—Physics 2002**,** B41, (1249).
239. R. Nowacki; B. Monasse; E. Piorkowska; A. Galeski; J. M. Haudin. Polymer 2004**,** 45, (14), 4877-4892.
240. R. R. Bresee; and; W. C. Ko. International nonwovens journal 2003**,** 12, (2), 21-28.
241. L. Shen; W. C. Tjiu; T. Liu. Polymer 2005**,** 46, (25), 11969-11977.
242. K. Wang; P. Z.; H. Y; L. Si; Q. Zhang; R. Du; Q. Fu; Z. Yu; E. Chen. Polymer 2006**,** 47, (20), 7103-7110.
243. N.G. McCrum; B. E. Read; and; G. Williams., Anelastic and dielectric effects in polymeric solids, . Wiley: London 1967.
244. T. Liu; K. Ping Lim; W. Chauhari Tjiu; K. P. Pramoda; Z.-K. Chen. Polymer 2003**,** 44, (12), 3529-3535.
245. Q. Yuan; R. D. K. Misra. Polymer 2006**,** 47, (12), 4421-4433.
246. L. Chen; S. C. Wong; S. Pisharath. Journal of Applied Polymer Science 2003**,** 88, 3298-3305.
247. T. T. Wang; T. Nishi. Macromolecules 1977**,** 10, 421.
248. C.J. Ong; F. P. Price. J. Polym. Sci polym Symp 1978**,** 63, 59.
249. G. C. Alfonso; T. P. Russel. Macromolecules 1986**,** 19, 1143.
250. J. P. Huang; A. Prasad; H. Marand. polymer 1994**,** 35, 1896.
251. J. W. Mullin, Crystallization. Fourth Edition ed.; Butterworth-Heinemann: 2001.

252. S. Z. B. Z. H. Q. F. W. M. Y. Shaobo Xie. Polymer International 2005**,** 54, (12), 1673-1680.
253. F.S. Dainton; D. M. Evans; F. E. Hoare; and; T. P. Melia. Polymer 1962**,** 3, (286).
254. P. D. Calvert, Ryan, T. G. Polymer 1978**,** 19, (611).
255. E. A. DiMarzio, In.
256. G. M. M. Elico passsaglia. 1964, 519-527.
257. Y. Mubarak; E. M. A. Harkin-Jones; M. P.J.; and; A. M. Plast. Rubber Compos 2000**,** 29, (7), 307–315.
258. H. Janeschitz-Kriegel; E. Ratajski; and; H. Wippel. Colloid. Polym. Sci 1999, 217-226.
259. C. Albano; J. Papa; M. Ichazo; J. González; C. Ustariz. Composite Structures 2003**,** 62, (3-4), 291-302.
260. R. M. Patel; and; J. E. Spruiell. Polymer Engineering & Science 1991**,** 31, (10), 730-738.
261. H. H. Kausch, Polymer Fracture. Springer-Verlag: Berlin--Heidelberg--New York, 1978.
262. S. Matsuoka. Polym. Eng. Sci. 1965**,** 7, (142).

APPENDIX

Statistical analysis

1. Nylon 6 film composites

Film Thickness (µM)
Regression Plot

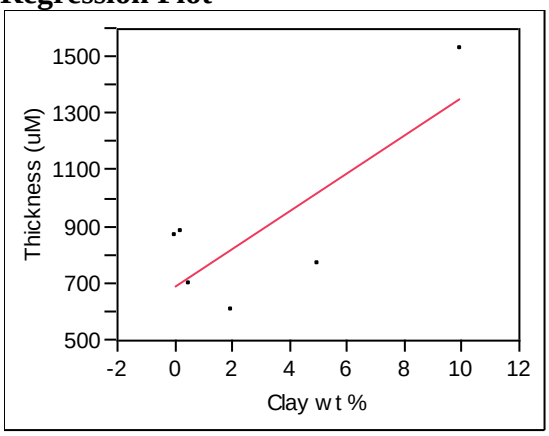

Figure 5. 1. Thickness of nylon-6 films with nanoclay.

Leverage Plot

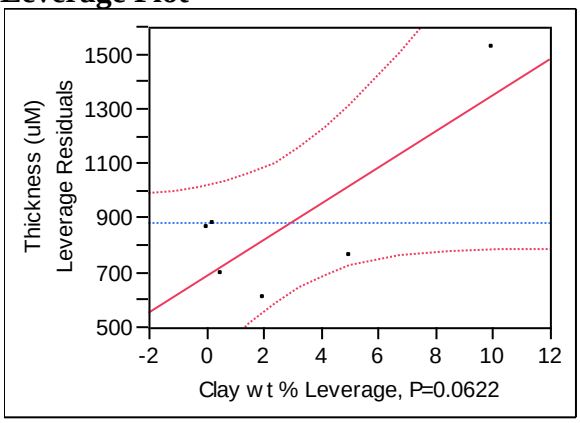

Figure 5. 2. Thickness of nylon-6 films with nanoclay.

Summary of Fit

RSquare	0.622227
RSquare Adj	0.527784
Root Mean Square Error	225.5109
Mean of Response	884
Observations (or Sum Wgts)	6

Analysis of Variance

Source	DF	Sum of Squares	Mean Square	F Ratio
Model	1	335053.31	335053	6.5884
Error	4	203420.69	50855	Prob > F
C. Total	5	538474.00		0.0622

Parameter Estimates

Term	Estimate	Std Error	t Ratio	Prob>|t|
Intercept	688.60315	119.4609	5.76	0.0045
Clay wt %	66.049641	25.73245	2.57	0.0622

Peak force (gms)

Regression Plot

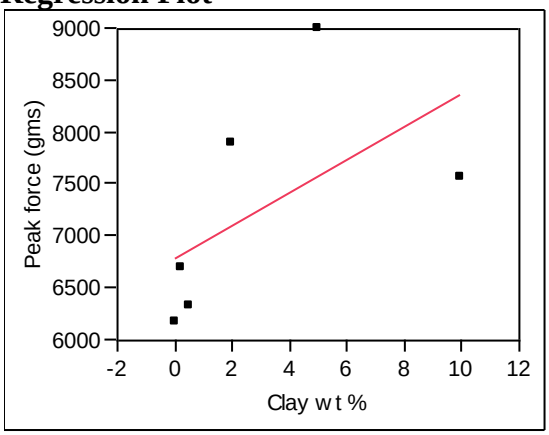

Figure 5. 3. Peak force of nylon-6 films with nanoclay.

Leverage Plot

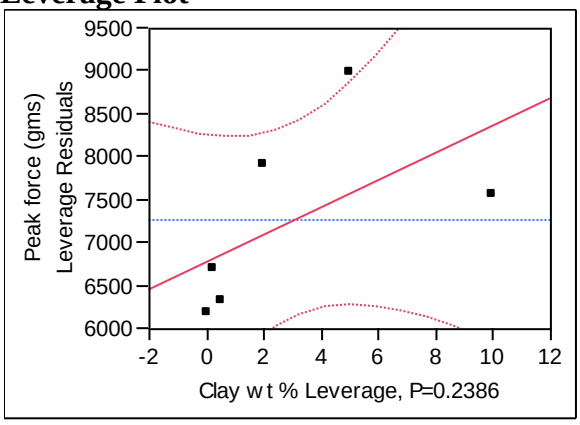

Figure 5. 4. Peak force of nylon-6 films with nanoclay.

Analysis of Variance

Source	DF	Sum of Squares	Mean Square	F Ratio
Model	1	1902155.8	1902156	1.9151
Error	4	3973010.2	993253	Prob > F
C. Total	5	5875166.0		0.2386

Parameter Estimates

Term	Estimate	Std Error	t Ratio	Prob>|t|
Intercept	6787.4314	527.9441	12.86	0.0002
Clay wt %	157.37529	113.7217	1.38	0.2386

Peak elongation (%)
Regression Plot

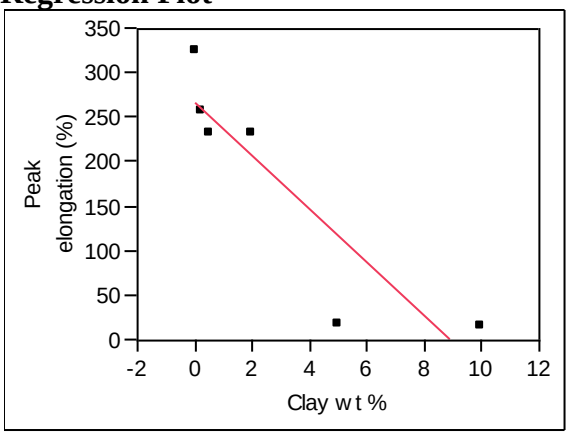

Figure 5. 5. of nylon-6 films with nanoclay.

Leverage Plot

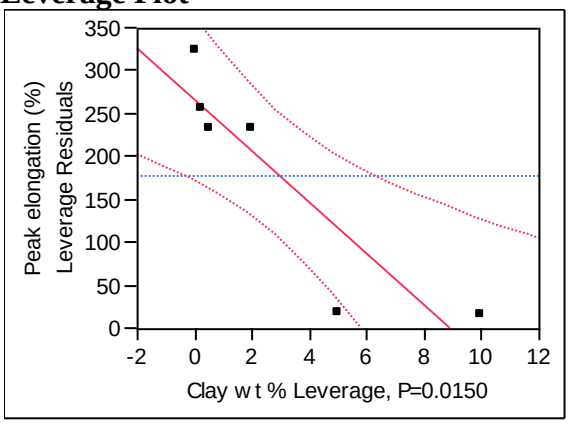

Figure 5. 6. Peak elongation of nylon-6 films with nanoclay.

Summary of Fit

RSquare	0.806836
RSquare Adj	0.758544
Root Mean Square Error	64.29658
Mean of Response	178.1667
Observations (or Sum Wgts)	6

Analysis of Variance

Source	DF	Sum of Squares	Mean Square	F Ratio
Model	1	69070.634	69070.6	16.7077
Error	4	16536.199	4134.0	Prob > F
C. Total	5	85606.833		0.0150

Parameter Estimates

Term	Estimate	Std Error	t Ratio	Prob>|t|
Intercept	266.88377	34.0601	7.84	0.0014
Clay wt %	-29.98888	7.33671	-4.09	0.0150

Response Tear strength (cN)
Regression Plot

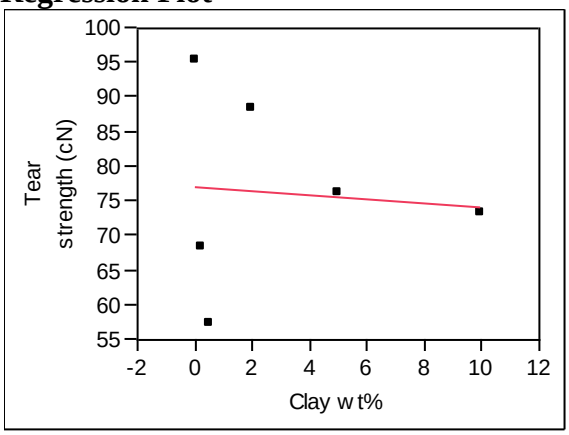

Figure 5. 7. Tear strength of nylon-6 films with nanoclay.

Leverage Plot

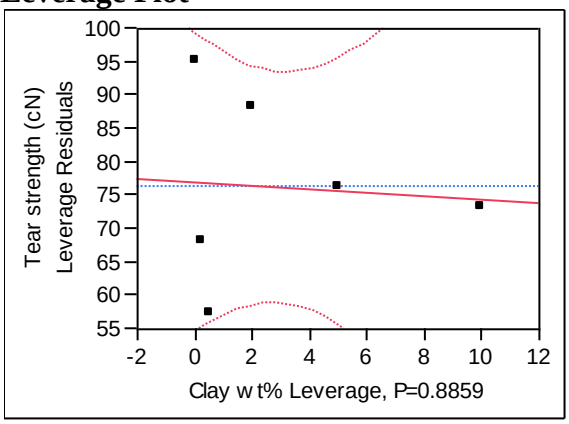

Figure 5. 8. Tear strength of nylon-6 films with nanoclay.

Summary of Fit

RSquare	0.005805
RSquare Adj	-0.24274
Root Mean Square Error	15.27566
Mean of Response	76.16667
Observations (or Sum Wgts)	6

Analysis of Variance

Source	DF	Sum of Squares	Mean Square	F Ratio
Model	1	5.44964	5.450	0.0234
Error	4	933.38370	233.346	Prob > F
C. Total	5	938.83333		0.8859

Parameter Estimates

Term	Estimate	Std Error	t Ratio	Prob>|t|
Intercept	76.9547	8.092044	9.51	0.0007
Clay wt%	-0.266377	1.743065	-0.15	0.8859

Response Burst strength (Mpa)

Regression Plot

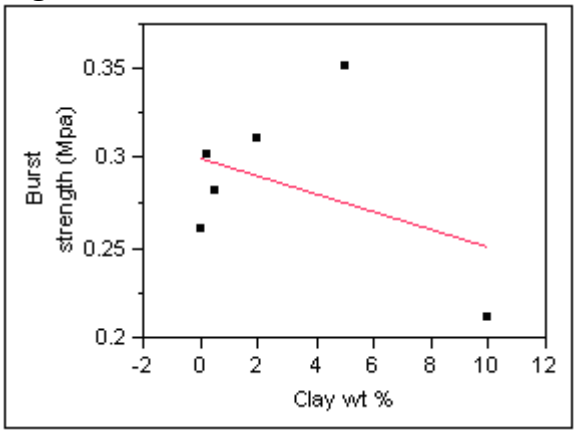

Figure 5. 9. Burst strength of nylon-6 films with nanoclay.

Leverage Plot

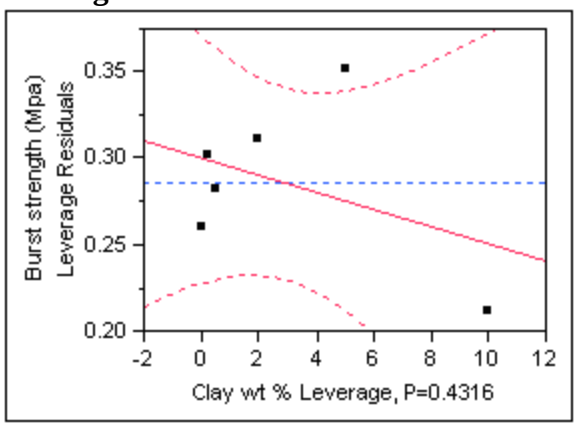

Figure 5. 10. Burst strength of nylon-6 films with nanoclay.

Summary of Fit

RSquare	0.160248
RSquare Adj	-0.04969
Root Mean Square Error	0.048814
Mean of Response	0.285
Observations (or Sum Wgts)	6

Analysis of Variance

Source	DF	Sum of Squares	Mean Square	F Ratio
Model	1	0.00181882	0.001819	0.7633
Error	4	0.00953118	0.002383	Prob > F
C. Total	5	0.01135000		0.4316

Parameter Estimates

Term	Estimate	Std Error	t Ratio	Prob>|t|
Intercept	0.2993964	0.025858	11.58	0.0003
Clay wt %	-0.004866	0.00557	-0.87	0.4316

2. Spunbond web with nanoclay

Birefringence

One-way Analysis of Birefringence by Sample

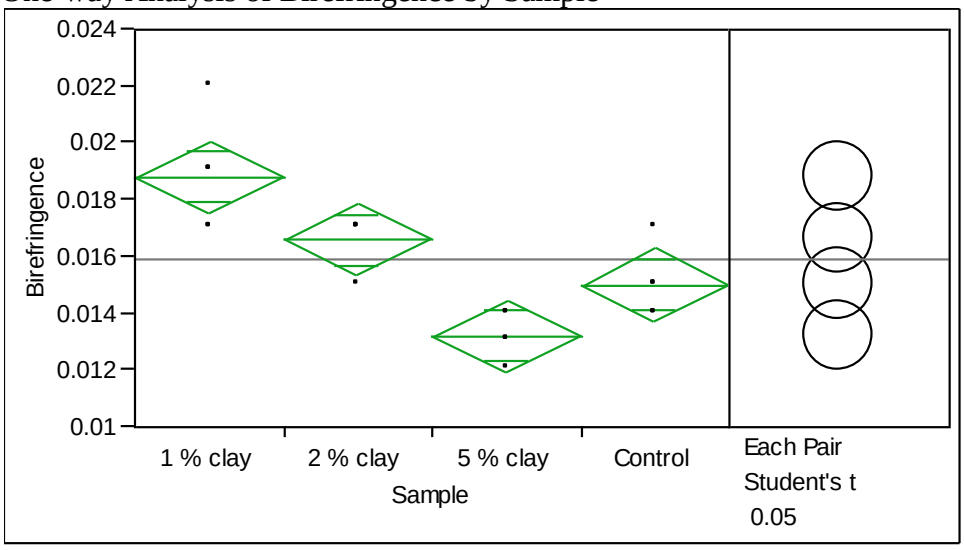

Figure 5. 11. Birefringence of SB samples.

Oneway Anova

Summary of Fit

Rsquare	0.746924
Adj Rsquare	0.699473
Root Mean Square Error	0.001342
Mean of Response	0.0159
Observations (or Sum Wgts)	20

Analysis of Variance

Source	DF	Sum of Squares	Mean Square	F Ratio	Prob > F
Sample	3	0.00008500	0.000028	15.7407	<.0001
Error	16	0.00002880	1.8e-6		
C. Total	19	0.00011380			

Means for Oneway Anova

Level	Number	Mean	Std Error	Lower 95%	Upper 95%
1 % clay	5	0.018800	0.00060	0.01753	0.02007
2 % clay	5	0.016600	0.00060	0.01533	0.01787
5 % clay	5	0.013200	0.00060	0.01193	0.01447
Control	5	0.015000	0.00060	0.01373	0.01627

Std Error uses a pooled estimate of error variance

Means Comparisons

Comparisons for each pair using Student's t

t	Alpha
2.11991	0.05

Abs(Dif)-LSD	1 % clay	2 % clay	Control	5 % clay
1 % clay	-0.00180	0.00040	0.00200	0.00380
2 % clay	0.00040	-0.00180	-0.00020	0.00160
Control	0.00200	-0.00020	-0.00180	0.00000
5 % clay	0.00380	0.00160	0.00000	-0.00180

Positive values show pairs of means that are significantly different.

Connecting letter report

Level			Mean
1 % clay	A		0.01880000
2 % clay		B	0.01660000
Control		B	0.01500000
5 % clay		C	0.01320000

Levels not connected by same letter are significantly different.

Ordered difference report

Level	- Level	Difference	Lower CL	Upper CL	p-Value	Difference
1 % clay	5 % clay	0.0056000	0.003801	0.0073988	<.0001	
1 % clay	Control	0.0038000	0.002001	0.0055988	0.0004	
2 % clay	5 % clay	0.0034000	0.001601	0.0051988	0.0010	
1 % clay	2 % clay	0.0022000	0.000401	0.0039988	0.0196	
Control	5 % clay	0.0018000	0.0000012	0.0035988	0.0499	
2 % clay	Control	0.0016000	-0.000199	0.0033988	0.0776	

Oneway Analysis of Peak force (gms)

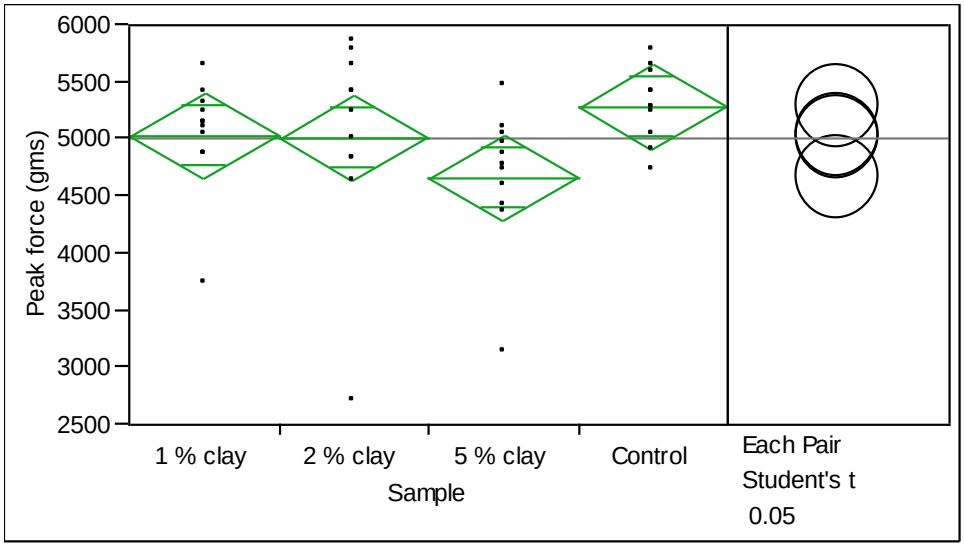

Figure 5. 12. SB web peak force (gms).

Oneway Anova

Summary of Fit

Rsquare	0.128257
Adj Rsquare	0.062876
Root Mean Square Error	604.4043
Mean of Response	4999.394
Observations (or Sum Wgts)	44

Analysis of Variance

Source	DF	Sum of Squares	Mean Square	F Ratio	Prob > F
Sample	3	2149850	716617	1.9617	0.1352
Error	40	14612182	365305		
C. Total	43	16762033			

Means for Oneway Anova

Level	Number	Mean	Std Error	Lower 95%	Upper 95%
1 % clay	11	5030.84	182.23	4662.5	5399.1
2 % clay	11	5015.17	182.23	4646.9	5383.5
5 % clay	11	4665.07	182.23	4296.8	5033.4
Control	11	5286.50	182.23	4918.2	5654.8

Std Error uses a pooled estimate of error variance

Means Comparisons

Comparisons for each pair using Student's t

t	Alpha
2.02108	0.05

Abs(Dif)-LSD	Control	1 % clay	2 % clay	5 % clay
Control	-520.87	-265.20	-249.53	100.56
1 % clay	-265.20	-520.87	-505.20	-155.10
2 % clay	-249.53	-505.20	-520.87	-170.77
5 % clay	100.56	-155.10	-170.77	-520.87

Positive values show pairs of means that are significantly different.

Connecting letter report

Level			Mean
Control	A		5286.5018
1 % clay	A	B	5030.8364
2 % clay	A	B	5015.1665
5 % clay		B	4665.0698

Levels not connected by same letter are significantly different.

Ordered difference report

Level	- Level	Difference	Lower CL	Upper CL	p-Value	Difference
Control	5 % clay	621.4320	100.563	1142.301	0.0206	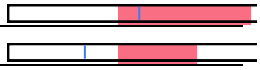
1 % clay	5 % clay	365.7665	-155.103	886.636	0.1636	
2 % clay	5 % clay	350.0967	-170.773	870.966	0.1819	
Control	2 % clay	271.3353	-249.534	792.205	0.2987	
Control	1 % clay	255.6655	-265.204	776.535	0.3271	
1 % clay	2 % clay	15.6698	-505.199	536.539	0.9518	

Tear strength

Oneway Analysis of Tear strength (cN) By Sample

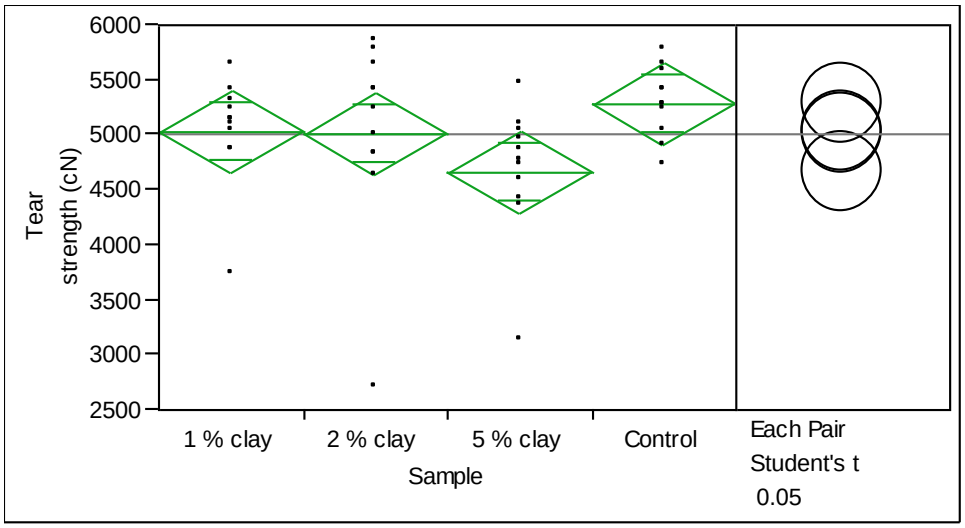

Figure 5. 13. Tear strength for different SB samples.

Oneway Anova

Summary of Fit

Rsquare	0.128257
Adj Rsquare	0.062876
Root Mean Square Error	604.4043
Mean of Response	4999.394
Observations (or Sum Wgts)	44

Analysis of Variance

Source	DF	Sum of Squares	Mean Square	F Ratio	Prob > F
Sample	3	2149850	716617	1.9617	0.1352
Error	40	14612182	365305		
C. Total	43	16762033			

Means for Oneway Anova

Level	Number	Mean	Std Error	Lower 95%	Upper 95%
1 % clay	11	5030.84	182.23	4662.5	5399.1
2 % clay	11	5015.17	182.23	4646.9	5383.5
5 % clay	11	4665.07	182.23	4296.8	5033.4
Control	11	5286.50	182.23	4918.2	5654.8

Std Error uses a pooled estimate of error variance

Means Comparisons

Comparisons for each pair using Student's t

t	Alpha
2.02108	0.05

Abs(Dif)-LSD	Control	1 % clay	2 % clay	5 % clay
Control	-520.87	-265.20	-249.53	100.56
1 % clay	-265.20	-520.87	-505.20	-155.10
2 % clay	-249.53	-505.20	-520.87	-170.77
5 % clay	100.56	-155.10	-170.77	-520.87

Positive values show pairs of means that are significantly different.

Connecting letter report

Level			Mean
Control	A		5286.5018
1 % clay	A	B	5030.8364
2 % clay	A	B	5015.1665
5 % clay		B	4665.0698

Levels not connected by same letter are significantly different.

Ordered difference report

Level	- Level	Difference	Lower CL	Upper CL	p-Value	Difference
Control	5 % clay	621.4320	100.563	1142.301	0.0206	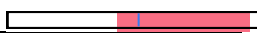
1 % clay	5 % clay	365.7665	-155.103	886.636	0.1636	
2 % clay	5 % clay	350.0967	-170.773	870.966	0.1819	
Control	2 % clay	271.3353	-249.534	792.205	0.2987	
Control	1 % clay	255.6655	-265.204	776.535	0.3271	
1 % clay	2 % clay	15.6698	-505.199	536.539	0.9518	

Bending length

Oneway Analysis of bending length (cms) By Sample

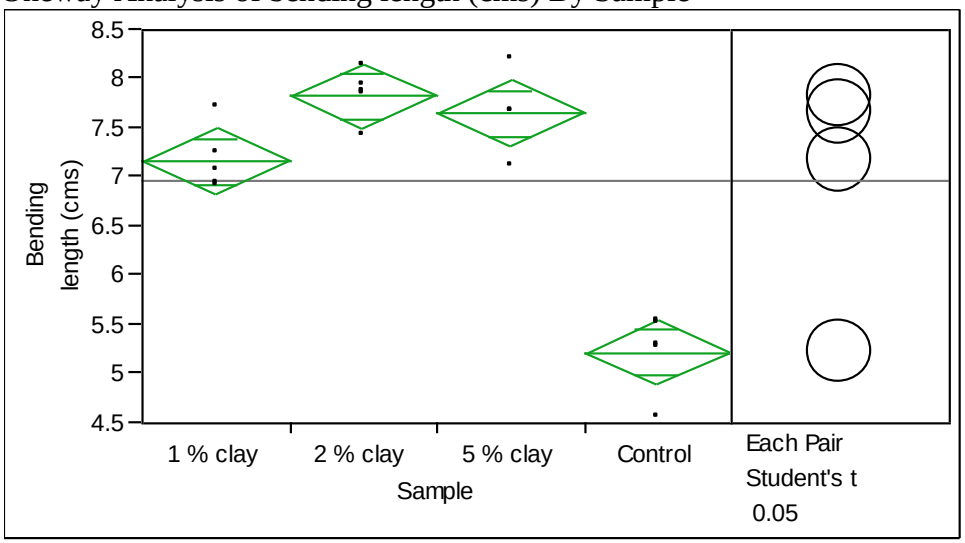

Figure 5. 14. Bending length of samples.

Oneway Anova

Summary of Fit

Rsquare	0.917043
Adj Rsquare	0.901488
Root Mean Square Error	0.348322
Mean of Response	6.96375
Observations (or Sum Wgts)	20

Analysis of Variance

Source	DF	Sum of Squares	Mean Square	F Ratio	Prob > F
Sample	3	21.459344	7.15311	58.9568	<.0001
Error	16	1.941250	0.12133		
C. Total	19	23.400594			

Means for Oneway Anova

Level	Number	Mean	Std Error	Lower 95%	Upper 95%
1 % clay	5	7.16000	0.15577	6.8298	7.4902
2 % clay	5	7.82500	0.15577	7.4948	8.1552
5 % clay	5	7.65000	0.15577	7.3198	7.9802
Control	5	5.22000	0.15577	4.8898	5.5502

Std Error uses a pooled estimate of error variance

Means Comparisons

Abs(Dif)-LSD	2 % clay	5 % clay	1 % clay	Control
2 % clay	-0.4670	-0.2920	0.1980	2.1380
5 % clay	-0.2920	-0.4670	0.0230	1.9630
1 % clay	0.1980	0.0230	-0.4670	1.4730
Control	2.1380	1.9630	1.4730	-0.4670

Positive values show pairs of means that are significantly different.

Connecting letter report

Level			Mean
2 % clay	A		7.8250000
5 % clay	A		7.6500000
1 % clay		B	7.1600000
Control		C	5.2200000

Levels not connected by same letter are significantly different.

Ordered difference report

Level	- Level	Difference	Lower CL	Upper CL	p-Value	Difference
2 % clay	Control	2.605000	2.13799	3.072011	<.0001	
5 % clay	Control	2.430000	1.96299	2.897011	<.0001	
1 % clay	Control	1.940000	1.47299	2.407011	<.0001	
2 % clay	1 % clay	0.665000	0.19799	1.132011	0.0082	
5 % clay	1 % clay	0.490000	0.02299	0.957011	0.0409	
2 % clay	5 % clay	0.175000	-0.29201	0.642011	0.4386	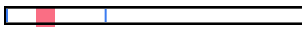

3. Melt blown web with nanoclay

Fiber diameter

Oneway Analysis of Column 2 By Column 1

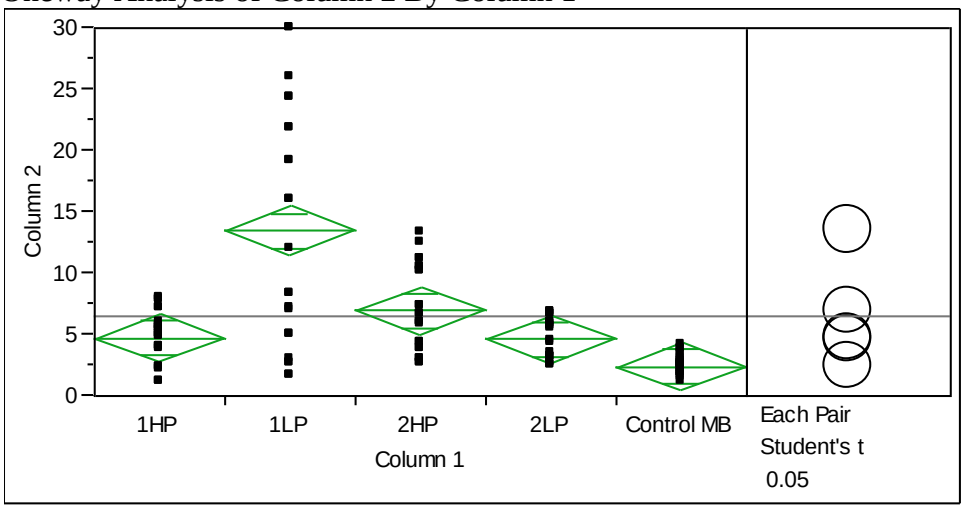

Figure 5. 15. Meltblown web fiber diameter measurements.

Oneway Anova

Summary of Fit

Rsquare	0.402628
Adj Rsquare	0.380906
Root Mean Square Error	4.735049
Mean of Response	6.422261
Observations (or Sum Wgts)	115

Analysis of Variance

Source	DF	Sum of Squares	Mean Square	F Ratio	Prob > F
Column 1	4	1662.2692	415.567	18.5350	<.0001
Error	110	2466.2758	22.421		
C. Total	114	4128.5450			

Means for Oneway Anova

Level	Number	Mean	Std Error	Lower 95%	Upper 95%
1HP	23	4.7283	0.98733	2.772	6.685
1LP	23	13.4635	0.98733	11.507	15.420
2HP	23	6.9230	0.98733	4.966	8.880
2LP	23	4.6104	0.98733	2.654	6.567
Control MB	23	2.3861	0.98733	0.429	4.343

Std Error uses a pooled estimate of error variance

Means Comparisons

Comparisons for each pair using Student's t

t	Alpha
1.98177	0.05

Abs(Dif)-LSD	1LP	2HP	1HP	2LP	Control MB
1LP	-2.7671	3.7733	5.9681	6.0859	8.3103
2HP	3.7733	-2.7671	-0.5723	-0.4545	1.7698
1HP	5.9681	-0.5723	-2.7671	-2.6493	-0.4249
2LP	6.0859	-0.4545	-2.6493	-2.7671	-0.5428
Control MB	8.3103	1.7698	-0.4249	-0.5428	-2.7671

Positive values show pairs of means that are significantly different.

Connecting letter report

Level			Mean
1LP	A		13.463478
2HP		B	6.923043
1HP		B	C 4.728261
2LP		B	C 4.610435
Control MB			C 2.386087

Levels not connected by same letter are significantly different.

Ordered difference report

Level	- Level	Difference	Lower CL	Upper CL	p-Value	Difference
1LP	Control MB	11.07739	8.31027	13.84451	<.0001	
1LP	2LP	8.85304	6.08592	11.62016	<.0001	
1LP	1HP	8.73522	5.96810	11.50234	<.0001	
1LP	2HP	6.54043	3.77332	9.30755	<.0001	
2HP	Control MB	4.53696	1.76984	7.30408	0.0015	
1HP	Control MB	2.34217	-0.42494	5.10929	0.0963	
2HP	2LP	2.31261	-0.45451	5.07973	0.1005	
2LP	Control MB	2.22435	-0.54277	4.99147	0.1140	
2HP	1HP	2.19478	-0.57234	4.96190	0.1189	
1HP	2LP	0.11783	-2.64929	2.88494	0.9329	

Fit of model for MB web properties

Leverage Plot

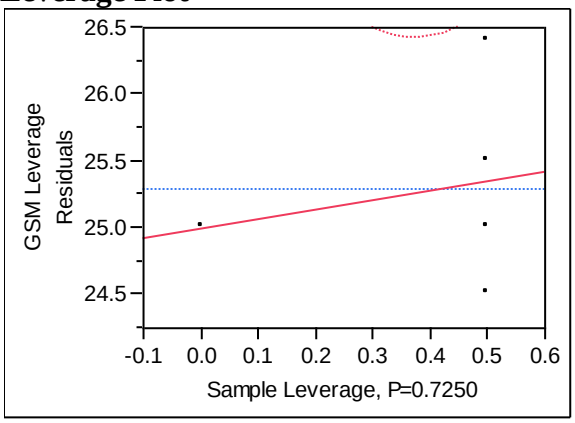

Figure 5. 16. MB web GSM.

Analysis of Variance

Source	DF	Sum of Squares	Mean Square	F Ratio
Model	1	0.0980000	0.098000	0.1492
Error	3	1.9700000	0.656667	Prob > F
C. Total	4	2.0680000		0.7250

Parameter Estimates

Term	Estimate	Std Error	t Ratio	Prob>|t|
Intercept	25	0.81035	30.85	<.0001
Sample	0.7	1.811997	0.39	0.7250

Thickness (mm)
Whole Model

Leverage Plot

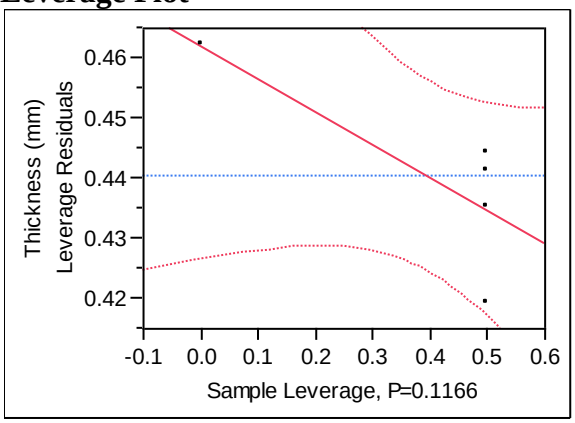

Figure 5. 17. MB web thickness.

Analysis of Variance

Source	DF	Sum of Squares	Mean Square	F Ratio
Model	1	0.00059405	0.000594	4.7811
Error	3	0.00037275	0.000124	Prob > F
C. Total	4	0.00096680		0.1166

Parameter Estimates

Term	Estimate	Std Error	t Ratio	Prob>|t|
Intercept	0.462	0.011147	41.45	<.0001
Sample	-0.0545	0.024925	-2.19	0.1166

Response Yellowness
Leverage Plot

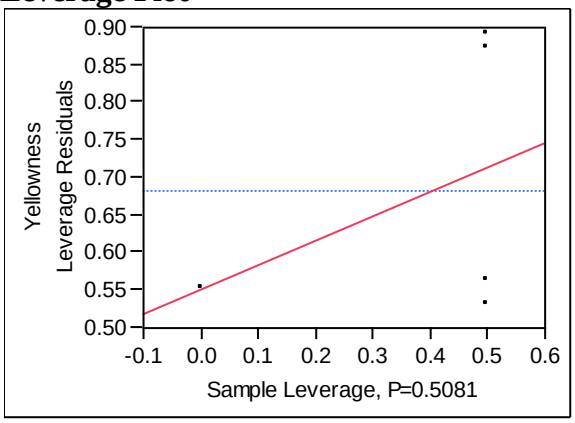

Figure 5. 18. MB web yellowness.

Analysis of Variance

Source	DF	Sum of Squares	Mean Square	F Ratio
Model	1	0.02112500	0.021125	0.5615
Error	3	0.11287500	0.037625	Prob > F
C. Total	4	0.13400000		0.5081

Parameter Estimates

Term	Estimate	Std Error	t Ratio	Prob>|t|
Intercept	0.55	0.193972	2.84	0.0659
Sample	0.325	0.433734	0.75	0.5081

Response bending length (cms)

Leverage Plot

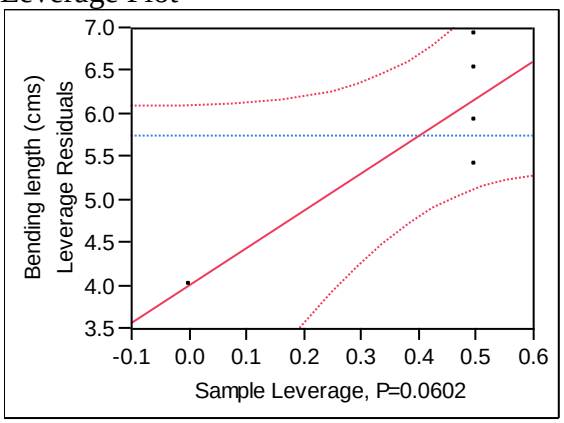

Figure 5. 19. MB web bending length.

Analysis of Variance

Source	DF	Sum of Squares	Mean Square	F Ratio
Model	1	3.7845000	3.78450	8.6834
Error	3	1.3075000	0.43583	Prob > F
C. Total	4	5.0920000		0.0602

Parameter Estimates

Term	Estimate	Std Error	t Ratio	Prob>|t|
Intercept	4	0.660177	6.06	0.0090
Sample	4.35	1.4762	2.95	0.0602

Air permeability (cm3/cm2/sec)

Leverage Plot

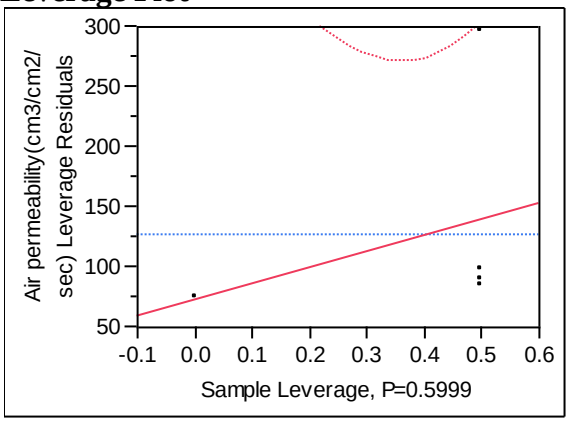

Figure 5. 20. MB web air permeability.

Analysis of Variance

Source	DF	Sum of Squares	Mean Square	F Ratio
Model	1	3615.360	3615.4	0.3417
Error	3	31737.388	10579.1	Prob > F
C. Total	4	35352.748		0.5999

Parameter Estimates

Term	Estimate	Std Error	t Ratio	Prob>|t|
Intercept	73.2	102.8549	0.71	0.5280
Sample	134.45	229.9905	0.58	0.5999

Response Peak force (Kgs)

Leverage Plot

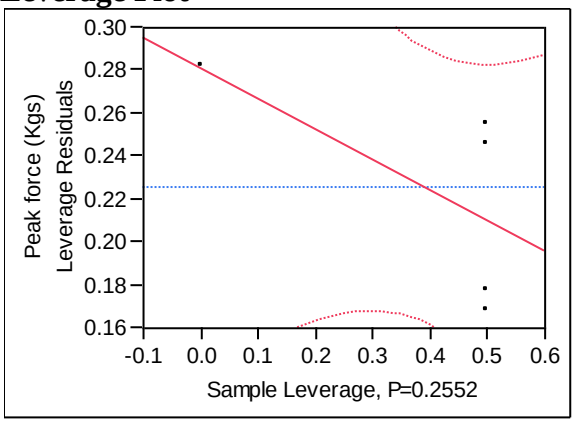

Figure 5. 21. MB web peak force.

Analysis of Variance

Source	DF	Sum of Squares	Mean Square	F Ratio
Model	1	0.00395457	0.003955	1.9679
Error	3	0.00602856	0.002010	Prob > F
C. Total	4	0.00998313		0.2552

Parameter Estimates

Term	Estimate	Std Error	t Ratio	Prob>|t|
Intercept	0.281232	0.044828	6.27	0.0082
Sample	-0.140616	0.100238	-1.40	0.2552

Peak Elongation (%)
Leverage Plot

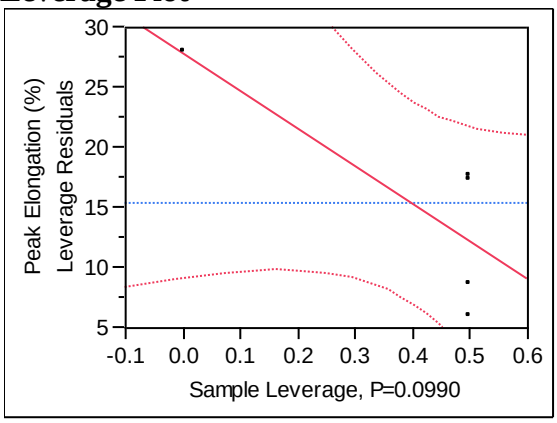

Figure 5. 22. MB web peak elongation.

Analysis of Variance

Source	DF	Sum of Squares	Mean Square	F Ratio
Model	1	195.31250	195.312	5.5901
Error	3	104.81610	34.939	Prob > F
C. Total	4	300.12860		0.0990

Parameter Estimates

Term	Estimate	Std Error	t Ratio	Prob>|t|
Intercept	27.9	5.910897	4.72	0.0180
Sample	-31.25	13.21717	-2.36	0.0990

4. Injection molded PP composites

Crystallinity index

Regression Plot

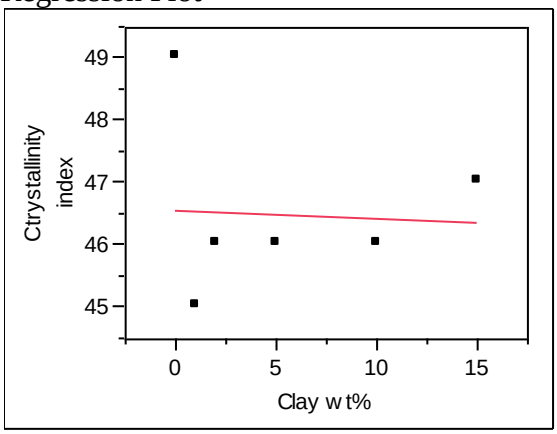

Figure 5. 23. Results of fiber crystallinity.

Analysis of Variance

Source	DF	Sum of Squares	Mean Square	F Ratio
Model	1	0.0360231	0.03602	0.0152
Error	4	9.4639769	2.36599	Prob > F
C. Total	5	9.5000000		0.9077

Parameter Estimates

Term	Estimate	Std Error	t Ratio	Prob>|t|
Intercept	46.579251	0.898247	51.86	<.0001
Clay wt%	-0.014409	0.116777	-0.12	0.9077

Leverage Plot

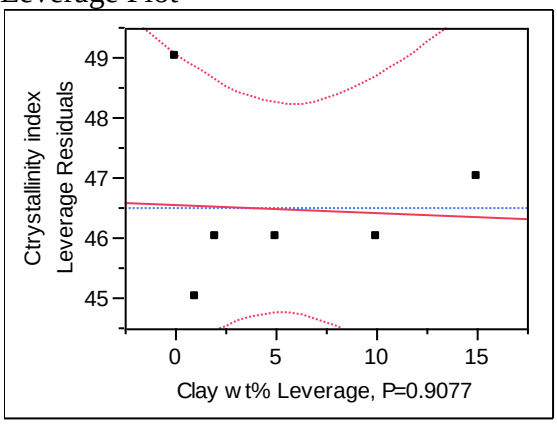

Figure 5. 24. Results of fiber crystallinity.

Response Modulus (Gpa)

Regression Plot

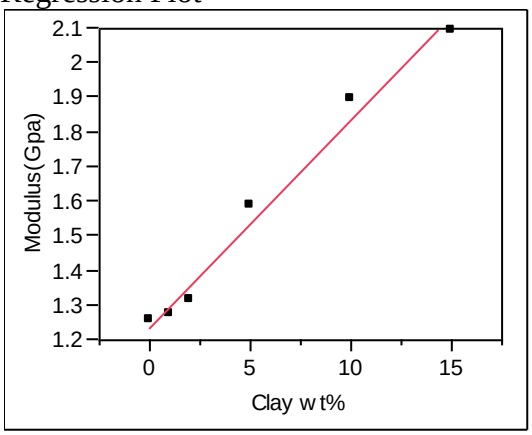

Figure 5. 25. Tensile properties of injection molded samples.

Analysis of Variance

Source	DF	Sum of Squares	Mean Square	F Ratio
Model	1	0.62268148	0.622681	232.6363
Error	4	0.01070652	0.002677	Prob > F
C. Total	5	0.63338800		0.0001

Parameter Estimates

Term	Estimate	Std Error	t Ratio	Prob>|t|
Intercept	1.2365072	0.030212	40.93	<.0001
Clay wt%	0.0599078	0.003928	15.25	0.0001

Leverage Plot

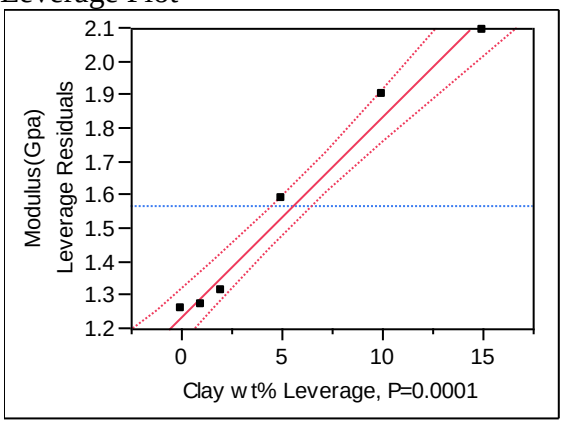

Figure 5. 26. Tensile properties of injection molded samples.

Response Tensile strain (mm/mm)

Regression Plot

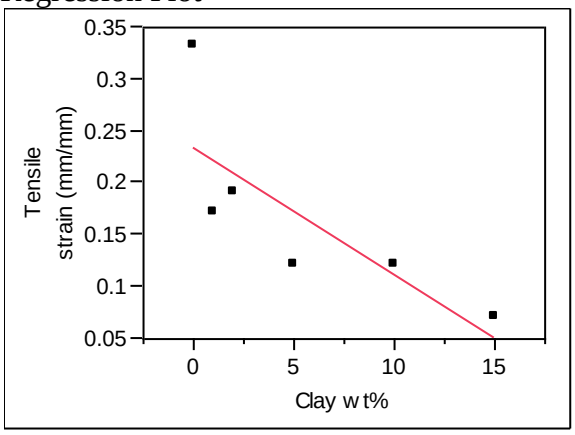

Figure 5. 27. Tensile properties of injection molded samples.

Analysis of Variance

Source	DF	Sum of Squares	Mean Square	F Ratio
Model	1	0.02564836	0.025648	6.6279
Error	4	0.01547914	0.003870	Prob > F
C. Total	5	0.04112750		0.0617

Parameter Estimates

Term	Estimate	Std Error	t Ratio	Prob>|t|
Intercept	0.2333718	0.036327	6.42	0.0030
Clay wt%	-0.012159	0.004723	-2.57	0.0617

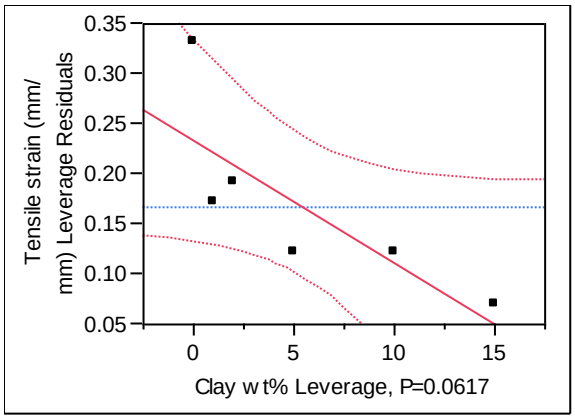

Figure 5. 28. Leverage Plot of tensile properties of injection molded samples.

BE (J)

Oneway analysis of BE (J) by Clay wt%

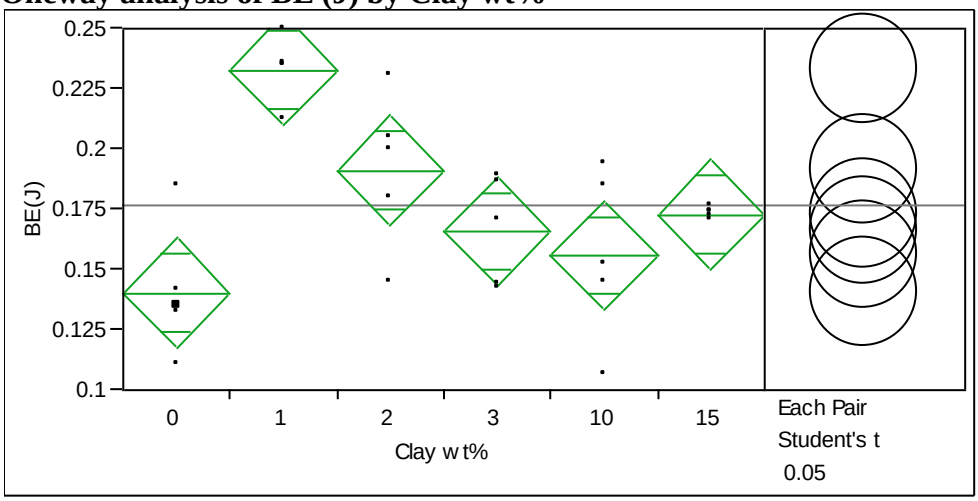

Figure 5. 29. Breaking energy BE(J) for different injection molded samples.

Oneway Anova

Analysis of Variance

Source	DF	Sum of Squares	Mean Square	F Ratio	Prob > F
Clay wt%	5	0.02630057	0.005260	8.6570	<.0001
Error	24	0.01458280	0.000608		
C. Total	29	0.04088337			

Results indicate presence of variance in the group.

Means Comparisons

Comparisons for each pair using Student's t

t	Alpha
2.06390	0.05

Connecting letter report

Level				Mean
1	A			0.23280000
2		B		0.19120000
15		B	C	0.17280000
3		B	C D	0.16580000
10			C D	0.15580000
0			D	0.14020000

Levels not connected by same letter are significantly different.

Ordered difference report

Level	- Level	Difference	Lower CL	Upper CL	p-Value	Difference
1	0	0.0926000	0.060424	0.1247761	<.0001	
1	10	0.0770000	0.044824	0.1091761	<.0001	
1	3	0.0670000	0.034824	0.0991761	0.0002	
1	15	0.0600000	0.027824	0.0921761	0.0008	
2	0	0.0510000	0.018824	0.0831761	0.0032	
1	2	0.0416000	0.009424	0.0737761	0.0134	
2	10	0.0354000	0.003224	0.0675761	0.0324	
15	0	0.0326000	0.000424	0.0647761	0.0473	
3	0	0.0256000	-0.006576	0.0577761	0.1136	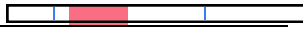
2	3	0.0254000	-0.006776	0.0575761	0.1163	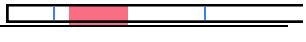
2	15	0.0184000	-0.013776	0.0505761	0.2495	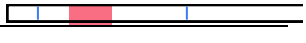
15	10	0.0170000	-0.015176	0.0491761	0.2863	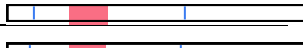
10	0	0.0156000	-0.016576	0.0477761	0.3270	
3	10	0.0100000	-0.022176	0.0421761	0.5273	
15	3	0.0070000	-0.025176	0.0391761	0.6575	

Whole Model

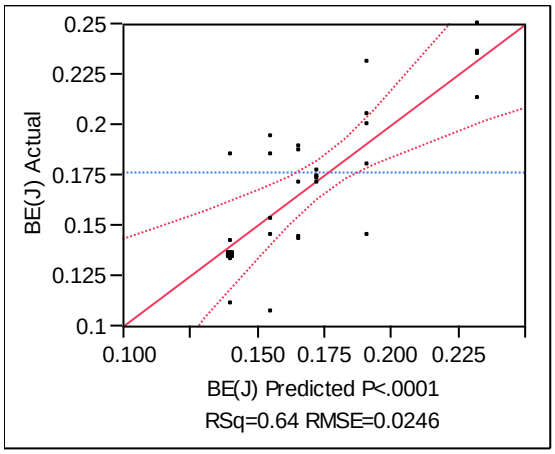

Figure 5. 30. Predicted plot of breaking energy BE (J) for different injection molded samples.

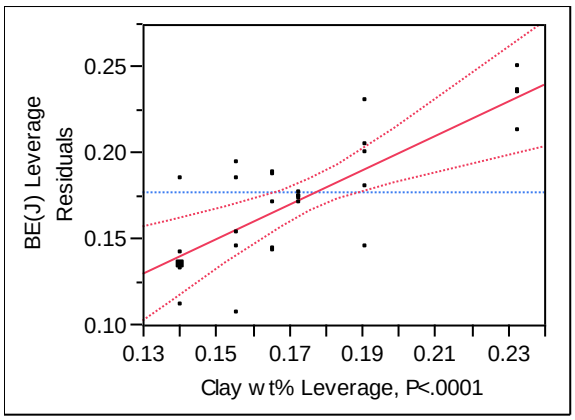

Figure 5. 31. Leverage Plot of breaking energy BE(J) for different injection molded samples.

Analysis of Variance

Source	DF	Sum of Squares	Mean Square	F Ratio
Model	5	0.02630057	0.005260	8.6570
Error	24	0.01458280	0.000608	Prob > F
C. Total	29	0.04088337		<.0001

Effect Tests

Source	Nparm	DF	Sum of Squares	F Ratio	Prob > F
Clay wt%	5	5	0.02630057	8.6570	<.0001

Vita

Raghavendra R Hegde was born in Kumta Karnataka, India. He attended Govt. SKSJT Institute Bangalore, India (1998-2002) from where he graduated with a Bachelor of Textile Technology in Engineering. Raghavendra came to the United States of America in the spring of 2004 for his Master's degree in the Department of Materials science and Engineering at University of Tennessee, Knoxville. He worked as Graduate Research assistant for dissertation research under advice of Dr. Gajanan Bhat and obtained M.S degree in Materials science and Textiles in spring of 2006.

In 2006 Raghavendra accepted a Graduate Research Assistantship position at University of Tennessee at Knoxville and began his PhD degree in Polymer Engineering under the advisory of Dr. Gajanan Bhat from Polymer Engineering department and later under co advisory of Dr. Dayakar Penumadu of Civil and Environmental Engineering department. Raghavendra Hegde has graduated as a Doctor of Philosophy in August 2009.